Search for the Decay $K_L \to \pi^0 \nu \overline{\nu}$

Kazunori Hanagaki

September 23, 1998

Acknowledgements

My first thanks go to Yorikiyo Nagashima, my advisor, for giving me a wonderful opportunity for the research of high energy physics, and for his gentle support. I would like to thank M. Takita, M. Hazumi, T. Hara, and I. Suzuki for their invaluable advice on physics and experimental technique.

The work presented here is the result of the efforts of many people. I would like to thank those who struggled to design and construct the experiment, to start it up, to take data, to calibrate the detectors, and to develop the code for analysis. In particular, I would like to thank Y.B. Hsiung, Y.W. Wah, B. Winstein, and T. Yamanaka who proposed this exciting experiment.

I would like to thank K. Higashijima, T. Kishimoto, Y. Nagashima, T. Nakano, and T. Yamanaka, who gave me invaluable advice as members of referees of this thesis. I especially enjoyed discussions with T. Nakano.

My special thanks go to T. Nakaya who taught me both physics and analysis. Besides, my comfortable life in U.S. was due to his useful advice. I greatly appreciate the help of L. Bellantoni, R. Ben-David, E. Cheu, R. Kessler, and P. Shawhan. Their advice on physics and analysis was crucial for this thesis. Especially, I enjoyed the discussion on physics with R. Ben-David. I would like to thank L. Bellantoni, R. Ben-David, B. Hsiung, R. Kessler, and R.J. Tesarek who corrected English grammar and gave me invaluable comments on this thesis.

I would like to appreciate the kindness and friendship of R.J. Tesarek. Without him, there should not be wonderful three years in U.S.. I don't forget the barbecue in front of Newmuon. I also enjoyed discussions with S. Bright, G. Graham, B. Quinn and E.D. Zimmerman, who played important roles in calibration/data taking in E799, as well as L. Bellantoni and R.J. Tesarek. For the life at Newmuon, I never forget smile of A. Alavi-Harati and T. Alexopoulos. My special thanks go to R. Coleman for his comments on the beam line. A wonderful memory at Arizona was due to J. Belz, R. Ford, H. Nguyen, M. Pang, R.E. Ray, P. Shanahan, R. Tschirhart, and T. Yamanaka.

I really appreciate the kindness of J. Jennings and S. Field at the beginning of the life as a KTeVer. They taught me about KTeV and English.

I would like to thank T. Kawasaki and T. Yamaguchi for their kindness and friendship. To the colleagues at Osaka: M. Sadamoto, K. Senyo, S. Hidaka, K. Kurebayashi, and K. Mori, I appreciate their help. Really I enjoyed Fermilab life with M. Sadamoto, K. Senyo, and S. Hidaka. I am indebted to S. Tsuzuki for her gentle support over the years. I really appreciate it.

My special thanks go to Shinya Taniguchi for his friendship for a decade. Really I enjoyed discussions with him on physics and other stuff. Seven years in Osaka was invaluable experience by the relation with him.

I would like to thank my parents, Kunitoshi and Sekie Hanagaki, for their encouragement and support since I was a child. I also acknowledge my family, Yoshihiko, and Aiko Hanagaki, for their wonderful support. My special thanks should go to my wife, Tomoko Hanagaki, for her continuous support and encouragement. Without her invaluable help, this thesis would not exist. For my parents, family and wife, high energy physics must be really eccentric research. I really appreciate the supports for such a study.

Finally, I would like to thank Taku Yamanaka for his supervising over the years and his enthusiasm for my work. He taught me physics, experimental technique, analysis and more. I am sure this thesis did not exist without his help and advice. Even my interest in high energy physics may come from him. He made me select a wrong track, but I like this way.

Now, it's over!

Contents

List of Tables

List of Figures

Abstract

This thesis describes a search for $K_L \to \pi^0 \nu \bar{\nu}$ decay, carried out as a part of E799-II experiment at Fermilab. Within the Standard Model, the $K_L \to \pi^0 \nu \bar{\nu}$ decay is dominated by the direct CP violating processes, and thus a discovery of the decay implies confirmation of the direct CP violation. Due to theoretically clean calculations, a measurement of $Br(K_L \to \pi^0 \nu \bar{\nu})$ is one of the best ways to determine the CKM parameter, and is one of the most sensitive probes for a new physics. No such events were observed, and we set an upper limit

$$Br(K_L \to \pi^0 \nu \bar{\nu}) < 5.9 \times 10^{-7},$$

at the 90% confidence level. This result represents an improvement of a factor of 98 over the current limit listed by Particle Data Group, and of a factor of 3 over the recent preliminary result.

Chapter 1

Introduction

There are some symmetries and invariances in nature. Physics, especially particle physics, has been developing by the study of these symmetries or invariances. Indeed, some of the greatest concepts were discovered from such pursuits of the symmetries and invariances.

In elementary particle physics, the search and study of symmetries have been continuing. Of particular interest in this field are three discrete symmetries:

- Charge conjugation(C), interchange of particle and anti-particle.
  $C\psi(\vec{x},t) = \bar{\psi}(\vec{x},t)$.
- Parity(P), space inversion.
  $P\psi(\vec{x},t) = \psi(-\vec{x},t)$.
- Time reversal(T), inversion of the time coordinate.
  $T\psi(\vec{x},t) = \psi(\vec{x},-t)$.

For each operation or a product of operations, physical states have an eigenvalue of $+1$ or -1 if they are in eigenstates. We call the eigenstate with an eigenvalue of $+1(-1)$ as even(odd) state. General principles of relativistic field theory require invariance under the operation of these products CPT [1, 2], called CPT theorem. All the experimental results up to date are consistent with the CPT theorem. This CPT symmetry predicts the equality of masses, lifetimes and magnitude of electric charge of particles and anti-particles. It had been believed in the early days that particle interactions would be invariant under each of three individual operators C, P and T.

There was a mystery in particle physics, called $\tau - \theta$ puzzle, where two particles with the same mass and lifetime(they were K^+ in fact) decayed into both a P even two-pion state(θ^+ decays) and a P odd three-pion state(τ^+ decays). Based on a concept of parity conservation, two different particles were needed to explain this phenomenon. In 1956, Lee and Yang claimed no necessity for invariance to the parity operation in weak interactions and proposed that parity violation could explain the $\tau - \theta$ puzzle [3]. They suggested that evidence for parity nonconservation could be established through the observation of angular asymmetry in the β decay of oriented nuclei. This is because the flight direction of the emitted electron is inversed by the parity operation while the direction of the spin($-\vec{x} \times -\vec{p} = \vec{x} \times \vec{p}$) stays the same and thus one can distinguish between the original world and that transformed by parity operation. By Wu *et. al.* [4], an asymmetry in direction of emitted electrons was soon observed in the β decay,

$$^{60}Co \rightarrow {}^{60}N_i + e^- + \bar{\nu_e} \ ,$$

where the spin of ^{60}Co nuclei was oriented with the same direction by external magnetic field. The

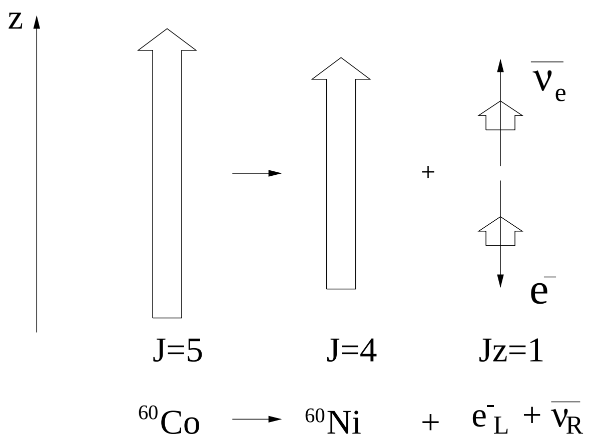

Figure 1.1: β decay in ^{60}Co. Electrons prefer to emit opposite to the spin direction of ^{60}Co nuclei.

electrons prefer to emit opposite to the spin orientation of ^{60}Co nuclei. The puzzle was solved: the parent particles were the same, but parity was violated in the decays.

We can now explain the origin of P or C violation[1]. They arise from the left-handed nature of the W boson, i.e. weak interactions couple only to left-handed neutrinos or to right-handed antineutrinos(see Figure 1.1). However, there has been the new puzzle of discrete symmetry violation, CP violation, which interests particle physicists today.

Lee, Oehme and Yang derived from the CPT theorem that if one of the operations, C, P or T is not conserved, then at least one of the others is not conserved [5]. However, the product CP had been believed to be conserved in the weak interaction because the CP operation corresponds to a transformation from left-handed neutrinos to right-handed antineutrinos and these two states are physically observable. On the other hand, operation of C or P alone transforms the neutrino into one of the charge conjugate states, which has not been observed. In 1964, this world view was upset by the discovery of CP violation in decays of long lived component of the neutral kaon demonstrated by Christenson, Cronin, Fitch and Turley [6]. The long lived neutral kaon had been believed to be purely CP odd state, but it was found that they also decay to CP even two-pion state. Since then, CP violation has been observed only in the weak interactions in neutral kaon system. In addition, such discrete asymmetry as C, P, or CP violation, was observed only in weak interactions, and the strong and electromagnetic interactions are invariant under the operation in all experiments to date.

Although it has been more than 30 years since its initial discovery of the CP violation, we have not yet completely understood the origin of CP violation. The Standard Model may be able to explain the phenomena of CP violation by introducing a CP violating phase. It may also be possible to explain CP violation by theories outside the Standard Model. Currently we do not have enough information to choose correct theory.

This thesis describes a search for rare decay $K_L \to \pi^0 \nu\bar{\nu}$, which is believed to be one of the best ways to understand the origin of the CP violation. As will be discussed in the following introduction, a branching ratio of $K_L \to \pi^0 \nu\bar{\nu}$ have a potential to choose a correct theory to describe the nature. A discovery of $K_L \to \pi^0 \nu\bar{\nu}$ decays at the level predicted by the Standard Model will bring an end of the puzzle of CP violation. If the branching ratio differs from the Standard Model expectation, it strongly suggests an effect beyond the Standard Model.

[1]The C symmetry is also violated in weak interactions.

In this introduction, we will cover the theoretical background for the $K_L \to \pi^0 \nu \bar{\nu}$. It starts with the description of phenomenology for neutral kaon system and the CP violation. Next, we introduce the treatment of CP violation in the Standard Model, which is the most popular explanation in this field. In Section 1.3, we describe the $K_L \to \pi^0 \nu \bar{\nu}$ decay in the context of the Standard Model, and other explanation derived from models outside the Standard Model. Past experimental results are also mentioned there. Section 1.4 summarizes the introduction. The last part in this chapter outlines the rest of this thesis.

1.1 Neutral Kaon and CP Violation

In order to understand the theoretical interest of $K_L \to \pi^0 \nu \bar{\nu}$ decay, one needs to know about the CP violation in neutral kaon system. To explain the CP violation, we describe the kaon phenomenology as a beginning of the introduction.

The K^0 and $\bar{K}^0$ mesons are strangeness eigenstates:

$$K^0 = (d, \bar{s}) \ ; \ \bar{K}^0 = (\bar{d}, s) \ , \tag{1.1}$$

produced through strong interactions, such as:

$$\pi^- + p \to K^0 + \Lambda \ .$$

It was recognized in very early days that K^0 decays, like $K^0 \to \pi^+\pi^-$, did not conserve the strangeness, and that the final state of the charge conjugate decay was identical to that of the original one [7]. This can be interpreted that the K^0 decays as a mixture of both K^0 and $\bar{K}^0$ states through virtual transition by the weak interaction. It implies that $\langle K^0|H|\bar{K}^0\rangle \neq 0$, where the H consists of the strong interaction H_S producing masses, and the weak interaction H_W leading to decays. We begin the kaon phenomenology with the effective Hamiltonian H_{eff} [8, 9, 10] to describe neutral kaon system.

If we define H_{eff} as a second order Hamiltonian, and a and $\bar{a}$ as time dependent amplitudes for K^0 and $\bar{K}^0$ states, respectively, then H_{eff} must contain Δ S = 2 weak Hamiltonian which mixes K^0 and $\bar{K}^0$. Therefore, we can write a Schrödinger equation like

$$i\frac{d}{dt}\begin{pmatrix} a \\ \bar{a} \end{pmatrix} = H_{eff}\begin{pmatrix} a \\ \bar{a} \end{pmatrix} , \tag{1.2}$$

where H_{eff} is a 2×2 matrix connecting K^0 and $\bar{K}^0$:

$$H_{eff} = \begin{pmatrix} \langle K^0|H_{11}|K^0\rangle & \langle K^0|H_{12}|\bar{K}^0\rangle \\ \langle \bar{K}^0|H_{21}|K^0\rangle & \langle \bar{K}^0|H_{22}|\bar{K}^0\rangle \end{pmatrix} .$$

Using the fact that H_W can be treated as perturbative term with respect to the H_s, we write H_{eff} as the combination of two Hermitian matrices, M and Γ:

$$\begin{aligned} H_{eff} &\equiv M - i\frac{\Gamma}{2} && (1.3) \\ &= \begin{pmatrix} M_{11} - \frac{i}{2}\Gamma_{11} & M_{12} - \frac{i}{2}\Gamma_{12} \\ M_{21} - \frac{i}{2}\Gamma_{21} & M_{22} - \frac{i}{2}\Gamma_{22} \end{pmatrix} , && (1.4) \end{aligned}$$

$$\begin{aligned} M_{ij} &= M_i\delta_{ij} + \langle i|H_W|j\rangle + P\sum \frac{\langle i|H_W|n\rangle\langle n|H_W|j\rangle}{M_i - E_n} , \\ \Gamma_{ij} &= 2\pi \sum \delta(M_i - E_n)\langle i|H_W|n\rangle\langle n|H_W|j\rangle . \end{aligned}$$

The Γ is called decay matrix and is responsible for kaon decays into physically accessible states. The M is called mass matrix, and its off-diagonal elements mix K^0 and $\bar{K^0}$ states. These two matrices results in the CP violation in neutral kaon system, as will be explained later.

Let us turn our attention to the CP of neutral kaons in order to start the discussion of CP violation. As shown in Equation 1.1, the K^0 and $\bar{K^0}$ are CP conjugate states to each other:

$$CP|K^0\rangle = |\bar{K^0}\rangle\,, \tag{1.5}$$

$$CP|\bar{K^0}\rangle = |K^0\rangle\,. \tag{1.6}$$

Although there is still an ambiguity on the phase between these two states, we can choose the phase as the above because the phase is physically unobservable. Since our interest is a CP violation, we need to introduce CP eigenstates instead of K^0 and $\bar{K^0}$ which are not in CP eigenstates. Let us define K_1 and K_2 as

$$|K_1\rangle = \frac{1}{\sqrt{2}}(|K^0\rangle + |\bar{K^0}\rangle)\,, \tag{1.7}$$

$$|K_2\rangle = \frac{1}{\sqrt{2}}(|K^0\rangle - |\bar{K^0}\rangle)\,. \tag{1.8}$$

As shown the equations below,

$$CP|K_1\rangle = \frac{1}{\sqrt{2}}(|\bar{K^0}\rangle + |K^0\rangle) = |K_1\rangle\,, \tag{1.9}$$

$$CP|K_2\rangle = \frac{1}{\sqrt{2}}(|\bar{K^0}\rangle - |K^0\rangle) = -|K_2\rangle\,, \tag{1.10}$$

K_1 is a CP even, and K_2 is a CP odd state. Since $\pi^+\pi^-$ or $\pi^0\pi^0$ is a CP even, and $\pi^0\pi^0\pi^0$ is a CP odd state[2], K_1 can decay to the $\pi^+\pi^-$ or $\pi^0\pi^0$ final states, and K_2 can decay to the $\pi^0\pi^0\pi^0$ state. Therefore it had been believed that the short lived kaon should correspond to the K_1 and the long lived kaon to the K_2, in which the difference in lifetimes arose from the amount of phase space to the final states, until CP violation was observed in 1964.

In our current knowledge, there is a possibility to have two kinds of CP violation, one is called "indirect CP violation" and the other is called "direct CP violation". The following two sections describe these two phenomena.

1.1.1 Indirect CP Violation

For the sake of clarity, we will assume that the CPT symmetry is conserved in the following discussion.

In 1964, CP violation was first observed in the decay of long lived kaons into two-pion final states. To explain this process, the long lived kaon, K_L, and the short lived kaon, K_S, were interpreted as a superposition of the K_1 and K_2, as shown in Equation 1.11 and 1.12, where the ϵ determines the size of $K_1(K_2)$ contamination to the $K_L(K_S)$, and the first coefficient are for normalization. They imply that the $K^0 - \bar{K^0}$ mixing is asymmetric by $|\epsilon|$. The contaminated K_1

[2]The CP state of 2π or 3π is explained below.
$C\pi^0 = \pi^0$, $P\pi = -\pi$. Because of $\pi^+ \leftrightarrow \pi^-$ by C operation, C and P operations are equivalent for $\pi^+\pi^-$, and thus $CP(\pi^+\pi^-) = +1$. In case of $\pi^0\pi^0$, CP operation is equivalent to exchange of the two particles because π^0's are spin-less. Thus, $CP(\pi^0\pi^0) = +1$ by the Bose symmetry. This also means that the angular momentum between the two π^0's are even. For $\pi^0\pi^0\pi^0$, the angular momentum between the $\pi^0\pi^0$ system and π^0 must be even because the total momentum equals to zero and the two π^0 system has an even angular momentum. Therefore, $CP(3\pi^0) = -1$ because $CP(\pi^0) = -1$ and $CP(2\pi^0) = +1$.

in the K_L is considered to decay into the two-pion final state [11]. Therefore, decay processes do not contribute to the CP violation, and the small contamination of the K_1 caused the CP violation.

$$\begin{aligned} |K_L\rangle &= \frac{1}{\sqrt{1+\epsilon^2}}(|K_2\rangle + \epsilon|K_1\rangle) \\ &= \frac{1}{\sqrt{2(1+\epsilon^2)}}((1+\epsilon)|K^0\rangle - (1-\epsilon)|\bar{K^0}\rangle)\,, \end{aligned} \tag{1.11}$$

$$\begin{aligned} |K_S\rangle &= \frac{1}{\sqrt{1+\epsilon^2}}(|K_1\rangle + \epsilon|K_2\rangle) \\ &= \frac{1}{\sqrt{2(1+\epsilon^2)}}((1+\epsilon)|K^0\rangle + (1-\epsilon)|\bar{K^0}\rangle)\,. \end{aligned} \tag{1.12}$$

This CP violating effect due to the asymmetric $K^0 - \bar{K^0}$ mixing is called "indirect CP violation".

In order to see the origin of non-zero value of ϵ, and thus the asymmetric $K^0 - \bar{K^0}$ mixing, we consider mass eigenstates of K_L and K_S. Diagonalizing Equation 1.2 and given definite masses $m_{L,S}$ and lifetimes $\tau_{L,S}$ (L and S represent the long and short lived neutral kaons, respectively), we obtain

$$H_{eff}|K_{L,S}\rangle = (m_{L,S} - i\Gamma_{L,S}/2)|K_{L,S}\rangle\,. \tag{1.13}$$

Substituting Equation 1.11 and 1.12 into Equation 1.13, we derive the relation:

$$\epsilon = \frac{\langle\bar{K^0}|H_{eff}|K^0\rangle - \langle K^0|H_{eff}|\bar{K^0}\rangle}{2\Delta m + i(\Gamma_S - \Gamma_L)}\,, \tag{1.14}$$

to the first order in ϵ. In this expression, Δm is the mass difference between the long and short lived kaons:

$$\Delta m \equiv m_L - m_S\,. \tag{1.15}$$

As shown in Equation 1.14, non-zero value of the ϵ arises from the different amplitudes between $K^0 \to \bar{K^0}$ and $\bar{K^0} \to K^0$. If the CP symmetry were exactly conserved, matter and anti-matter in the universe would be coupled and disappeared, except for those which accidentally did not find their partners. However, there must have been CP violating effect to keep matter in the universe, which generated galaxy, planets, etc., and this CP violation in the weak interaction could have played a small role in this process.

We now evaluate the magnitude of ϵ.

Assuming $\Delta S = \Delta Q$ rule[3], $K^0 \to \pi^- l^+ \nu_l$ and $\bar{K^0} \to \pi^- l^- \bar{\nu_l}$ processes, as shown in Figure 1.2, are allowed in semi-leptonic decays. Based on the above assumption and Equation 1.11, the amplitude $K_L \to \pi^- l^+ \nu_l (K_L \to \pi^+ l^- \bar{\nu_l})$ is linear to $1+\epsilon(1-\epsilon)$. Therefore, the mixing parameter ϵ is obtained from the decay asymmetry δ in semi-leptonic decay of K_L defined as

$$\delta = \frac{\Gamma(K_L \to \pi^- l^+ \nu_l) - \Gamma(K_L \to \pi^+ l^- \bar{\nu_l})}{\Gamma(K_L \to \pi^- l^+ \nu_l) + \Gamma(K_L \to \pi^+ l^- \bar{\nu_l})}\,. \tag{1.16}$$

Substituting Equations 1.11 and 1.12 into Equation 1.16 yields

$$\delta \approx 2Re(\epsilon)\,. \tag{1.17}$$

[3] In the Standard Model, the $\Delta S = \Delta Q$ rule is exact at tree level, and is allowed to violate at higher order processes. However, these processes are expected to be highly suppressed [12], and the experimental value is 0.006 ± 0.018 [13]. Therefore we can assume $\Delta S = \Delta Q$.

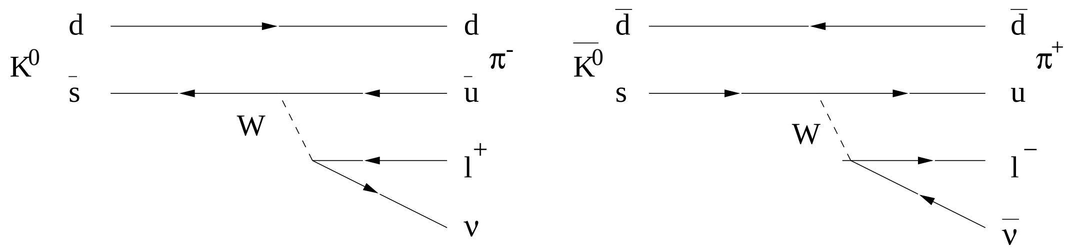

Figure 1.2: Feynman diagrams of semi-leptonic decays in neutral kaons.

Experimentally, the current world average for the charge asymmetry is [13]

$$\delta = (0.327 \pm 0.0012) \times 10^{-2} . \tag{1.18}$$

To extract ϵ from Equation 1.17 and 1.18, we need to know the phase of the ϵ, ϕ_ϵ. To relate ϕ_ϵ with physically observables, we further transform Equation 1.14. Since we are assuming CPT invariance, the diagonal elements of the Hamiltonian should be equal:

$$\langle K^0|H|K^0\rangle = \langle \bar{K^0}|H|\bar{K^0}\rangle \, , \tag{1.19}$$

and the off diagonal elements in the mass and decay matrices must be complex conjugates because the matrices are Hermitian:

$$\langle K^0|M|\bar{K^0}\rangle = \langle \bar{K^0}|M|K^0\rangle^* \, , \tag{1.20}$$

$$\langle K^0|\Gamma|\bar{K^0}\rangle = \langle \bar{K^0}|\Gamma|K^0\rangle^* \, . \tag{1.21}$$

Using the assumptions that M and Γ are Hermitian, Equation 1.14 is rewritten as

$$\epsilon = \frac{ImM_{12} - \frac{1}{2}iIm\Gamma_{12}}{i\Delta m - \frac{1}{2}(\Gamma_S - \Gamma_L)} . \tag{1.22}$$

Equation 1.22 implies that both the mass matrix and the decay matrix contribute to the asymmetric mixing of the K^0 and $\bar{K^0}$, leading to the indirect CP violation. Then, the phase of ϵ, which we have tried to extract, is given as

$$\phi_\epsilon = \tan^{-1}(\frac{2\Delta m}{\Gamma_S - \Gamma_L}) - \tan^{-1}(\frac{Im\Gamma_{12}}{2ImM_{12}}) \, . \tag{1.23}$$

To extract the numerical value of ϕ_ϵ, we now ignore $Im\Gamma_{12}$ by using a experimental fact that $ImM_{12} \gg Im\Gamma_{12}$, then Equation 1.23 becomes

$$\phi_\epsilon = \tan^{-1}(\frac{2\Delta m}{\Gamma_S - \Gamma_L}) \, . \tag{1.24}$$

Substituting the world averages of $\Delta m(= 0.5304 \times 10^{10} \hbar s^{-1})$ and the lifetimes($\tau_S = 0.8927 \times 10^{-10}$ sec, $\tau_{\mathrm{L}} = 5.17 \times 10^{-8}$ sec) [13] into Equation 1.24, we obtain

$$\phi_\epsilon = 43.49^\circ \pm 0.12^\circ \, . \tag{1.25}$$

This leads to

$$|\epsilon| = (2.25 \pm 0.08) \times 10^{-3} \, . \tag{1.26}$$

To summarize, a CP violating decay $K_L \rightarrow \pi\pi$ is explained with the indirect CP violation where asymmetric $K^0 - \bar{K^0}$ mixing results in small contaminations of K_1 component in K_L. The size of contamination, parametrized by ϵ, was measured to be of order 10^{-3}.

1.1.2 Direct CP Violation

Let us now consider CP violating effects in decay processes. It is interesting to consider the ratio of the decay amplitude $K_L \to f$ to that of $K_S \to f$, where f is a CP even eigenstate:

$$r_f = \frac{\langle f|H_{eff}|K_L\rangle}{\langle f|H_{eff}|K_S\rangle} . \tag{1.27}$$

This r_f is a measure of CP violating effect because it shows the ratio of CP violating to CP conserving amplitudes. If we define

$$a_f = \langle f|H_{eff}|K^0\rangle$$

and

$$\bar{a_f} = \langle f|H_{eff}|\bar{K^0}\rangle ,$$

which are the decay amplitudes including final state interactions(cf. Equation 1.33), substituting Equations 1.11 and 1.12 into Equation 1.27 yields

$$r_f = \frac{(a_f - \bar{a_f}) + \epsilon(a_f + \bar{a_f})}{\epsilon(a_f - \bar{a_f}) + (a_f + \bar{a_f})} . \tag{1.28}$$

If a_f and $\bar{a_f}$ are not equal, Equation 1.28 shows that the decay matrix will not only affect $K^0 - \bar{K^0}$ mixing through ϵ, but also directly contribute to a CP violation through a term of $a_f - \bar{a_f}$ because the decay amplitude is governed by the decay matrix. If we define the decay asymmetry

$$\chi_{\pi^+\pi^-} \equiv \frac{a_{\pi^+\pi^-} - \bar{a}_{\pi^+\pi^-}}{a_{\pi^+\pi^-} + \bar{a}_{\pi^+\pi^-}} \tag{1.29}$$

in the CP violating decay $K_L \to \pi^+\pi^-$, we obtain

$$r_{\pi^+\pi^-} = \frac{\epsilon + \chi_{\pi^+\pi^-}}{1 + \epsilon\chi_{\pi^+\pi^-}} \approx \epsilon + \chi_{\pi^+\pi^-} \tag{1.30}$$

by using the fact that the ϵ is of order 10^{-3}. Equation 1.30 shows that there is an additional contribution to CP violation besides mixing due to ϵ. The K^0 and $\bar{K^0}$ decay asymmetrically, resulting in a CP violating amplitude in the decay process. This is called "direct CP violation".

As discussed in the previous section, indirect CP violation has already been observed, for example, in $K_L \to \pi\pi$ and in the measurement of the charge asymmetry in K_L decays. On the other hand, we have not yet observed the existence of direct CP violating effect, but it has been studied most extensively in $K_L \to \pi\pi$ decays.

Direct CP Violation in $\pi\pi$ Decay

In order to discuss CP violation in $\pi\pi$ decays, we define some physically observable quantities. We redefine $r_{\pi^+\pi^-}$ in the more traditional notation as

$$\eta_{+-} \equiv \frac{\langle\pi^+\pi^-|H_{eff}|K_L\rangle}{\langle\pi^+\pi^-|H_{eff}|K_S\rangle} = r_{\pi^+\pi^-} . \tag{1.31}$$

We define a similar quantity for the neutral decay mode:

$$\eta_{00} \equiv \frac{\langle\pi^0\pi^0|H_{eff}|K_L\rangle}{\langle\pi^0\pi^0|H_{eff}|K_S\rangle} = r_{\pi^0\pi^0} . \tag{1.32}$$

Since there are strong final state interactions in $\pi\pi$ decays, we formulate the final state in terms of the strong eigenstate, i.e. the isospin eigenstate. Let us define

$$\langle I|H_{eff}|K^0\rangle = a_I \equiv A_I e^{i\delta_I} , \tag{1.33}$$

where I denotes the isospin of $\pi\pi$ which can be either 0 or 2 because of the Bose symmetry of π's, and δ_I is the phase shift induced by final state strong interactions. Our assumption of CPT invariance leads to

$$\langle I|H_{eff}|\bar{K^0}\rangle = \bar{a_I} \equiv A_I^* e^{i\delta_I} . \tag{1.34}$$

Breaking down the $\pi^+\pi^-$ eigenstate into I=0 and I=2 components, we have

$$|\pi^+\pi^-\rangle = \sqrt{\frac{2}{3}}|0\rangle + \sqrt{\frac{1}{3}}|2\rangle . \tag{1.35}$$

Substituting this expression and Equation 1.33 into Equation 1.29, we obtain

$$\begin{aligned} \chi_{\pi^+\pi^-} &= \frac{iImA_2 e^{i(\delta_2-\delta_0)}}{\sqrt{2}A_0 + ReA_2 e^{i(\delta_2-\delta_0)}} \\ &= \frac{\epsilon'}{1+\omega/\sqrt{2}} , \end{aligned} \tag{1.36}$$

where we define the parameters ϵ' and ω as

$$\epsilon' \equiv \frac{i}{\sqrt{2}} e^{i(\delta_2-\delta_0)} \frac{ImA_2}{A_0} , \tag{1.37}$$

and

$$\omega \equiv \frac{ReA_2}{A_0} e^{i(\delta_2-\delta_0)} . \tag{1.38}$$

In these calculations, we adopt the Wu-Yang phase convention [14], and take A_0 to be real[4]. If we select another convention, there will be a contribution into direct CP violation from $Im\,A_0$. However, physical observables are independent of the choice of phase.

The parameter ω represents a ratio of the CP conserving $\Delta I = 3/2$ amplitude to CP conserving $\Delta I = 1/2$ amplitude in $K_S \to \pi\pi$ decay. We know experimentally that $\Delta I = 3/2$ transitions are suppressed [15, 16] as

$$|\omega| \sim \frac{1}{22} . \tag{1.39}$$

Since ω is small as shown in the above, we see that ϵ' is the scale of direct CP violation in Equation 1.36. Substituting Equation 1.36 into Equation 1.30, we obtain

$$\eta_{+-} \approx \epsilon + \epsilon' . \tag{1.40}$$

A similar calculation for neutral mode gives

$$\eta_{00} \approx \epsilon - 2\epsilon' . \tag{1.41}$$

[4] In the usual phase convention in the Standard Model, the ϵ' is expressed as

$$\epsilon' \equiv \frac{i}{\sqrt{2}} e^{i(\delta_2-\delta_0)} \frac{ReA_2}{ReA_0} [\frac{ImA_2}{ReA_2} - \frac{ImA_0}{ReA_0}] .$$

In order to measure these quantities, we need to measure a physically accessible quantity. In this case, a double ratio of decay rates is one such quantity. The signature of direct CP violation is expressed as

$$\frac{\Gamma(K_L \to \pi^+\pi^-)/\Gamma(K_S \to \pi^+\pi^-)}{\Gamma(K_L \to \pi^0\pi^0)/\Gamma(K_S \to \pi^0\pi^0)} = \frac{|\eta_{+-}|^2}{|\eta_{00}|^2} \approx \frac{\epsilon + \epsilon'}{\epsilon - 2\epsilon'} \approx 1 + 6Re(\frac{\epsilon'}{\epsilon}) . \tag{1.42}$$

Non-zero value of $Re(\epsilon'/\epsilon)$ indicates an existence of the direct CP violation. The most recent measurements of $Re(\epsilon'/\epsilon)$ have been reported by two groups, E731 [17] at Fermilab and NA31 [18] at CERN.

$$Re(\frac{\epsilon'}{\epsilon}) = [7.4 \pm 5.2(stat.) \pm 2.9(syst.)] \times 10^{-4} \quad \text{(E731)} \tag{1.43}$$

$$Re(\frac{\epsilon'}{\epsilon}) = [23 \pm 3.4(stat.) \pm 5.5(syst.)] \times 10^{-4} \quad \text{(NA31)} \tag{1.44}$$

From these two results, we cannot confirm a non-zero value of ϵ', because of the relatively large experimental uncertainties. The E832 experiment at Fermilab, which uses almost the same detector as described in this thesis, expects to measure $Re(\epsilon'/\epsilon)$ with an accuracy of order 10^{-4}. The NA48 group at CERN also plans to measure it with roughly the same accuracy.

1.2 CP Violation in the Standard Model

There are some theories which explain the CP violation. This section describes the CP violation in the Standard Model.

In the Standard Model, CP violation occurs through charged current interactions. There are many reviews which explain the origin and phenomena of CP violation [19], and only the general features are described here. The charged current in the weak interaction has the form

$$g[\bar{u}_j V_{ji} \gamma_\mu (1 - \gamma_5) d_i W^\mu + h.c.], \tag{1.45}$$

where the same indices are summed over, and $u_j = (u, c, t)$ are up-type quarks and $d_i = (d, s, b)$ are down type quarks. V is the 3×3 unitary CKM(Cabibbo-Kobayashi-Maskawa) matrix which connects up-type quarks with down-type quarks:

$$V = \begin{pmatrix} V_{ud} & V_{us} & V_{ub} \\ V_{cd} & V_{cs} & V_{cb} \\ V_{td} & V_{ts} & V_{tb} \end{pmatrix} . \tag{1.46}$$

This unitary matrix was first introduced by Kobayashi and Maskawa [20], based on the mixing concept originally introduced by Cabibbo [21]. V has 9 real free parameters but the number of these parameters is reduced to 4 by the redefinition of the quark field phase. A convenient parametrization of V by Maiani [22] is

$$V = \begin{pmatrix} c_{12}c_{13} & s_{12}c_{13} & s_{13}e^{i\delta} \\ -s_{12}c_{23} - c_{12}s_{23}s_{13}e^{i\delta} & c_{12}c_{23} - s_{12}s_{23}s_{13}e^{i\delta} & s_{23}c_{13} \\ s_{12}s_{23} - c_{12}c_{23}s_{13}e^{i\delta} & -c_{12}s_{23} - s_{12}c_{23}s_{13}e^{i\delta} & c_{23}c_{13} \end{pmatrix} , \tag{1.47}$$

where $c_{ij} = \cos\theta_{ij}$ and $s_{ij} = \sin\theta_{ij}$.

As shown in Equation 1.45 and 1.46, the matrix elements of V express the coupling strength at vertex of W and up-type and down-type quarks. Therefore, experimental data on strange particle and B decay rates can determine the magnitudes of V_{us}(by semi-leptonic decays in charged or neutral kaons), V_{cb}(by semi-leptonic decays in B mesons), and V_{ub}(by $b \to u$ transition in B

mesons). The data show that the mixing angles have a hierarchical structure. This hierarchy of coupling strengths led Wolfenstein to introduce a conventional parametrization of the CKM matrix [23], in powers of the sine of the Cabibbo angle, $\lambda = \sin\theta_{12}$. Expanding V in powers of λ to order λ^3, we see that the matrix has the simple form

$$V = \begin{pmatrix} 1-\frac{\lambda^2}{2} & \lambda & A\lambda^3(\rho - i\eta) \\ -\lambda & 1-\frac{\lambda^2}{2} & A\lambda^2 \\ A\lambda^3(1-\rho-i\eta) & -A\lambda^2 & 1 \end{pmatrix} . \tag{1.48}$$

Under this parametrization, V is CP invariant to order λ^2, and CP violation shows up first in order λ^3. Numerical value of each parameter is determined from experiments as discussed in the end of this section. Currently, they are determined to be: A is of order unitity; λ, ρ, and η are of order 10^{-1}.

All CP violating observables are proportional to a quantity J [24, 25, 26], which is independent of the choice of phase parametrization:

$$J = Im(V_{ij}V_{lk}V^*_{ik}V^*_{lj}) \, , \, i \neq l, \; j \neq k \, . \tag{1.49}$$

where l and k denote up-type and down-type quarks, respectively. Using the parametrization of Equation 1.48, J becomes

$$J \approx A^2\lambda^6\eta \, . \tag{1.50}$$

Applying the unitarity condition to the first and third columns, we obtain

$$V^*_{ub}V_{ud} + V^*_{cb}V_{cd} + V^*_{tb}V_{td} = 0 \, . \tag{1.51}$$

We can take $V_{ud} \approx 1$ to the first order in λ, and the unitarity condition becomes

$$V^*_{ub} + V_{td} = A\lambda^3 \, . \tag{1.52}$$

Figure 1.3 shows the triangle obtained from this relationship. The area of the triangle is proportional to the measure of CP violation, J. This means that in the Standard Model, a measurement of the CP violating magnitude is equivalent to evaluating the area of the unitarity triangle in Figure 1.3.

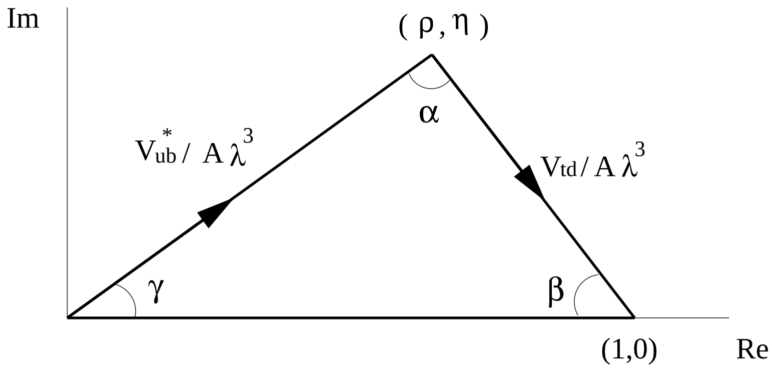

Figure 1.3: The unitarity triangle on $\rho - \eta$ plane.

Therefore, an existence of imaginary amplitude is the essence of CP violation in the Standard Model. Such amplitudes are introduced by $|V_{td}|$ or $|V_{ub}|$ component in the diagrams of CP violating processes.

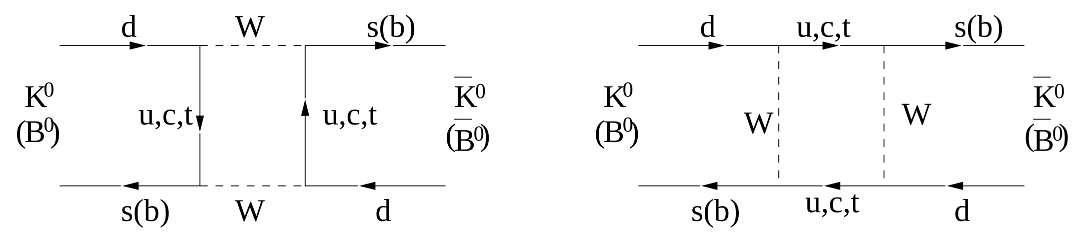

Figure 1.4: The box diagrams which are expected to provide the dominant contribution to $K^0 - \bar{K}^0$ or $B^0 - \bar{B}^0$ mixing.

Let us now briefly look at two examples for the Standard Model interpretation, $K_L \to \pi\pi$, and $K_L \to \pi^0 e^+ e^-$.

In the case of $K_L \to \pi\pi$, the indirect CP violating effect through asymmetric mixing arises from box diagrams shown in Figure 1.4. There is a $|V_{td}|$ component, and thus an imaginary amplitude, in the intermediate states. The direct CP violating amplitude comes from penguin diagrams((b) in Figure 1.5). The penguin diagram also has a $|V_{td}|$ element, and thus $i\eta$. Next, let us compare the size of indirect and direct CP violation. The dominant contributions in the decay process come from the first order tree diagrams((a) in Figure 1.5), which are $O(\lambda)$ for the K_1, and zero for the K_2. The penguin diagram is of order $O(A^2) \times O(\lambda^5) \times |\eta|$ for the K_2. Therefore, even accommodating ϵ, the tree level decay rate $\epsilon K_1 \to \pi\pi$ is two or three orders of magnitude larger than that of the penguin diagrams, where we have ignored some kinematical and QCD corrections. This implies $\epsilon'/\epsilon \ll 1$ in $K_L \to \pi\pi$ process.

In the second example $K_L \to \pi^0 e^+ e^-$, the direct CP violation comes from a diagram (c) in Figure 1.6. The $|V_{td}|$ in the penguin diagram contains $i\eta$, and thus CP violating amplitude. The $K_L \to \pi^0 e^+ e^-$ is expected to have a relatively larger direct CP violating contribution than that in $K_L \to \pi\pi$. However, because of an existence of long-distance interactions in $K_L \to \pi^0 e^+ e^-$, theories predict that the CP conserving and the indirect CP violating processes, shown in (a) and (b) of Figure 1.6, have the same order of contributions as that from direct CP violation [27, 28, 29, 30] (see Appendix A for more details). This implies $\epsilon'/\epsilon \sim O(1)$ in $K_L \to \pi^0 e^+ e^-$ decay. Therefore, it will be necessary to separate the CP conserving and the indirect CP violating contributions in order to claim the existence of direct CP violation.

Current Status of the CKM Parameters

As shown in Equation 1.50, A, λ, and η determine the size of CP violation in the Standard Model. They are also used in theoretical calculations to predict a branching ratio of $K_L \to \pi^0 \nu\bar{\nu}$, as will be discussed in the next section. Therefore, we here briefly summarize the current status of constraints on the CKM parameters, which are imposed from a combination of various experiments.

As shown in Equation 1.46 and 1.48, the A and λ directly relate to $|V_{us}|$ and $|V_{cb}|$. The former is determined from strange particle decay rates, and the latter is from semi-leptonic decays in B mesons. They are determined to be $A = 0.81 \pm 0.04$, and $\lambda = 0.2205 \pm 0.0018$, respectively [31].

The constraints on (ρ, η) plane are imposed from mainly three types of experiment. The first one is the $|\epsilon|$ in K_L, obtained from the measurement of the charge asymmetry in semi-leptonic decays, as discussed in Section 1.1.1. Within the Standard Model, size of the ϵ and thus asymmetric $K^0 - \bar{K}^0$ mixing is dominated by the contribution of W-box diagrams shown in Figure 1.4. Since V_{td} is involved in these processes, the ϵ is related to ρ and η through [19]

$$|\epsilon| = 3.4 \times 10^{-3} A^2 \eta B_K [1 + 1.3 A^2 (1-\rho)(\frac{m_t}{m_W})^{1.6}] \ ,$$

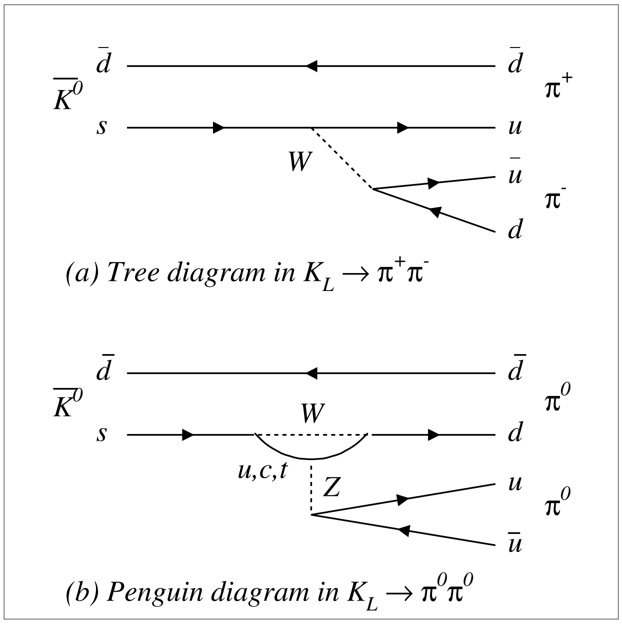

Figure 1.5: Feynman diagrams contributing to $K_L \to \pi\pi$ decays.

where B_K is the ratio of the true matrix element to that obtained using vacuum insertion, and is estimated to be 0.90 ± 0.09 [31]. As can be seen from the above equation, the $|\epsilon|$ gives a hyperbola in the ρ-η plane as shown in Figure 1.7. The second constraint on η is imposed from $|V_{ub}|/|V_{cb}|$ obtained by measurements of the $b \to u$ transition rate in B mesons. By definition, the ratio $|V_{ub}|/|V_{cb}|$ represents a circle centered at zero in the (ρ, η) plane:

$$|\frac{V_{ub}}{V_{cb}}|^2 = \lambda^2(\rho^2 + \eta^2) ,$$

as displayed in Figure 1.7. The third constraint is applied from Δm_B defined as the mass difference of the two mass eigenstates of the B meson measureed by the $B_d^0 - \bar{B}_d^0$ oscillation frequency. The $B_d^0 - \bar{B}_d^0$ mixing is governed by W-box diagrams as shown in Figure 1.4. Since there are V_{tb} and V_{td} couplings in the diagrams, the evaluation of the box diagram yields [32]:

$$\Delta m_B = \frac{G_F^2}{6\pi^2}|V_{td}|^2|V_{tb}|^2 m_W^2 m_B f_B^2 B_B \eta_B S(\frac{m_t^2}{m_W^2}) ,$$

where B_B is analogous to the B_K mentioned above, f_B is a decay constant of the B meson, η_B is a QCD correction, and $S(x)$ is a correction factor for calculating loop processes as a function of x. This relation implies that the Δm_B scales like $|V_{td}|^2$ because $|V_{tb}| \simeq 1$. Since the $|V_{td}|^2$ can be expressed as

$$|V_{td}|^2 = |A\lambda^3|^2(1-\rho)^2 + \eta^2 ,$$

the measurement of the Δm_B gives a circle centered at (1,0) (see Figure 1.7). In our calculation, values in references [31, 33, 34] are used as the numerical inputs. The band of each constraint in Figure 1.7 corresponds to an error of 1 σ, which is dominated by theoretical uncertainties. In

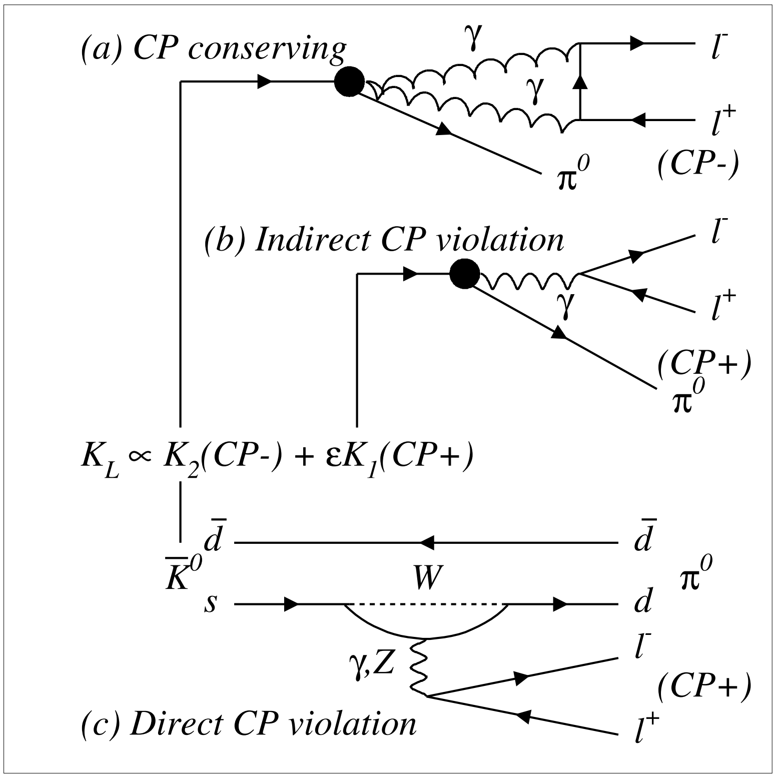

Figure 1.6: Some of the contributions to decay $K_L \rightarrow \pi^0 e^+ e^-$: (a) CP conserving process through the intermediate $\pi^0\gamma\gamma$ state, (b) Indirect CP violating process through the intermediate $\pi^0\gamma$ state, (c) Direct CP violating process by short-distance interactions. The shaded circles represent long-distance interactions.

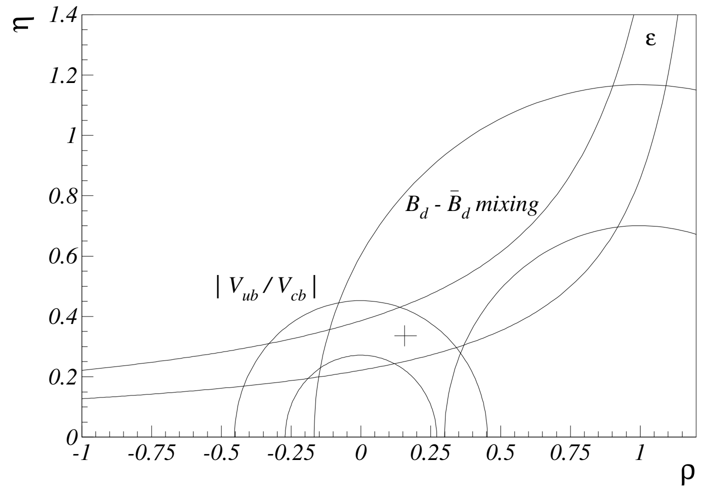

Figure 1.7: The allowed region with 1 σ of an error for ρ and η. The constraints are given by the measurements of $|\epsilon|$, $|V_{ub}/V_{cb}|$ and Δm_{B_d}. The cross shows current most probable value expected in ref [34].

$B_d^0 - \bar{B}_d^0$ mixing, for instance, theoretical estimation of $B_B\sqrt{f_B}$ still contains an uncertainty of 18%, in spite of a 4% in measurement of Δm_B from experiment. Combining all the uncertainties of each equation, each of the three constraints includes more than 25% uncertainty.

Combining the three types of experimental results, the current information places ρ in the range from 0.0 to 0.3, and η in the range from 0.2 to 0.4.

1.3 $K_L \to \pi^0\nu\bar{\nu}$ Decay

This section describes a theoretical interpretation for the decay of interest, $K_L \to \pi^0\nu\bar{\nu}$. In Section 1.3.1, we discuss it in the context of the Standard Model. In Section 1.3.2, we introduce some other predictions by models outside the Standard Model. Section refsec:limit briefly summarizes the past searches for $K_L \to \pi^0\nu\bar{\nu}$.

1.3.1 The Standard Model

Let us first explain the mechanism of CP violation in the $K_L \to \pi^0\nu\bar{\nu}$ decay within the Standard Model. We also here emphasize the theoretical interests in the $K_L \to \pi^0\nu\bar{\nu}$ process.

The CP conserving and indirect CP violating contributions to $K_L \to \pi^0\nu\bar{\nu}$ through long-distance interactions are negligible, as will be described below. The long-distance interactions involve photons in their intermediate states. However, the photons do not couple to the neutrinos in the final state. In addition, we can ignore intermediate Z's or W's in the long-distance interactions because the effective coupling constant in the weak interaction is four orders of magnitude smaller than that in the electromagnetic interaction due to heavy mass of the Z and W. Hence, the $K_L \to \pi^0\nu\bar{\nu}$ decay does not suffer from the long-distance contributions and is governed by the short-distance.

Because of the lack of long-distance effect, the amplitude for $K_L \to \pi^0\nu\bar{\nu}$,

$$A(K_L \to \pi^0\nu\bar{\nu}) = \epsilon A(K_1 \to \pi^0\nu\bar{\nu}) + A(K_2 \to \pi^0\nu\bar{\nu}) \,, \tag{1.53}$$

is dominated by short-distance physics. In the decay processes, we can ignore first order tree diagrams, because the $K_L \to \pi^0\nu\bar{\nu}$ decay requires at least second order diagrams for flavor changing neutral current. Thus, the amplitudes in Equaion 1.53 are dominated by such as penguin and W-box diagrams shown in Figure 1.8. The amplitudes, $A(K_1 \to \pi^0\nu\bar{\nu})$ and $A(K_2 \to \pi^0\nu\bar{\nu})$, are about the same size $(O(A^2) \times O(\lambda^5) \times [\ |\eta| \text{ or } |1-\rho|\ ])$ in the penguin or W-box diagram, but the branching ratio for indirect CP violating process is suppressed by ϵ^2 as shown in Equation 1.53. To be more concrete, the magnitude of indirect CP violating(CP conserving) contributions is estimated as three(less than four) orders of magnitude smaller than that of the direct CP violating contributions [35] [36] within the framework of the Standard Model. Therefore, the $K_L \to \pi^0\nu\bar{\nu}$ decay is dominated by the direct CP violating effect [35, 37, 38, 39].

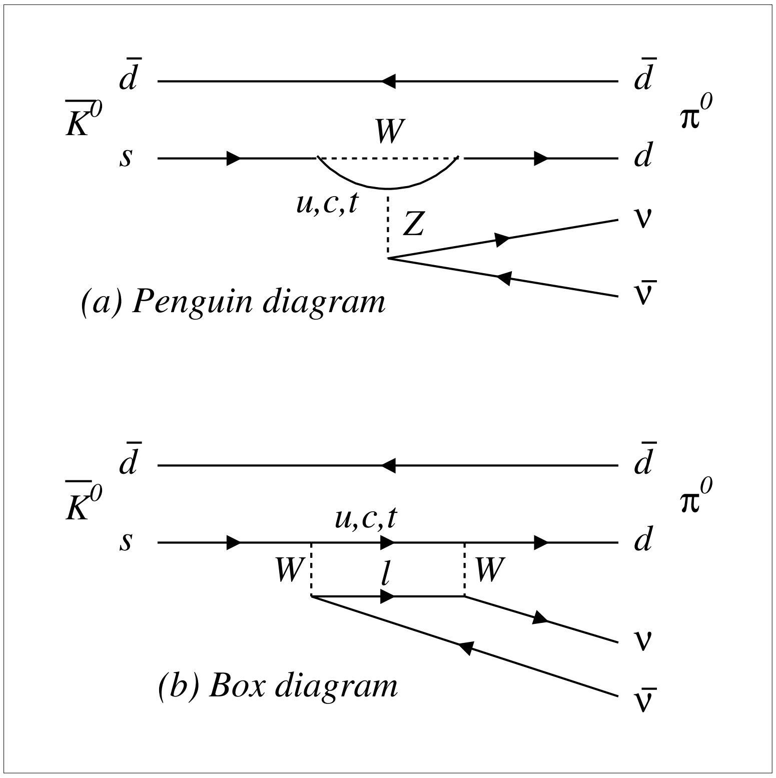

Figure 1.8: Feynman diagrams which are expected to provide the dominant contribution in $K_L \to \pi^0\nu\bar{\nu}$ process.

Now let us point out the source of the CP violating effect. Since the $K_L \to \pi^0\nu\bar{\nu}$ is dominated by direct CP violation, i.e. $K_2 \to \pi^0\nu\bar{\nu}$, within the framework of the Standard Model, we consider only the K_2 decay process using the two diagrams in Figure 1.8. From the facts that K_2 is a superimposition of K^0 and $\bar{K}^0$, and that there can be a top quark in the intermediate state, the amplitude of K_2 can be written as

$$A(K_2 \to \pi^0\nu\bar{\nu}) \propto V_{td}^* V_{ts} - V_{ts}^* V_{td} \propto 2i\eta \; . \tag{1.54}$$

Therefore, $Br(K_L \to \pi^0\nu\bar{\nu})$ is proportional to $|\eta|^2$, and the CP does not conserve before and after the interaction because of the existence of an imaginary part in the amplitude, i.e. CP violating phase.

As seen in the above, the decay $K_L \to \pi^0\nu\bar{\nu}$ is dominated by the direct CP violating effect within the Standard Model, in contrast to other CP violaing decays such as $K_L \to \pi\pi$ or $K_L \to \pi^0 e^+ e^-$. It is an unique feature, and thus it offers the cleanest window into a discovery of the direct CP violation.

There is another reason why the $K_L \to \pi^0\nu\bar{\nu}$ is believed to be one of the best ways to understand the origin of CP violation. In the Standard Model, theoretical uncertainties in the decay $K_L \to \pi^0\nu\bar{\nu}$ are extremely small. According to recent calculations [40, 41, 42, 43], the remaining theoretical uncertainty for $Br(K_L \to \pi^0\nu\bar{\nu})$ is reduced to $O(1\%)$. Therefore, a measurement of $Br(K_L \to \pi^0\nu\bar{\nu})$ can provide one of the cleanest ways to test the Standard Model.

Theoretical Prediction

Using Equation 1.54, the $K_L \to \pi^0\nu\bar{\nu}$ branching ratio can be written as [43]

$$Br(K_L \to \pi^0\nu\bar{\nu}) = 0.354 \times 10^{-4}\eta^2 A^4 \lambda^8 X^2(x_t) \, , \tag{1.55}$$

where x_t is the squared mass ratio between the top quark and the W boson, $x_t = m_t^2/M_W^2$; and the $X(x_t)$ is a QCD correction factor [40, 41]. The numerical coefficient is obtained from the isospin relation between the $K_L \to \pi^0\nu\bar{\nu}$ and $K^+ \to \pi^+\nu\bar{\nu}$ amplitudes with an isospin-breaking correction in which the theoretical uncertainty is estimated to be below $\pm 0.5\%$ [44, 45, 46]. This enables us to eliminate the hadronic matrix element using experimental results for the $Br(K^+ \to \pi^0 e^+ \nu)\tau_{K_L}/\tau_{K^+}$. The combined experimental error on this quantity is $\pm 1.5\%$, dominated by the uncertainty in $Br(K^+ \to \pi^0 e^+ \nu)$ [13]. The next-to-leading order QCD corrections to $K_L \to \pi^0\nu\bar{\nu}$ ($\bar{s}dZ$ vertex) have reduced the theoretical uncertainty due to the choice of the renormalization scales in the leading order expressions [42] from $O(25\%)$ to $O(3\%)$. Therefore, the total uncertainty in the theoretical calculation is expected to be a few percent.

Using experimental inputs of the CKM parameters: η, A, and λ, for Equation 1.55, recent calculations predict the branching ratio of $K_L \to \pi^0\nu\bar{\nu}$ with small theoretical uncertainties. Some predictions are listed in Table 1.1. Due to the uncertainties on the CKM parameters, these predic-

Table 1.1: Theoretical predictions of $Br(K_L \to \pi^0\nu\bar{\nu})$ within the framework of the Standard Model.

$Br(K_L \to \pi^0\nu\bar{\nu})$	Reference
2.84×10^{-11}	[41]
3.00×10^{-11}	[43, 45]
2.78×10^{-11}	[44]

tions still contain an error of $\sim 2 \times 10^{-11}$. Again, one should note that the theoretical uncertainty itself has a magnitude of $O(1\%)$.

Impact to CKM Matrix Parameters

While the CKM parameters deduced from the combination of the above experiments are used to predict the branching ratio of $K_L \to \pi^0\nu\bar{\nu}$, Equation 1.55 shows that a direct measure of the height in unitarity triangle, shown in Figure 1.3, is provided through the measurement of the branching ratio of $K_L \to \pi^0\nu\bar{\nu}$. Moreover, if we could measure the length of the side opposite to γ(see Figure 1.3), the unitarity triangle would be determined uniquely. The charged mode $K^+ \to \pi^+\nu\bar{\nu}$ is closely related to $K_L \to \pi^0\nu\bar{\nu}$. The measurement of the $Br(K^+ \to \pi^+\nu\bar{\nu})$ [47] allows the extraction of $|V_{td}|$ with least theoretical uncertainty, corresponding to the length of the side we want. Combining this measurement with $K_L \to \pi^0\nu\bar{\nu}$, some CKM parameters are determined as shown in Table 1.2 [45], assuming we will obtain some input parameters as below:

$$V_{cb} = 0.040 \pm 0.002 \tag{1.56}$$

$$m_t = (170 \pm 3)\ \text{GeV} \tag{1.57}$$

$$Br(K_L \to \pi^0\nu\bar{\nu}) = (3.0 \pm 0.3) \times 10^{-11} \tag{1.58}$$

$$Br(K^+ \to \pi^+\nu\bar{\nu}) = (1.0 \pm 0.1) \times 10^{-10} \tag{1.59}$$

Since the theoretical uncertainty of $K_L \to \pi^0\nu\bar{\nu}$ decay is very small($\sim 1\%$) as discussed in previous section, we can see from Table 1.2 that the measurement of $Br(K_L \to \pi^0\nu\bar{\nu})$ can directly determine CKM parameters with small uncertainty.

Table 1.2: Comparison of the determination of the CKM parameters from $K \to \pi\nu\bar{\nu}$ and from CP violating asymmetries in B decays. The relative input is as described in the text. $\bar{\eta}$ and $\bar{\rho}$ are redefined as $\bar{\eta} = \eta(1 - \lambda^2/2)$ and $\bar{\rho} = \rho(1 - \lambda^2/2)$ to an accuracy of better than 0.1%.

	$\sin 2\beta$	$\bar{\eta}$	$\bar{\rho}$	$\|V_{td}\|/10^{-3}$
$K \to \pi\nu\bar{\nu}$	0.62 ± 0.05	0.38 ± 0.04	-0.10 ± 0.16	10.3 ± 1.1
$B \to \pi\pi, J/\psi K_S$	0.60 ± 0.06	0.32 ± 0.04	0.04 ± 0.02	8.9 ± 0.5

In contrast to $K \to \pi\nu\bar{\nu}$ decays, the measurements of the CP asymmetries in neutral B decays determine the angles of the unitarity triangle illustrated in Figure 1.3. The angle β can be extracted from $B^0 \to J/\psi K_S$ and α from $B^0 \to \pi^+\pi^-$. Measuring these CP asymmetries determines the CKM matrix parameters shown in Table 1.2. As can be seen in Table 1.2, the accuracy of CKM parameters that can be determined from $K \to \pi\nu\bar{\nu}$ is comparable to that from the CP asymmetries in B decays except for ρ. In addition, extraction of $\sin 2\alpha$ from $B \to \pi\pi$, where the main contribution comes from tree level diagrams and the mixing, is complicated by the presence of penguin diagrams. To isolate this so-called penguin pollution, a careful isospin analysis, which uses a combination of several modes, including a challenging decay $B \to \pi^0\pi^0$, is required. The CKM analysis in $K \to \pi\nu\bar{\nu}$ is less complicated and has an advantage in the determination of the unitarity triangle.

There is also an additional proposal that not only η but also $|V_{cb}|$ can be determined from the $K_L \to \pi^0\nu\bar{\nu}$ decay [42]. Using the unitarity condition and the Wolfenstein parametrization with $|V_{cb}| = A\lambda^2$, it is clear that $|V_{cb}|$ gives the overall scale, A, in the top quark couplings, V_{td} and V_{ts}, which are the only CKM couplings in $K_L \to \pi^0\nu\bar{\nu}$. From this point of view, it is very natural to measure the parameter A in a short distance process, involving the top quark, and to use unitarity of the CKM matrix to extract the value of $|V_{cb}|$. This strategy is free from hadronic uncertainties in contrast to tree-level B decays.

1.3.2 Test of Models Outside the Standard Model

In the previous section, we discussed the decay $K_L \to \pi^0 \nu\bar{\nu}$ in a framework of the Standard Model. A measurement of $K_L \to \pi^0 \nu\bar{\nu}$ branching ratio is one of the cleanest methods to determine the CKM parameters. Therefore, a discrepancy between the measured value and the theoretical prediction indicates new physics. This section briefly introduces some models outside the Standard Model.

Superweak

In 1964, the Superweak hypothesis was introduced by Wolfenstein [48] in which a new $\Delta S = 2$ interaction causes CP violation. To explain the small size of the CP violating effect, this interaction has to be on the order of 10^7 or 10^8 times weaker than the standard weak interaction. Superweak interactions would contribute only to the mass matrix. Therefore, direct CP violation does not exist as a consequence of the superweak model. This implies that establishing a nonzero branching ratio of $K_L \to \pi^0 \nu\bar{\nu}$ rules out a pure superweak explanation for CP violation.

On the other hand, the popular $B \to J/\psi K_S$ mode available at B factories would not allow us to discriminate this model from the Standard Model [49, 50]. Even measurements of both $\sin 2\beta$ and $\sin 2\alpha$ might not be able to rule out the Superweak Model [51]. The two models are identical when $\sin 2\alpha + \sin 2\beta = 0$. This equation defines a curve in the (ρ, η) plane called the ambiguity curve. Even with a luminosity of 100 fb^{-1} at the $\Upsilon(4S)$ in B factories, which is the proposed statistics, the errors on the measurements of $\sin 2\beta$ and $\sin 2\alpha$ are estimated to be 5% and 10%, respectively. Taking into account these errors, there is a significant region in which we cannot distinguish between the Standard Model and the Superweak Model, as shown in Figure 1.9. The

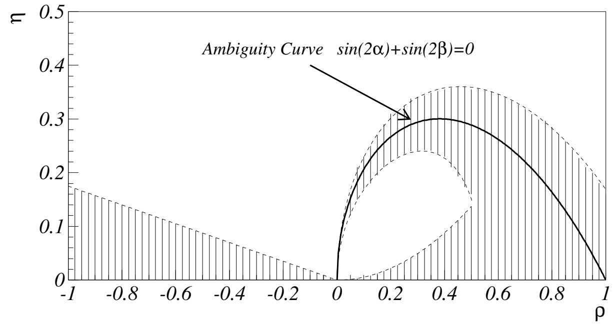

Figure 1.9: The ambiguity curve, $\sin 2\alpha + \sin 2\beta = 0$ in the (ρ, η) plane, equivalent to $\eta = (1-\rho)\sqrt{\rho/(1-\rho)}$ for $\rho > 0$. The hatched regions corresponds to points that are less than 3 σ from the ambiguity curve.

shaded area corresponds to a 3 σ region from the ambiguity curve. If the nature chooses ρ and η in this region, the confirmation of direct CP violation would be the best method to discriminate between the two models.

Exotic Particle

There are other possible non Standard Model contributions to the $K_L \to \pi^0 \nu\bar{\nu}$ decay. One such model contains an extra Higgs doublet, in which CP violation arises from the CKM sector and there are charged Higgs bosons in the loop instead of just W in Figure 1.8 [52]. In this case, the decay rate is expected to increases by up to 50%-100% [52, 53].

Another possibility is spontaneous CP violation in the Higgs sector [54]. Extended Higgs models are discussed in [52]. In the two-doublet model of spontaneous CP violation by Liu and Wolfenstein [55], as in the three-doublet model by Weinberg [56], it is found that the branching ratio of $K_L \to \pi^0 \nu \bar{\nu}$ would be much smaller than that expected from the Standard Model.

Recently a paper came out [57], in which the branching ratio of $K_L \to \pi^0 \nu \bar{\nu}$ is calculated with a four generation model. Using the constraints from nine parameters, such as Δm in the neutral kaon system and Δm_B in B meson obtained from experimental results, they determined the size of mixing of the fourth generation. As the consequence, they expect the $Br(K_L \to \pi^0 \nu \bar{\nu})$ to be $(0.05 - 10) \times 10^{-10}$.

Lepton Flavor Violation

The consequence that $K_L \to \pi^0 \nu \bar{\nu}$ decay is dominated by direct CP violating amplitude comes from an assumption of lepton flavor conservation [58, 59]. If, however, lepton flavor is violated, the final state in $K_L \to \pi^0 \nu_i \bar{\nu_j}$ $(i \neq j)$ is not necessarily a CP eigenstate. In such a case, the CP conserving contribution can be significant and may even be dominant. Reference [58] demonstrates the development of a theory of lepton flavor violation, using Light Leptoquarks Model as an example. The expected branching ratio is larger than that of the Standard Model, i.e. a measurement of $Br(K_L \to \pi^0 \nu \bar{\nu})$ has the ability to discriminate between the Standard Model prediction and that from lepton flavor violation.

Theoretical Limit

There is an upper limit imposed by a theoretical estimation [58, 59];

$$Br(K_L \to \pi^0 \nu \bar{\nu}) < 1.1 \times 10^{-8} .$$

It is derived from the isospin relation between $K_L \to \pi^0 \nu \bar{\nu}$ and $K^+ \to \pi^+ \nu \bar{\nu}$ using an experimental bound on $Br(K^+ \to \pi^+ \nu \bar{\nu}) < 2.4 \times 10^{-9}$ [60][5] and a lifetime ratio between the K_L and the K^+. They claim the limit to be independent of the choice of models. If it is true, a discovery of $K_L \to \pi^0 \nu \bar{\nu}$ signal in the sensitivity larger than their limit implies a new phenomenon not only beyond the Standard Model but also outside every model or theory that has been proposed so far.

1.3.3 Previous Searches

The first search was performed by Littenberg [35]. He extracted a limit from the work of Cronin *et. al.* [62, 63] for $K_L \to \pi^0 \pi^0$. The limit was

$$Br(K_L \to \pi^0 \nu \bar{\nu}) < 7.6 \times 10^{-3} \text{ (90\% C.L.)} .$$

The experimental search for $K_L \to \pi^0 \nu \bar{\nu}$ decay has been carried out twice. The former result came from E731 experiment at Fermilab, and gave an upper limit of [64]

$$Br(K_L \to \pi^0 \nu \bar{\nu}) < 2.2 \times 10^{-4} \text{ (90\% C.L.)} .$$

The other experiment, E799-I at Fermilab, found [65]

$$Br(K_L \to \pi^0 \nu \bar{\nu}) < 5.8 \times 10^{-5} \text{ (90\% C.L.)} .$$

Although it is a very interesting decay mode as discussed in the previous sections, the current upper limit is far from the theoretical predictions.

[5] The same experimental group later claimed the discovery of $K^+ \to \pi^+ \nu \bar{\nu}$ process [61].

1.4 Summary

The decay of $K_L \to \pi^0 \nu\bar{\nu}$ is a strong signal of the direct CP violation in the Standard Model. It is one of the cleanest modes in CP violating decays. Theoretical uncertainty itself is $O(1\%)$. Therefore, the CKM parameters can be determined with high precision from the measurement of $Br(K_L \to \pi^0 \nu\bar{\nu})$ combined with $Br(K^+ \to \pi^+ \nu\bar{\nu})$. This precision is comparable to that from the CP asymmetry measurement in B meson.

Because of small theoretical uncertainties in the Standard Model, a measurement of $Br(K_L \to \pi^0 \nu\bar{\nu})$ is very sensitive to the physics beyond the Standard Model.

On the other hand, the current upper limit is far from the theoretical predictions. The results are limited by statistics and/or the existence of backgrounds. Therefore, we searched for this interesting decay $K_L \to \pi^0 \nu\bar{\nu}$ with significantly better sensitivity. In order to gain statistics, the number of K_L's and detector acceptance were largely increased compared to the previous searches. For background rejection, detectors with full of new technology were used with sophisticated and optimized analysis algorithm. A discovery of the $K_L \to \pi^0 \nu\bar{\nu}$ decay, as a result of these efforts, at the level predicted by the Standard Model could solve the final puzzle imposed for the Standard Model. Or a discovery with a larger branching ratio would indicate an existence of new physics beyond the Standard Model or outside every model so far considered. Thus, the experimental result in the search for $K_L \to \pi^0 \nu\bar{\nu}$ has an impact on the selection of the right model used to describe the nature and thus the CP violation.

1.5 Overview of This Thesis

We have discussed the basic issues regarding the neutral kaon, CP violation, and $K_L \to \pi^0 \nu\bar{\nu}$ decay in this chapter. The rest of this thesis describes a new experimental result we obtained by searching for $K_L \to \pi^0 \nu\bar{\nu}$ decay. The next chapter will outline an overview of the experimental technique used to search for $K_L \to \pi^0 \nu\bar{\nu}$. The details of detector and run condition will be described in Chapter 3.

In order to measure the branching ratio, we need to understand the detector acceptance. This is obtained from Monte Carlo simulation, which will be summarized in Chapter 4. Chapter 5 is devoted to the event reconstruction used in data analysis. Chapter 6 will discuss the event selection to suppress backgrounds. Since there were various types of backgrounds, each source required a careful study. In Chapter 7, we will present the estimation of background level. Chapter 8 will cover the discussion of the systematic error in this experiment. In Chapter 9, the result and discussion will be presented. Chapter 10 will conclude this thesis.

Chapter 2

Experimental Technique

In this chapter, we describe experimental techniques to search for $K_L \to \pi^0\nu\bar{\nu}$ decays. As shown in Section 1.3.3, a search for $K_L \to \pi^0\nu\bar{\nu}$ is experimentally very challenging because of two missing particles. To do such a challenging experiment, new technologies and ideas were developed. Those ideas are described here.

In Section 2.1, we discuss the signature of $K_L \to \pi^0\nu\bar{\nu}$ decay and its signal detection. In Section 2.2, we explain the background sources in this search, and introduce basic idea to eliminate the backgrounds. Section 2.3 discusses how to measure a branching ratio, and an experimental sensitivity. In Section 2.4, we cover the experimental technique to measure the number of K_L decays. Section 2.5 summarizes this chapter.

2.1 The Signature

Since two of the decay products, ν and $\bar{\nu}$ from $K_L \to \pi^0\nu\bar{\nu}$, cannot be detected practically, the signature of $K_L \to \pi^0\nu\bar{\nu}$ was an isolated π^0. The π^0 decays immediately with a short life time ($\tau_{\pi^0} = [8.4 \pm 0.6] \times 10^{-17}$ sec), and thus we must reconstruct π^0 from its decay products.

There are several channels in π^0 decays, but we can utilize only two modes actually, $\pi^0 \to \gamma\gamma$(referred to as "two photon mode") or $\pi^0 \to e^+e^-\gamma$(referred to as "Dalitz mode"), because the other decay channels have small branching ratio as shown in Table 2.1.

Table 2.1: π^0 branching ratio for various decay modes.

Decay mode	BR
$\pi^0 \to \gamma\gamma$	$(99.798 \pm 0.032)\%$
$\pi^0 \to e^+e^-\gamma$	$(1.198 \pm 0.032)\%$
$\pi^0 \to e^+e^-e^+e^-$	$(3.14 \pm 0.30) \times 10^{-5}$
$\pi^0 \to e^+e^-$	$(7.5 \pm 2.0) \times 10^{-8}$

In the following, we discuss the two experimental techniques to identify π^0 decays. First, we describe the π^0 detection using the Dalitz mode. Second, we present the technique in the two photon mode. The last subsectin summarizes the π^0 detection.

2.1.1 $\pi^0 \to e^+e^-\gamma$ Detection

The signature of $K_L \to \pi^0\nu\bar{\nu}$ decay with the Dalitz mode was an isolated $\pi^0 \to e^+e^-\gamma$ decay.

The invariant mass of $e^+e^-\gamma$ provides helpful information to identify π^0's. To reconstruct the invariant mass, it was crucial to measure the momenta and positions of the three particles as well as the decay vertex position. An electron identification was also necessary.

To measure the momenta and positions of the two charged particles, we used a spectrometer consisting of four drift chambers and an analyzing magnet. This also enabled us to determine the decay vertex point. To measure the position and energy of photons, an electromagnetic calorimeter was used. The calorimeter also measured the energy of charged particles, which was used to discriminate electrons from the other charged particles in combination with the momentum measurement(see Section 5.4). Further π/e separation was given by Transition Radiation Detectors(TRDs). Using these devices, the invariant mass of $e^+e^-\gamma$ was calculated event by event basis. Requiring the reconstructed invariant mass to be consistent with π^0 mass allowed us to select a real π^0 decay.

In order to ensure that the reconstructed $\pi^0 \to e^+e^-\gamma$ decays were isolated events, many veto counters were used to detect missing particles from the fiducial area of the calorimeter[1]. No activities in those veto counters were required.

2.1.2 $\pi^0 \to \gamma\gamma$ Detection

Since the final state particles are two photons, their positions at the calorimeter and energy are the only measurable quantities. To identify decayed π^0 from these observables, we assume the π^0 mass and calculate its vertex position along the K_L's flight direction [69]. The event whose vertex position is in the decay volume is regarded as a π^0 decay. Plus, if there is no other activities in any other veto detectors, that event is attributed to $K_L \to \pi^0\nu\bar{\nu}$.

2.1.3 Summary

In the Dalitz mode, we can positively identify π^0 decays by reconstructing their invariant mass, thanks to the vertex information. The vertex information is also crucial to suppress various kinds of backgrounds. On the other hand, any events with two photons basically could fake a signal in the $\pi^0 \to \gamma\gamma$ mode. The only effective way to suppress backgrounds is veto events with any extra activities in detectors.

By these differences, it was expected for the Dalitz mode to give one or two orders of magnitude lower background level than the two photon mode. And thus, the Dalitz mode was expected to have better sensitivity. Therefore, we searched for $K_L \to \pi^0\nu\bar{\nu}$ using $\pi^0 \to e^+e^-\gamma$ decay mode. The comparison of the two techniques using data is described in Section 9.4.

2.2 Backgrounds

Since the signature of $K_L \to \pi^0\nu\bar{\nu}$ decay was an existence of an isolated π^0, there were various kinds of background. The background sources including their PDG [13] branching ratios are listed in Table 2.2.

These background sources are classified into 4 groups described below.

1. Only one π^0 in the final state is reconstructed and other decay products, mainly hadrons, are not detected.
   eg. $K_L \to \pi^+\pi^-\pi^0_D$ (charged pions are not detected).
   eg. $\Lambda \to n\pi^0_D$ (a neutron is not detected).
   eg. $\Xi \to \Lambda(\to p\pi^-)\pi^0_D$ (a proton and a charged pion are not detected).

[1] Since our experiment was a fixed target experiment, the geometrical coverage of the calorimeter was far from 100%. See Chapter 3 for more details.

Table 2.2: Branching ratio and kinematical limit for signal and backgrounds in $K_L \to \pi^0\nu\bar{\nu}$ search with π^0 Dalitz decay mode, where π^0_D denotes $\pi^0 \to e^+e^-\gamma$ decay. The listed branching ratio is a product of branching ratios involved in each background process, including combinatorial factor to pick one π^0 for Dalitz decay. The p_{max} denotes π^0's maximum momentum at the parent particle's rest frame.

Decay mode	BR	p_{max} (MeV/c)
$K_L \to \pi^0\nu\bar{\nu}$	–	231
$K_L \to \pi^0\pi^0\pi^0_D$	7.41×10^{-3}	139
$K_L \to \pi^0\pi^0_D$	2.22×10^{-5}	209
$K_L \to \pi^+\pi^-\pi^0_D$	1.50×10^{-3}	133
$K_L \to \pi e \nu$	38.78%	–
$\Lambda \to n\pi^0_D$	4.29×10^{-3}	104
$\Xi \to \Lambda(\to n\pi^0_D)\pi^0$	4.22×10^{-3}	104+X
$\Xi \to \Lambda(\to p\pi^-)\pi^0_D$	7.62×10^{-3}	135
$\Xi \to \Lambda(\to n\pi^0)\pi^0_D$	4.22×10^{-3}	135
$n + X \to \pi^0 X'$	–	–

2. Only one π^0 can be identified due to undetected photons decayed from other π^0('s). In this case, a wrong pairing of photon with e^+e^- in the event reconstruction can occur.
   eg. $K_L \to \pi^0\pi^0\pi^0_D$.
   eg. $K_L \to \pi^0\pi^0_D$.
   eg. $\Xi \to \Lambda(\to n\pi^0)\pi^0_D$.
   eg. $\Xi \to \Lambda(\to n\pi^0_D)\pi^0$.

3. No π^0 is involved in the final state, but the decay products are mis-identified as a π^0.
   eg. $K_L \to \pi e \nu + \gamma_{acc}$,
   eg. $K_L \to \pi e \nu + \gamma_{rad}$,
   where γ_{acc} and γ_{rad} denote an accidentally overlapped photon, and a photon radiated from an electron, respectively.

4. A neutron in the beam interacts with detector material and produces one or more π^0's.
   eg. $n + X \to \pi^0 + X'$.

To reject background in category 1, we made a use of a kinematical feature in a $K_L \to \pi^0\nu\bar{\nu}$ decay. The π^0 from a signal decay can have higher momentum at the K_L's rest frame than that of other decays, as seen in Table 2.2. Therefore, selecting a high momentum π^0 in the parent's rest frame would suppress the background in category 1.

In general, the backgrounds in category 2 should be eliminated by the kinematical requirements just mentioned above, except for $K_L \to \pi^0\pi^0_D$ which can have a momentum in the K_L's rest frame close to the signal decay. However, a wrong combination of a photon to e^+e^- in the reconstruction could distort the kinematical variables. Therefore, photon veto counters were necessary to suppress type 2 backgrounds by vetoing the events with extra photons escaping from the fiducial area of the calorimeter.

The background in the third category was related to $K_L \to \pi^+e^-\bar{\nu}$(or $K_L \to \pi^-e^+\nu$)(referred to as K_{e3}). A misidentification of charged pion as an electron with an additional photon, which might be accidental overlap or a radiation from an electron, could make the event reconstructed as π^0. Even if we had a perfect condition without any accidental activities, an electron radiates a photon($E^*_\gamma > 1$ MeV) with a probability of 11% [68]. In addition, the high branching fraction of $K_L \to \pi e \nu$ made a K_{e3} a severe background. Therefore, identification of electron was crucial to reduce K_{e3} backgrounds. Also some kinematical constraints, which utilized another feature in the Dalitz decay(Section 6.2.1), were applied to achieve more suppression.

For the fourth category, the π^0's produced by beam neutron interactions with detector material can be distinguished from signal by the vertex position. Otherwise, the rejection of this background was difficult because they could have p_t comparable with $K_L \rightarrow \pi^0\nu\bar{\nu}$, and no other final state particles might be produced and/or detected.

2.3 Sensitivity

To measure the branching ratio of $K_L \rightarrow \pi^0\nu\bar{\nu}$, we have to know the number of K_L's decayed in detector's fiducial area. For such purpose, we collected data not only for signal decays but also for another decay mode whose branching ratio was already known well. Such a decay channel is called "normalization" mode. The following equation shows the relation between the branching ratio to be measured and some input variables:

$$Br(signal) = \frac{N_{signal}}{A_{signal}} \times \frac{A_{norm}}{N_{norm}} \times Br(norm) \ , \tag{2.1}$$

where N_{signal} and N_{norm} represent the number of observed signal and normalization events, and A_{signal} and A_{norm} denote the acceptances for signal and normalization modes, respectively.

As can be seen in Equation 2.1, higher acceptance and larger number of K_L decays allow us to measure a smaller branching ratio. In our experiment, K_L's were produced by proton beam striking a fixed target. In order to achieve a high K_L flux, high intensity proton beam was used. The detailed discussion on the beam is found in Chapter 3.

The branching ratio that an experiment is expected to see one event is called "Single Event Sensitivity(SES)" of the experiment, which is expressed as

$$SES = \frac{1}{A_{signal}} \times \frac{A_{norm}}{N_{norm}} \times Br(norm) \ . \tag{2.2}$$

In another words, if the branching ratio of the signal is $Br(signal)$, then the experiment is expected to observe $Br(signal)$/SES events on average. It is a measure of experimental sensitivity to the rare decay. Since a secondary $\pi^0 \rightarrow e^+e^-\gamma$ decay was a signature in our $K_L \rightarrow \pi^0\nu\bar{\nu}$ search, a branching ratio of $\pi^0 \rightarrow e^+e^-\gamma$ must be involved to calculate the SES as

$$SES = \frac{1}{A_{signal}} \times \frac{A_{norm}}{N_{norm}} \times \frac{Br(norm)}{Br(\pi^0 \rightarrow e^+e^-\gamma)} \ . \tag{2.3}$$

2.4 Normalization

By selecting a normalization mode which has a similar kinematics with a signal, we can cancel out the difference in a trigger efficiency, in particle identification etc., which are the sources of systematic error. Therefore, in a branching ratio measurement, normalizing to another decay mode is more reliable [67] than normalizing to to the number of absolute K_L decays.

In the search for $K_L \rightarrow \pi^0\nu\bar{\nu}$ whose π^0 undergoes $e^+e^-\gamma$, we used $K_L \rightarrow e^+e^-\gamma$ decay as a normalization mode. Its branching ratio is known to 5% of itself [13],

$$Br(K_L \rightarrow e^+e^-\gamma) = (9.1 \pm 0.5) \times 10^{-6} \ .$$

Since the final state of $K_L \rightarrow e^+e^-\gamma$ was exactly the same with the signal mode, systematic errors due to detector efficiencies and kinematical cuts were expected to cancel out.

2.5 Summary

So far, $K_L \to \pi^0\nu\bar{\nu}$ decay have been searched for using π^0 Dalitz mode [64, 65], because of the benefit from vertex information. As well as the past experiments, our search for $K_L \to \pi^0\nu\bar{\nu}$ was carried out using the Dalitz mode, because it was expected to give a better sensitivity than that by the two photon mode. We will cover the search with the Dalitz mode in this thesis.

In the search for $K_L \to \pi^0\nu\bar{\nu}$ decay, there were some critical detectors for rejecting backgrounds. As already mentioned in previous sections, one of the critical systems was a photon veto counter. Vetoing events by detecting photons coming from extra π^0's was one of the most powerful weapons to reject backgrounds in category 2. In order to remove a background related to K_{e3}'s, the most important tool was particle identification. This required good performance of the calorimeter and the Transition Radiation Detectors.

In the following chapter, we will discuss the experiment and the details of our detectors including these key elements.

Chapter 3

The Apparatus and Run

This chapter describes the kaon beam production, detector elements and special features of the run in the $K_L \to \pi^0 \nu\bar{\nu}$ search. It begins with the overview of the experiment. In Section 3.2 and 3.3, we give a brief description of K_L beam production and each detector element. Along with the actual data flow, the nexts of the detector's descriptions are trigger and data acquisition system(DAQ). In Section 3.6, we explain the run condition. More details can be found in reference [66]. Only the essential features in $K_L \to \pi^0 \nu\bar{\nu}$ analysis are covered here.

3.1 Overview of the Experiment

The experiment was carried out as a part of Fermilab experiment E799-II [1] The data was collected in two periods, from January to March in 1997(referred to as "Winter Run") and from August to September in 1997(referred to as "Summer Run").

Two nearly parallel K_L beams were produced by an 800 GeV proton beam from Tevatron incident on a BeO target. After some collimations and sweeping of charged particle, the neutral beam went into a vacuum decay volume located 90 m through 159 m downstream of the target. The trajectories and momenta of charged particles were measured by a spectrometer composed of four drift chambers and an analyzing magnet. The position and energy of photon were measured with a CsI calorimeter located at 186 m from the target. Two scintillator hodoscopes were placed between the spectrometer and the calorimeter for triggering on charged particles. There were several veto counters for photons escaping from the calorimeter's fiducial area. A total of eight Transition Radiation Detectors were used for the particle identification, namely π/e separation, which was located between the spectrometer and trigger hodoscope. Using 800 GeV protons to produce K_L, we could attain high acceptance for multi-body decay and high energy resolution for photon.

3.2 K_L Beam Production

The Fermilab Tevatron delivered 800 GeV protons in a 23 second period, known as a "spill", and there was such a spill in every 60 seconds. The spill itself was divided into many "buckets", which was determined by a 53 MHz radio frequency (RF) of the Tevatron. This RF substructure provided a basic timing information to form trigger logic. The buckets were separated by 19 nsec, and the

[1] Both E832, whose goal was to measure direct CP violating parameter ϵ' with an accuracy of 10^{-4}, and E799-II experiment at Fermilab are called "KTeV". They used the same detector with slightly different setups. whose main focus was to search for direct CP violation in the decays, $K_L \to \pi^0 e^+ e^-$, $K_L \to \pi^0 \mu^+ \mu^-$ and $K_L \to \pi^0 \nu\bar{\nu}$.

protons arrived in a 2 nsec period at the beginning of each bucket. The target typically received 5.0×10^{12} protons per spill for winter run, and 3.5×10^{12} for summer run.

The K_L beams were produced by an 800 GeV proton beam incident on a beryllium oxide target which was 30.5 cm long($\sim$ 0.9 nuclear interaction length) with a cross section of 3.0 mm $\times$ 3.0 mm. The targeting angle was chosen to be 4.8 mrad in vertical so that we would obtain both high kaon flux and good kaon to neutron ratio in the beams, because beam neutrons would interact with detector materials and could be serious backgrounds in the $K_L \to \pi^0 \nu\bar{\nu}$ search(and in all the physics modes). At z=90 m, the contamination of neutrons, Λ, and Ξ in K_L beams were estimated to be 3.5, 0.02, and 7.5×10^{-4}, respectively. Figure 3.1 shows the K_L momentum spectrum at z = 90 m reproduced by the simulation which is described in Chapter 4. In order to shape two

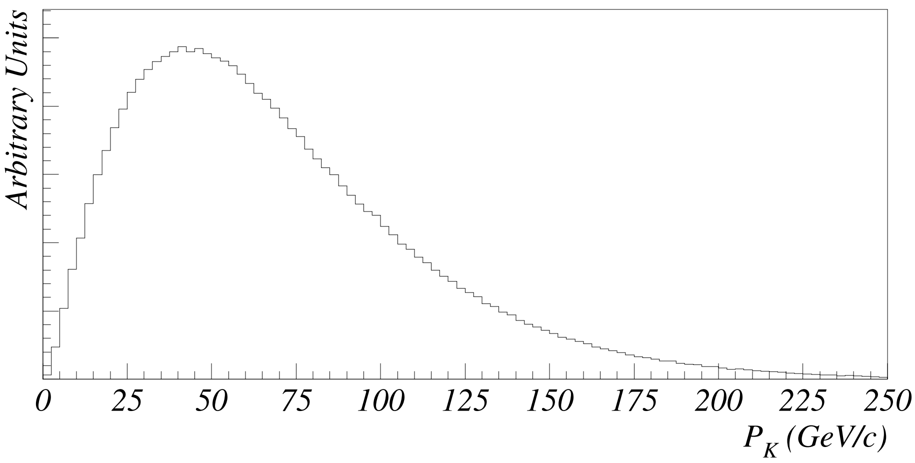

Figure 3.1: K_L's momentum distribution at z = 90 m.

nearly parallel beams, to remove charged particles, and to reduce photons and neutrons in the beams, some collimators, absorbers, and sweeping magnets were located downstream of the target as shown in Figure 3.2. The absorber made of 7.6 cm long lead was placed at 18.5 m downstream of the target in the beam to convert photons to electron-positron pairs which would be removed by sweeping magnet.

We used two sizes of beam. For Winter Run, the solid angle of each beam was collimated to 0.5 mrad $\times$ 0.5 mrad with three collimators explained below. The first collimator, called as primary collimator, located 19.8 m downstream of the target and was made of 1.5 m long thick combination of steel and brass with two holes, followed by a set of sweeping magnets. The hole size was 1.09 cm $\times$ 1.09 cm each at the upstream end of the collimator and the centers of those two holes were separated by 3.19 cm. Following the primary collimator was steel slab collimator with 2 m long, which was located at 38.8 m downstream of the target in order to prevent hadrons scattering in the absorbers from crossing-over to the neighboring beam. At 85.0 m downstream of the target, defining collimator, made of steel was placed to define the edges of the two beams. The beam holes' size was 4.25 cm $\times$ 4.25 cm each. These sets of collimators produced beams whose centers were separated by about 15 cm when they were 186 m downstream of the target.

For Summer Run, each beam had a solid angle of 0.7 mrad $\times$ 0.7 mrad. That was obtained by a primary collimator and defining collimator with a beam hole size 1.4 times larger than that of Winter Run. Other dimensions and materials of those collimators were the same as Winter Run. Since elastic scattering at the absorber from one beam quickly became much larger than the

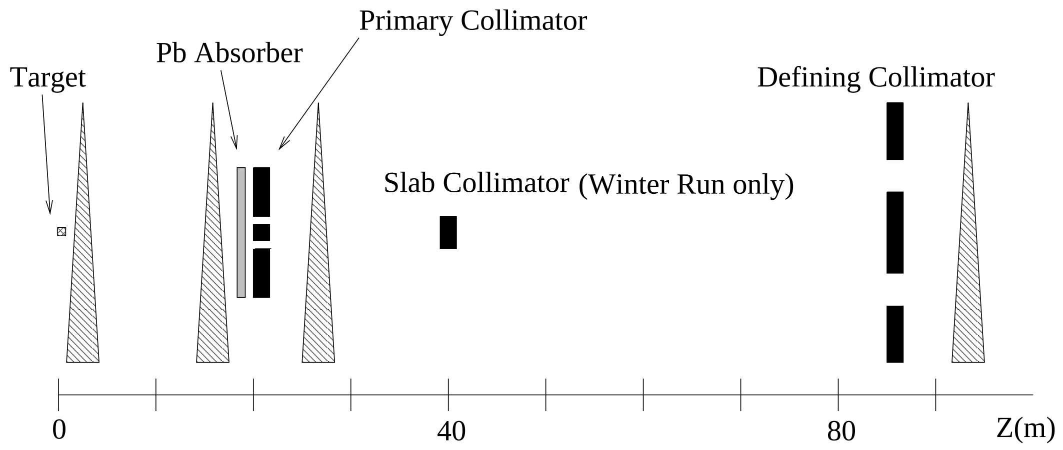

Figure 3.2: Schematic plan view of the collimation and sweeping system used to produce the two K_L beams.

cross-over problem in the larger beams, we did not use the slab collimator. The increased solid angle of beam compensated for the lower beam intensity during the Summer Run. The beam size was limited by the radiation damage in the CsI crystals located near the beam holes.

In order to reduce the interaction of the beam with materials, the beam entered in cylindrical vacuum tank. The vacuum was held at $\sim 1.0 \times 10^{-6}$ torr, starting at ~ 50 m(the decay region started from 90 m) and ending at 159 m downstream of the target. Downstream end of the vacuum region was sealed by a window with a diameter of 0.9 m made of Kevlar and aluminized mylar, called as "vacuum window". The thickness of the vacuum window was estimated to as 0.16% in radiation length.

3.3 Detector Elements and Layout

Figure 3.3 shows a schematic drawing of all the elements in E799-II detector, and their locations and dimensions are listed in Table 3.1. A global coordinate system was defined to describe the positions and orientations of the detector elements. The z direction is defined by the vector pointing from the center of the target to the very center of the CsI electromagnetic calorimeter. The y coordinate is defined to be vertical, with upward direction to be positive, and the x coordinate is given in the clockwise system. Each detector element is described in this section.

3.3.1 Spectrometer

The main purpose of the spectrometer, which consisted of four drift chambers(DC's) and an analyzing magnet, was to detect charged particles, to measure the momenta of charged particles, and to give vertex position. These informations were used to reconstruct $\pi^0 \to e^+e^-\gamma$ events. Two of the drift chambers were located upstream of the analyzing magnet, and the rests of two were downstream of the magnet. Helium bags were placed between all of the drift chambers to reduce the effects of multiple scattering on the measurement of particle trajectories and momenta. Measuring charged particle trajectories with a momentum kick given by the magnet, we extracted momenta of charged particles.

As shown in Figure 3.4, cells of the drift chamber consisted of a sense wire located at the center of a hexagon defined by six field wires. The wires in a sense plane were separated by 12.7 mm, and

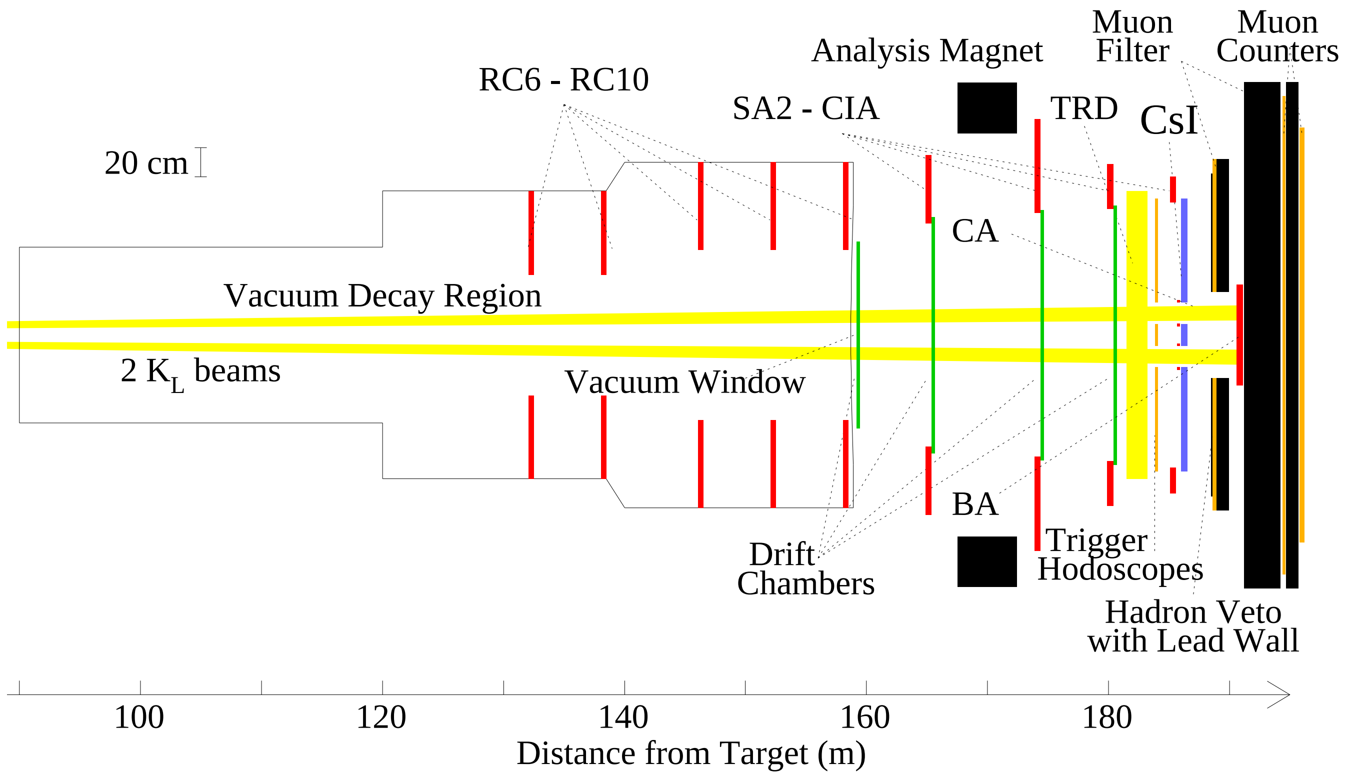

Figure 3.3: Schematic drawing of KTeV detector.

Table 3.1: Positions and Dimensions of the detector elements. All units in meter.

Detector Element	Distance from Target(m) at front face of the detector	Transverse Size(m)
RC6	132.596	inner : 0.84×0.84
		outer radius : 1.00
RC7	138.598	inner : 0.84×0.84
		outer radius : 1.00
RC8	146.598	inner : 1.18×1.18
		outer radius : 1.44
RC9	152.600	inner : 1.18×1.18
		outer radius : 1.44
RC10	158.599	inner : 1.18×1.18
		outer radius : 1.44
Vacum Window	158.890	-
DC1(x plane)	159.419	1.30×1.30
SA2	165.116	inner : 1.540×1.366
		outer : 2.500×2.500
DC2(x plane)	165.565	1.64×1.44
Analyzing Magnet	170.008	inner : 2.9×2.0
SA3	173.985	inner : 1.692×1.600
		outer : 3.000×2.400
DC3(x plane)	174.589	1.74×1.64
SA4	180.018	inner : 1.754×1.754
		outer : 2.372×2.372
DC4(x plane)	180.486	1.90×1.90
TRD1	181.171	2.184×2.184
TRD2	181.484	2.184×2.184
TRD3	181.796	2.184×2.184
TRD4	182.109	2.184×2.184
TRD5	182.421	2.184×2.184
TRD6	182.734	2.184×2.184
TRD7	183.046	2.184×2.184
TRD8	183.359	2.184×2.184
V bank	183.903	1.900×1.900
V' bank	183.953	1.900×1.900
CIA	185.191	inner : 1.842×1.842
		outer : 2.200×2.200
CA	185.913	inner : 0.150×0.150
		outer : 0.180×0.180
CsI	186.013	1.900×1.900
HA	188.966	2.24×2.24
BA	191.087	0.60×0.30
Mu2	194.827	3.93×2.99

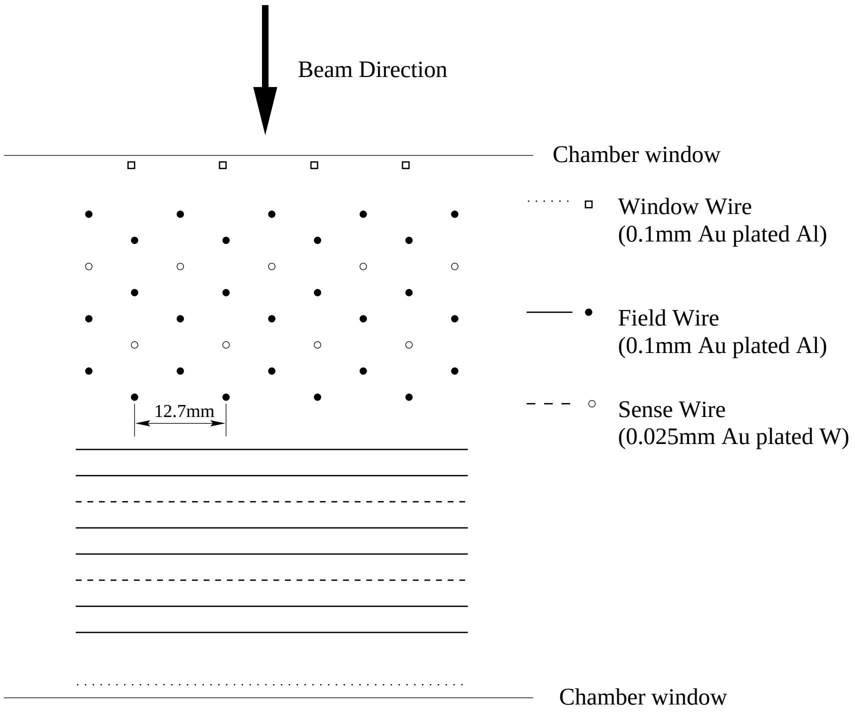

Figure 3.4: Layout of the field shaping and sense wires used in all drift chambers. This is the view looking down on the chambers, with the vertical wires which measure x position in the front and the horizontal wires which measure y position in the rear of the chamber.

both the x and y views of each chamber had two sense planes, referred to as $x(y)$ and $x'(y')$ plane, offset by half that distance. The field shaping wires were made of 100 μm gold-plated aluminum and the sense wires were 25 μm gold-plated tungsten. This yielded a drift distance of 6.35 mm perpendicular to a wire and an unambiguous determination of the side of the wire by which a particle passed. The most upstream chamber was the smallest, 1.3 m $\times$ 1.3 m, and each successive chamber increased in size, the largest being 1.9 m $\times$ 1.9 m.

The chambers used two kinds of gas mixture during the run. One was 49.75% Argon, 49.75% Ethane, and 0.5% isopropyl alcohol by volume. The other consisted of 49.5% Argon and 49.5% Ethane with 1.0% isopropyl for additional quenching. With the typical applied voltage of -2500V, the drift velocities in these chamber were of the order of 50 μm/ns.

The pulses from the drift chambers were amplified and discriminated in front end cards mounted on the chambers themselves. The discriminated signals with 40 nsec width were then sensed by LeCroy 3377 time to digital converters(TDCs) with a resolution of 0.5 ns. The TDCs were operated in "common stop mode" where an incoming pulse would start a TDC channel and a later stop pulse from the first level trigger would stop all triggered channels. The resulting time distribution is shown in Figure 3.5. The in-time window was defined as $115 < \text{time(ns)} < 350$. The tail seen

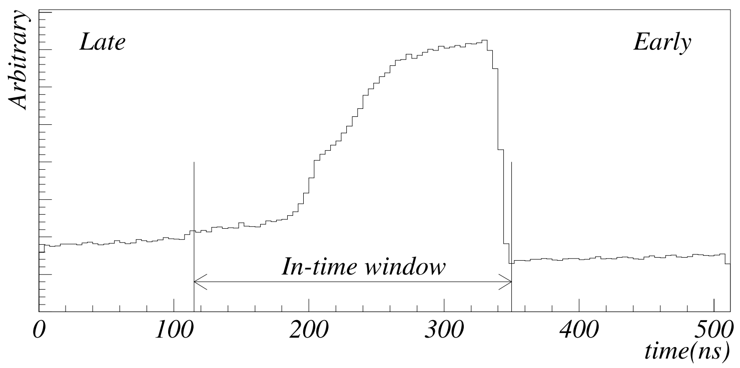

Figure 3.5: Time distribution of Drifit Chamber TDC. Only the hits between 115 ns and 350 ns were used as in-time hit.

in the time less than 200 ns was due to a hit very far from sense wire and between the field wires where electromagnetic field did not have a proper slope. The slope between 200 ns and 270 ns was due to non-linearity of drift velocity at the region far from sense wires.

The TDC counts in drift chambers were translated to a distance from sense wire to the closest point of the charged particle trajectory. The position resolution of each chamber was determined from the measurement of a sum of the two drift distance(SOD) in each view. Since the offset of two sense wires were 6.35 mm, the sum of distance should equal to 6.35 mm. Figure 3.6 shows the distribution of the SOD after subtracting the 6.35 mm offset, which has a clear peak at 0 mm. The width of the distribution, considered as a resolution in one plane, was roughly 150 μm as shown in the figure. It implies that each chamber plane had a resolution of 150 μm $\times 1/\sqrt{2} \simeq 100$ μm by taking account the fact that the SOD was obtained from two individual measurements.

Between the second and third drift chambers, the charged particles were given a transverse momentum kick by a dipole magnet with a vertical field of about 2 kG. The magnetic gap was 2.9 m $\times$ 2.0 m $\times$ 3.1 m. The transverse momentum kick transferred, Δp_t, was typically 205 MeV.

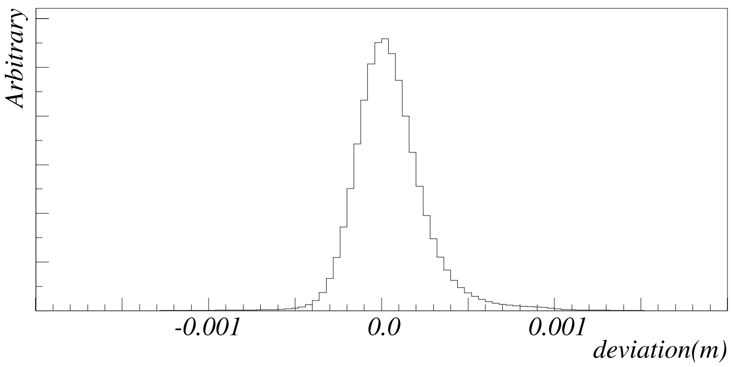

Figure 3.6: The deviation of sum of drift distance from the offset of 6.35 mm.

The drift chamber's intrinsic resolution was measured to be

$$\frac{\sigma p}{p} = 0.016\% \times p + 0.38\% \,, \tag{3.1}$$

where p is the momentum of a charged particle in GeV/c. The multiple scattering in the spectrometer caused the constant term of 0.19%. The term linear in momentum resulted from the finite resolution of measuring the space point in each chamber.

Besides the main purposes described the above, the signal from the drift chamber was viewed by two devices for triggering.

First device was the hit counting module at front end. It counted the number of in-time hits in each drift chamber plane(Section 3.4.1). The prompt output, which arrived in(or less than) half the maximum drift time in each chamber, was used to form trigger logic after the discrimination.

Another device was the track finding processor, mainly consisted of custom made Trigger TDCs. This device determined the number of hit-pairs in each chamber by defining a time window for sum of the TDC counts of two planes in one chamber. The Trigger TDC did not measure times with as accurate as the conventional one; however, the digitized time was much faster, which was available in use of trigger logic.

3.3.2 Electromagnetic Calorimeter

The primary purpose of electromagnetic calorimeter was to measure the energy and position of photon. The second purpose was a particle identification, namely π/e separation. In addition, measuring the charged particle position at the calorimeter enabled us to resolve the x-y ambiguity in the track reconstruction. For these purposes, we used CsI array as an electromagnetic calorimeter. In our $K_L \to \pi^0\nu\bar{\nu}$ search, the π/e separation factor of 400 or 500 was needed to suppress K_{e3} backgrounds. The detailed description of this calorimeter can be found in reference [72], so only the essential part is described here.

CsI Crystals

As shown in Figure 3.7, the calorimeter composed of 3100 pure CsI crystals with a length of 50 cm(=27X_0). There were two sizes of crystals. For inner part of 120 cm × 120 cm area, 2232 of 2.5 cm × 2.5 cm crystals were placed with two beam holes whose sizes were 15 cm × 15 cm each. For outside of the 120 cm × 120 cm area, 868 of 5 cm × 5 cm crystals were stacked. A 80% of all crystals were composed from two halves(25 cm long each) glued with Epo-Tek 305 epoxy, which was chosen for its high UV transmission. The remaining 20% was 50 cm long single crystal without connection.

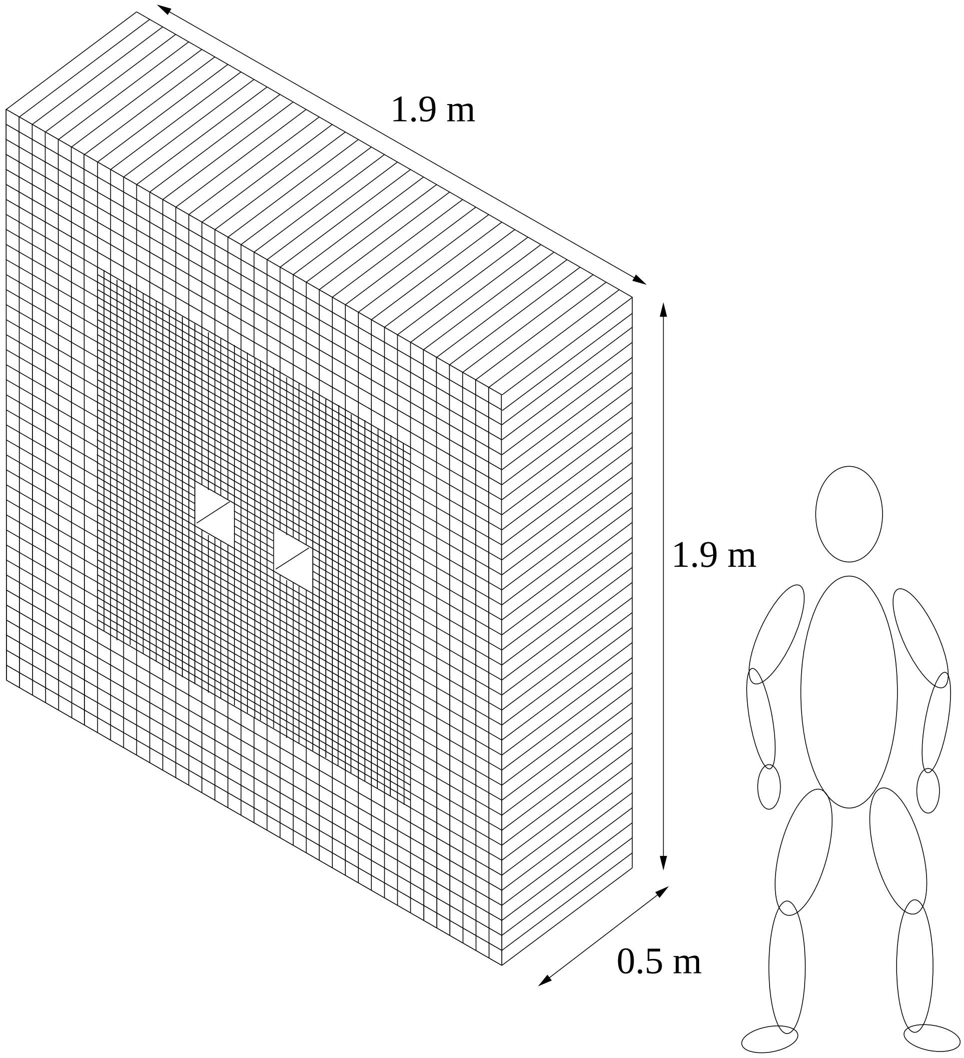

Figure 3.7: The CsI array consisting of the electromagnetic calorimeter.

In order to optically isolate each crystal and to make the light collection effective, each crystal was wrapped by mylar with thickness of 13 μm. The upstream section of the mylar wrapping was aluminized, and the downstream section was painted with black ink. The location of the boundary between the aluminized and black mylar sections was tuned for each crystal such that the light yield was nearly uniform along z. The resulting non-uniformities were typically several percent.

The CsI crystal yielded typically 20 photoelectrons per MeV, hence photo-statistics contributed less than 0.4% to the energy resolution for energy greater than 3 GeV. The scintillation spectrum can be approximately characterized by a 'fast' and a 'slow' component. The fast spectrum peaked at 315 nm with a time constant of $\sim$20 ns. The slow one peaked at 420 nm and had a time constant of $\sim 1\ \mu$m. From 80 to 90% of the scintillation light was emitted within 100 ns.

The CsI light yield depends on the temperature with -1.5% per degree Celsius. In oreder to reduce the gain fluctuations due to the temperature variation, the array was placed in a light-tight blockhouse where the temperature was controlled to $\pm 0.1°$C.

Photomultiplier Tubes

The scintillation light produced by electromagnetic showers in the CsI crystal was detected by the photomultiplier tube(PMT) mounted on the back of each crystal. The large crystal was viewed by 1.5 inch Hamamatsu R5330 PMT with six stage dynodes, and small crystal was viewed by 3/4 inch Hamamatsu R5364 with five stage dynodes. Both type of the PMTs had a gain of 5000 with a typical high voltage of -1200V. Those were linear in their response to within $\pm 0.5\%$ for peak anode current up to 30 mA(= roughly 80 GeV of energy deposited in the CsI). The front face of the PMT was made of UV transmitting glass to accommodate the emission spectrum of the fast scintillation light from the CsI crystals. The PMTs were wrapped with two layers of 0.002 inch kapton for the insulation, and with one layer of 0.006 inch mu-metal between the two layers of kapton. The mu-metal served as an RF shield, and shared a common ground with the anode and dynode signal produced by the PMT.

The PMTs were coupled to the crystals with two layers of General Electric RTV 656. Between the two RTV layers, 1 mm thick Schott UG 11 glass filter was attached, which had good transmission for the fast UV scintillation light while absorbing most of the slow light component. The refractive index of CsI was 1.80, and the photocathode of PMT was 1.40. The RTV was chosen to reduce the light reflection between the two materials.

Readout Electronics

The digital photomultiplier tube base(DPMT) was used for readout of signal from the calorimeter. The main components of the DPMT were a high voltage divider for the photomultiplier tube, a charge integrating and encoding(QIE) custom integrated circuit, an Analog Devices AD9002 8-bit flash ADC(FADC), and a driver/buffer/clocking(DBC) custom integrated circuit. The system was operated at 53MHz(= accelerator RF), corresponding to 19 ns clock cycle.

The DPMT had nine non-overlapping sensitivity ranges. For each clock cycle it produced a 12-bit floating point number; an 8-bit mantissa and a 4-bit exponent. For a given input current integrated over a clock cycle, the QIE selected the appropriate sensitivity range and sent a voltage to the 8-bit FADC. The sensitivity range was encoded as the 4-bit exponent while the output from the FADC formed the 8-bit mantissa.

The operation of the digitizing circuit was shown in Figure 3.8. The crucial component of the DPMT was the QIE, which added a fixed bias current to the PMT anode signal current, divided the total current into nine binary range(I/2, I/4, ... , I/512), and simultaneously integrated the divided currents on nine separate 1 pF capacitors. The nine capacitor voltages were then compared to a common reference voltage. The result of this comparison was used to form the 4-bit exponent and to select the capacitor which would send its voltage to the FADC.

The QIE operations were pipelined, with four identical circuits functioning in a round-robin fashion. The duration of each operation was one clock cycle[2]. This enabled us to read out the signal from PMTs without andy dead time. Each QIE had a total of 36 capacitors, with four capacitors per range. To label the capacitor in the pipeline, the QIE generated a capacitor identification bit every clock cycle.

The DBC chip synchronized the mantissa and exponent information. For each clock cycle, the 12-bit floating point output and the capacitor ID bit were transferred into a custom built VME

[2] In this thesis, we refer to each clock cycle as "slice".

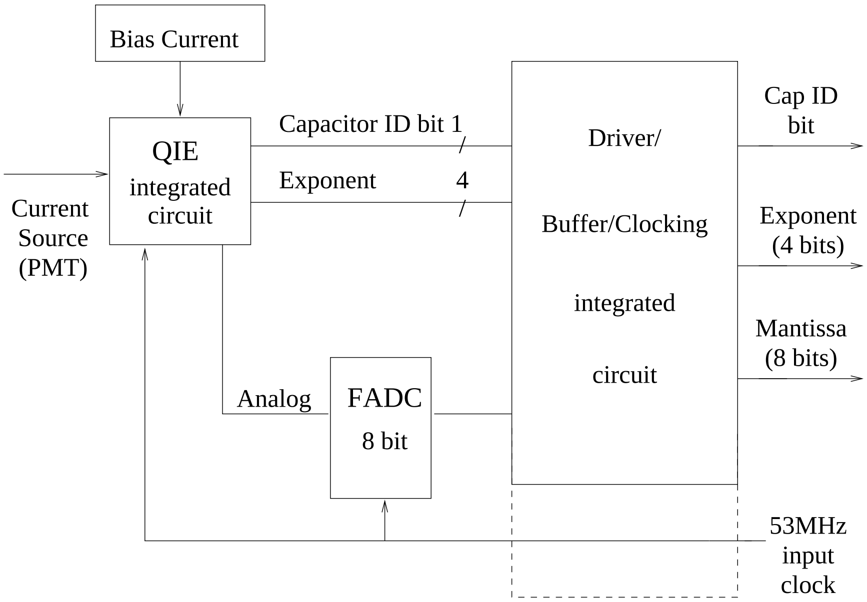

Figure 3.8: A block diagram of the operation of the digitizing base.

data buffer. Upon receipt of a trigger, the digital information was held in the data buffer until readout.

The dead time free read out system in DPMT made it possible to reduce the accidental effect, because the readout energy was divided into 19 ns time slices and one could compare the time distribution of the energy or charge(Section 5.5). The combination of mantissa and exponent enabled us to achieve a big dynamic range(a few MeV to over 60 GeV). The digitization of the output pulse from PMT without transmitting long cable, which caused attenuation and smearing of the pulse, allowed us to achieve the linearity less than 0.5%.

Laser Calibration System

The gain of the nine-range DPMT was monitored with a laser/dye system that injected a measured amount of light into each PMT. Quartz fibers attached to the back of crystals delivered pulses of light from a laser/dye system. The amplitude of each pulse was monitored independently by two PIN photodiodes so that one would associate the FADC and range values with the PIN photodiode signal. From this monitored information, the gain of each tube was corrected by adjusting the supplied high voltage, and the relation between light yield and charge output was calibrated.

Triggering information

The signals from the CsI array were used in trigger logic as well as digitized by the DPMT. There were two systems for providing the input as trigger source signals.

The first system was used to produce a very rapid measure of the total energy, (E_t), in the array at any time. The summing system consisted of sixty first level sum boards, each of which generated a sum of between 19 and 57 input channels. They were custom made and suitable for VME crate. The input to this system was a dinode signal from the last stage of the photomultiplier tubes, which was roughly 16 pC per 1 GeV energy deposited in the crystal. The first level sums were further summed, on the second level sum boards, to provide quadrant and full analog sums. The E_t system had another function providing a hit crystal information to cluster counting system described in the next paragraphs. It tagged those RF buckets for which the crystal in question had an energy deposit in excess of a preset threshold. The E_t system tagged the crystals with energy above the threshold, which is called HCC bit. This information was stored in 9×512 FIFO buffer memory. After receipt of a first level trigger, all 3100 signals were transmitted to the Column Alignment Buffer board in a single strobe, which served to latch the data from the front end electronics, sorted it into columns, and sent it to the cluster counting system.

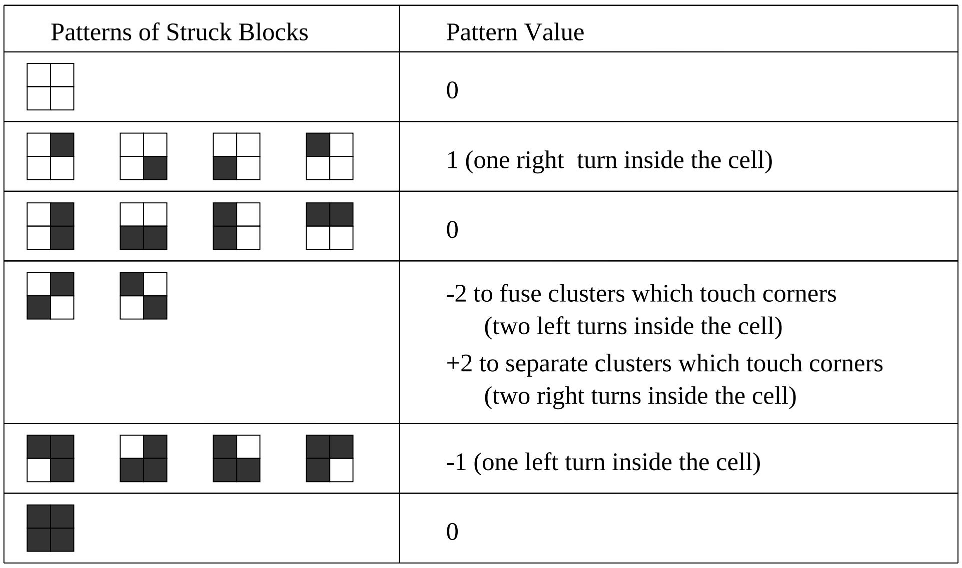

Figure 3.9: All possible hit patterns for a 2×2 array of blocks. The value assigned to each group of patterns is shown to the right.

The second device was a hardware cluster counting(HCC), which counted the number of clusters[3] in the CsI calorimeter.

The cluster finding algorithm started with the idea that an isolated cluster could be enclosed by a continuous perimeter. To make the perimeter, only the crystals which contained the energy above 1 GeV, based on the information from the E_t board, were used. While traveling clockwise around the perimeter, if we assign $+1$ for every right turn and -1 for every left turn, the sum of right turn minus left turn should be four because our CsI calorimeter consists of rectangular crystals. If we apply this procedure to the whole calorimeter, the resulting number of right turns subtracted by the number of left turns should be four times the number of clusters.

Right or left turns were determined by examing the pattern of the hits in 2×2 arrays. Figure 3.9 shows all the possible configuration of such group and the assigned number for each pattern. Since each crystal belonged to four different 2×2 grids, each crystal was used to determine four different pattern values. The sum of all 2×2 pattern value was four times the number of isolated clusters in whole arrays.

Once received data from Column Alignment Buffer, Cluster Counting Unit executed the cluster counting algorithm and produces a 4-bit cluster count. This 4-bit count was used to form a second level trigger.

[3] In this context, a cluster is referred to as contiguous island of blocks with energy above a threshold.

Details of the algorithm was published elsewhere [73, 74], and the detail of HCC itself can be found in reference [75].

Performance

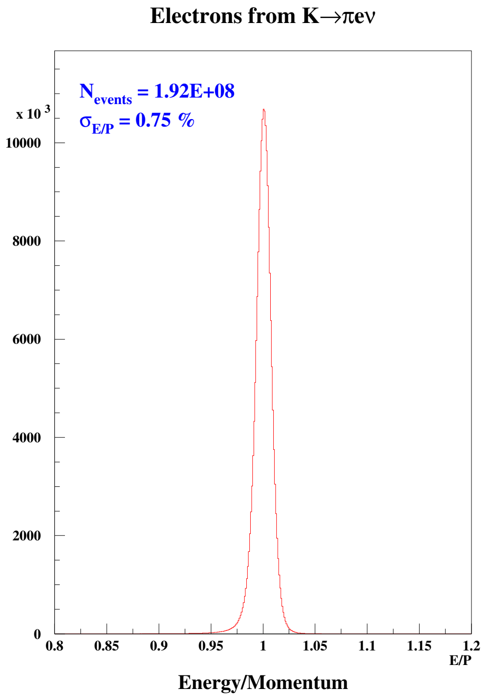

Figure 3.10: E/p for electron in K_{e3}'s, where E denotes an energy measured at the calorimeter, and p represents a momentum measured by a spectrometer. The fit with Gaussian give a sigma of 0.78%.

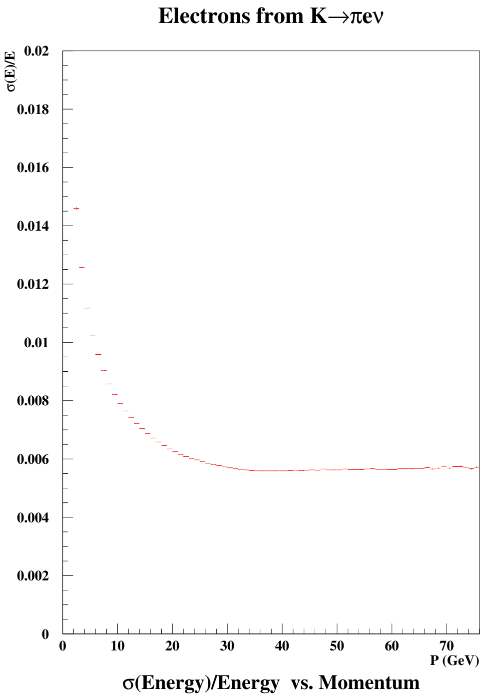

Figure 3.11: The calorimeter's intrinsic energy resolution measured in K_{e3} events as a function of electron momentum.

Figure 3.10 shows E/p for electron in K_{e3} events, where E denotes the energy measured by the CsI calorimeter and p represents the electron momentum measured by the spectrometer. Since the CsI calorimeter had 27 radiation lengths, electrons deposited most of their energy in the calorimeter and had a peak of unity in the E/p distribution. Due to a finite resolution in momentum measurement, the E/p was being smeared with the resolution expressed in Equation 3.1. Subtracting the resolution effect in p quadratically, the intrinsic resolution of the calorimeter is shown in Figure 3.11 as a function of electron momentum. The energy dependence had a form of

$$\frac{\sigma E}{E} = 0.6\% + \frac{0.6\%}{\sqrt{E}} \; .$$

The $1/\sqrt{E}$ dependence resulted from photo-statistics in scintillation light. The constant term of 0.6% accommodated other effects such as non-uniformity in light collection efficiency, uncorrected light leakage, internal calibration error, fluctuation of light yield due to temperature variation, electronic noise etc.

3.3.3 Photon Veto Counters

Events with extra photons missing the calorimeter could be backgrounds in the $K_L \to \pi^0 \nu \bar{\nu}$ search as mentioned in Chapter 2. There were four types of photon veto counters in total used in both online trigger and offline event selection in order to catch the particles escaping from fiducail area of the spectrometer and electromagnetic calorimeter. Each photon veto counter had a sandwich structure of radiators and scintillators. The light yield in the scintillator was detected by PMTs.

We had five Ring Counters(RC6-RC10) located the most upstream of all the detectors and inside the evacuated volume. The shape of RC was round at outside, such that it fit to the shape of the vacuum tank, and square at inside as shown in Figure 3.12. They consisted of 24 layer scintillator tiles with a thickness of 2.5 mm followed by lead sheets. For the first 16 layers, the lead sheets were 0.5 radiation length each. For the rest of 8 layers, the lead was 1 X_0 thick each, resulting in a total amount of lead to be 16 X_0.

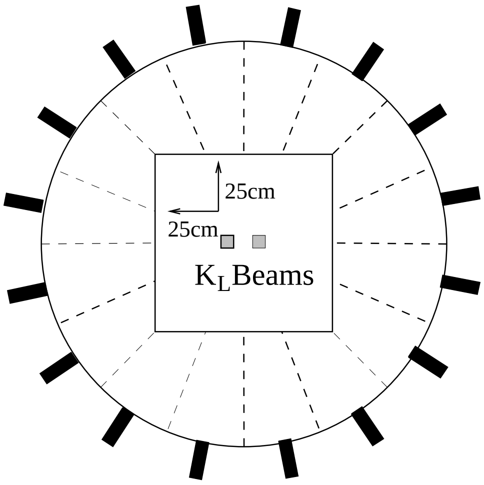

Figure 3.12: RC6 viewed from upstream, located inside the vacuum region. RC6 and RC7 were the same dimensions, and RC8 through RC10 had the same size.

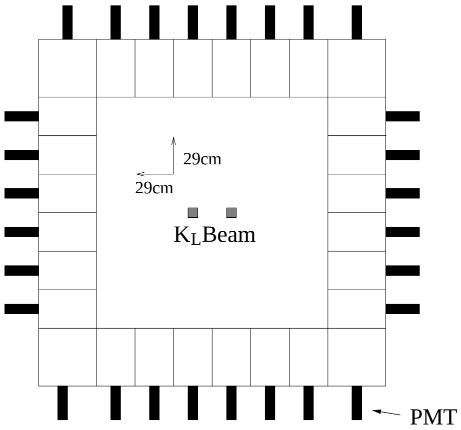

Figure 3.13: SA4 viewed by upstream. Each SA or CIA had the different dimensions as shown in Table 3.1 and the different number of modules.

There were three Spectrometer Antis(SA2-SA4) outside and just upstream of drift chambers 2 to chamber 4. The CsI Anti(CIA) covered outside of the CsI calorimeter. The shape of SA and CIA were rectangle to match the outer shape of the drift chambers and the CsI calorimeter. Figure 3.13 shows a schematic picture of the SA4, facing downstream. The general configuration of the three SA's and CIA were the same. Their sandwich structure consisted of 32 layers of lead sheets with a thickness of 0.5 X_0 each, and scintillators with a thickness of 2.5 mm, leading to 16 X_0 lead in total as well as RC's.

For the fiducialization around the beam holes of the calorimeter, Collar Anti(CA) was located in front of the calorimeter and around the beam holes like a picture frame. It consisted of 3 layers of 1 cm thick scintillator followed by 2.9 X_0 tungsten. Figure 3.14 shows a schematic picture of the CA.

Back Anti(BA) was placed downstream of the calorimeter and in neutral beam region to detect the photons escaping into the beam holes. It was composed of 60 layer lead-scintillator sandwich, and the total depth of lead was 30 radiation length with 0.5 X_0 sampling, which was roughly one nuclear interaction length. Each scintillator tile with a thickness of 2.5 mm was segmented to 2.5 cm width. The shape of BA was rectangle in cross section and divided into 3 parts longitudinally to

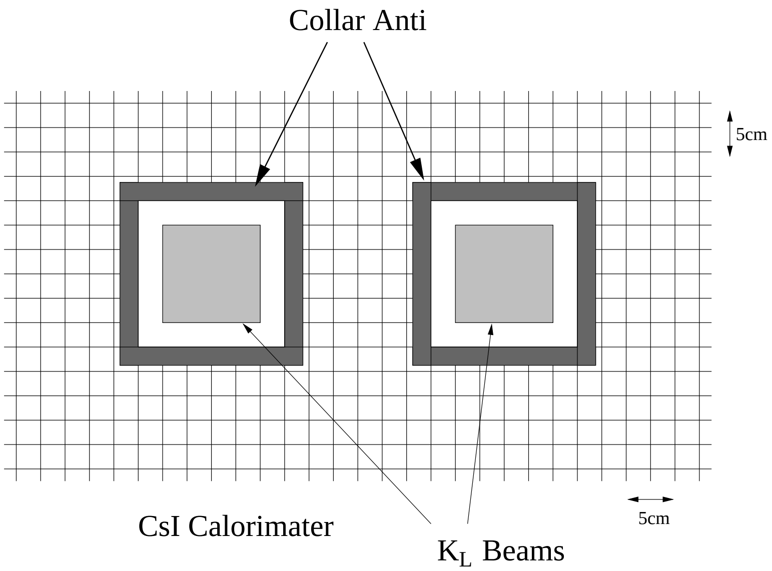

Figure 3.14: Collar Anti located just upstream of the CsI calorimeter. It was 1.5 cm wide and had 6 cm thickness in total.

distinguish electromagnetic and hadronic shower from its shower shape, as shown in Figure 3.15. Each section was referred to as BA1, BA2, and BA3, respectively. The first two sections were aimed to detect photons and the last one for hadrons. In addition, the readout of scintillation light was segmented into $+x$ and $-x$, so that we could use BA individually in $+x$ and $-x$.

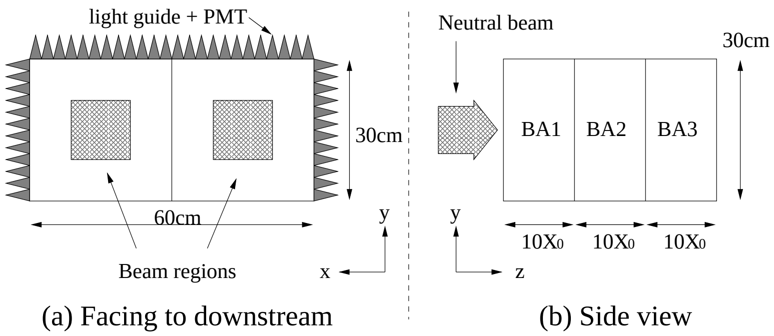

Figure 3.15: Back Anti(BA)'s configuration. (a): The view facing to downstream. BA is segmented into $+x$ and $-x$. (b): Side view of BA. It is segmented into 3 parts.

For all the photon veto detectors except for BA, the fibers with wave length shifter(WLS), Kuraray SCSF-B21, were used for reading out the light yield from the scintillator, Kuraray SCSN-88. The scintillation light(380 nm) was absorbed by the WLS in the fibers, and the light with wavelength of 420 nm was re-emitted from the WLS. The fiber had different refractive index in the core(n=1.59) and the clad(n=1.49) so that the emitted light in the WLS would be propagated effectively inside the core due to total reflection at the boundary of the core and clad. This blue light from WLS gave a benefit of high quantum efficiency at PMTs photocathodes and a faster pulse than that of conventional green WLS. The signal width was typically 20 nsec at base-to-base. Since the accelerator RF was 53 MHz(19 nsec interval), this faster pulse was helpful to reduce the accidental activities from the buckets which were the previous or post bucket of triggered one, and to achieve a good resolution. With respect to PMT, RC's, SA's, and CIA used EMI 9954KB, CA used Hamamatsu H1161P, and BA used Hamamatsu out of spec R5330.

The BA used scintillation tile with 1000 ppm 3HF WLS viewed by PMTs through light guides. The radiation hardness in 3HF was suitable for the use in the environment in which radiation dose level was estimated to reach several hundred Krad for the beam region[4].

At the front end, the pulse from the PMT was shaped by custom made module so that the pulse width was narrow enough(<35 ns) even after propagating long(close to 100 m) co-axis RG-58 cables to reach ADCs. The output pulse from the PMT was sensed by FERA ADC(LeCroy 4300B). Just before entering the ADC inputs, the pulse was amplified to recover the charge to the same level of the original pulse.

In order to use these photon veto counters as a part of online trigger, except for BA, each channel's gain was adjusted to within $\pm 10\%$ from an energy deposit of Minimum Ionizing Particle(MIP), where we used charged pions and muons. The energy scale for photon of all the photon veto detectors were calibrated by exploiting photons decayed from π^0 in $K_L \to \pi^+\pi^-\pi^0$ events. The details of these procedures is described in Appendix B.

Some property of the photon veto counters are summarized in Table 3.2.

Table 3.2: Summary for photon veto counter's property. (*) denotes Hamamatsu.

counter	sampling	radiator	PMT	light transmission	light yield (p.e./MIP)
RC	$0.5X_0 \times 16 + 1X_0 \times 8$	lead	EMI 9954KB	fiber	~ 40
SA/CIA	$0.5X_0 \times 32$	lead	EMI 9954KB	fiber	~ 55
CA	$2.9X_0 \times 3$	tungsten	Ham*H1161P	fiber	~ 24
BA	$0.5X_0 \times 60$	lead	Ham* R5330	light guide	unknown

3.3.4 Transition Radiation Detector

As discussed in Section 2.2, K_{e3} evetns could be the source of severe background for the $K_L \to \pi^0\nu\bar{\nu}$ search. Therefore, π/e separation was crucial to remove such backgrounds. For the electron identification, eight Transition Radiator Detectors(TRDs) were placed between the drift chambers and the trigger hodoscopes. Details of the transition radiation phenomena have been reviewed by many authors [70, 71], and only the description of our system is presented here.

Figure 3.16 shows the schematic drawing of a plane of the TRD. The size of active fiducial area was 2.2 m $\times$ 2.2 m. Each TRD consisted of a radiator, active MWPC volume, and two buffered gas volume. The radiator to produce 10 keV TR X-ray was 10 cm thick(=0.25X_0) polypropylene fiber mat(density of 0.06 g/cm^2). There were two beam holes in the radiator with a size of 15.5 cm$\times$15.5 cm each to reduce beam interactions. The gas volumes and radiators were segmented by aluminized mylar, called entrance window. MWPC consisted of vertically mounted cathodes and anodes. The cathode was a wire plane consisting of 85 μm diameter Be/Cu wires with 2.5 mm spacing. The entrance window was kept at a slightly higher voltage than the cathode forming a 1.5 mm mini-drift gap. The anode to cathode gap was 6.5 mm, and the anode was a wire plane consisted of 25 μm diameter gold plated tungsten wires with a 5 mm spacing. The planes were

[4]This dose level is calculated only for 3HF, not including radiator.

lined up so that each anode wire sit directly behind a cathode wire. The anode wires were ganged into channels consisting of two wires each in the central 60 cm covering the two beam holes with an effective pitch of 1 cm. In the outer region, 4 wires were summed into a channel with an effective pitch of 2 cm. This gave a total of 112 channels/plane, or 224 channels/chamber. Therefore, there were 1792 channels for the 8 chambers.

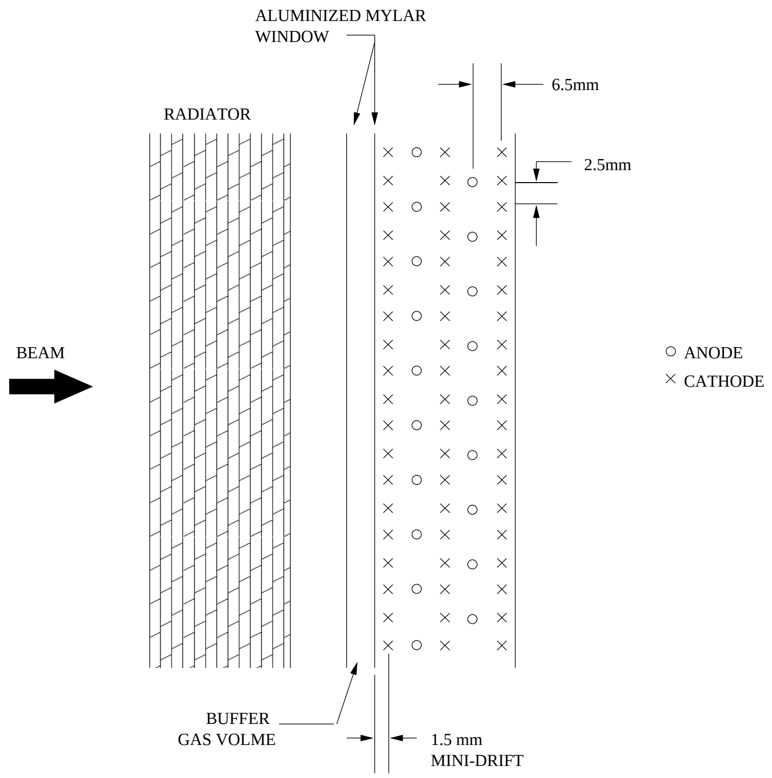

Figure 3.16: The schematic view of a TRD. Looking down to the TRD.

For the purpose of absorption, xenon was a main component of active volume gas. The ionization energy loss could fake a TR signal and reduce the π/e separation ability. To achieve both high yield of TR and minimization of the ionizing energy deposit, gas mixture of 80% Xe and 20% CO_2 was chosen. Since a 0.1% change in concentration of main components could result in a 1% change in gain, the composition of active volume gas was monitored by gas chromatography system at 100 ppm levels. With the typical high voltage of -2400V, which was automatically adjusted by monitoring the gas pressure so that each chamber gain was equal, the gas mixture gave a drift velocity of 5 cm/μsec.

The buffer volume was filled with a safe gas of C_2F_6 that was X-ray transparent and the same order of density with xenon so that it helped to support the entrance window. This kept the inner aluminized window flat to within 100 μm.

The pulse from each channel was sent to the preamp mounted directly on the chamber. It amplified the current pulse to produce an output voltage which was directly proportional to the input. In order to achieve a good signal to noise ratio, the preamp had to have as high level of gain as possible. It had a gain of $\sim$ 40. The output of the preamp was differential to improve noise rejection, which was passed into postamp by a cable whose length was a part of time delay requirement of the trigger system. The postamp first translated the differential input into a single-ended signal. Next, the pulse was shaped so that the length of the pulse tail was reduced. Tail reduction was necessary in order to keep the ADC gate width as narrow as possible to minimize accidentals. As a last stage of postamp, the shaped pulse was sent to a low gain amplifier stage. This additional stage of amplification allowed the signal channel to be tuned for optimizing its gain.

After the second amplification, an output was sensed by ADCs(LeCroy 4300B FERA ADC) with a gate width of 300 ns through co-axis RG-58 cables. Another output after the pulse shaping was discriminated at also the front end of TRD, and used to form a second level trigger signal, referred to as "TRD Trigger". This trigger logic used informations from the trigger hodoscopes, which is described in Section 3.3.5, in order to define the track region in the TRD planes. There were two discriminating thresholds so that the pattern recognition of hitting plane would be more intelligent. The pattern recognition was performed with LeCroy 2366 programmable logical unit by using the two levels of discriminating output for track region.

3.3.5 Trigger Hodoscopes

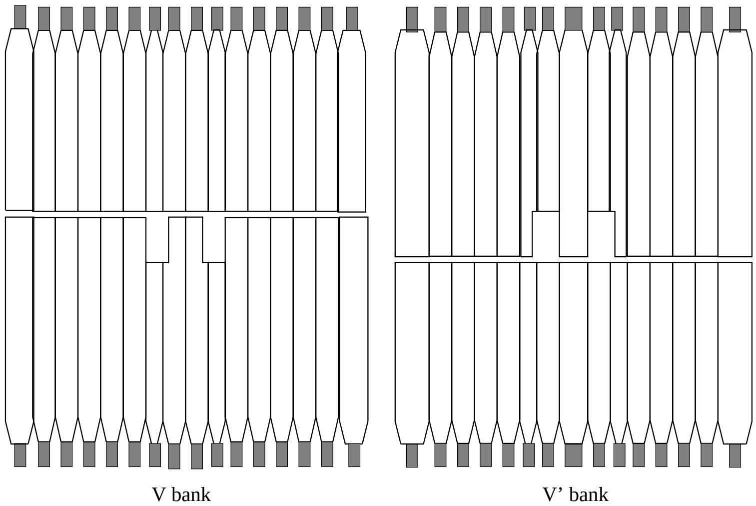

Figure 3.17: Schematic drawing of V and V' bank. Beam went into page. The width of each counter varied from 9.9 cm to 17.8 cm, and a total of 5 different width counters were used.

In order to provide fast signals to form trigger logic, two planes of scintillator hodoscopes were installed in front of the CsI calorimeter. We could count the number of charged particles by the hodoscopes in trigger level. As shown in Figure 3.17, the hodoscopes had a dimension of 1.9 m $\times$ 1.9 m with two beam holes. There were 5 different width counters: 9.92 cm, 11.82 cm, 13.74 cm, 15.63 cm and 17.76cm. The upstream hodoscope was called V bank, and the other was called V' bank. Both V and V' bank consisted of 1 cm thick scintillators viewed by PMTs mounted through light guides. There were no overlaps between the counters in each bank to avoid a double counting by a single particle.

3.3.6 Hadron Anti and Muon Counter

Scintillator hodoscopes followed by lead bricks were located at downstream of the CsI calorimeter, called Hadron Anti(HA). Its purpose was to reduce the trigger rate by vetoing the events involving charged pions or muons. Figure 3.18 shows HA's configuration and dimensions. The HA was placed upstream of BA as far as possible to minimize the rate due to backsplash beam neutrons from BA. The HA had a 34 cm $\times$ 64 cm beam hole so that the photon going into beam holes would be detected by BA. In order to absorb leakage of electromagnetic showers out of the back of the CsI calorimeter, the thickness of lead bricks was chosen to be 15 cm. The combined thickness of the CsI calorimeter and the lead bricks corresponded to 2.3 nuclear interaction length. The light yield produced by the scintillation counter was detected by PMTs. An analog sum from all the HA's counters provided an information to form first level trigger.

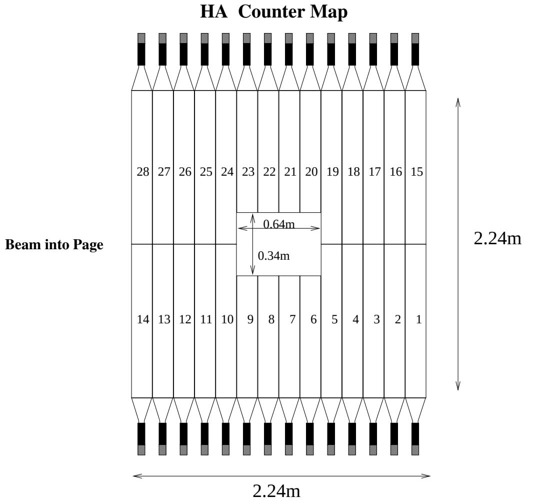

Figure 3.18: Ths HA hodoscope, which was composed from same size of 28 scintillation counters. This was followed by Pb wall.

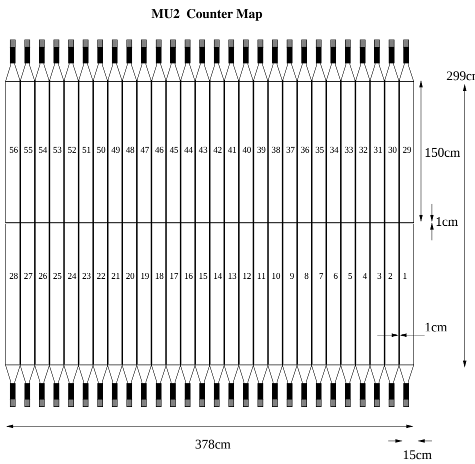

Figure 3.19: The Mu2 counter.

To reduce the trigger rate by rejecting events involving muons, we used Muon Counter(Mu2) consisting of scintillation hodoscope followed by roughly 5 m thick steel at downstream of the HA. Most particles penetrating such a large amount of material were considered as muons. The Mu2 had the largest dimensions of all the detectors because it was located at the most downstream, and had to catch the muons scattered significantly at the filtering steel. The hodoscope consisted of 56 scintillation counters viewed by PMTs, as illustrated in Figure 3.19. Each counter had dimensions of 15 cm $\times$ 150 cm, and they were overlapped by 1 cm in each other to reduce the inefficiency for the muon going through the gap between the two counters.

3.3.7 Accidental Counter

There were three 3HF scintillation counters sensed by Hamamatsu R1398 PMTs to form an Accidental Trigger(see Section 3.4.4). They were placed of an angle of 90° from the other detector elements, and 1.8 m from the target. Since the target was shielded with iron, the target was viewed by the counters through a $1/4'' \times 1/4''$ hole located at roughly the mid-point of the target in z. Each counter had a cross-section of $3/4'' \times 3/4''$ with $7/16''$ thickness. Those three counters were separated by ~1.5". Coincidence hits of the three counters formed the Accidental Trigger. Since these accidental counters' activities were independent of the other detector elements although it depended on the primary proton intensity, the data collected by the Accidental Trigger could sample the accidental activities in the main detector elements.

3.4 Trigger

The online trigger was formed in three stages. The first and second stages used the logic constructed from only hardwares, such as simple NIM logic or more complicated processor. At the last stage, online event reconstruction was carried out to filter the events. These three levels of trigger had a hierarchy in their decision time: the first level took within 19 ns, i.e. it produced no dead time; the second level took ~ 3 μs; the third level took ~ 3 ms.

In addition to the three stages of trigger, there were two types of trigger in our experiment: Beam Trigger and Calibration Trigger. All the physics triggers belonged to Beam Triggers. Calibration Triggers were designed to collect data for pedestal measurements the CsI laser calibration etc..

This section covers mainly Beam Trigger, and begins with descriptions for each trigger stage in the Beam Trigger. After the descriptions, the trigger requirements used in data taking at the experiment are presented. At last, Calibration Trigger is described briefly.

3.4.1 Level 1 Trigger

The first level trigger(Level 1 trigger) was based only on information which could be obtained very quickly, such as the scintillation hodoscopes. There were 80 Level 1 logic sources in total, which were formed by NIM logic. They provided a decision every 19 ns RF cycle with no dead time. Table 3.3 summarizes the Level 1 trigger sources used in data taking for $K_L \to \pi^0 \nu\bar{\nu}$ and $K_L \to e^+e^-\gamma$.

These trigger sources were sent to a series of LeCroy 4508 Programmable Lookup Units(PLU) and LeCroy 4516 Programmable Logic(PL), which were programmed and could be changed via CAMAC. At the same time, RF signal provided by Fermilab was passed into the PLU and PL to strobe the trigger sources. We call the time strobed RF bucket as "in-time" bucket. A combination of PLU and PL generated an output signal by looking at the firing pattern of the Level 1 trigger sources. This output was fed into the next stage of triggering.

Table 3.3: Trigger sources in Level 1 and Level 2 trigger.

Detector	Symbol	Description
	Level 1	
Trigger hodoscopes	V	Hits in V bank.
	V'	Hits in V' bank.
Drift chamber	$DC12$	≥ 1 hits in DC1 and DC2.
Photon Veto	$RC6 - RC10$	Energy $>$ 500 MeV.
Counters	$SA2 - SA4, CIA$	Energy $>$ 400 MeV.
	CA	Energy $>$ 14 GeV.
CsI calorimeter	E_t	Total energy $>$ 18(or 24) GeV.
Hadron Anti	HA	Summed Energy $>$ 6 MIPs
Muon counter	$Mu2$	Energy $>$ 0.5 MIPs
	Level 2	
Drift chamber	$1HCX$	≥ 1 track in x view in DC1 and DC2.
	$1HCY$	≥ 1 track in y view in all DCs.
CsI calorimeter	HCC34	Number of hardware clusters = 3 or 4.
TRD	$TRD1e$	≥ 1 track identified as electron.

3.4.2 Level 2 Trigger

When the event satisfied the Level 1 requirements, the output signal from Level 1 trigger started a digitization of ADCs and provided a stop signal for TDCs. The trigger system went to the next stage, called Level 2 trigger. The Level 2 trigger consisted of information which took longer time to obtain, either because the detector element had a slow response like the drift chamber, or because the pattern recognition took some time like HCC. Each source is listed in Table 3.3.

These input signals from Level 2 sources were sent to another series of PLUs(LeCroy 2373) with a Level 1 signal. Again, PLUs did a pattern recognition of trigger sources, and determined whether to go to the next stage of the triggering. When the event satisfied the Level 2 requirements, each PLU generated the outputs, which were used to form a 16 bit trigger mask; the bitwise-AND of all the lookup units was the final 16 bit trigger mask. This means that we could have 16 Beam triggers in maximum. If an event failed at this stage, that event would be aborted before finishing ADC digitization, and would go to next event.

If the event rate was too high after the Level 1 trigger, some types of trigger was prescaled by an additional module with an integral prescaling factor before the Level 2 trigger.

Since the Level 2 decision took 3.3 μsec on average and the Level 1 trigger rate was $\sim$ 80KHz, Level 2 dead time was 3.3 μsec $\times$ 80 KHz $\simeq$ 26%. More details in Level 1 and 2 are described in reference [76, 77].

3.4.3 Level 3 Trigger

The events that satisfied the Level 2 requirements were sent to the final stage of triggering(Level 3 trigger), where it was reconstructed in the UNIX machine with software. Therefore, all the readout including digitization was completed before the Level 3.

Each input event to Level 3 contained the Level 2 mask. The Level 3 made a final decision of writing it out to tape devices, based on the selection criteria imposed on the tagged trigger. The software in Level 3 shared most codes with offline use; however, it was tuned to minimize the processing time. A total of 24 Challenge SGI CPUs(200MHz$\simeq$160mips each) was used to process and filter the events. The resulting time to process was 3 ms per event.

3.4.4 Beam Trigger

Physics Trigger

Since the final states in $K_L \to \pi^0 \nu\bar{\nu}$ with $\pi^0 \to e^+e^-\gamma$ and the normalization mode, $K_L \to e^+e^-\gamma$, were identical, data sample was collected by the same trigger requirements for both the signal and normalization mode, called “Dalitz Trigger”.

The combined requirements in Level 1 and 2 were expressed as

$$2VV' * E_t * DC12 * \overline{HA} * \overline{Mu2} * \overline{PHV} \qquad (Level\ 1)$$

$$*1HCY * 1HCX * HCC34 * TRD1e \qquad (Level\ 2)\,,$$

where 2VV' is defined as 2 or more hits in V bank and 1 or more hits in V' bank, or vice versa. $DC12$ represents at least 1 hit in each x and y view in DC1 and DC2. $\overline{PHV}$ is written as

$$\overline{RC6} * \overline{RC7} * \overline{RC8} * \overline{RC9} * \overline{RC10} * \overline{SA2} * \overline{SA3} * \overline{SA4} * \overline{CIA} * \overline{CA}\,.$$

The Level 2 trigger required to have: at least 1 hit-pair found in y view in all DCs($1HCY$), at leasst 1 in x view of DC1 and DC2($1HCX$), 3 or 4 hardware clusters($HCC34$), and at least 1 track satisfied TRD trigger requirement($TRD1e$).

At the Level 3, two charged tracks and the decay vertex position had to be found. E/p was required to be greater than 0.75 for both tracks as an electron identification, which gave the most reduction at Level 3 since K_{e3} dominated the remaining events after the Level 1 and 2 requirements because of its high branching ratio(38.8%). In addition, randomly selected small fraction of events were collected without any Level 3 requirements to study the bias in the Level 3 filtering. Since the Level 3 requirements overlapped with the offline event reconstruction, the details of the algorithm and reconstruction procedure is covered in Chapter 5 and Chapter 6.

Other Trigger

There were 16 Beam Triggers in E799-II experiment. Besides the physical motivation, some triggers were necessary to understand the basic detector response and trigger bias. For such purposes, "Minimum Bias Trigger" and "Accidental Trigger" were formed as a part of the Beam Trigger.

The Minimum Bias Trigger was composed of

$$2V * DC12 * 2HCY \ ,$$

where $2HCY$ is defined as 2 hits in each y plane of all DCs. All two track events would satisfy these requirements. In the analysis described in this thesis, the decays $K_L \rightarrow \pi^+\pi^-\pi^0$, $K_L \rightarrow \pi^+\pi^-$ and K_{e3} collected in the Minimum Bias Trigger were used to study the detector performance during the run, to calibrate the CsI calorimeter, and to measure the momentum kick given by the analyzing magnet. The Minimum Bias Trigger was prescaled by 500, and the resulting Level 1 rate was $\sim$ 1.2 KHz. It was 2% of total Level 1 rate, but the occupancy in recorded data was 23% of all the data, the biggest data sample, because the Level 3 filtering did not require tight cuts not to introduce the filtering bias.

In order to collect the events to monitor the detector's accidental activities, the Accidental Trigger was formed from the signal of accidental counters described in Section 3.3.7. Since the rate in this trigger should be proportional to the proton flux at the target, one could understand accidental activities in detector elements as a function of proton intensity. This data set were also used in Monte Carlo simulation to embed the accidental activity or electric noises in detector responses.

3.4.5 Calibration Trigger

The Calibration trigger involved the following: laser calibration of the CsI calorimeter; pedestal measurements in all the detectors; uniformity measurements of the CsI by using cosmic muons. They were generated from local logic, and did not use any additional logic from PLU.

The trigger of laser calibration was formed by the flash of laser/dye system described in Section 3.3.2.

The pedestal was collected by intentionally opening ADC gates. The frequency of opening the gate could be controlled through CAMAC. Data taking was performed in both on-spill and off-spill.

There were additional muon telescopes located top and bottom of the CsI blockhouse for triggering the cosmic muon event. These events were used to measure the CsI uniformity in response along the z direction. To form this trigger, the coincidence of top and bottom telescopes was required.

Since these trigger rates were so low, the fraction of the data to all the accepted events was negligible.

3.5 Data Acquisition

To achieve a high rate capability(Level 2 rate was 11 KHz, and the typical event size was 8 KBytes) in reading out a data, the data acquisition system(DAQ) had a very unique feature, as shown in reference [78, 79]. Here, the essence is described briefly.

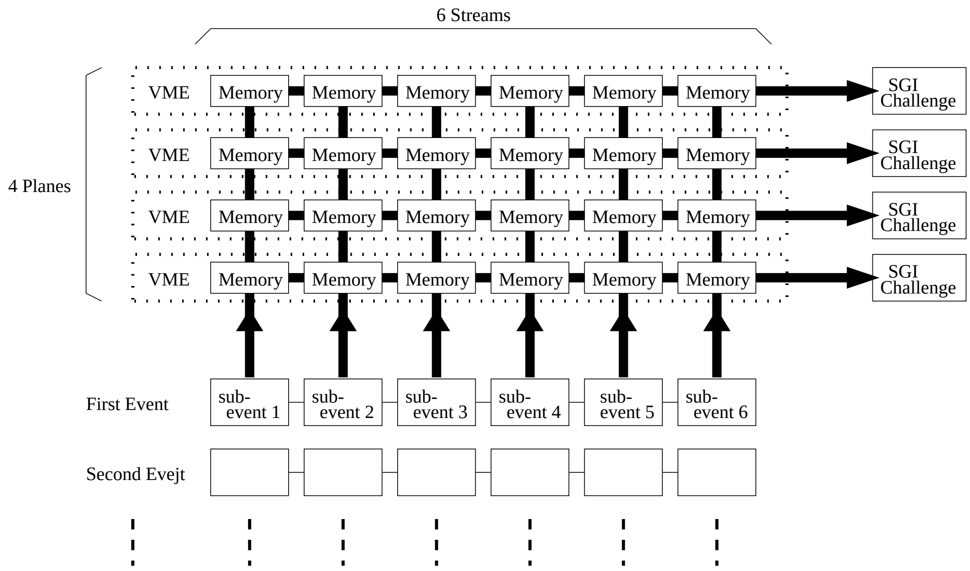

Figure 3.20: Conceptual design of DAQ system. Of those 4 planes, 3 planes were used for Level 3 trigger, and the other was for online monitoring of detector performance and online calibration. Each stream had a different type of data, for example, one stream held only the calorimeter information.

The DAQ system can be visualized as a matrix in which each element corresponded to a memory node in VME for event storage(Figure 3.20). The data from an entire spill was stored in these VME memories to use the full spill cycle for reading out, filtering, and logging the event. A total amount of memories was 4 GBytes, which was big enough to buffer data from an entire spill($\sim$ 2 GB = 11 KHz $\times$ 8 KBytes $\times$ 23 sec/spill). The front end crates and the DAQ were connected with RS485 lines whose bandwidth was 40 MBytes/sec/line. Since there were 6 RS485, or 6 "streams", the bandwidth of 240 MBytes/sec was achieved. The 6 sub-events on 6 streams flew asynchronously into the memory nodes on VME, which were linked via the VME bus. Each memory was connected to the internal VME bus of the SGI Challenge, forming a "plane". In a total 4 planes, three of them were used for the Level 3 triggering. The other plane monitored the detector response and performed online calibration.

All of the front end data was read out through a FERA DATA bus, where custom made modules designed and built by Fermilab, DYC3 and CTIRC, were used with FIFO. These readout modules pushed the data from its FIFO into RS485 line, or stream. The first crate in the stream also attached the plane destination information to the top of the data.

Each memory node consisted of three modules, DM115, DC2, and a 6390 VSB/VME Dual Port Memory(DPM), which was called "DDD". The DM115 was an I/O module which received data from the RS485 line, and pushed it into the DC2 FIFO if the event plane number matched the DM115 plane number. The main task of DC2 was to transfer data from the FIFO to DPM. In addition to that task, the DC2 attached the event size to the top of each subevent, made a table of VME address for all the events on VEM memory, counted the total number of events written into VME memory in each spill, and finally cleared the VME memory after processing in a spill. The data throughoutput of the DDD was 22 MBytes per second, which was limited by the VSB side of the DPM. After passing through the DDD, data on the VME flew into shared memory in the Challenge, which was controlled and/or setup by gateway between the DDD and the memories.

The resulting readout time for the event that satisfied Level 2 trigger requirements was 15 μsec. It gave an additional 17% dead time at a 11 KHz Level 2 trigger rate. Once the data was read out, the online event reconstruction was carried out on the Challenge, and was filterd as described in Section 3.4.3. An event passing the Level 3 trigger was written to DLT tape. Each Challenge or plane had 3 or 4 DLT drives.

3.6 The Run

The data taking was not only for collecting physics data but also for detector calibration, monitoring etc. This section briefly describes the running condition in the data taking.

3.6.1 Physics Run

There were some differences in beam parameters and the requirements in the Dalitz Trigger between Winter and Summer runs. These differences affected trigger rates, which are summarized in Table 3.4. In addition, first part of Winter run was imposed a Level 1 prescale factor of 1.5. This prescaling factor was changed to 1(=no prescale) when we added $TRD1e$ requirement in the Level 2 trigger.

Table 3.4: Typical trigger rate and other environments.

	Winter run(a)	Winter run(b)	Summer run
Run Number	8028-8399	8400-8913	10458-11000
Proton Beam Intensity	5.0×10^{12}	5.0×10^{12}	3.5×10^{12}
Beam Size at CsI	10cm $\times$ 10cm	10cm $\times$ 10cm	12cm $\times$ 12cm
E_t threshold	18 GeV	18 GeV	24 GeV
TRD trigger	None	In	In
Level 1 Prescale in Dalitz trigger	1.5	1.0	1.0
Level 1 rate in Dalitz trigger	27 KHz	53 KHz	36 KHz
Level 1 rate(after dead time correction) in Dalitz trigger	17 KHz	34 KHz	23 KHz
Level 2 rate in Dalitz trigger	3.1 KHz	2.5 KHz	2.4 KHz
Total Level 1 rate	82 KHz		83 KHz
Total Level 1 rate (after dead time correction)	51 KHz		52 KHz
Total Level 2 rate	11 KHz		11 KHz

The data was logged to about 500 "raw" data tapes in total($\sim$ 12 GB per tape). The 500 tapes were split based on the trigger type. The final number of DLT tapes for Dalitz trigger was 63.

The analysis can be separated in two stages. A first pass was made through all the Dalitz output tapes by using very loose analysis cuts[5]. The cuts were designed loose enough so that minor changes in the final tight cuts or modification of algorithm would not affect the final event sample. Candidate events were split again into much smaller subsets(15 DLTs) of data summary tapes(DSTs). The final analysis run through these DSTs.

The data samples for calibrating the CsI calorimeter, pedestal measurements, accidental detector response, and Minimum Bias Trigger were collected at the same time with physics modes as a part of Beam Triggers. These samples were also split based on the event type.

[5]Before this moment, Level 3 trigger actually applied the similar cuts.

3.6.2 Special Run

Besides the normal physics run, the special runs were needed for calibration of the detector, or other special purposes. "Muon Run", "Pedestal Run, and "Laser Run" were the main components of the special run.

In order to determine the drift chamber positions relative to the CsI calorimeter accurately, straight trajectory of charged particle was necessary. To get such events, the Muon Run was performed once a day by putting two beamstops, which were made of steel with 28.5 cm and 21.1 cm thickness and located at 46.4 m and 50.1 m downstream of the target, respectively, and by turning off the analyzing magnet. Since most of the hadrons were absorbed in the beamstops, only muons could enter the fiducial region. This event was triggered by the coincidence hits in any V, V', and the muon counters. Another purpose of the Muon Run was to understand the gain of each counter, and to calibrate it. The calibration of photon veto detectors at Muon Runs is described in Appendix B.

Data takings for measuring pedestals were also carried out as a special run. Although the pedestal data were collected during the off-spills on physics run, there were some cases which needed much more pedestal data. For example, it was performed after a swapping the modules of the detectors.

Another special run, Laser Run, was carried out for calibrating DPMT as described in Section 3.3.2. As well as the Pedestal Run, the response for laser was collected during the off-spill, but sometime its data sample was not big enough, mainly after the swapping DPMT. In such cases, Laser Runs were carried out.

Chapter 4

Monte Carlo Simulation

In order to measure the branching ratio, the acceptance ratio of signal to normalization mode must be understood. The Monte Carlo simulation(MC) was used to calculate the detector acceptances for both signal and normalization mode. In addition, the MC was crucial in the background level estimation because the acceptances for background sources were also evaluated by using the MC. To obtain detector acceptances for signal decay, normalization mode, and some background sources, the MC reproduced events by simulating the parent particles' production, the decays of the particles, the movements of the parent and daughter particles with interactions with detector materials, the detectors' response, and the digitization of detector's response.

The output of the MC had the same format with real data. This allowed us to analyze real data and MC events with the same algorithm and with the same cuts, and thus simplified the codes.

This chapter consists of three sections. Section 4.1 describes the event generation which was composed from kaon(or hyperon) beam generation, the decay of parent particle, and the propagation of the decay products. After the event generation, a simulation of the detector response is covered in Section 4.2. Since there were accidental activity or noise in the detectors at some level, those effect had to be added to the simulation. Section 4.3 presents how the effect was included to the MC.

4.1 Event Generation

The event generation in the simulation can be divided into 3 parts, K_L(or hyperon) beam production at the target, decays of the particles, and the propagation of the decay products.

4.1.1 The Beam Production

The Monte Carlo simulation began with the generation of K_L(or hyperon) beam with correct energy spectrum and angular divergence.

K_L production

Let us start with a parametrization by Malensek [82] for the K^+ and K^- spectrum for protons incident on a beryllium target. In the parametrization, the number of kaons with momentum p into a solid angle dΩ at a polar angle θ was

$$\frac{d^2N}{dpd\Omega} = \frac{B}{400}x\frac{(1-x)^A(1+5e^{-Dx})}{(1+p_t^2/M^2)^4} \quad , \tag{4.1}$$

where, x denotes the ratio of the produced particle momentum(p) to the beam energy(E_B), $x = p/E_B$, and p_t represents the transverse momentum of the produced particle relative to the incident beam direction. B, A, D, and M^2 were determined from the experimental data obtained by 400 GeV/c proton beam(Table 4.1). Both p and p_t have a unit of GeV/c.

Table 4.1: The parameters used by Malensek [82].

	K^+	K^-
A	2.924	6.107
B	14.15	12.33
M^2	1.164	1.098
D	19.89	17.78

If we define σ as a production probability for a $u\bar{u}$ or a $d\bar{d}$ pair, and σ_s as that for an $s\bar{s}$ pair, K^+ production probability, $\sigma(K^+)$, would be proportional to $2\sigma_s + \sigma\sigma_s$ because the kaon could be produced by using either of the valence u quarks of the proton, or with a u quark from the sea. From the same arguments, we can get the following relation:

$$\begin{aligned}
\sigma(K^+) &\sim 2\sigma_s + \sigma\sigma_s \ , \\
\sigma(K^-) &\sim \sigma\sigma_s \ , \\
\sigma(K^0) &\sim \sigma_s + \sigma\sigma_s = \frac{\sigma(K^+) + \sigma(K^-)}{2} \ , \\
\sigma(\bar{K^0}) &\sim \sigma\sigma_s = \sigma(K^-) \ .
\end{aligned}$$

Based on Equation 4.1 and the above relations between neutral kaons and charged kaons, we tentatively extracted the production probabilities for K^0 and $\bar{K^0}$.

Our spectrum was tuned further, to match kaon momentum measured by $K_L \to \pi^+\pi^-$ events in the real data. The measured correction factor, $\xi(p)$:

$$\xi(p) = 1 + 1.0655x - 0.55337x^2 + 0.060033x^3 \ ,$$

where $x = p$ / 100 [GeV/c], was multiplied to the generation probabilities as

$$\frac{d^2N}{dpd\Omega}(K^0) = \frac{1}{2}\left[\frac{d^2N}{dpd\Omega}(K^+) + \frac{d^2N}{dpd\Omega}(K^-)\right] \times \xi(p) \ , \qquad \frac{d^2N}{dpd\Omega}(\bar{K^0}) = \frac{d^2N}{dpd\Omega}(K^-) \times \xi(p) \ . \quad (4.2)$$

The kaon energy distribution produced with this correction is shown in Figure 3.1. Based on Equation 4.2, the MC produced K^0's or $\bar{K^0}$'s at the target.

After the production of a K^0 or $\bar{K^0}$, it was propagated to the decay point. In case of $K_L \to \pi^0\nu\bar{\nu}$ or $K_L \to e^+e^-\gamma$ simulation, the decay point was simply determined by K_L's proper life time τ, where the τ was distributed exponentially, and its Lorentz factor shown as;

$$\Delta z = \frac{p[GeV/c]}{m_K[GeV/c^2]} c\tau \ .$$

In case of the other kaon decays, the interference between K_L and K_S was taken into account the determination of the decay position. The detail can be found in reference [69].

Hyperon production

Hyperons were generated with a probability shown as

$$E\frac{d^3\sigma}{dp^3} = exp(C_1 + C_2x^2 + C_3x + C_4xp_t + C_5P_t^2 + C_6p_t^4 + C_7p_t^6) \times (1-x)^{C_8+C_9p_t^2} \ ,$$

where x represents the ratio of the produced particle momentum(p) to the beam energy(E_B), $x = p/E_B$, and E denotes the energy of produced particle. This formula was determined by fits empirically in experiments at Fermilab Meson Center [83, 84], and the coefficients are listed in Table 4.2. Based on the momentum spectrum produced by using these constants, Λ's spectrum

Table 4.2: Coefficients in empirical fits for hyperon spectrum.

	pBe $\to \Lambda$	pBe $\to \Xi$
C_1	1.68	-1.21
C_2	0.44	1.16
C_3	0.28	-0.72
C_4	-0.58	-0.48
C_5	-2.62	-1.85
C_6	0.40	0.17
C_7	-0.03	-0.008
C_8	0.86	2.87
C_9	0.20	0.04

was tuned so that the spectrum measured in $\Lambda \to p\pi^-$ events matched to that in MC. As a result, the MC's spectrum was scaled by 90% in E. For Ξ, the production spectrum based on the Table 4.2 was used without corrections. The decay position of hyperons was simply determined by their proper life times and their momenta.

4.1.2 The Decays

Once the decay vertex has been chosen for a specific decay mode, the next step was a decay of the parent particle. Here, we discuss the simulation only for some types of decay, which were relevant in our analysis.

$K_L \to \pi^0\nu\bar{\nu}$ Decay

Using an analogy to $K^+ \to \pi^+\nu\bar{\nu}$, the decay dynamics of $K_L \to \pi^0\nu\bar{\nu}$ were determined. Assuming neutrinos to be massless, and from the Standard Model calculation [85], the decay rate as a function of π^0 energy, E_π, can be represented as

$$\frac{d\Gamma}{dE_\pi} \sim \lambda f_+^2[(m_K^2 - m_\pi^2 - q^2)^2 - \frac{2}{q^2}(\frac{q^2\lambda^2}{3} + m_\pi^2 q^4)] \ , \tag{4.3}$$

where m_K and m_π denote the mass of K_L and π^0, respectively, and

$$q^2 = m_K^2 + m_\pi^2 - 2m_K E_\pi \ , \qquad \text{and} \qquad \lambda = [(m_K^2 + m_\pi^2 - q^2)^2 - 4m_K^2 m_\pi^2]^{1/2} \ .$$

The form factor, f_+, was parametrized as $f_+ = 1 + \lambda_+ q^2/m_\pi^2$, with $\lambda_+ = 0.032$, which was measured in K_{e3} and $K_{\mu 3}$ experiments [86]. The kinematical constraint,

$$m_\pi \leq E_\pi \leq (m_K^2 + m_\pi^2)/2m_K \ ,$$

was also required.

Once the π^0 obtained its energy from the spectrum expressed in Equation 4.3, the decaying direction was determined isotropically in the K_L rest frame. Since π^0's life time($c\tau = 25.1$ nm) is much smaller than the detector resolution, the π^0 immediately decayed to $ee\gamma$ in the MC as described in the following. On the other hand, remaining decay products ν and $\overline{\nu}$ were not traced anymore.

Dalitz Decay

Because our signature for $K_L \to \pi^0\nu\bar{\nu}$ contains the decay of $\pi^0 \to e^+e^-\gamma$, most of backgrounds also had a $\pi^0 \to e^+e^-\gamma$ decay as a secondary decay. Besides, the normalization mode was a $K_L \to e^+e^-\gamma$ decay, therefore, the Dalitz decay was one of the most important decays for our analysis. In both $K_L \to e^+e^-\gamma$ and $\pi^0 \to e^+e^-\gamma$, the Dalitz decay has an intermediate virtual photon which would convert to an electron positron pair. Without any radiative correction, the differential decay rate respect to the square of invariant mass of e^+e^-, m_{ee}^2, has been calculated by Kroll and Wada [87]. Defining M to be the mass of parent decay particle, the formula is expressed as

$$\frac{d\Gamma}{dx} = \frac{2\alpha}{3}|f(x)|^2\frac{(1-x)^3}{x}(1+\frac{2m_{ee}^2}{xM^2})(1-\frac{4m_{ee}^2}{xM^2})^{1/2} , \tag{4.4}$$

where $x = m_{ee}^2/M^2$, and $f(x)$ is a form factor.

The form factor originated from an internal structure in a K_L or π^0; however we used a constant form factor of unity for both $\pi^0 \to e^+e^-\gamma$ and $K_L \to e^+e^-\gamma$ decays in the simulation because the change in the distribution of $m_{e^+e^-}$ due to the form factor did not affect the acceptance calculations as Chapter 8 quantifies the change[1].

Once the m_{ee} was assigned by the Kroll-Wada formula the real photon was generated in back-to-back for the e^+e^- system at the parent particle's rest frame so that the total momentum would be conserved. The direction of the real photon or e^+e^- system was isotropically thrown. The energy of e^+e^- was assigned as

$$E_{e^\pm} = \frac{M}{4}[(1+x) \pm y(1-x)] ,$$

where y basically gave the energy asymmetry between e^+ and e^-, and it is expressed as

$$y = \frac{p_{e^-} - p_{e^+}}{|\vec{p_{e^-}} + \vec{p_{e^+}}|} ,$$

where $p_{e^-}(p_{e^+})$ denotes four-momenta of electron(positron), and $\vec{p_{e^-}}(\vec{p_{e^+}})$ is a momentum vector of electron(positron). Finally, all the decay products were boosted to the lab. frame according to the momentum of parent particle.

Semi-leptonic Decay

Mis-identification of pion plus overlapping either accidental or radiative photon could fake a signal. Therefore, the MC needed to reproduce both normal K_{e3} decay and K_{e3} with a photon radiated from electron, referred to as "radiative K_{e3}".

In the non-radiative K_{e3} event, the decay was first generated over flat phase space, and then its generation probability was weighted by the matrix element for semi-leptonic decay [91]. For the form factor, we took into account the effect only from pure vector term with a linear q^2 dependence [92].

[1] Besides, α^*, which is an important parameter in a form factor, has a discrepancy in measurements between $K_L \to e^+e^-\gamma$ and $K_L \to \mu\mu\gamma$.

For the radiative decays, the algorithm was composed from two decay chains. First, the kaon decayed into neutrino and $\pi e\gamma$ system, in which the invariant mass of the $\pi e\gamma$ system was generated between $(m_e + m_\pi)^2$ and m_K^2, where m_e, m_π, and m_K denote masses of electron, π and K_L, respectively. Next step was the decay of $\pi e\gamma$ system with energy cutoff of the photon at 1 MeV in the kaon center of mass frame. Invariant mass of $e\gamma$ system was generated with $1/m^2$ dependence. Given the $m_{e\gamma}$ and the cutoff energy of photon, $m_{\pi\gamma}$ was determined again with $1/m^2$ dependence. After the selection of the flight direction of the $\pi e\gamma$ system, the radiative K_{e3} matrix element was calculated using the determined phase space as inputs. Finally generation probability was weighted by this matrix element.

Other Decays

Besides the decays described in the above, the other kaon or hyperon decays were generated in the MC in background studies. They used their own matrix elements in the decay reproduction, which were well understood so far.

4.1.3 Particle Tracing

Once the decayed particles had been generated in the parent particle's rest frame, they were boosted to the lab frame with Lorentz factor of the parent particle. The daughter particles traveled from the decay vertex and through the detector until they escaped from fiducial region, or hit photon veto detectors, or reached the CsI calorimeter. Since charged pion could decay as $\pi^\pm \to \mu^\pm \nu(\overline{\nu})$, muons were also traced in the MC.

Charged particles traversing material in the detector between the vacuum region and the calorimeter could change its flight direction by the Coulomb multiple scattering. The scattering angle was simulated using the theory of Molière [93, 94, 95] in which δ-ray was also generated with some probability to reproduce the long tail in the scattering distribution.

The bremsstrahlung by electrons was also implemented in the MC. The Bethe-Heitler [96] cross section was referred as a probability of emitting a bremsstrahlung photon as well as the emitting angle, θ, which was defined as the angle between the electron and the emitted photon. The relation can be written as

$$\frac{d\sigma}{d\theta} \sim \frac{1}{\theta^4}\,, \quad \text{and} \quad \overline{\theta} = \frac{m_e}{E}\,,$$

where m_e is an electron mass and E is the energy of electron.

The Monte Carlo simulation handled the photon conversion at the material for the energy above 0.1 GeV. The conversion probability was computed as $(1 - e^{-\frac{7}{9}X})$ where X denotes the amount of material in terms of radiation length. The energy spectrum of electron-positron pair was determined by Bethe-Heitler formula. For the opening angle of electron and positron, we used an algorithm found in EGS4 shower simulation package [97, 98].

If a new particle was born in the above interactions, the same propagation procedure was repeated for the produced particle.

4.2 Detector Response

Once the MC event was generated as described in the previous section, the detector response must be simulated as a next step. In addition, the response had to be correctly digitized so that analysis code would work for both real data and MC data with the same cuts. Especially for DPMT, the simulation of digitization was crucial point to reproduce the calorimeter's response. This section describes the simulation of responses in main detector elements.

4.2.1 Photon Veto Detectors

For a photon or an electron(positron), the energy deposited to the photon veto counter was determined using calibration constants(Appendix B) according to the energy of incident particle. The deposited energy was smeared by Gaussian distribution whose width was also derived from data, which are listed in Table B.1.

Other charged particles were treated as MIPs, and their deposited energy was smeared by Gaussian. The width and mean of the deposited energy were determined from another set of calibration constants derived from Muon Runs.

If the smeared deposit energy was above trigger threshold applied on each counter, the trigger latch bit was turned on. At last, the deposited energy was digitized to ADC counts based on the gain of each counter which had been also calibrated from a data set collected by Muon Runs.

4.2.2 Drift Chamber

When charged particles traveled through the drift chambers, the drift distance, i.e. the distance from the particle trajectory to the closest wire in each plane, was converted to the drift time. The conversion factor was calibrated in advance so that the sum of drift distance(SOD) equaled to 6.35 mm(Section 3.3.1). The drift time was smeared based on the calibration result, and was recorded as TDC counts. The inefficiency for each plane was implemented by not recording the hit information randomly. Only the earliest hit in multiple hits were recorded if they were within the same time window of 235 ns.

The δ-rays emission in the chamber gas was simulated in the following 3 steps. First, when a highly relativistic particle is passing through the length L(m), the emission probability in a material with Z(Atomic Number) and A(Atomic Mass) is

$$P = 154(\mathrm{KeV}) * \frac{Z}{A} * d(\mathrm{g/cm^3}) * L(\mathrm{cm}) * \frac{1}{E},$$

where d represents the density of material and E is the particle energy. With this probability, P, a δ-rays was emitted perpendicular to the parent particle trajectory. Its range was determined based on the emitted energy. If the electron emitted as the δ-ray stopped outside the original cell, the flight distance was considered as the size of cell. At last, the distance from the δ-rays to the closest wire was computed. The hits due to the δ-ray were also recorded by the same method used for normal charged particles. The resulting hit information was used in the Level 1 $DC12$ simulation, which counted the number of hits in the defined in-time window(235 ns).

4.2.3 TRD and Trigger Hodoscopes

The TRD's π/e separation capability was not simulated in the MC. Only multiple scattering for charged particles and conversion of photons traversing through the TRD was reproduced as described in Section 4.1.3. In the analysis of MC events, the efficiencies for electrons and pions were added by hand, which were estimated from real data.

When a charged particle passed through the trigger hodoscope, the latch bit corresponding to the firing counter was set based on the efficiency of the counter measured from real data. The latch bit was used to simulate Level 1 triggering.

4.2.4 CsI Calorimeter

The simulation of the CsI calorimeter first determined the energy deposited to each crystal, based on the kinds, energy, and position of a particle hitting the calorimeter. Once the deposited energy was determined in an event, the scintillation light yield was simulated, and was digitized. The triggering devices, E_{tot} and HCC were also simulated using the result of the simulation for the calorimeter.

Shower in CsI

In our MC simulation, when electron(or photon) reached to the CsI, the transverse position was defined at shower mean depth approximated by:

$$z_e\ (\mathrm{m}) = 0.11 + 0.018 \times \ln \mathrm{E}\ ,$$

$$z_\gamma\ (\mathrm{m}) = 0.12 + 0.018 \times \ln \mathrm{E}\ ,$$

where E is the energy of electron(or photon) in units of GeV/c.

Using the transverse position and energy of electron or photon as inputs, the energy deposited to the CsI crystals was derived from lookup tables referred to as shower library. The shower library was created in advance by collecting the CsI response for electrons in K_{e3} events in which the position and momentum of electrons was measured by the spectrometer.

The shower library was segmented in depth(z) with 25 bins, and binned in energy; 2, 4, 8, 16, 32 and 64 GeV, and binned in position. Each 2.5 cm $\times$ 2.5 cm crystal had six size of the position bin, which varied from 0.2 mm $\times$ 0.2 mm to 0.7 mm $\times$ 0.7 mm with a difference of 0.1 mm with respect to the length of the side. The shower library was composed of 13 $\times$ 13 small(=2.5 cm $\times$ 2.5 cm) CsI crystal array. The segmentation in z was intended to correct for the position dependence along z of the light yield in each crystal. The correction factor was obtained before the installation of the CsI crystals by using cosmic ray muons. Once a sample shower was picked from the shower library, the energy scale was normalized to original energy of the particle incident to the CsI.

The same shower library was used for both 2.5 and 5.0 cm crystals. If any 5.0 cm crystals were present in the shower, they were treated as four 2.5 cm crystals. This simplified the treatment around the boundary between the two different crystal sizes.

For charged pions, the position was defined at the surface of the calorimeter. As well as e/γ, the CsI response was derived from a shower library created by GEANT simulation.

For a muon, deposited energy was determined by Landau distribution [99, 100] based on dE/dx in the 50 cm long CsI.

Digitization

After deciding the energy deposited in each crystal, the Monte Carlo simulated digitization process. It started with the simulation of the scintillation light yield, and then the light was converted to charge. Finally, the charge was digitized to ADC counts.

The CsI time spectra were modeled with three exponential decays, in which two were fast components with roughly 10 and 40 nsec decay constants. The other had a decay constant of order 1 μsec. Based on the pre-measured time constants, the timing on the scintillation was smeared. Because the DPMT operation was synchronized with accelerator RF, time jitter in the CsI signal respect to the RF must be also simulated. The time jitter was modeled by Gaussian distribution with a sigma of 0.6 nsec [101], which was applied to all the CsI crystals on event-by-event basis.

After the determination of energy ratio for each slice, the energy in each slice was smeared individually with photo-statistics. The number of photo-electrons per GeV, $N(p, e)$, had been measured for each crystal. The energy was smeared by Gaussian whose width was defined as

$$\sigma(E) = \sqrt{\frac{E}{N(p.e)}}\ .$$

The least count of DPMT was equivalent to 0.6 MeV, and the CsI crystal had typically 20 photo-electrons per 1 MeV, so that one count corresponded to roughly 12 photo-electrons. Therefore, the Gaussian approximation for the fluctuation was considered as sufficient.

Next step was to convert the smeared energy into charge. It was simply translated using the constants for each crystal which was calibrated with real data. The electrons with well measured momentum from K_{e3} decays were used for this calibration.

The final part of the calorimeter simulation was the digitization of charge in each slice, QIE simulation. The constants obtained from laser calibration were used to simulate the QIE, which were: slopes and intercepts for each capacitor, range, and crystal; the errors in slopes and offsets; the pedestals for each capacitor and range. Each central value was smeared with the error in the set of constants.

E_{tot} and HCC

At this moment, the energy deposited in each crystal, which was the input to E_{tot} and HCC simulation, was reproduced. The energy only in in-time slice[2] was used for the E_{tot} simulation. Summing over the energy for the whole calorimeter formed the E_{tot} signal, to which a threshold was applied. HCC was simulated by tabulating crystals whose in-time energy was above the HCC threshold. The completed table was sent to the cluster counting algorithm already described in Section 3.3.2.

4.3 Accidental Activity

In contrast to the Monte Carlo events, actual detector had many accidental activities, which could be caused by particles in the neutral beam scattering and hitting active part of the detector, or related to electronic noise in the detector. It must be added on an event-by-event basis. In any cases, those activities should be independent of the kaon decay of interest.

This section first discusses such an accidental effect, and next describes how the effect was implemented in the simulation.

4.3.1 The Accidental Effect

The accidental effect was crucial from two points as below.

First, it affected the acceptance calculation. Especially, the detectors located in the neutral beam area had a significant contribution from beam related activity. For example, let us look at the effect on BA. Figure 4.1 shows the BA1's energy distribution in real events kinematically identified as $K_L \to e^+e^-\gamma$(see Section 6.4). Applying a threshold on BA was equivalent to randomly prescaling signal events, because the final state particles in $K_L \to e^+e^-\gamma$ sample did not hit BA. For instance, a threshold of 5 GeV led to a signal loss of 45.5%. This kind of signal loss originated from all the detectors must be correctly reproduced in the MC.

Second, the accidental activity contributed to the magnitude of background level. For example, an accidental photon and other two charged particles might fake a signal. This was especially true for K_{e3} background because of its high branching ratio. Hence the simulation of detector's accidental activity was crucial to correctly evaluate the background level.

4.3.2 Accidental Overlay

To simulate the accidental activity in the Monte Carlo, the data collected by Accidental Trigger was overlaid on the generated MC event with the following procedure. After the event generation, all the detector's response was recorded as ADC counts, TDC counts and latch bit by digitization. Then, the digitized quantities in an accidental data were added to the MC data. ADC counts were

[2] The read out slice was synchronized with accelerator RF. We refer to the slice with the same phase of "in-time bucket"(Section 3.4.1) as "in-time" slice.

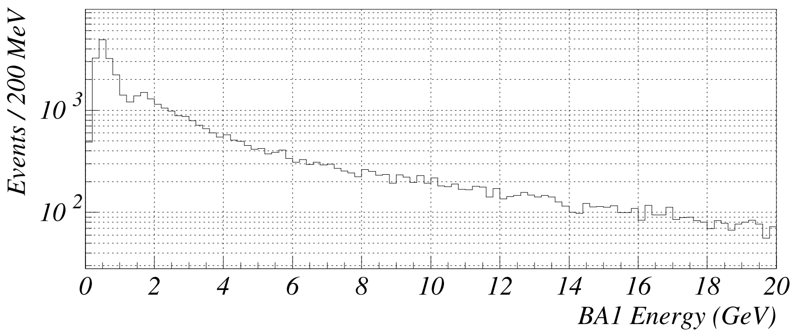

Figure 4.1: BA1 energy distribution in data reconstructed as $K_L \rightarrow e^+e^-\gamma$, in which the activity resulted from accidental particle incident to the BA.

simply summed together, latch bits were ored, and only the first hit in TDC reading was kept. Once the accidental data was appended, trigger requirements for each counter were tested again.

Chapter 5

Event Reconstruction

Our goal in this analysis is to search for $K_L \to \pi^0\nu\bar{\nu}$. In order to identify the signal, we looked for isolated $\pi^0 \to e^+e^-\gamma$ events. This chapter describes the basic event reconstruction used to identify the π^0 Dalitz decay.

The outline of the event reconstruction is:

1. Track finding from the drift chamber information.
2. Energy Cluster finding with the CsI calorimeter.
3. Vertex reconstruction with the spectrometer.
4. Particle identification. We select two electrons[1] and one photon in the final state.
5. Discriminating clusters generated by particles in the in-time RF bucket from accidental clusters in the CsI calorimeter.
6. Calculating kinematical variables.

In the following sections, details in each reconstruction procedure are presented. With respect to the cuts, only the basic requirements which were essential in the event reconstruction, are discussed and the cuts on kinematics are not described here.

Further background suppression must be carried out by imposing some selection criteria on variables obtained from the reconstruction. The optimization of selection criteria for kinematical variables is described in Chapter 6.

5.1 Track Finding

In the first step, track candidates were searched for in each x and y view individually without attempting to match them. The matching between x and y views were performed after the cluster finding because the cluster positions at the CsI calorimeter were used to resolve the ambiguity in the x-y matching, which is discussed in Section 5.3.

The track finding algorithm began with a search for hit pairs, where a pair is the sense wires closest to a particle trajectory in $x(y)$ and $x'(y')$ plane, in each chamber. The TDC counts of a hit were converted to a drift distance. This conversion was calibrated from muons in Muon Runs. The in-time window was defined to be than 235 ns, and if there were multiple hits in the same time window, only the earliest hit was used. Since the interval between the two sense wires

[1] Charge conjugates are implied unless otherwise mentioned in this thesis. Actually we looked for an electron and positron pair.

was 6.35 mm, a sum of drift distances(SOD) was required to be 6.35 mm $\pm$ 1 mm for x view two upstream chambers and y view all chambers. For x view two downstream chambers, it was required to be 6.35 mm $\pm$ 1.5 mm.

Once hit pairs were found in each chamber, the sets of pairs in y views were grouped into linear track segments. For each combination of a chamber 1 pair and a chamber 4 pair, the track position was projected to the chamber 2 and 3. Then pairs in the chamber 2 and 3 were required to be within 5 mm from the projected position. For those pairs which satisfied the above requirement, a least squares fit for the difference between the projected position and hit position at the chamber plane i was carried out. If we define δ_i as the difference at i-th plane, the pairs which satisfied the relation;

$$(\sum_{i=1}^{N_{hits}} \delta_i^2)/(N_{hits}-2) < 4.0 \times 10^{-6}(\mathrm{m}^2) ,$$

were accepted as a y track candidate, where N_{hits} represents the number of planes which had a hit, and thus $(N_{hits}-2)$ was equivalent to the degree of freedom in the least squares fit.

The next step was to find x track candidates. After finding hit pairs, sets of hit pairs in the chamber 1 and 2 were grouped to make segments. The same procedure was repeated for the downstream two chambers. For those two segments, the position projected at the plane in the middle of analyzing magnet was calculated. Any combination of the upstream and downstream segments with the separation distance between the two projected positions less than 6 mm was accepted as an x track candidate.

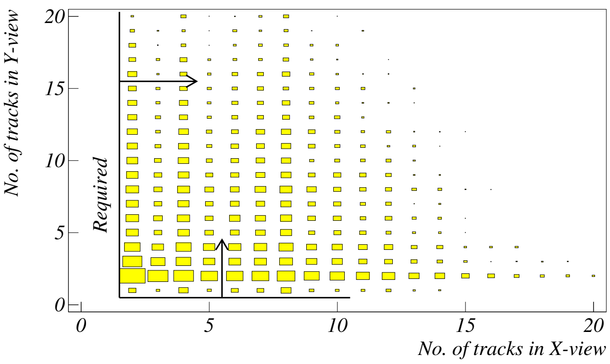

Figure 5.1: The number of track candidates in x and y view for $K_L \to \pi^0\nu\bar{\nu}$ MC events, drawn in log scale. A small opening angle between electron and positron made it difficult to identify two tracks in y view. Accidental activity in drift chambers due to high beam rate produced many fake tracks or actual accidental tracks.

Figure 5.1 shows the number of tracks in the x and y views found in $K_L \to \pi^0\nu\bar{\nu}$ MC events. Since Dalitz decay has a small opening angle between electron and positron, the two trajectories could overlap in the y view. On the other hand, momentum kick given by analyzing magnet bent their trajectories in the x view and made them identifiable as two tracks. Therefore, the event was required to have two or more x and at least one y track candidates.

5.2 Cluster Finding

There were two clustering algorithms used to find the energy clusters in the CsI calorimeter. After applying the two methods, the energy and position of each cluster were extracted with some corrections.

The first clustering algorithm was called as "hardware clustering". It searched for local maxima among the crystals with HCC bit set by the Level 2 processor(Section 3.3.2). For each crystal which had this bit set, the energy was compared with that of the adjacent crystals sharing on edge which also had HCC bit set. The crystals with the highest energy of all the neighbors were regarded as cluster seeds. The crystals around the seed with energy greater than the read out threshold were considered as a cluster. For 2.5 cm $\times$ 2.5 cm crystals, the maximum size of a cluster was 7×7 crystals centered around the seed block. In the case of 5.0 cm $\times$ 5.0 cm crystals, the maximum size of a cluster was 3×3 crystals. The cluster found by this algorithm is referred to as hardware cluster.

Second algorithm, the so-called "software clustering" was used to find the lower energy clusters. It considered all the crystals with energy greater than 100 MeV [2] and HCC bit off as candidates for cluster seeds. For those seed candidates, the local maxima were searched for by the same method as used in the hardware clustering. After finding the local maxima, the energy in all the crystals of a cluster candidate was summed over. Cluster candidates with summed energy greater than 250 MeV were accepted as software clusters.

In both clustering algorithms, we needed to be careful with the cluster near the boundary between large and small crystals. For that area, four small crystals were grouped together and regarded as one large crystal. However, the energy of each 2.5 cm $\times$ 2.5 cm crystal was treated individually.

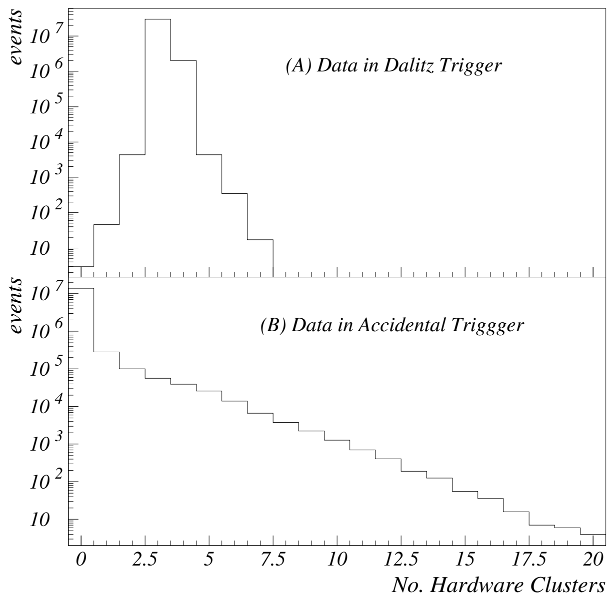

Figure 5.2: The number of hardware clusters in Dalitz Trigger(A) and Accidental Trigger(B). The Dalitz Trigger selected only 3 or 4 hardware clusters. The small fraction of events were collected as minimum bias events without such a requirement in the Dalitz Trigger, as can be seen as a small tail. The number of accidental clusters decreased exponentially, except for big peak at zero, as shown in the bottom.

Figure 5.2 shows the number of hardware clusters for data. Since our signal should have three energy clusters at the calorimeter, the number of hardware clusters was required to be exactly

[2] The output from each crystal had already been converted to energy by using calibration constants. Calibration constants were extracted, using electrons in K_{e3} events, so that measured energy was equal to the electron's momentum measured by the spectrometer.

three. Although accidental photons could make a cluster, the energy of those photon tended to be too low to make a hardware cluster. Therefore, the requirement for the number of hardware cluster did not cause a severe signal loss, which was estimated to be 3.7% based on the accidental data as also shown in Figure 5.2.

Once we obtained the clusters, the next step was to measure the position and energy of incident particles. Particle position at the calorimeter was extracted from the transverse shower shape by using a lookup table. We computed the energy ratio between the center and adjacent rows or columns, and used the lookup table to determine the position. There were 12 lookup tables in total. Half of them was for small crystals, and the other half was for large crystals, covering 6 different energy ranges. To make these lookup tables, electrons from K_{e3}'s whose momenta and positions were well measured by the spectrometer were used. The resulting resolution in position was estimated to be roughly 1 mm for 15 GeV photons.

To find the energy of a cluster, the energy in each crystal in the cluster was summed up. For regions near the beam hole or near the outside edge, the energy leakage was corrected for by using the lookup table created from K_{e3} events(Section 4.2.4). Overlapping clusters were separated, i.e. the crystals which had contributions from multiple particles had their energy split by also looking at the same table. Finally, the total energy of the cluster was corrected for the energy leakage outside of 7×7 crystal array(for small crystals), back of those crystals, and energy loss in the wrapping materials Based on a study by using GEANT, the fraction of the missing energy were independent of the energy of the incident particle, and depended only on the size of crystals. The constants were 1.0/0.9599(=1.042) for 7×7 small crystals, and 1.0/0.9441(=1.059) for 3×3 large crystals(also for boundary region of large and small crystals), respectively.

5.3 Vertex Finding

In order to obtain the trajectories of charged particles, the right combination of a track candidates in x and y views was selected by matching the track (x, y) positions at the calorimeter to the cluster locations. The intersection of two oppositely charged particles gives the decay point of the π^0.

To check if a track matched a cluster position, we defined "separation distance" as the difference between the track (x, y) position at the calorimeter[3] and the cluster (x, y) position. Tracks with the separation distance less than 7.0 cm were considered to match the cluster. The combination of tracks in the x and y view, which gave the smallest separation distance, were coupled together to reconstruct a physical three dimensional trajectory. For these trajectories, the momenta of the charged particles were calculated by using a known momentum kick in the x view. Among the three hardware clusters, one cluster which did not have an associated track was regarded as a photon cluster.

Only events with two tracks with opposite charge were used to find π^0 decay vertices. The intersection of the two tracks were computed in the x view and y view separately. After verifying that these were downstream of the target and upstream of the drift chamber 1, the first guess of the vertex position in z was performed with

$$Z_{vertex} = \frac{X_{int} \times \delta^2_{\theta x} + Y_{int} \times \delta^2_{\theta y}}{\delta^2_{\theta x} + \delta^2_{\theta y}} \quad ,$$

where $X(Y)_{int}$ is the z position of the intercepts in $x(y)$ view, $\delta_{\theta x(y)}$ is the opening angle of the two tracks in $x(y)$ view.

Based on this initial vertex position, various corrections for hit position at each drift chamber were applied. The fringe field of analyzing magnet, chamber rotation, different propagation times

[3] The projected position in z was not on the face of the calorimeter, but 17 cm downstream of the front face. The location was a mean of shower development in z, determined with GEANT study.

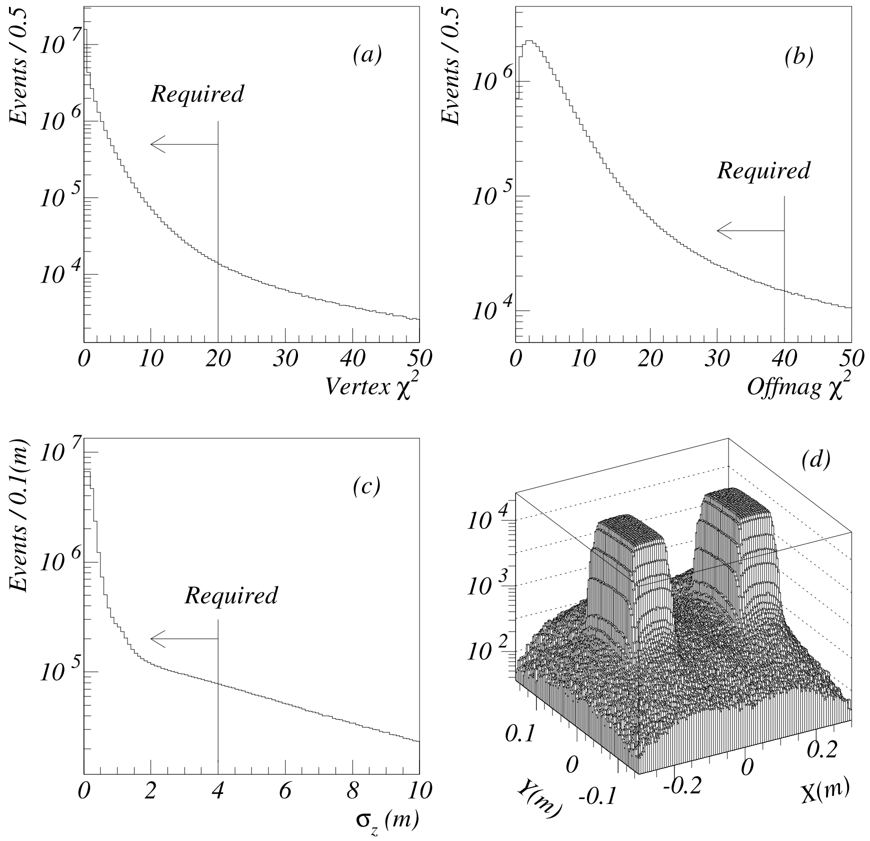

Figure 5.3: The quality variables with respect to vertex finding in data. Vertex χ^2(a), offmag χ^2(b), σ_z(c), and vertex position projected from target to the front face of the CsI calorimeter(d). There are three contributions to (c). The huge peak and steep slope at near zero is from kaon decay, $K_L \rightarrow e^+e^-\gamma$ and K_{e3} background. The next slope or bump between 1 m and 1.5 m in the σ_z is from π^0 Dalitz decay, mainly $\Lambda \rightarrow n\pi^0_D$. The last component in the σ_z greater than 2.5 m arises from the wrong determination of vertex position.

depending on the position of hits along the wire were all taken into account. The vertex position was finally determined from the fit with two charged trajectories weighted according to their multiple scattering angle and the error in the hit position measurement in each chamber. If there were multiple vertex candidates, the final position was determined by comparing three vertex quality variables. The first one, "vertex χ^2", was derived from the final fitting. Another quality variable, the "offmag χ^2", was the χ^2 of the offset at the analyzing magnet between the upstream segments and downstream segments. The last one was the number of hit pairs with good SOD in each drift chamber. To choose a final vertex position from the candidates, an artificial figure of merit was formed by subtracting the sum of the number of hit pairs in all chambers from the sum of "vertex χ^2" and "offmag χ^2". The vertex candidate which gave the minimum of the figure of merit was selected.

In order to avoid mis-measurements of the vertex position, we imposed some cuts on the vertex quality. The expected error on the vertex position in z computed in the final fitting, referred to as σ_z, was one of such variables. Another selection was applied to the vertex position extrapolated from the target to the front face of the CsI calorimeter. Events with vertex $\chi^2 < 20$, offmag $\chi^2 < 40$, $\sigma_z < 4$ m, and the projected vertex position within 10 cm squares centered at the beam holes(x=15 cm or -15 cm, and y=0 cm) were accepted as signal candidates. The signal efficiency for these four requirements was estimated to be 55.6% from MC. Figure 5.3 shows the four variables in data. Since the σ_z is directly related to the opening angle between the two charged trajectories, Dalitz decay gave a very poor vertex resolution as shown in the Figure 5.3, resulting such a low efficiency[4]. This effect was larger for decays in the upstream region, as shown in Figure 5.4. This was due to a larger geometrical uncertainty in the determination of the vertex z position in this region.

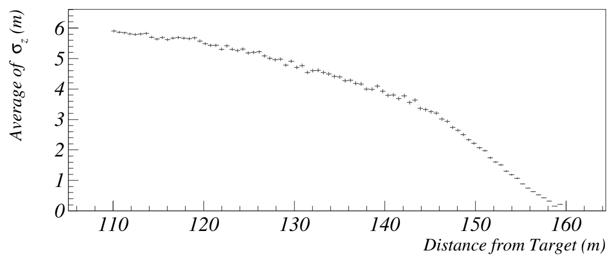

Figure 5.4: Average σ_z as a function of vertex position in z(m). Only the region $z > 110$(m) is shown here.

5.4 Particle Identification

In order to find π^0 Dalitz decays, we needed to identify charged particles as electrons. Since the trigger used the HA and/or the muon counter as veto, most muons were rejected before offline analysis. Therefore, the remaining part of particle identification was π/e separation. A part of the particle identification described in the following was carried out in the Level 3 triggering, and roughly 98% of pions were rejected online. The electron identification was performed with two devices, the CsI calorimeter and TRD's.

[4]The reason why we could not relax these requirements will be discussed in Section 6.2.4

5.4.1 CsI Calorimeter Information

Electrons deposit most of their energy to the CsI calorimeter in contrast to pions which deposit small fraction of their energy in the calorimeter because of the calorimeter's short interaction length, 1.4 λ_0. This enableed us to identify electrons by looking at the ratio of measured energy in the calorimeter,E, to the momentum, p, measured by the spectrometer.

The top plot in Figure 5.5 shows the E/p distribution in data. The low E/p tail was due to pions, and the high side tail was caused by overlapping clusters. Also shown is the E/p distribution in $K_L \to \pi^0\nu\bar{\nu}$ MC. We required the E/p to be unity within $\pm 5\%$ which was roughly 5σ of a Gaussian fit to the signal simulation. The π/e separation factor obtained from the E/p requirement was estimated from data sample identified as $K_L \to \pi^+\pi^-\pi^0$. [5] The bottom plot in Figure 5.5 shows the E/p distribution for two charged particles in $K_L \to \pi^+\pi^-\pi^0$ events. With our requirement, 99.6% of charged pions were rejected, whereas the efficiency for single electrons was calculated to be 93.7% from MC. Since we required two electrons to be identified in the signal, the efficiency for this requirement was 87.8%.

After the E/p requirement, the remaining pions deposited most of their energy at the calorimeter by producing hadronic showers. These showers consist of two components: a prompt energy deposit due to π^0 production equivalent to an electromagnetic shower, and a gradual shower development scaling as the interaction length due to hadronic activity. Because of this hadronic activity, the transverse dimension in the hadronic shower tends to be larger than that in the electromagnetic shower. This difference in the transverse shower shape allowed us to discriminate electrons from pions.

To distinguish electrons from pions, we calculated χ^2_{shape} defined as

$$\chi^2_{shape} = \frac{1}{N}\sum_{i=1}^{N}\left(\frac{E_i - E_i^{pre}}{RMS_i}\right)^2 ,$$

where N is the number of crystals in a cluster, E_i is the real energy in i-th crystal, E_i^{pre} is the expected energy from the electromagnetic shower, and RMS_i is the expected RMS for the i-th crystal. Here we have two expected values obtained from the shower library, as described in Section 4.2.4. Figure 5.6 shows the χ^2_{shape}, referred to as "shower shape χ^2", in data. For both charged and photon clusters, the shower shape χ^2 was required to be less than 5.0 to reject charged pions and fused clusters from multiple particles. The lower plot in the Figure 5.6 shows the χ^2 in $K_L \to \pi^+\pi^-\pi^0$ data sample. Our requirement rejected 47.3% of these pions with a cost of 17% signal loss.

[5] The outline of $K_L \to \pi^+\pi^-\pi^0$ selection was:

- Selected two track events.
- More than two hardware clusters and total of four clusters were required.
- No activity in muon counter was required.
- Vertex location must be $95 < z(\mathrm{m}) < 158$.
- Selected events which had good quality in vertex position.
- Invariant mass reconstructed from two photon, $M_{\gamma\gamma}$, must be $0.125 < M_{\gamma\gamma}(\mathrm{GeV/c^2}) < 0.145$.
- Sum of momenta in final state particles transverse to K_L beam direction, p_t, was required to satisfy $p_t{}^2 < 0.001(\mathrm{GeV/c})^2$.
- Invariant mass reconstructed from two charged particle and two photons, M, was required to be $0.45 < M(\mathrm{GeV/c^2}) < 0.55$

The background level in this $K_L \to \pi^+\pi^-\pi^0$ sample was negligible.

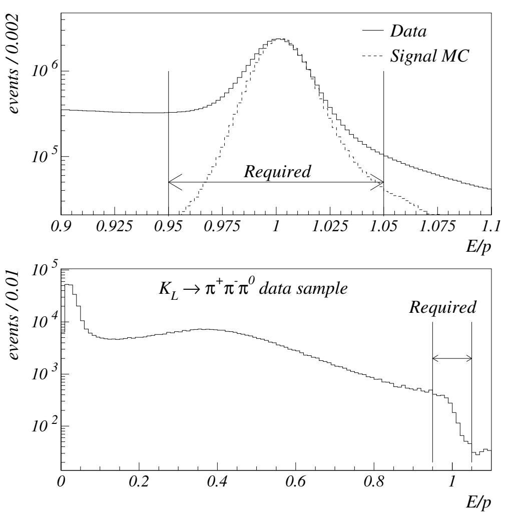

Figure 5.5: The top plot shows the E/p distribution for charged particles in data. Our requirement is indicated by the arrow. The bottom plot shows the E/p in data sample identified as $K_L \to \pi^+\pi^-\pi^0$, thus for charged pions.

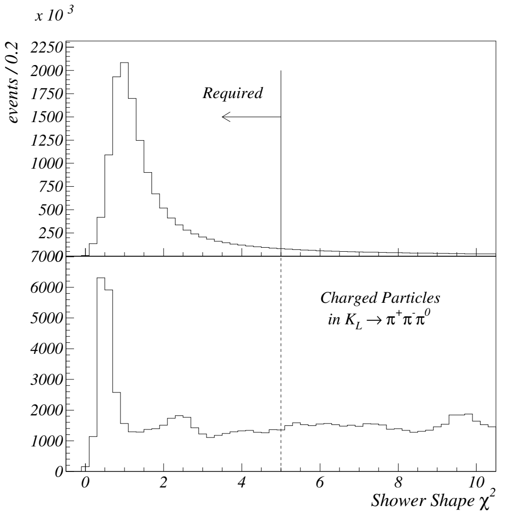

Figure 5.6: The shower shape χ^2 distribution for charged particles in data, where the applied cut is indicated by the arrow. Top plot is for electron sample selected by E/p requirement. The bottom plot is for pion sample in $K_L \to \pi^+\pi^-\pi^0$ events.

5.4.2 TRD

We had a second device for the pion rejection, the Transition Radiation Detectors(TRD's).

Electrons incident to TRD's produced X-ray due to transition radiation in each plane, while pions deposited their energy in the MWPC's only by dE/dx. Therefore, the energy deposited by electrons was larger than that by pions on average. This difference in the deposited energy allowed us to distinguish electrons from pions.

Pion/electron separation with the TRD began with estimating a confidence level in each plane to identify a particle to be a pion, based on the deposited energy in the plane. For a pulse in a TRD plane with the pulse height of h_0, the confidence level was derived as a fraction of events above the h_0 in the pion pulse height distribution. The original pulse height distribution for each plane was obtained from ADC counts with a gain correction on wire-by-wire basis, as shown in the top plot of Figure 5.7. In reality, the ADC distribution was then divided into 32 bins. To extract the fraction of events above a particular pulse height, we integrated the ADC spectra from right to left and normalized its maximum to unity, as shown in bottom of Figure 5.7; this worked as a lookup table. This lookup table was created on plane-by-plane basis with separate tables for gung 2 and gung 4 regions. In order to select the right wire to refer in each plane, we used the extrapolated track position. The ADC count at a wire in a cell traversed by the charged particle was the input to the lookup table after the gain correction. The output from the lookup table, i.e. a confidence level for a charged pion in the i-th plane was referred to as CL_i.

The next step was to combine the CL_i obtained from 16 planes to form a final confidence level for identifying the particle as a pion. Let us describe the procedure to combine the two confidence levels obtained from the first and second plane, CL_1 and CL_2, as an example. If we assume the two confidence level to be independent of each other, the product $P = CL_1 \times CL_2$ is the combined probability. In the (CL_1, CL_2) plane, the hyperbola $P = CL_1 \times CL_2$ gives such a combined probability and the event which have a higher confidence level will be above the hyperbola. Therefore, the hatched area indicated in Figure 5.8 can be considered as a unified

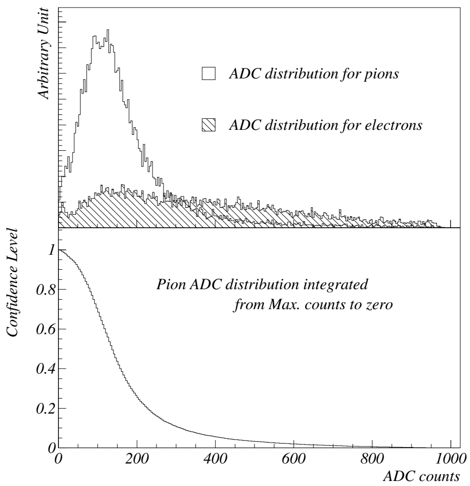

Figure 5.7: Top: The ADC distribution for pions(open histogram) and electrons(hatched histogram) in a plane. Bottom: The translation from ADC counts to confidence level. Integrating the ADC distribution for pions(top) from maximum ADC counts to zero gives the bottom plot. By normalizing the area of the original ADC distribution to unity, the distribution can be considered as a confidence level for charged pions.

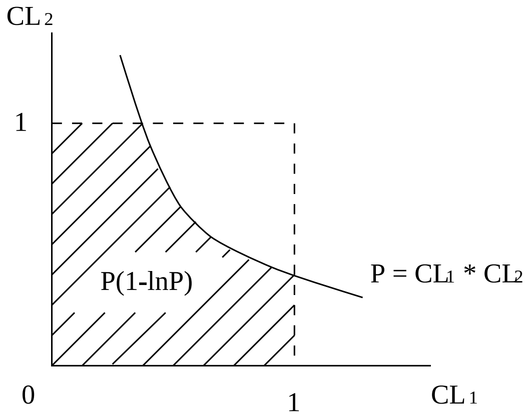

Figure 5.8: The hyperbola obtained from two independent confidence level, CL_1 and CL_2. The shaded area corresponds to the confidence level combined together from the two.

confidence level CL_{12}, which is expressed as

$$CL_{12} = 1 - \int_P^1 d(CL_2) \int_{P/CL_2}^1 d(CL_1)$$
$$= P(1 - \ln P) \ .$$

By analogy for the case of the two planes, and by defining $\prod_{i=1}^{16} CL_i \equiv P16$, the confidence level combined from $n(n \leq 16)$ planes can be expressed as

$$CL = P16 \times \sum_{i=0}^{15} \frac{(-\ln P16)^i}{i\,!} \ .$$

This expression was based on the assumption that the confidence level between each plane did not have a correlation. However, there were small correlations due to the limited binning in the stored lookup tables, and thus the CL did not uniformly distribute. In order to transform the CL to as flat in the region $CL < 0.8$ as possible, we applied the empirically found relation,

$$PCL = \frac{1}{2}[e^{CL \ln 3} - 1] \ ,$$

to compute the "Pion Confidence Level(PCL)".

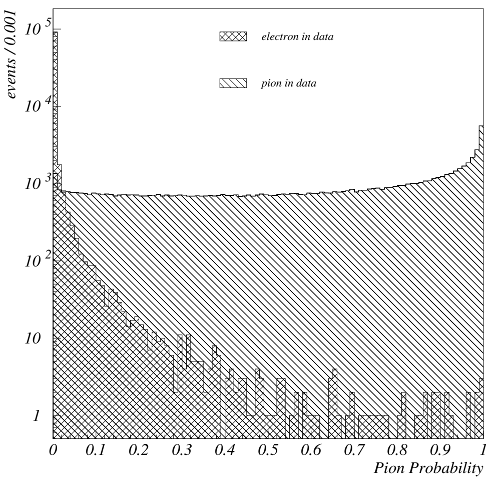

Figure 5.9: The Pion Probability for electrons in $K_L \to e^+e^-\gamma$ data and for pions in $K_L \to \pi^+\pi^-\pi^0$ data, respectively. The electrons have a huge peak at zero. The pions are distributed almost uniformly, but have a small peak at 1.

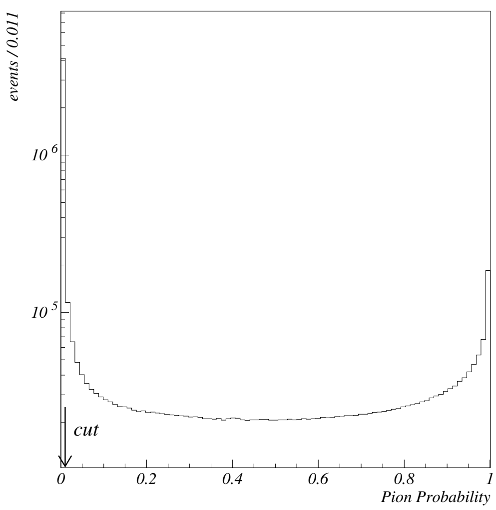

Figure 5.10: The PCL distribution in data after the E/p requirement. Still there is a contamination from pions in K_{e3}'s. They were largely removed by the TRD. Our requirement is shown by an arrow.

Figure 5.9 shows the PCL in two data samples identified as $K_L \to e^+e^-\gamma$ and $K_L \to \pi^+\pi^-\pi^0$. The difference in the distributions shows the π/e separation of TRD's. We required the PCL to be less than 0.01 to select electrons. In the $K_L \to \pi^+\pi^-\pi^0$ sample, the number of pions was reduced by a factor of 71, while the signal efficiency for two electrons was 90.3%, as estimated from $K_L \to e^+e^-\gamma$ data sample. Figure 5.10 shows the PCL for charged particles in data after the E/p requirement. There is a huge peak at zero from the electrons. There is also a contamination of pions mainly from K_{e3}'s which form a flat tail in the entire region and a peak at near 1.

5.5 Rejection of Accidental Photons in the Calorimeter

The time profile of the clusters allowed us to reject accidental particles, helping to remove K_{e3} decays overlapped with accidental photon, in which the pion was mis-identified as an electron. Since the DPMTs measured charge from phototubes every 19 nsec, we could compare the fraction of energy in each slice as shown in Figure 5.11. Here, 19 nsec operation in the DPMT was synchronized with the accelerator RF. The protons incident to the target occupied only in the first 2 nsec period in each RF bucket, and thus the K_L production was also synchronized with the RF timing. Therefore, the time profile of the pulse generated by particles in in-time RF bucket(Section 3.4.1) was always the same. By adjusting the DPMT readout phase, roughly 85% of energy deposited by an in-time particle was contained in the first slice. The lookup table to predict the time profile for each DPMT was generated by real events without particle identification, because the pulse shape was determined by the scintillation properties which was independent of the kind of particle. Timing χ^2 is defined by

$$\chi^2_{time} = \frac{1}{N}\sum_{j=1}^{N}\frac{1}{4}\sum_{i=1}^{4}\left(\frac{R_i - R_i^{pre}}{ERR_i}\right) ,$$

where N represents the number of crystals in the cluster, "4" corresponds to the number of slices read out, and R_i^{pre} denotes the predicted ratio on the lookup table.

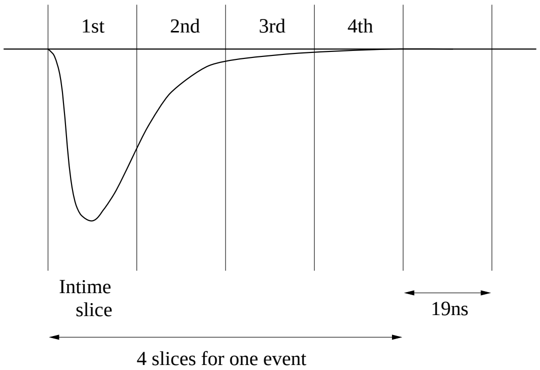

Figure 5.11: Schematic picture of time profile of a pulse at DPMT. The DPMT read out the charge every 19 ns which was synchronized with the accelerator RF.

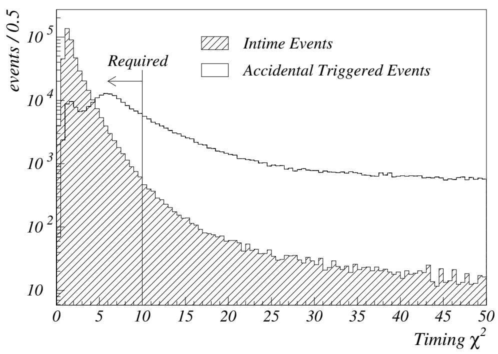

Figure 5.12: The timing χ^2 distribution in $K_L \to \pi^+\pi^-\pi^0$ data sample(hatched) and events collected with Accidental Trigger(open). Our requirement is indicated by arrow.

The hatched histogram in Figure 5.12 shows the χ^2_{time} distribution in a cleanly reconstructed $K_L \to \pi^+\pi^-\pi^0$ data sample, and the open histogram shows events collected with the Accidental Trigger. The $K_L \to \pi^+\pi^-\pi^0$ events have a peak at around 1.5 in the χ^2_{time}, whereas accidental events have almost flat distribution. The χ^2_{time} was required to be less than 10.0 for hardware clusters to select particles coming from in-time RF buckets. Approximately 98.3% of particles in physics data(i.e. non accidental triggered events) satisfied this requirement. These are called "in-time clusters"), and thus 95% of signals were expected to pass this cut. In contrast, 60% of Accidental Trigger data were rejected by this requirement.

5.6 Invariant Mass and Transverse Momentum of π^0

As described in Section 2.1, the π^0 in the final state can be identified from the reconstructed invariant mass, $m_{ee\gamma}$. It can be expressed as

$$m_{ee\gamma} = \sqrt{E_{tot}^2 - |P_x^2 + P_y^2 + P_z^2|}\ ,$$

where, E_{tot} denotes the total energy, P_x, P_y and P_z represent 3D components of the total momentum, respectively. For charged particles, trajectories measured in upstream of the analyzing magnet and momenta measured by the spectrometer were used to obtain the momentum vector. Since the charged particles were already identified as electrons, electron mass was assigned to the charged particles to compute the electron energy. For a photon, the direction of momentum vector was defined as a line extrapolated from the decay vertex to the cluster position at the calorimeter. Using the direction and energy measured by the calorimeter, the 3D momentum of the photon was computed.

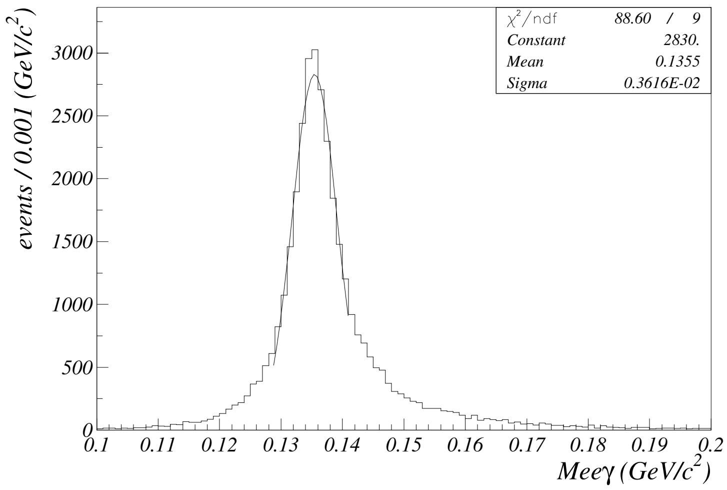

Figure 5.13: Invariant mass, $m_{ee\gamma}$, reconstructed from electrons and a photon in $K_L \to \pi^0\nu\bar{\nu}$ MC. The long tail was largely caused by the mis-measurement of the vertex position. By fitting only the peak with Gaussian, the resolution was obtained as 3.6 MeV.

Figure 5.13 shows the the $m_{ee\gamma}$ distribution for signal Monte Carlo. There is a clear peak at π^0 mass, indicating the capability to identify the π^0 based on the $m_{ee\gamma}$. The non-Gaussian tail is caused by a poor vertex resolution due to a narrow opening angle of e^+e^-. Fitting the Gaussian around the peak, we obtained σ of 3.6 MeV, and the mean of 135.5 MeV/c^2.

The reconstructed total momentum vector was projected onto the plane perpendicular to the K_L direction, which we will refer to as p_t. The K_L direction was measured as a vector projected from the target to the decay vertex point on an event-by-event basis. The p_t is independent of the reference frame, and stays within the kinematical limit shown in Table 2.2. This feature played an important role in background suppression, as will be described in Chapter 6.

Chapter 6

Event Selection

This chapter describes the event selection to suppress various type of backgrounds.

We first summarizes the remaining background sources. The next section describes the event selections in detail to suppress those backgrounds and to identify the signal decay.

In order to avoid a human bias on the selection criteria, we performed "Blind Analysis" technique, i.e. we first temporarily determined all the selection criteria only from Monte Carlo(MC) events, and defined a signal region on the final cuts, $m_{ee\gamma}$ and p_t, to be $125 < m_{ee\gamma}(\mathrm{MeV/c^2}) < 145$ and $160 < p_t(\mathrm{MeV/c}) < 240$. In this context, we refer to the data sample which does not contain events in the signal box in the $(m_{ee\gamma}, p_t)$ plane as "masked data". Then, without changing the final signal box in the $(m_{ee\gamma}, p_t)$ plane, we carried out adjustments of the other cuts using the masked data. Before we opened the signal box: we fixed all the cuts so that the final background level would be ~ 0.1 events; the consistency checks between data and MC were performed: the background levels were estiamted(described in Chapter 7); the consistency checks between the actual background level and our estimation in the side band region of the signal box were performed(described in Chapter 7). Therefore, all the plots for data shown in this chapter does not contain events in the signal box in $(m_{ee\gamma}, p_t)$ plane.

In Section 6.3, we summarize the signal acceptance optimized in Section 6.2.

In order to measure a branching ratio or to extract a single event sensitivity in a rare decay search, we must know the number of decayed parent particles, as discussed in Chapter 2, as well as the detector acceptance. Section 6.4 outlines the method to estimate the number of K_L decays. The MC simulation was used to extract the acceptances for both signal and normalization mode. Besides, the MC played an important role to estimate the remaining background level. The consistency check between data and MC is also mentioned in Section 6.4.

6.1 List of Background Sources

Figure 6.1 shows the 2-dimensional plots of p_t and $m_{ee\gamma}$ generated by MC for $K_L \to \pi^0\nu\bar{\nu}$ decay, and background sources, except for backgrounds related to a beam interaction with detector materials. There is a common feature in the scatter plots, i.e. a wrong vertex measurement caused the tails in both invariant mass and p_t distribution. The vertex position measured as more downstream than the actual position gave high mass and high p_t tail, and the reverse mis-measurement gave low mass and high p_t tail.

The backgrounds can be classified into four groups as described in Section 2.2. We summarize the feature of each background and the mechanisms why they became backgrounds below.

- Type 1 [$K_L \to \pi^+\pi^-\pi^0_D$, $\Lambda \to n\pi^0_D$, Cascade decays.]
  Common feature in these backgrounds was an existence of hadron(s) which was(were) not

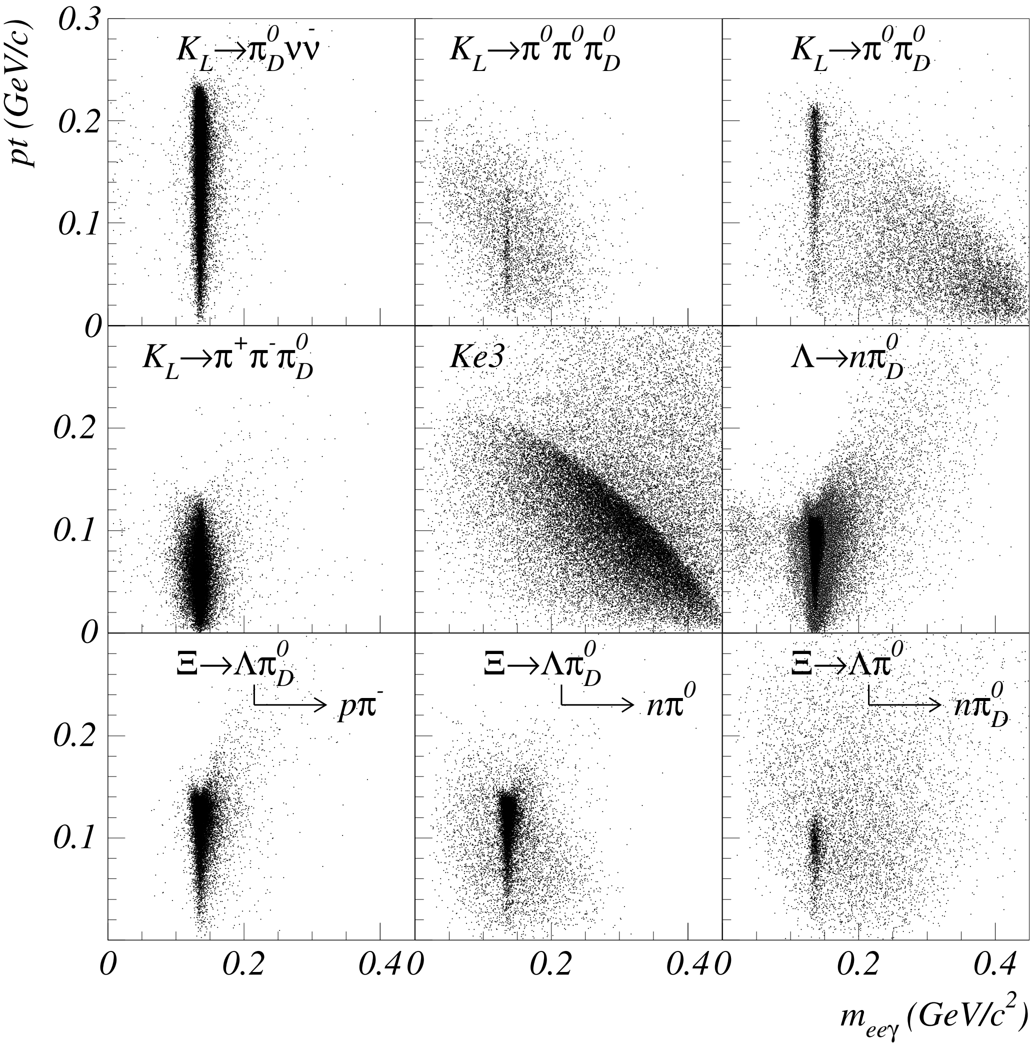

Figure 6.1: The p_t versus invariant mass, $m_{ee\gamma}$, distribution for signal MC, and for eight different backgrounds.

detected, and an existence of $\pi^0 \to e^+e^-\gamma$ decay. As a result, the events looked as if they had contained only one π^0 in the final states, and thus the most of events had the $m_{ee\gamma}$ consistent with π^0. This is the same signature with that in a $K_L \to \pi^0\nu\bar{\nu}$ decay.

- Type 2 [$K_L \to \pi^0\pi^0_D$, $K_L \to \pi^0\pi^0\pi^0_D$, $\Xi \to \Lambda(\to n\pi^0_D)\pi^0$, $\Xi \to \Lambda(\to n\pi^0)\pi^0_D$.]
There was at least one extra π^0 in the backgrounds in this group, resulting in two or more extra photons in the final states. Selection of a daughter photon from π^0 Dalitz decay gave π^0 mass and p_t less than the kinematical limit in each decay. On the other hand, mis-selection of photon, i.e. using a photon from the other π^0 decay to reconstruct the event, caused flat distributions in $m_{ee\gamma}$ and p_t. In any case, a failure to detect the extra photons from the CsI calorimeter made the final state identical with a signal.

- Type 3 [K_{e3}'s overlapping accidental photon referred to as "K_{e3} with accidentals", or overlapping radiated photon referred to as "radiative K_{e3}".]
In both cases, the mis-identification of pions as electrons and overlapping of photons could make a fake signal, and the high branching fraction of K_{e3}'s made them backgrounds. The distribution in $m_{ee\gamma}$ - p_t plane is generally flat except for a band structure from low mass high p_t region to high mass low p_t region, which was due to a kinematical limit. This was especially true for radiative K_{e3}'s, while the K_{e3}'s with accidentals could locate above the band region because of overlapping of uncorrelated high energy accidental photon.

- Type 4 [Beam interactions with detector materials.]
Beam interactions with detector material could produce π^0's mainly at the vacuum window. In a case of the single production of π^0, the situation mimicked type 1. The production of multiple π^0's mimicked type 2 backgrounds.

6.2 Event Selection

The following subsections describe the details of the event selection.

6.2.1 Dalitz Kinematics Cuts

We utilized a unique kinematical feature in Dalitz decay to distinguish signal from K_{e3} background.

In Dalitz decay, the invariant mass of e^+e^- system, $m_{e^+e^-}$, prefers to be small as characterized in Equation 4.4. On the other hand, an electron and mis-identified pion in semi-leptonic decay tends to have a larger $m_{e^+e^-}$ as can be seen in the top plot of Figure 6.2 which shows the ratio of $m_{e^+e^-}$ to $m_{ee\gamma}$ in signal and K_{e3} Monte Carlo. We required the ratio, $m_{e^+e^-}/m_{ee\gamma}$, to be less than 0.3 to select signal decays. The bottom plot of Figure 6.2 shows the ratio in masked data with our selection criteria indicated by an arrow. The peak near zero was enhanced by $\Lambda \to n\pi^0_D$, while the small bump at ~ 0.9 came from K_{e3}'s.

The same feature leads to another phenomenon that e^+e^- system and photon are emitted back-to-back in π^0 rest frame. It implies that the following quantity,

$$\sum \cos\theta \equiv \cos\theta_{e^+\gamma} + \cos\theta_{e^-\gamma} \ ,$$

has a peak at -2(top plot of Figure 6.3) for Dalitz decays, where $\theta_{e^-\gamma}(\theta_{e^+\gamma})$ denotes the opening angle between electron(positron) and photon in the π^0 rest frame. In contrast, K_{e3}'s had a peak near zero as also shown in the top of Figure 6.3. A radiative K_{e3} emits a photon nearly parallel to the electron, and thus the $\sum\cos\theta$ equals to zero. In K_{e3} with accidentals, the pion and electron were regarded as back-to-back in the kaon rest frame because of low energy of overlapping photons, and thus again the $\sum\cos\theta$ became close to zero. The $\sum\cos\theta$ distribution derived from masked data before the $m_{e^+e^-}/m_{ee\gamma}$ cut is shown in the bottom plot of Figure 6.3. There is an event

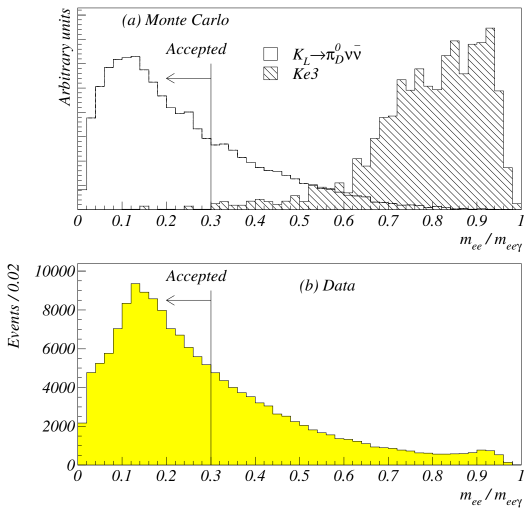

Figure 6.2: (a) The ratio $m_{e^+e^-}$ to $m_{ee\gamma}$ in MC The number of events is normalized with the area. (b) The ratio $m_{e^+e^-}$ to $m_{ee\gamma}$ in subsample(19.2%) of masked data. The peak at 0.25 came from $\Lambda \to n\pi^0_D$, and the shoulder at around 0.06 came from $K_L \to e^+e^-\gamma$. The difference in momentum between π^0 and K_L led to the different peak position. The small bump at 0.9 was caused by K_{e3}'s.

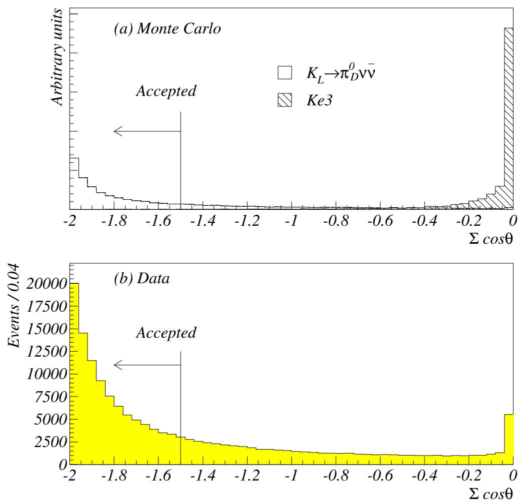

Figure 6.3: The $\sum\cos\theta$ distribution in signal and K_{e3} MC(a) and in masked data(b) before the $m_{e^+e^-}/m_{ee\gamma}$requirement. The $\sum\cos\theta$ is defined in the text. The two MC distribution in (a) are normalized with area.

cluster coming from K_{e3}'s at around zero. We discarded the events with $\sum\cos\theta$ larger than -1.5 to reject K_{e3}'s.

According to MC studies[1], the two cuts combined together, which we will call "Dalitz kinematics cuts", rejected 99.6% of K_{e3}'s, while 78% of $K_L \to \pi^0\nu\bar{\nu}$ signal events passed these requirements.

6.2.2 Charged Veto Cuts

Since we required a charged track position at the CsI calorimeter to match a cluster position measured by the calorimeter[2], charged particles going into the beam hole of the CsI calorimeter could not be found as trajectories. When two extra hadrons traveled through the beam hole in $K_L \to \pi^+\pi^-\pi^0_D$ or $\Xi \to \Lambda(\to p\pi^-)\pi^0_D$ decay, it became a fake signal with an isolated $\pi^0 \to e^+e^-\gamma$. In order to reduce these two backgrounds, we used the drift chamber tracking information.

Figure 6.4 (a) shows the number of track candidates in each x and y view for $K_L \to \pi^+\pi^-\pi^0_D$ MC. The four track events produced more track candidates than signal(Figure 5.1). Therefore, we required the number of x track candidates to be less than 10 and that of y view to be less than 20 as a signal candidate, as shown in Figure 6.4 (b).

As well as the number of track candidates, the four track events had a higher multiplicity of hit pairs in each drift chamber than real two track events. Ideally for signal decays, the number of hit pairs should be four in each chamber because there are two charged tracks in x and y views. The

[1] Monte Carlo simulation produced radiative photon with a probability of 11% [68] for cutoff energy of 1 MeV for the radiative photon.

[2] We could also reconstruct the charged trajectories without requiring the matching of clusters and charged tracks; however, the matching was necessary to obtain better vertex resolution which was critical in hyperon rejection as will be shown in Section 6.2.4.

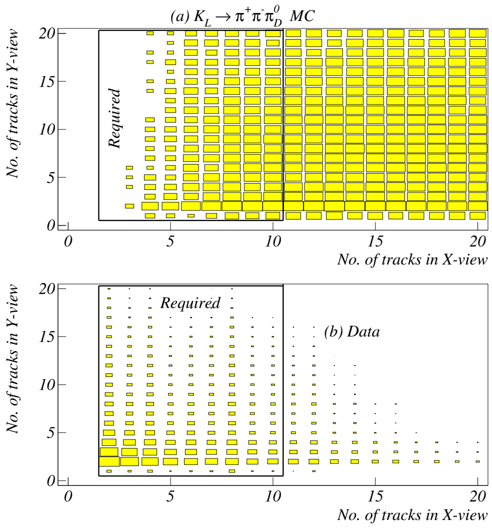

Figure 6.4: Scatter plot of number of track candidates in x and y view in $K_L \to \pi^+\pi^-\pi^0_D$ MC(a) and masked data(b), drawn in log scale. The required region is shown as a box. The determination of lower boundary was discussed in Section 5.1.

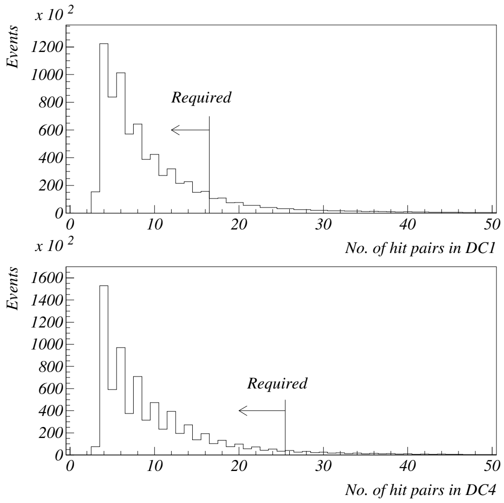

Figure 6.5: The number of hits pairs in DC1(top) and DC4(bottom) in masked data.

number of hit pairs in DC1(4) was required to be less than 16(25). Figure 6.5 shows the number of hit pairs in masked data with our cuts indicated by an arrow.

Based on MC, the cuts described in this subsection, referred to as "Charged Veto", rejected 92.3% of $K_L \to \pi^+\pi^-\pi^0_D$ and 41.2% of $\Xi \to \Lambda(\to p\pi^-)\pi^0_D$ events, while 75% of signals passed these requirements. The signal loss mainly arose from the accidental activities in the drift chambers, especially in the beam regions.

6.2.3 Photon Veto Cuts

In order to veto events involving extra photons, i.e. backgrounds in type 2 and 4(see Section 7.1), we used photon veto counters.

Table 6.1 lists the applied threshold to the photon veto detectors and signal losses, due to accidental activities, coming from each cut. To reduce the detection inefficiency due to photons hitting boundary of two modules in the photon veto detectors, or due to energy leakage to adjacent modules, we applied a cut on the sum of energies in the module with maximum energy and those in the adjacent modules of both sides for each detector. To decrease a signal loss, the cut on BA energy was applied separately between vertex side and the other side.

In order to use the CsI calorimeter as a part of photon veto detectors, we required the number of in-time software clusters to be zero in addition to the requirements of the number of hardware clusters to be three. As well as the π/e discrimination, the shower shape χ^2 was helpful to reject fused cluster because the fused cluster naturally had a different transverse shower shape from single cluster. The reason why we cut on only in-time clusters is that the extra photons in $K_L \to \pi^0\pi^0\pi^0_D$, $K_L \to \pi^0\pi^0_D$, and backgrounds from Cascade decays are in-time, and we wanted to minimize a signal loss due to out of time software clusters.

Figure 6.6 shows p_t vs $m_{ee\gamma}$ in masked data after applying all the cuts described in Section 6.2.1 and 6.2.2. The top is before the photon veto cuts, and the bottom is after the cuts. There is a cluster

Table 6.1: Energy thresholds applied to photon veto counters. BA1 was designed to detect photons, and BA3 was for hadron detection. Since there were more than $20X_0$ materials upstream of BA3, it could not be calibrated by photon, and the threshold was applied in terms of minimum ionizing particle equivalence. To reduce the signal loss in BAs, threshold was separately applied for positive and negative side in x. A total signal loss is not a product of each loss because there were some correlations in accidental activity between each detector.

Detector Element	Energy Threshold	Signal Loss(%)
RC6,7	0.2 GeV	
RC8	0.25 GeV	5 ± 0.1(Total in RCs)
RC9,10	0.1 GeV	
SAs/CIA	0.1 GeV	3 ± 0.06(Total in SAs and CIA)
CA	1.0 GeV	1 ± 0.03
BA1	5.0 GeV(vertex side)	30 ± 0.1(Total in BA1)
BA1	8.5 GeV(opposite side)	
BA3	200 MIPs(vertex side)	10 ± 0.2
BA3	None(opposite side)	
Total		41 ± 0.2

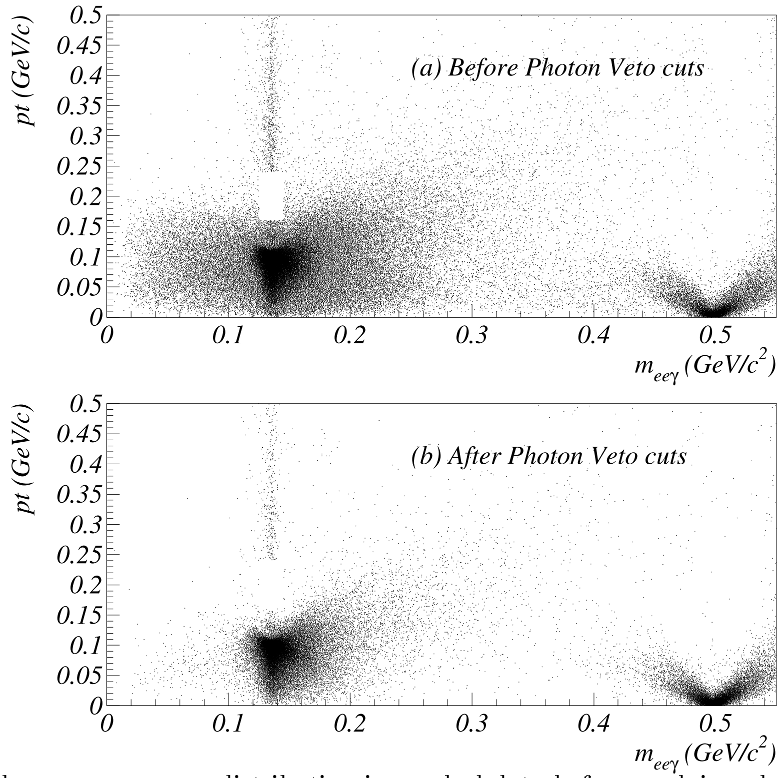

Figure 6.6: The p_t versus $m_{ee\gamma}$ distribution in masked data before applying photon veto cuts(a) and after the cuts(b). The V-shape for $K_L \to e^+e^-\gamma$ events was due to mis-measurements of the vertex position in z

of events coming from $K_L \to e^+e^-\gamma$ in K_L mass and low p_t region. As shown in Figure 6.1, the lower mass region than π^0's is enhanced by $K_L \to \pi^0\pi^0\pi^0_D$. Since K_{e3}'s were strongly suppressed by the Dalitz kinematics cuts, events with $150 < m_{ee\gamma}(\mathrm{MeV/c^2}) < 400$ and low p_t are governed by $K_L \to \pi^0\pi^0_D$ and $K_L \to \pi^0\pi^0\pi^0_D$ in the top plot of Figure 6.6. The cluster of events with π^0 mass and high p_t was associated with beam interactions in the vacuum window as will be mentioned in Section 6.2.4. Photon veto detectors cleaned up the events attributed to as $K_L \to \pi^0\pi^0_D$ and $K_L \to \pi^0\pi^0\pi^0_D$, as shown in the bottom plot of Figure 6.6. Although it is difficult to see in the figure, the events originated from $\Xi \to \Lambda(\to n\pi^0_D)\pi^0$ and $\Xi \to \Lambda(\to n\pi^0)\pi^0_D$ were also well suppressed by detecting extra photons.

The MC expected that the photon veto cuts rejected 99.5% of $K_L \to \pi^0\pi^0\pi^0_D$, over 99.99% of $K_L \to \pi^0\pi^0_D$, and 99.7% of $\Xi \to \Lambda(\to n\pi^0_D)\pi^0$ events. On the other hand, 59% of singal was expected to satisfy the requirements.

Hadron Detection by BA

In addition to vetoing photons, we used BA3 as well as BA1[3] to veto hyperon backgrounds because roughly 95% of neutrons decayed from hyperons hit BA because of their high momenta[4]. To reduce the signal loss caused by high rate(30 MHz) neutrons and non-decayed[5] K_L's in the beams, a cut with a threshold of 200 MIPs(Table 6.1) was applied on the energy in BA3 locating $+x(-x)$ when the vertex position in x was positive(negative). Applying the same threshold on BA3 without using such a vertex information in x resulted in 21.5% loss of signal in contrast to 11.9% loss for applying the cuts separately on positive and negative side of BA3.

By the cuts on BA, 71.9% of $\Lambda \to n\pi^0_D$ events[6] in data were rejected. This implies that BA's detection efficiency for neutron[7] with our cut thresholds was 53.5% by taking into account the accidental signal loss of 40%.

6.2.4 Vertex Cuts

Figure 6.7 shows z vertex distribution in masked data after applying all the cuts described so far. The entire shape was governed by $\Lambda \to n\pi^0_D$. The peak at $z \sim 159$ m was attributed to beam interactions at the vacuum window as discussed later in this subsection. We required the z to be $120 < z(\mathrm{m}) < 150$ from the reasons described below.

Upstream Cut

There were two reasons for rejecting upstream events.

[3] The requirement for BA1 was originally intended to veto photons, but it also helped to detect neutrons in spite of its short interaction length, 0.3 λ_0.

[4] Neutron mass much higher than π^0's carried most of the parent energy, and the parent energy itself was much higher than K_L's.

[5] About 3% of the K_L's entering to the vacuum decay region decayed inside the decay volume.

[6] The $\Lambda \to n\pi^0_D$ events were selected by simple requirements as below:

1. The invariant mass $m_{ee\gamma}$ must be $125 < m_{ee\gamma}(\mathrm{MeV/c^2}) < 145$.
2. The vertex position in z was required to be greater than 110 m and less than 120 m.
3. Photon veto cuts, except for BAs, were applied with the same threshold listed in Table 6.1.

[7] If we define the BA's detection efficiency for neutron as x, the relation;

$$x + 0.396 - 0.396 \times x = 0.719$$

was satisfied for the data kinematically identified as hyperon events, where 0.396 denotes the signal loss and 0.719 represents the fraction of events rejected by BA cuts including signal loss. From the above equation, x was computed to be 0.535.

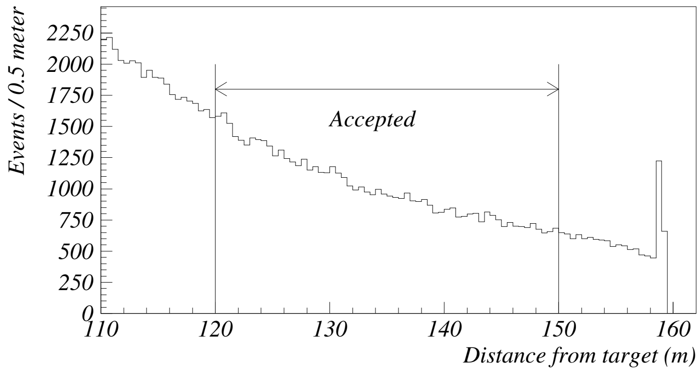

Figure 6.7: Vertex distribution in z in masked data. The accepted region is indicated by an arrow.

The first reason was to suppress backgrounds due to wrong measurements of vertex position which tended to occur in upstream region as shown in Section 5.3. Since hyperons have a shorter life time($c\tau$ = 7.89 cm for Λ, 8.71 cm for Ξ) than that of K_L's, events in upstream region were dominated by hyperon decays(Figure 6.8). For instance, 99% and 1% of events with $110 < z(\mathrm{m}) < 120$ came from $\Lambda \rightarrow n\pi^0_D$, and Ξ decays, respectively, according to MC. Therefore, the selection criterion was determined from high statistics MC studies for hyperons[8] so that the final background level after all the requirements, including cuts which are explained later in this chapter, would be ≤ 0.04 events for both Λ and Ξ backgrounds(Although $\Lambda \rightarrow n\pi^0_D$ had much higher yield than Ξ decays, the severity was almost the same between the two because of $\Xi's$ higher kinematical limit on p_t.).

The other reason for cutting upstream events was a rejection of backgrounds coming from $K_L \rightarrow \pi^0\pi^0\pi^0_D$. As shown in the bottom of Figure 6.8, which displays the z distribution of $K_L \rightarrow \pi^0\pi^0\pi^0_D$ MC after the photon veto cuts, the photons decayed from π^0 in upstream region had a greater chance of escaping detection simply because of a lack of photon veto coverage in that area. Therefore, rejecting the events with $z < 120$ m was crucial to suppress backgrounds from $K_L \rightarrow \pi^0\pi^0\pi^0_D$.

Downstream Cut

As already shown in Figure 6.6, there is a cluster of events with high p_t and π^0 mass. Those events corresponded to a cluster at π^0 mass and z of $\sim$159 m in the top of Figure 6.9, which shows $m_{ee\gamma}$ versus z for masked data with p_t greater than 240 MeV/c without photon veto and charged veto cuts. These events were due to beam(mostly neutron) interactions at the vacuum window[9]. This effect can be seen, for example, in SA2 because the beam interaction sometimes created multiple particles with a wide opening angle to the initial beam direction. The bottom of Figure 6.9 shows SA2's energy distribution in real data. The peak at around 200 MeV, which corresponds to an energy deposited of one MIP, is clearly associated with the beam interaction.

To suppress the background related to the beam interactions, we rejected the events with z greater than 150 m. Since such effects were not implemented in our MC, the remaining back-

[8] The Cascade and Lambda MC sample was 24 and 27 times larger than real data sample, respectively.

[9] Since the beam mainly consisted of neutron and K_L with a ratio of 3.5:1 and a hadronic cross section in neutron is about twice as that of K_L, we attributed the events to mainly neutron interaction.

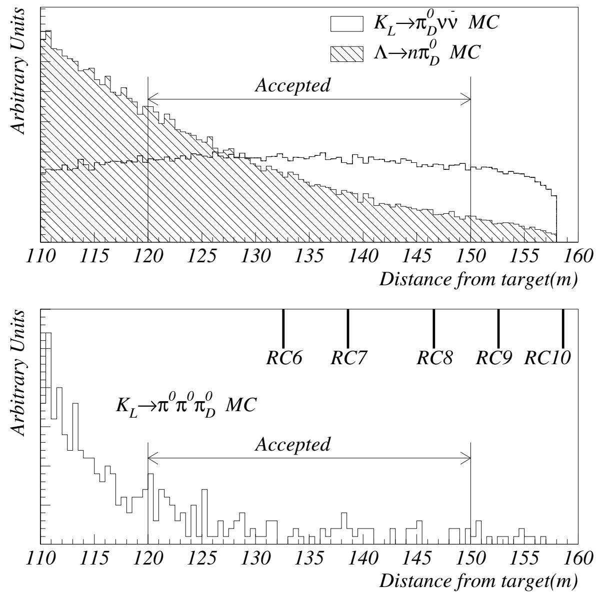

Figure 6.8: Top : The z distribution in signal(opened histogram) and $\Lambda \to n\pi^0_D$ (hatched histogram) in MC. The two distributions are normalized with area. Bottom : The z distribution in $K_L \to \pi^0\pi^0\pi^0_D$ MC with indications of photon veto counters' location.

ground level coming from the beam interaction was estimated by masked data, and is described in Section 7.1.1.

Based on MC studies, the requirements for the vertex position in z suppressed the number of events by a factor of 3.60 for $\Lambda \to n\pi^0_D$, by a factor of 2.08 for Cascade related backgrounds, and by a factor of 3.16 for $K_L \to \pi^0\pi^0\pi^0_D$. The signal efficiency for this cut was 59%.

6.2.5 Photon Energy Cut

We required photon energy measured by the CsI calorimeter, E_γ, to be $3 < E_\gamma(\mathrm{GeV}) < 50$.

Higher end of the cut was determined based on high statistics $\Lambda \to n\pi^0_D$ MC studies although the energy spectrum was almost identical between the signal and the $\Lambda \to n\pi^0_D$ and thus the same signal efficiencies. The lower end was determined from also MC studies to reduce K_{e3}'s by cutting on low energy photons as shown in Figure 6.10.

Figure 6.11 shows the photon energy spectrum in masked data with an arrow indicating our requirement. This cut gave an efficiency of 93% to signal, whereas 18% of K_{e3} and 6% of $\Lambda \to n\pi^0_D$ events were rejected.

6.2.6 Invariant Mass Cut

We identified π^0 in final states by requiring $m_{ee\gamma}$ to be $125 < m_{ee\gamma}(\mathrm{MeV/c^2}) < 145$. The signal window was 2.8 σ of mass resolution in signal MC. This cut reduced two kinds of backgrounds shown below:

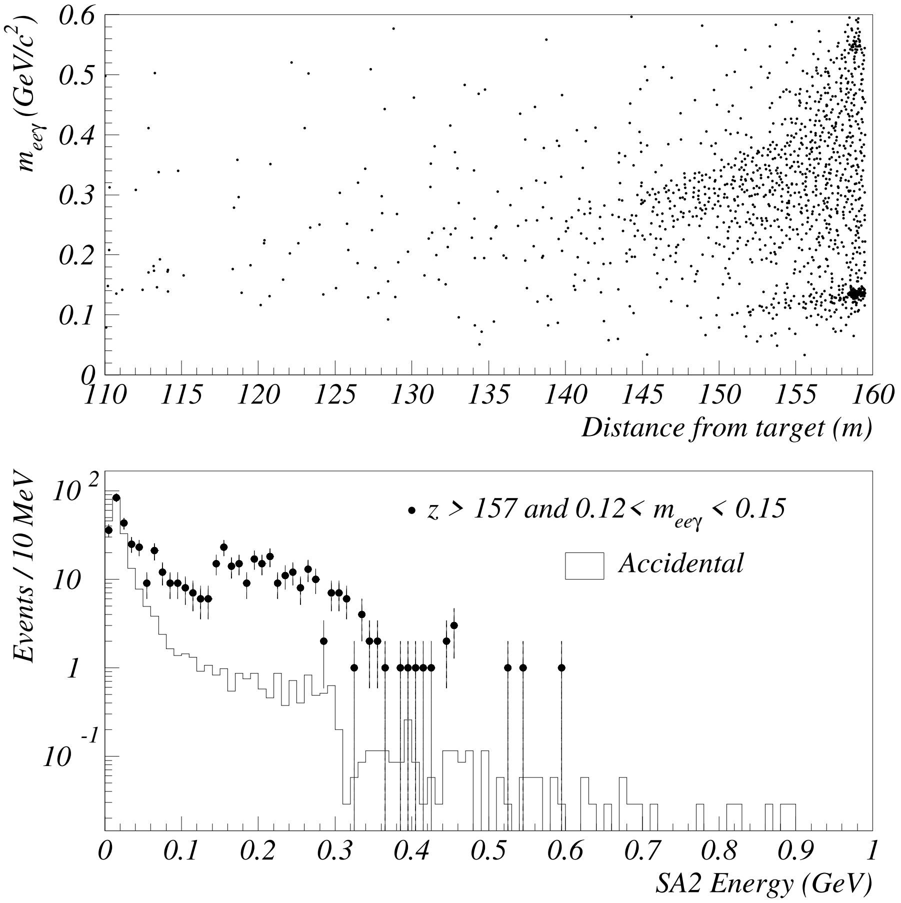

Figure 6.9: To enhance the events associated with a beam interaction, the photon veto and charged veto cuts are removed, and we only select events with $p_t > 160$ MeV/c for these plots. Top : The $m_{ee\gamma}$ versus z distribution in masked data. Beam interaction in vacuum window created π^0 and $\eta(m_{ee\gamma} \sim 550$ MeV/c^2). Bottom : SA2 energy distribution in $K_L \rightarrow e^+e^-\gamma$ data sample(open histogram) and in event sample with $z > 157$ m and π^0 mass(dots) in masked data. The two distributions are normalized with the peak height.

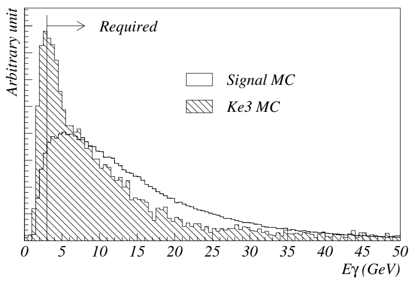

Figure 6.10: The photon energy in $K_L \to \pi^0 \nu \bar{\nu}$ MC(open histogram) and in K_{e3} MC(hatched) just after the basic event reconstruction without particle identification. The two histograms are normalized with their number of events.

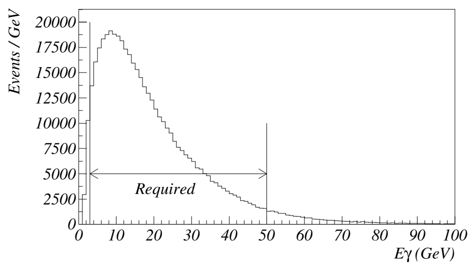

Figure 6.11: The photon energy in masked data. The accepted region is shown by an arrow.

1. Events actually did not involve a π^0 such as K_{e3}. Figure 6.12 shows the $m_{ee\gamma}$ in K_{e3} MC events without particle identifications. An assignment of electron mass to pion, and missing energy carried by neutrino generally led to the $m_{ee\gamma}$ lower than K_L mass. The $m_{ee\gamma}$ cut suppressed the number of K_{e3} events by a factor of 31.7, based on MC.

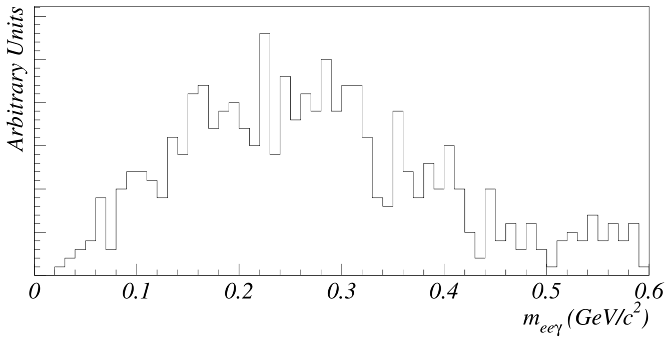

Figure 6.12: The $m_{ee\gamma}$ in K_{e3} MC without particle identifications(E/p, shower shape χ^2, and TRD requirements).

2. Events had at least one extra photon in their final states, in which a wrong photon was selected to build a $e^+e^-\gamma$ mass, such as $K_L \to \pi^0\pi^0_D$, $K_L \to \pi^0\pi^0\pi^0_D$, $\Xi \to \Lambda(\to n\pi^0)\pi^0_D$, and $\Xi \to \Lambda(\to n\pi^0_D)\pi^0$. Figure 6.13 shows the $m_{ee\gamma}$ of these four kinds of background MC events. Because $K_L \to \pi^0\pi^0\pi^0_D$ had more photons than the rest of three backgrounds, it had a higher possibility to choose a wrong photon. As a result, the fraction of events with π^0 mass in $K_L \to \pi^0\pi^0\pi^0_D$ was smaller than others. Based on MC studies, the cuts on $m_{ee\gamma}$ suppressed the number of events by a factor of 4.39 for $K_L \to \pi^0\pi^0_D$, by a factor of 6.41 for $K_L \to \pi^0\pi^0\pi^0_D$ by a factor of 1.30 for $\Xi \to \Lambda(\to n\pi^0)\pi^0_D$, and by a factor of 4.61 for $\Xi \to \Lambda(\to n\pi^0_D)\pi^0$.

The $m_{ee\gamma}$ distribution in masked data after all the requirements described so far is shown in Figure 6.14. The huge peak at π^0 mass was dominated by $\Lambda \to n\pi^0_D$. The peak at K_L mass is $K_L \to e^+e^-\gamma$ which was the normalization mode of this experiment.

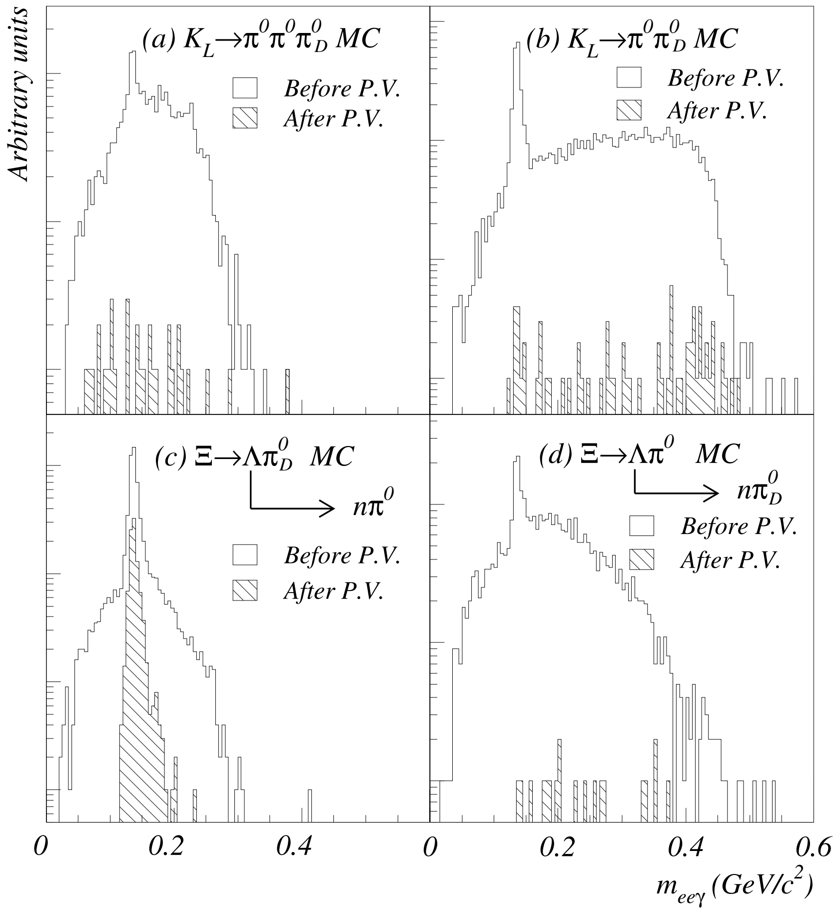

Figure 6.13: The invariant mass distribution in MC for four different background sources after all requirements described so far(hatched histograms). To enhance the events to understand each shape, same distributions before photon veto cuts are also shown as open histogram.

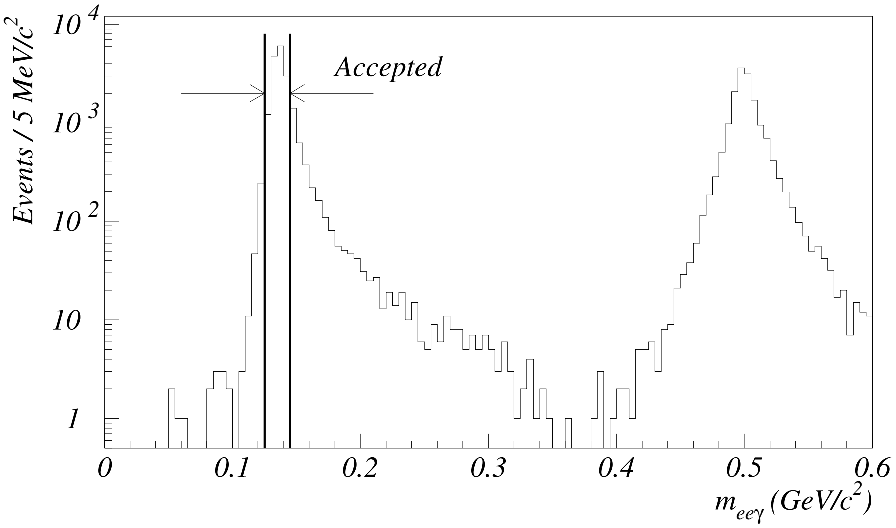

Figure 6.14: The invariant mass $m_{ee\gamma}$ distribution in data after all cuts described so far. The defined signal region is indicated by arrows. The $\Lambda \to n\pi^0_D$ dominated π^0 mass peak. The kaon mass peak was originated from $K_L \to e^+e^-\gamma$.

6.2.7 π^0 Transverse Momentum Cut

Figure 6.15 shows p_t distribution of signal MC events. Because K_L and π^0 are spinless and (anti)neutrino has a helicity of -1(+1) with a spin of 1/2, the π^0 are emitted opposite to neutrino-antineutrino system in kaon rest frame like a quasi two body decay. The p_t extends up to 231 MeV/c. Also shown in the figure are p_t distributions of $\Lambda \to n\pi^0_D$ and $\Xi \to \Lambda\pi^0_D$ MC[10].

As shown in the figure and in Table 2.2, a $K_L \to \pi^0\nu\bar{\nu}$ decay can have much higher p_t than the background events. Therefore, we required the p_t to be greater than 160 MeV/c to reject all backgrounds, which was optimized by $\Xi \to \Lambda\pi^0_D$ MC to suppress the background level to an order of 0.01 events. The upper boundary of the signal region was determined to be $p_t < 240$ MeV/c by the kinematical limit of $K_L \to \pi^0\nu\bar{\nu}$ decay, allowing the smearing effect due to a detector resolution.

The signal efficiency of this cut was expected to be 54%, based on MC. On the other hand, this cut was very effective to redeuce most types of backgrounds, as summarized in Section 7.1.2.

6.3 Acceptance

The previous section described in detail the event selection to suppress backgrounds to a sufficient level. Here we summarize the signal acceptance, and how the events in data were selected by those cuts.

Table 6.2 lists the signal efficiency and the acceptance at each stage estimated from MC. As can be seen in the table, there were three components to lower the acceptance. The first one was related to the poor vertex resolution due to a narrow opening angle between e^+ and e^-. The second came from high rate accidental activities in the photon veto detectors and the drift chambers. The final element was a phase space in p_t. Final acceptance for $K_L \to \pi^0\nu\bar{\nu}$ decay was calculated to be 0.15%.

[10] We refer to $\Xi \to \Lambda\pi^0_D$ as a combination of $\Xi \to \Lambda(\to p\pi^-)\pi^0_D$ and $\Xi \to \Lambda(\to n\pi^0)\pi^0_D$.

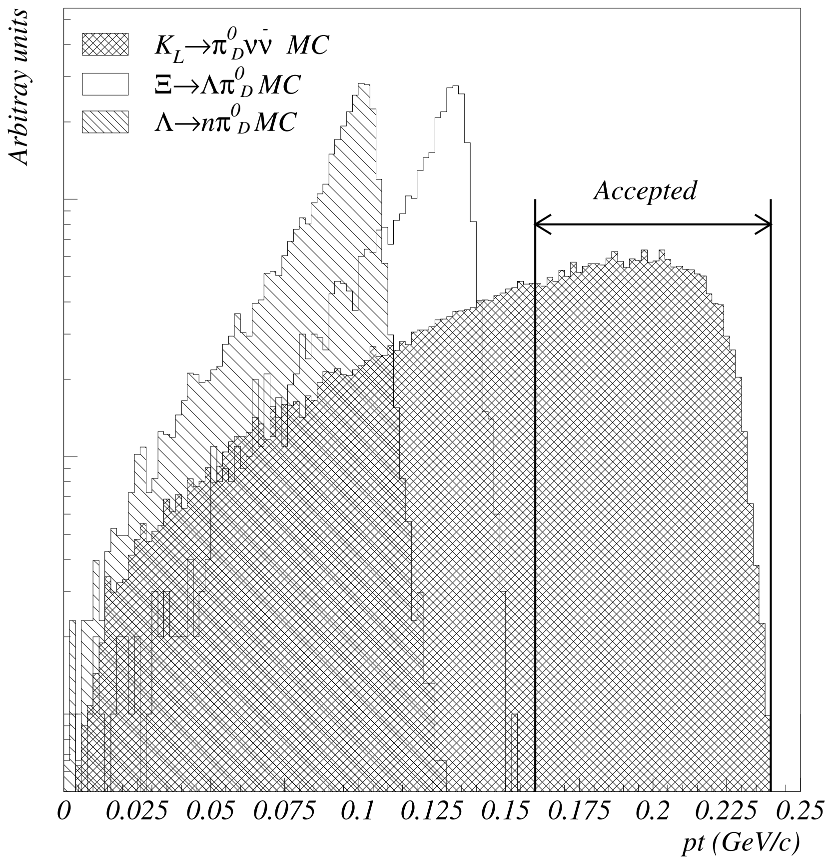

Figure 6.15: The p_t distribution in signal MC(double hatch histogram), $\Xi \rightarrow \Lambda\pi^0_D$(single hatched histogram), and $\Lambda \rightarrow n\pi^0_D$ (open histogram). The required signal region is indicated by arrow.

Table 6.2: The signal efficiency of each cut for $K_L \to \pi^0 \nu\bar{\nu}$ decay estimated from MC. The second column shows the overall acceptance by each stage. Also shown is the number of events passing each cut.

Cuts	Efficiency(%)	Acceptance(%)	Number of events
Level 1 and Level 2	10.6	10.6	
Track Finding	80.0	8.48	
Number of tracks	98.8	8.38	
Cluster Finding	100.	8.38	
Number of hardware clusters	95.8	8.03	
Vertex Finding	94.6	7.59	
Vertex quality	49.0	3.72	
E/p	87.8	3.27	
Shower shape & time profile	82.9	2.71	
TRD	90.3	2.45	
Zero software in-time clusters	84.0	2.05	1,554,974
Dalitz kinematics	77.5	1.59	558,794
Charged veto	74.8	1.19	379,485
Photon veto cuts	59.2	0.705	110,509
Vertex position	50.9	0.359	39,110
Photon energy cut	92.6	0.332	34,715
π^0 Mass cut	84.4	0.280	masked
p_t cut	54.1	0.152	masked

Also shown in the table is the number of events passing each cut for last parts of the event selection. As can be seen, the Dalitz kinematics cuts, photon veto cuts, and requirements for z gave huge reductions, indicating the contamination of K_{e3}'s, $K_L \to \pi^0\pi^0_D$ or $K_L \to \pi^0\pi^0\pi^0_D$, and hyperon decays. The data here is still masked, and thus we cannot mention the numbers for the final two cuts.

6.4 Normalization

The event selection for normalization mode, $K_L \to e^+e^-\gamma$, was performed with exactly the same algorithm and with almost the same cuts as used in signal mode. The only differences in the selection criteria were mass and p_t windows. Since there are no missing particles in $K_L \to e^+e^-\gamma$ events, its p_t must be zero due to momentum conservation. Therefore, we required the $m_{ee\gamma}$ to be $450 < m_{ee\gamma}(\mathrm{MeV/c^2}) < 550$, and ${p_t}^2$ to be less than 0.001 $(\mathrm{GeV/c})^2$ to select $K_L \to e^+e^-\gamma$ events.

Figure 6.16 shows the ${p_t}^2$ distributions for data and MC after all the cuts except for the ${p_t}^2$ cut. The two distributions are normalized by the measured number of K_L decays, which is equivalent to normalize by area of p_t or $m_{ee\gamma}$ distribution in this case because we measured the number of decayed K_L's by $K_L \to e^+e^-\gamma$, and we applied cuts on the two variables at the very end of the event selections. There is a huge peak at zero, indicating correct reconstruction of the events. Also shown in the bottom is a ratio between the two distributions. The uniform ratio indicates that the MC reproduced events correctly.

Figure 6.17 shows $m_{ee\gamma}$ distributions after the ${p_t}^2$ requirement for data and MC, and the ratio between the two distributions. The huge peak at K_L mass is an evidence of $K_L \to e^+e^-\gamma$ events. The entire shapes are in good agreement between data and MC. Although there is a

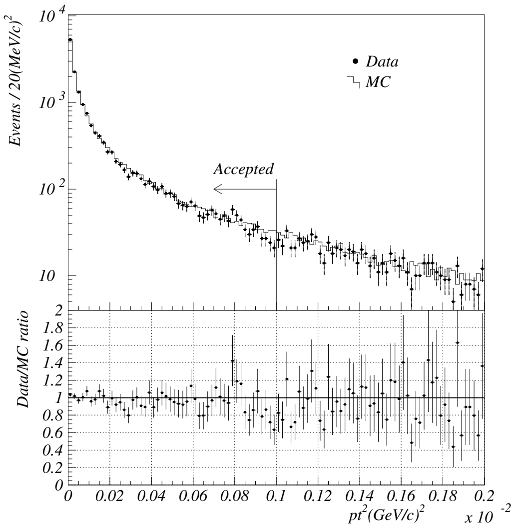

Figure 6.16: Top: The p_t^2 distribution after all cuts except for p_t^2 in data(dots) and MC(histogram). The signal region is indicated by an arrow. Bottom: The ratio of above two distributions, data/MC.

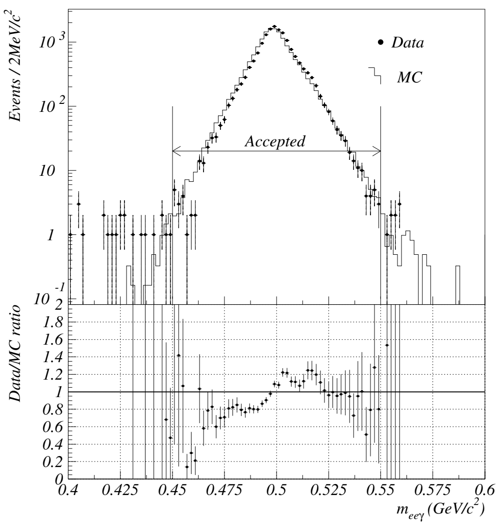

Figure 6.17: Top: The $m_{ee\gamma}$ distribution after all cuts except for $m_{ee\gamma}$ in data(dots) and MC(histogram). The signal region is indicated by an arrow. Bottom: The ratio of above two distributions, data/MC.

0.9 MeV/c^2(0.2%) of discrepancy in the peak position, the effect on the number of $K_L \to e^+e^-\gamma$ decays were negligible as will be discussed in Section 8.3.

In order to ensure the acceptance calculation, we also compared two more distributions in data with MC, which are significantly sensitive to the detector acceptance. These distributions were normalized between data and MC by the number of measured K_L decays. We first compare z distributions for $K_L \to e^+e^-\gamma$ sample in Figure 6.18. As can be seen, they are in good agreement except for the very downstream region. Since our normalization did not use the events in such region, the acceptance calculation was not largely affected, and the quantitative discussion is presented in Chapter 8.

Figure 6.19 compares total momentum distributions of $K_L \to e^+e^-\gamma$ events. The agreement is excellent.

Figure 6.20 shows the p_t^2 versus $m_{ee\gamma}$ in data. Also shown is the defined signal box. The tails in high p_t^2 and low mass or high mass region was due to a mis-measurement of a vertex position. We observed 15,951 $K_L \to e^+e^-\gamma$ events in our signal box. The only background source we considered was K_{e3}'s, which was estimated to be less than 0.1 events by the MC studies. Therefore, we conclude that it is negligible. The tight selection criteria for signal mode automatically yielded such a pure $K_L \to e^+e^-\gamma$ sample.

Based on MC, we calculated the detector acceptance for $K_L \to e^+e^-\gamma$ to be 0.815%. Using the number of observed events, the acceptance, and $Br(K_L \to e^+e^-\gamma)$, 9.1×10^{-6} [13], we measured the number of K_L between 20 and 220 GeV in energy that decayed between 90 and 160 m from the target to be 2.15×10^{11}.

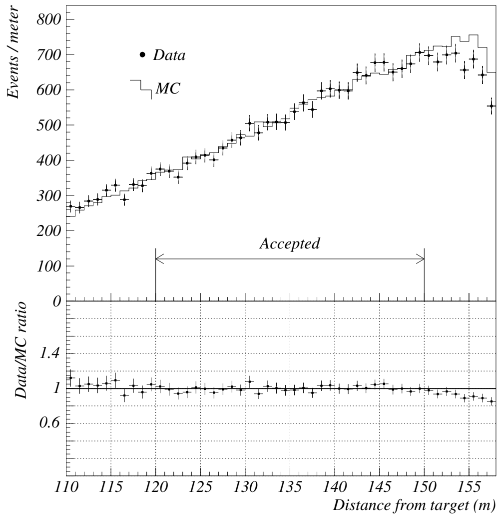

Figure 6.18: Top: The z distribution for $K_L \to e^+e^-\gamma$ events after all cuts except for z in data(dots) and MC(histogram). The signal region is indicated by an arrow. Bottom: The ratio of above two distributions, data/MC.

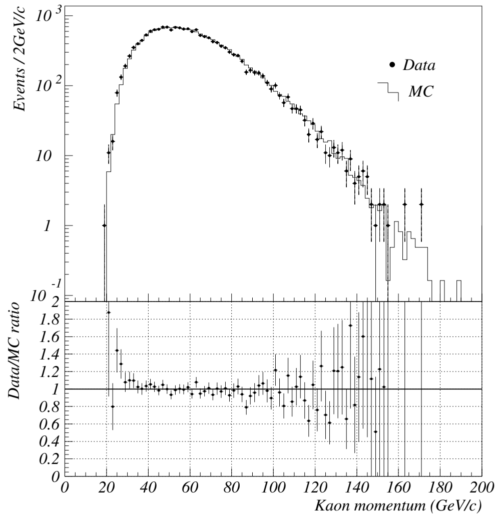

Figure 6.19: Top: The total momentum for $K_L \to e^+e^-\gamma$ events after all cuts in data(dots) and MC(histogram). Bottom: The ratio of above two distributions, data/MC.

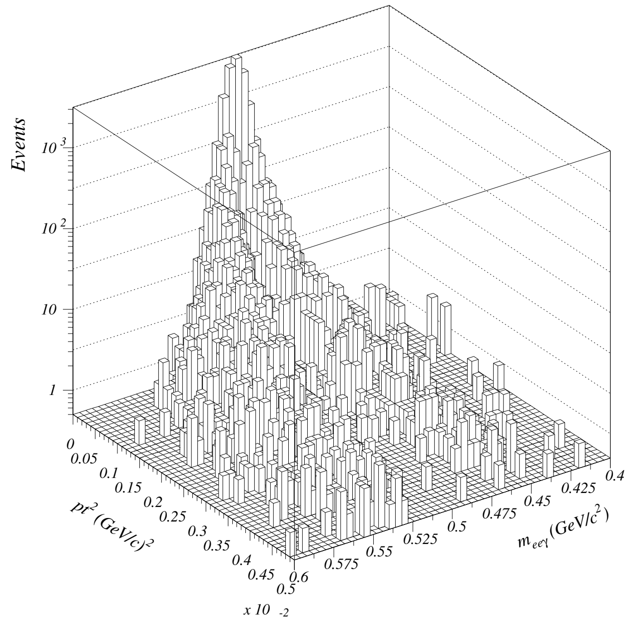

Figure 6.20: The p_t^2 versus $m_{ee\gamma}$ in data after all cuts. The peak came from $K_L \to e^+e^-\gamma$. The only area near the cluster of $K_L \to e^+e^-\gamma$ events are displayed here.

Chapter 7

Background Estimation

This chapter describes the estimation of the remaining background level, which is important to judge whether a remaining event is signal or background.

In Section 7.1, we first estimate the background level due to beam interactions, and then summarize the expected level for all the background sources. In order to ensure our understanding of backgrounds, we performed consistency checks between data and MC. Section 7.2 describes a consistency check of the performance of photon veto counters, which played an important role in background suppression, and were directly related to the size of backgrounds associated with extra photons. We then present two comparisons. The first is a comparison of the shape of background distributions, which is covered in Section 7.3. The other is a comparison of the number of events in the side band region in $(m_{ee\gamma}, p_t)$ plane, which is described in Section 7.4.

7.1 Background Level

We first discuss the background level for beam interactions which was estimated with masked data. We then summarize the expected size of contributions from each background.

7.1.1 Estimation of Background Level from Beam Interaction

Figure 7.1 shows p_t versus z in masked data after applying all the cuts except for the requirements on p_t and z. There is a cluster of events at $z \simeq 159$ m, which clearly indicates an existence of beam interactions in the vacuum window. There were two cases in this background. One was a single production of π^0 or at least $e^+e^-\gamma$ was reconstructed with a right combination if there were multiple π^0's. They had a π^0 mass with z near the vacuum window. The other case was a multi-production of π^0's or other particles such as $\eta' s$ or charged pions. η's were identified in the top of Figure 6.9 as a cluster of events at $z = 159$ m with $m_{ee\gamma}$ of ~ 550 MeV/c^2. Charged pions were candidates for causing the activities in SA2 as described in Section 6.2.4. Escapes of extra particles from the calorimeter caused a mis-selection of photon to build an event. Therefore, photon veto and charged veto cuts were crucial to suppress this type of backgrounds as well as the z requirement. The two veto cuts reduced the number of events attributed to beam interactions by a factor of 20.

By evaluating the contamination of events to the signal region in the (z, p_t) plane, we predicted the background level coming from beam interactions. The estimation consisted of two steps.

First, we looked into the z distribution of events with $125 < m_{ee\gamma}(\mathrm{MeV/c^2}) < 145$ and $p_t >$ 240 MeV/c, in which the beam interactions dominated the events, as shown in Figure 7.2. There were two components in the distribution; one was the peak at $z = 159$ m, and the other was an exponential tail. In order to evaluate the contamination to the signal region in z($<$150 m), the

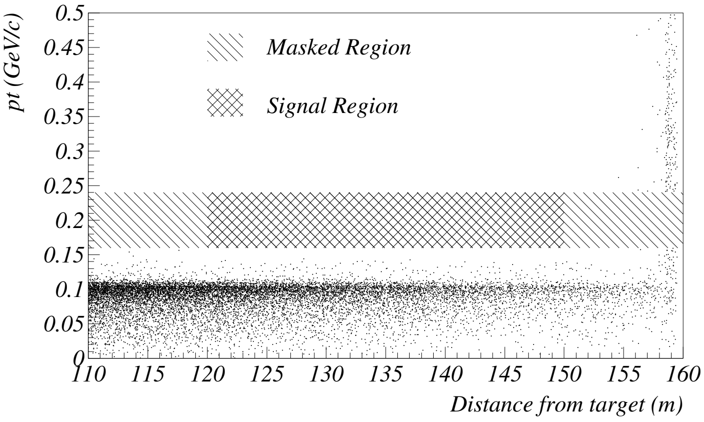

Figure 7.1: The p_t versus z in masked data. All the cuts are applied. The signal region is marked by a double hatched box, and the masked region is indicated by a single hatched box.

shape was fitted with exponential between $z = 158.5$ m and 157 m. Based on the fit, we modeled the distribution to be

$$f(z) = exp[-111.7 + 0.7167 \times z/\mathrm{m}] \ ,$$

for the histogram with a binning of 0.25 m interval. Integrating the above function between $z = 120$ m and 150 m, we expected that 0.084 events from the beam interactions contaminated in the range, $120 < z(\mathrm{m}) < 150$ and $p_t > 240$ MeV/c, although we did not observe any events in the region. The variation in the slope was studied as a source of systematic uncertainty, as described in Appendix D.

Next, the contamination of the 0.084 events to the signal region along p_t was investigated. Figure 7.3 shows p_t distribution of the events with $125 < m_{ee\gamma}(\mathrm{MeV/c^2}) < 145$ and p_t greater than 240 MeV/c, and without the z requirement. In order to derive a ratio of the number of events in the signal region($160 < p_t(\mathrm{MeV/c}) < 240$) and in the region above 240 MeV/c, we fit the distribution with an exponential function. As shown in Figure 7.3, the shape was determined to be

$$f(p_t) = exp[4.408 - 5.432 \times p_t/(\mathrm{GeV/c})] \ ,$$

for the histogram with a 10 MeV of binning. Based on this form, the number of events in the signal region was predicted to be 50.1% of those in $p_t > 240$ MeV/c by integrating the above function. This ratio was constant as $(50.1 \pm 4.7)\%$ for the change of selection criteria, such as relaxing the charged veto and/or photon veto cuts.

Since there were no correlations between p_t and z, as shown in Figure 7.4, we expected the number of events in the final signal region coming from the beam interactions to be $0.084(\mathrm{events}) \times 0.501(p_t\,\mathrm{shape}) = 0.042$.

7.1.2 Summary of Background Level

Table 7.1 summarized the efficiencies of each cut for all the background sources except for beam interactions. In the table, the efficiencies of cut (8)(=E/p) and (9)(=shower shape and time profile) for K_{e3}'s, and (10)(=TRD) for all the background sources were evaluated from real data. The other cuts were all estimated from MC. As can be seen in the table, there were four kinds of

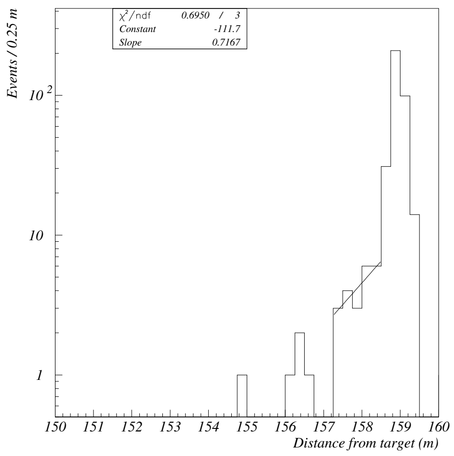

Figure 7.2: The z distribution in data in the region of $125 < m_{ee\gamma}(\mathrm{MeV/c^2}) < 145$ and $p_t > 240$ MeV/c. All the cuts except for the z requirements are applied.

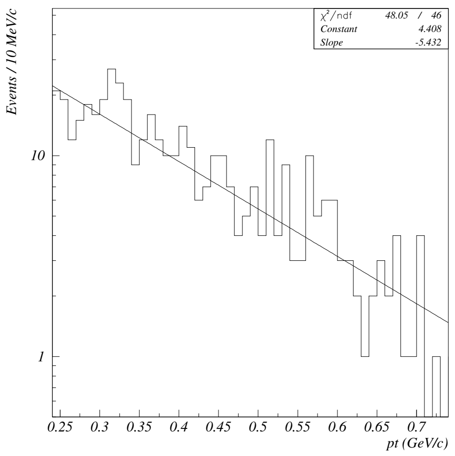

Figure 7.3: The p_t distribution in events with $125 < m_{ee\gamma}(\mathrm{MeV/c^2}) < 145$ and $p_t > 240$ MeV/c. Except for the z cut, all the other cuts are applied.

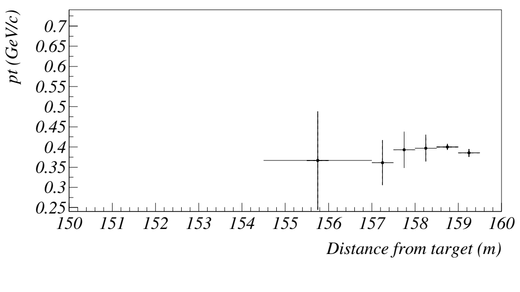

Figure 7.4: The average of p_t as a function of z in masked data for the events with $p_t > 240$ MeV/c. No correlation between the p_t and z can be seen.

Table 7.1: Efficiencies of each cut for every background source. Since there are some correlations between the cuts, each efficiency might depend on the order of selection. The numbers in the table were based on the order actually applied in the analysis. For some strongly correlated multiple cuts, their efficiencies are shown with a combined form. The MC statistics used in these studies was from 8×10^{-3} to 30 times larger than real data sample. If we found two or more cuts which did not correlate with each other, each efficiency was evaluated with the MC sample enriched by removing one of the uncorrelated cuts(see Appendix D.2.3).

Cuts	Efficiency		
	$K_L \to \pi^0\pi^0\pi^0_D$	$K_L \to \pi^+\pi^-\pi^0_D$	$K_L \to \pi^0\pi^0_D$
(1) Level 1 and Level 2	8.57E-3	8.39E-3	6.32E-2
(2) Track Finding	0.364	0.992	0.609
(3) Number of tracks	0.961	0.165	0.977
(4) Cluster Finding	0.999	0.999	0.988
(5) Number of hardware cluster	0.115	0.925	0.162
(6) Vertex Finding	0.404	0.736	0.728
(7) Vertex quality	0.756	0.572	0.581
(8) E/p	0.620	0.215	0.794
(9) Shower shape & time profile	0.281	0.804	0.875
(10) TRD	0.903	0.903	0.903
(11) No in-time software clusters	0.291	0.570	0.569
(12) Dalitz kinematics	0.801	0.840	0.896
(13) Charged veto cuts	0.633	7.80E-3	0.742
(14) Photon veto cuts	5.33E-3	0.625	<1.09E-4
(15) Vertex position	0.316	0.443	0.434
(16) Photon energy cut	0.918	0.921	0.434
(17) π^0 Mass and p_t cuts	4.11E-3	<5.57E-5	8.17E-2
Total	1.55E-11	<4.42E-11	<2.11E-9

Cuts	Efficiency				
	K_{e3}	$\Lambda \to n\pi^0_D$	$\Xi \to \Lambda(\to p\pi^-)\pi^0_D$	$\Xi \to \Lambda(\to n\pi^0)\pi^0_D$	$\Xi \to \Lambda(\to n\pi^0_D)\pi^0$
(1)	3.14E-3	0.164	0.105	0.101	9.70E-2
(2)	0.982	0.861	0.973	0.726	0.664
(3)	0.980	0.901	0.200	0.981	0.979
(4)	0.999	1.00	1.00	1.000	0.999
(5)	0.672	0.960	0.921	0.263	0.137
(6)	0.938	0.949	0.842	0.764	0.701
(7)	0.986	0.435	0.482	0.461	0.528
(8)	4.37E-3	0.986	0.587	0.773	0.753
(9)	0.539	0.859	0.829	0.826	0.858
(10)	1.40E-2	0.903	0.903	0.903	0.903
(11)	0.418	0.830	0.735	0.709	0.712
(12)	4.29E-3	0.828	0.803	0.775	0.810
(13)	0.833	0.798	0.593	0.752	0.772
(14)	0.619	0.284	0.362	0.157	2.70E-3
(15)	0.513	0.278	0.497	0.454	0.493
(16)	0.821	0.943	0.929	0.933	0.927
(17)	7.56E-3	<1.41E-6	4.48E-5	1.29E-4	1.69E-2
Total	1.82E-13	<2.23E-9	8.87E-9	1.36E-8	1.73E-8

cuts which gave the major suppression for backgrounds. The first kinds were cuts on $m_{ee\gamma}$ and p_t. These cuts were effective to reduce most types of backgrounds, especially for backgrounds in type 1 in Section 6.1. The second kinds were photon veto cuts to suppress the backgrounds associated with extra photons, namely backgrounds in type 2. The third ones were particle identifications reducing K_{e3}'s(background in type 3). The fourth ones were the Dalitz kinematics cuts also effective to K_{e3} reduction(background in type 3).

The number of decayed K_L's was evaluated in Section 6.4 to be 2.15×10^{11}. The numbers of decayed Λ's and Ξ's were measured to be 4.30×10^9 and 1.61×10^8, respectively, as described in Appendix C. Using these numbers, branching ratios listed by the Particle Data Group(Table 2.2), and efficiencies on the Table 7.1, we predicted the remaining background levels as listed in Table 7.2. The biggest contribution came from beam interactions. In short, we expected $0.12^{+0.051}_{-0.038}$

Table 7.2: Summary of expected background contribution in the final signal region.

Decay mode	Expected number
$K_L \to \pi^0\pi^0\pi^0_D$	0.03 ± 0.030
$K_L \to \pi^0\pi^0_D$	< 0.01
$K_L \to \pi^+\pi^-\pi^0_D$	< 0.01
$K_L \to \pi e\nu + \gamma$	0.02 ± 0.018
$\Lambda \to n\pi^0_D$	< 0.04
$\Xi \to \Lambda(\to p\pi^-)\pi^0_D$	$0.01^{+0.006}_{-0.004}$
$\Xi \to \Lambda(\to n\pi^0)\pi^0_D$	$0.01^{+0.006}_{-0.004}$
$\Xi \to \Lambda(\to n\pi^0_D)\pi^0$	0.01 ± 0.010
$n + X \to \pi^0 X'$	$0.04^{+0.035}_{-0.008}$
Total	$0.12^{+0.051}_{-0.038}$

background events in total in the final signal region, where we did not add the contributions from $\Lambda \to n\pi^0_D$, $K_L \to \pi^0\pi^0_D$, and $K_L \to \pi^+\pi^-\pi^0_D$ at the calculation of the total number. The estimation of the error on the predicted level is discussed in Appendix D.2.

7.2 Consistency Check of Photon Veto

Since the performance of photon veto detectors was directly related to the level of backgrounds with extra photons, we compared the performance predicted by MC with the actual performance in two ways.

The first comparison was based on a detection efficiency for photons. To measure the position and energy of photon hitting photon veto counters, the same technique used in the calibration of the energy scale was utilized(Appendix B). The measured inefficiency in the RC with a threshold of 100 MeV is shown in Figure 7.5 as a function of incident photon energy. The dots represent data and open squares are for MC. For the entire energy range, data and MC are consistent within 3 σ of statictical error.

The second was a direct comparison of rejection factor. Selecting low $m_{ee\gamma}(< 0.1$ GeV/c$^2)$ and low $p_t(< 0.15$ GeV/c) region without photon veto cuts allowed us to obtain data sample enriched by $K_L \to \pi^0\pi^0\pi^0_D$ (55% of a purity is expected from MC studies, the other 29% comes from a combination of $K_L \to \pi^0\pi^0_D$, $\Xi \to \Lambda(\to n\pi^0)\pi^0_D$, and $\Xi \to \Lambda(\to n\pi^0_D)\pi^0$, and the remaining comes from $\Lambda \to n\pi^0_D$). For real data, (1.04 ± 0.35)% of events satisfied the requirements. For the MC sample consisting of background sources mixed with the above ratio, (1.57 ± 0.52)% of the events passed the photon veto cuts. These two numbers agreed within the error of 1 σ.

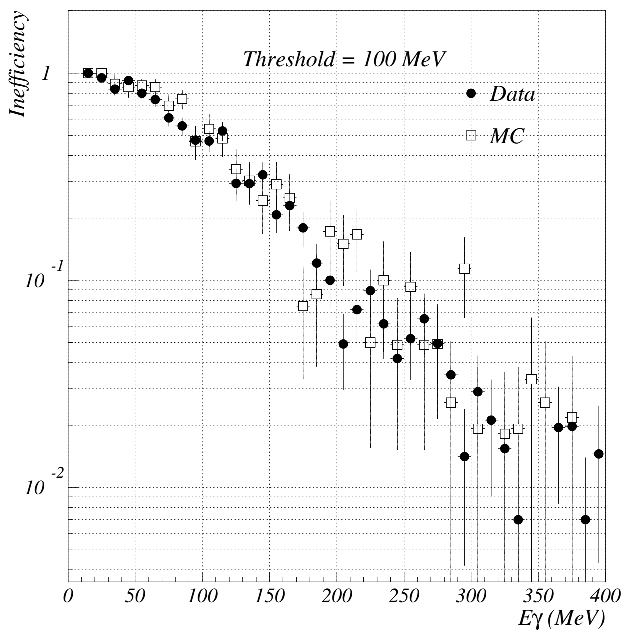

Figure 7.5: Measured inefficiency in the RC10 for photons as a function of incident photon energy. A threshold of 100 MeV is applied. The dots represent data, and open squares are for MC.

7.3 Background Shape

We confirm our understanding of the shape of backgrounds in this section. The consistency check was carried out by comparing some distributions between data and MC. In order to compare the distributions, the cut applied on the variable to be compared is removed. In addition, the other cuts may be relaxed to enhance statistics.

Figure 7.6 shows four kinematical variables in masked data and MC. In the four distributions, the number of events was normalized to the measured number of parents' decays, and each background shape in MC was summed up to one histogram(open) so that any discrepancy in the distributions between data and MC would suggest an existence of an unknown background source and/or an overestimation of the background level.

In the top left of Figure 7.6, the $m_{ee\gamma}$ distribution in the masked data is compared with MC. The requirement on p_t is changed to be $p_t < 160$ MeV/c, and the photon veto cuts were also relaxed(the cut was applied on only BA1 with a threshold of 8.5 GeV without distinction of the vertex position in x). You can see that the entire shape is in good agreement, and the long tails in both K_L and π^0 mass peak were well reproduced in the simulation. Since the MC distribution was normalized by the observed number of $K_L \rightarrow e^+e^-\gamma$ decays, the good agreement seen in the π^0 peak implies that the relative number of Λ decays, which dominates the π^0 mass peak, was correctly measured. In addition, the agreement in the side band region of π^0 mass indicates that $K_L \rightarrow \pi^0\pi^0\pi^0_D$ and $K_L \rightarrow \pi^0\pi^0_D$ yields were well understood. Besides the agreement, since we already confirmed the rejection power by the photon veto counters in Section 7.2, the estimation of background level for $K_L \rightarrow \pi^0\pi^0_D$ and $K_L \rightarrow \pi^0\pi^0\pi^0_D$ is concluded to be reliable.

Next, we look into the p_t as shown in the top right of Figure 7.6. One thing to note here is that the signal region in $(m_{ee\gamma}, p_t)$ plane is still masked off. All the cuts, except for p_t itself, are applied, thus the events plotted here should be dominated by $\pi^0 \rightarrow e^+e^-\gamma$ decays. There is a Jacobian

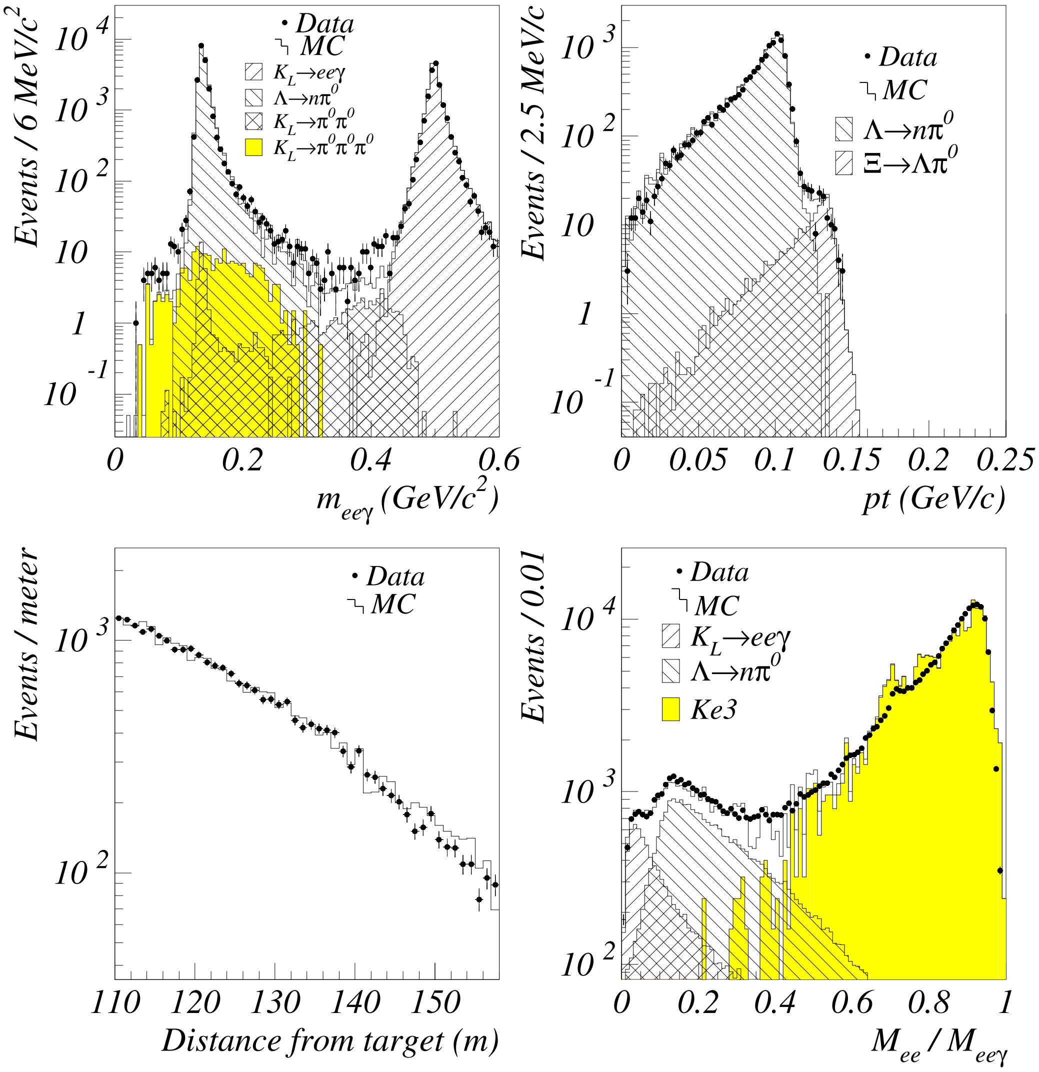

Figure 7.6: Comparison of distributions in masked data with MC. Note that the data used in these comparisons is masked data and thus the distribution in signal region cannot be compared. For all the four plots, the dots represent data and open histograms are for summed MC events. Top left: The $m_{ee\gamma}$ distribution with $p_t < 240$ MeV/c and with relaxed requirements for photon veto detectors. The cut is applied only on BA1 without using the vertex information in x with a threshold of 8.5 GeV. The other cuts are the same as final selection criteria. Top right: The p_t distribution. Except for the p_t requirement, all the other cuts are applied. Bottom left: The z distribution without the p_t requirement. Bottom right: The ratio of $m_{e^+e^-}$ to $m_{ee\gamma}$. The Dalitz kinematics cuts, $m_{ee\gamma}$ cut, p_t cut, and the particle identification with the TRD are removed.

peaks at p_t of 104 MeV/c arising from $\Lambda \to n\pi^0_D$, and a small shoulder at 135 MeV/c from Ξ decays. Checking the agreements in the high p_t tails from Λ and Ξ decays is important because the slope of the tails directly relates to the size of contamination of $\Lambda \to n\pi^0_D$ and Ξ decays to the signal region, and the p_t cut gave the most of suppression for $\Lambda \to n\pi^0_D$ and Ξ decays. In order to correctly reproduce the high p_t tails in MC, there are two crucial points. First, we need to know the correct amount of detector materials, as well as the spectrometer's resolution. For instance, a reduction of detector materials from 0.35% in radiation length, which was measured by performing special run[1] in the experiment [104], to 0.25% caused a 26% of shift in the slope of the exponential tail. The second was a momentum distributions in $\Lambda's$ and $\Xi's$. The good agreement seen in the figure implies the validity of our knowledge for the above two points. Although there is a small discrepancy at around $p_t \sim 106$MeV/c, most of the other points are consistent within a statistical error of 1 σ. This ensures the expected contamination of background events to the signal region. The excellent agreement for the entire shape implies the absence of unknown background source and the fair estimation for each source.

The z distribution of events in π^0 mass region, $125 < m_{ee\gamma}(\mathrm{MeV/c^2}) < 145$, with no p_t requirement is shown in the bottom left of Figure 7.6. The agreement between data and MC is excellent over the entire range. Since the events shown in this plot is completely governed by $\Lambda \to n\pi^0_D$ events, the agreement in the exponential slope indicates the validity of the simulation for Λ's.

We examined the understanding for K_{e3} events in the bottom right of Figure 7.6, which shows the ratio of $m_{e^+e^-}$ to $m_{ee\gamma}$ for subsample(19% of the full data) of masked data. To enhance K_{e3}'s, the cuts on $m_{ee\gamma}$, p_t, Dalitz kinematics, and the particle identification by the TRD were removed. There are three main components in this plot. The first one is K_{e3}'s dominating the high $m_{e^+e^-}/m_{ee\gamma}$ ratio region. The others are $\Lambda \to n\pi^0_D$ and $K_L \to e^+e^-\gamma$ events, in which the difference in the peak positions came from the momentum dependence of the detector acceptance. You can see a good agreement for the whole region. Hence, we are confident on the rejection factor for K_{e3}'s due to the Dalitz kinematics cuts.

7.4 Comparisons in Side Band

In the previous section, we visually confirmed our understanding for the contribution from each source. In this section, by counting the number of events in the side band region in $(m_{ee\gamma}, p_t)$ plane, and by comparing it between data and MC, we quantitatively verify the understanding of the shape of backgrounds.

Figure 7.7 shows p_t versus $m_{ee\gamma}$ in data near masked region with the number of events in each kinematical range from (a) to (i). The number in bold indicates the data, and the oblique for MC. The events in region (h) were 100% dominated by $\Xi \to \Lambda\pi^0_D$. More than 95% of the events in (i) arose from $\Lambda \to n\pi^0_D$, in which the vertex position was mis-measured to be more downstream than the actual one because of the poor vertex resolution in upstream region as discussed in Section 5.3, and the high yield in the upstream region. This contamination of the $\Lambda \to n\pi^0_D$ events also extended into region (f). In the kinematical region (f), 1/3 of the events came from $\Lambda \to n\pi^0_D$ and 2/3 of the events was from $\Xi \to \Lambda\pi^0_D$. The remaining few events in the range from (a) to (e) and (g) were governed by backgrounds from Ξ decays. For the whole range, the agreement was quite good. The numbers in every region were consistent between data and MC to within 1.2 σ of statistical error. The biggest discrepancy is seen in region (e), however, an observing zero events while expecting two events has a 14% of Poisson probability.

Furthermore, we compared the numbers in the same kinematical region by relaxing some cuts in order to obtain more confidence on our background estimation. The number of events in region

[1] The amount of detector materials was measured by counting the conversion probability of photons decayed from π^0's in $K_L \to \pi^0\pi^0\pi^0$.

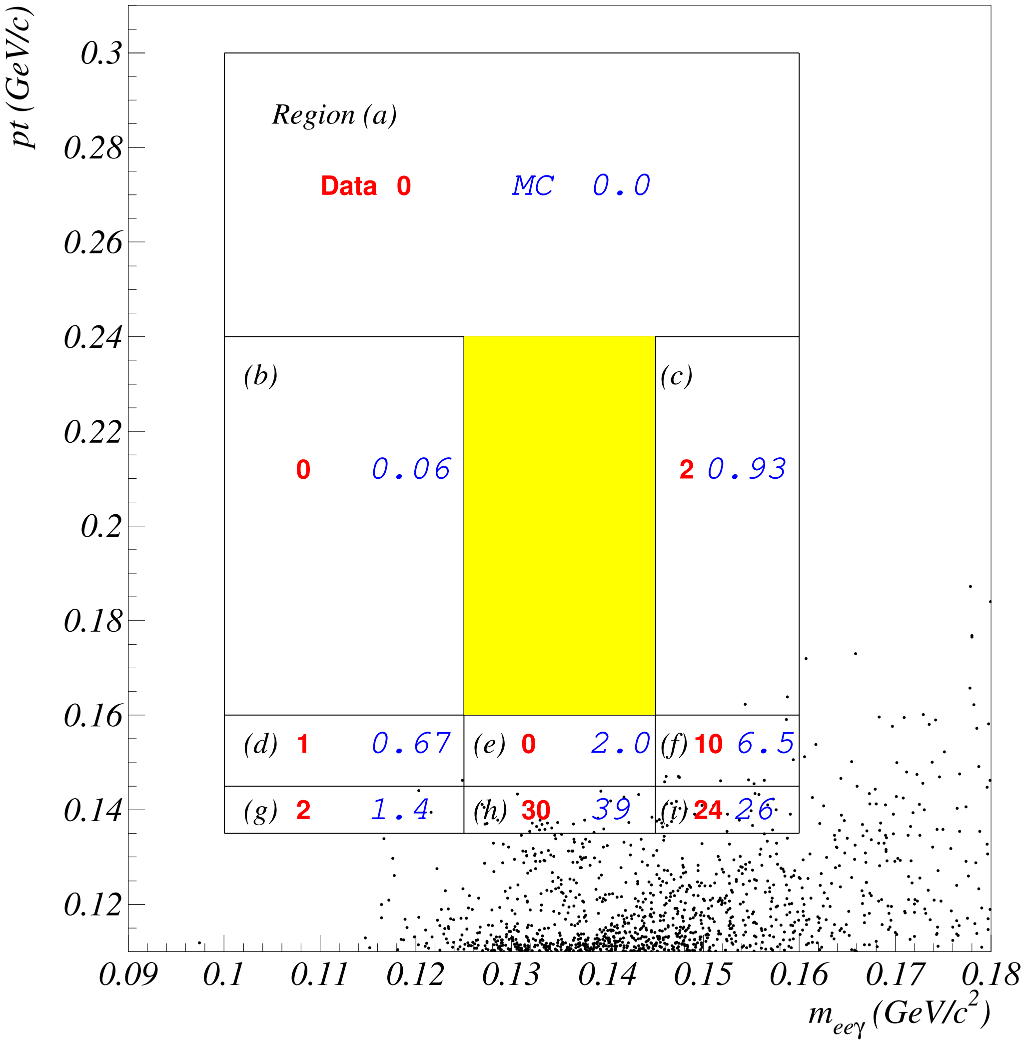

Figure 7.7: The p_t versus $m_{ee\gamma}$ in the masked data. The shaded area corresponds to the signal region. Also shown is the number of events in region (a) to (i). The left numbers(bold) represent data and right(oblique) for MC.

Table 7.3: Comparisons of the number of events in data with MC prediction in kinematical region (a) through (i) indicated in Figure 7.7. Four types of selection criteria are individually relaxed. For photon veto cuts, we applied a cut only on BA1 with a threshold of 8.5 GeV without using a vertex information with respect to x. To check a rejection power for backgrounds with extra tracks, all the requirements so-called charged veto cuts were removed. For the vertex quality, the requirements for σ_z, vertex χ^2 and offmag χ^2 were removed. The requirement for z was relaxed to be $110 < z(\mathrm{m}) < 158$.

Relaxed cut	(a)	(b)	(c)	(d)	(e)	(f)	(g)	(h)	(i)
Photon Vetos									
Data	3	4	6	6	6	19	4	74	46
MC	0.0	0.17	2.7	2.2	4.7	15	2.3	59	50
Charged Vetos									
Data	0	1	10	3	5	17	2	46	32
MC	0.0	0.11	2.4	1.5	2.6	9.9	3.0	49	31
Vertex Quality									
Data	2	1	9	6	5	22	12	42	71
MC	0.0	0.59	4.6	4.4	4.9	25	9.3	48	65
Z position									
Data	9	0	5	2	3	10	2	45	31
MC	0.09	0.13	2.5	1.6	2.9	9.4	1.6	47	33

(a) to (i) in data and MC prediction are summarized in Table 7.3, in which each type of cut was relaxed. Since a relaxation of one cut enhanced only one(or a few) type of background, we could find a source of discrepancy if it existed. On the other hand, equally relaxed cuts would simply decrease the yields in both data and MC, and we could not distinguish the discrepancy even if it existed. You can see excellent agreements between data and MC, except for high p_t region (a), (b) and (c), which was expected to be dominated by beam interactions at the vacuum window. The studies for the background estimation related to the beam interactions are described in Appendix D.

Based on the discussions since Section 7.2, we conclude that the background sources considering in this analysis should be good enough for the estimation of the background level in this search, and the shape of each source is correctly reproduced in MC.

Chapter 8

Systematic Errors

So far, we calculated the acceptances for signal and normalization mode, and collected a large number of $K_L \to e^+e^-\gamma$ sample. The background level in the signal region was evaluated. The remaining part in the analysis before opening the signal box is to estimate the size of systematic uncertainty on a branching ratio or on a single event sensitivity(we also considered the size of uncertainty on the background estimation, which is covered in Appendix D). Since we have not yet opened the signal box at this moment, here we only describe an error on the SES.

Since the SES is extracted from the relation shown in Equation 2.3, the systematic error arises from three components. First, it comes from branching ratios of normalization mode and π^0 Dalitz decay. The second is a statistical uncertainty associated with observed normalization events and MC sample to calculate the acceptances. The last one is a ratio of detector acceptances between signal and normalization modes.

The first two sources can be estimated with very straightforward manner as described in Section 8.1 and Section 8.2. The third component resulted from a discrepancy between data and MC, which was caused by an imperfect simulation for the detector's response, modeling of the decay kinematics, the kaon production scheme, theoretical calculation etc.. Section 8.3 discusses the source and size of such a disagreement, and accounts them into the systematic errors.

8.1 Branching Ratio

We used the PDG's value [13] as a branching ratio of normalization mode, $K_L \to e^+e^-\gamma$, which is $(9.1 \pm 0.5) \times 10^{-6}$. The uncertainty of 5.5 % becomes a part of systematic errors in the single event sensitivity of this search. Another branching ratio, $Br(\pi^0 \to e^+e^-\gamma)$, was also used to extract the SES. Again the PDG's value, $(1.198 \pm 0.032)\%$, was used in the calculation of the SES. It has an uncertainty of 2.7 %.

8.2 Data and MC Statistics

The statistics in the collected $K_L \to e^+e^-\gamma$ events contributed to the uncertainty on SES. We refer to the uncertainty from the statistics of the collected $K_L \to e^+e^-\gamma$ events as "statistical error", and the other uncertainties as "systematic error". Thus, the statistics in MC sample of signal and normalization modes was included into the systematic error.

The error coming from $K_L \to e^+e^-\gamma$ statistics was evaluated by a normal distribution, and those from MC statistics in acceptance calculations were evaluated by a binomial distribution. As summarized in Table 8.1, the collected data sample of $K_L \to e^+e^-\gamma$ gave the error of 0.792%. The MC statistics gave the additional contribution of 0.739% and 0.318% for $K_L \to \pi^0\nu\bar{\nu}$ and $K_L \to e^+e^-\gamma$, respectively.

Table 8.1: Statistical contribution on the single event sensitivity.

Real Data	Number of events		Stat. Error	
$K_L \to e^+e^-\gamma$	15,951		0.792%	
MC	No. MC generation	No. accepted events	Acceptance	Stat. Error
$K_L \to \pi^0\nu\bar{\nu}$	11,999,910	18,209	$0.152 \pm 0.00112\%$	0.739%
$K_L \to e^+e^-\gamma$	11,999,869	97,810	$0.815 \pm 0.00260\%$	0.318%

If we observe $K_L \to \pi^0\nu\bar{\nu}$ signal when we open the signal box in Chapter 9, we would quadratically add a statistical uncertainty due to an observed number of $K_L \to \pi^0\nu\bar{\nu}$ events to that on the SES to complete the estimation of the size of uncertainty on a branching ratio.

8.3 Acceptance Ratio

As discussed in Section 2.4, the normalization mode was carefully chosen to minimize the error on the acceptance ratio between signal and normalization modes. This section quantifies the error on the acceptance ratio, which is included into the systematic uncertainty.

Since the final states in signal and normalization mode are identical, most of the detection efficiency could be canceled out. However, two differences between $\pi^0 \to e^+e^-\gamma$ and $K_L \to e^+e^-\gamma$ decays might introduce a systematic error which is not canceled. First, total momenta, and thus momenta of final state particles, are different between the two modes, because undetected neutrinos in $K_L \to \pi^0\nu\bar{\nu}$ decays carry energy. The other is a small difference in the kinematical distribution with respect to Dalitz decay. The decay mechanism is the same, but the differences in the parent particles' mass and/or the momenta of the daughter particles could yield different shapes in Dalitz kinematical variables.

In order to study the uncertainty caused by the above differences, we considered the following as major sources of systematic error.

- The tracking inefficiency in the neutral beam region at the drift chambers.
- The energy measurement by the CsI calorimeter.
- The momentum measurement by the spectrometer.
- The particle identification by the TRD.
- The simulation of the E_{tot} system.
- Decay kinematics in Dalitz decays.
- Form factor in Dalitz decay generation in the MC.

The first five sources could be originated from a difference in the momentum, and the last two are associated with Dalitz kinematical variables.

The next subsections describe the evaluation of the uncertainty arising from each source.

8.3.1 Drift Chamber Inefficiency

Since a π^0 in signal decay and a K_L in the normalization mode had a different momentum spectrum and thus a slightly different opening angle between e^+e^-, the position dependence of the drift chamber efficiency might affect the acceptance ratio.

We observed a few percent discrepancy in the drift chamber illumination; the real data seemed to have more inefficiencies in the neutral beam region than that in MC. This is because: a long non-Gaussian tail in the SOD distribution in real data(Figure 3.6) was not well reproduced in MC due to a poor modeling of ionization density in the drift chamber gas; the tracking efficiency was sensitive to the SOD distribution by the requirement on the SOD in the tracking algorithm(the intrinsic chamber efficiency for each wire matched well, the disagreement was negligible). The resulting inefficiency can be seen in Figure 6.18 as a discrepancy of z distribution near the DC1.

To evaluate the size of error caused by this disagreement, we added artificial inefficiencies in the drift chamber simulation for the wires located in the neutral beam region. Table 8.2 lists the artificial inefficiency embedded in each chamber to match data. As the inefficiency increased, the

Table 8.2: Artificial inefficiency added in wires sitting in the beam area.

plane	Added inefficiency(%)	plane	Added inefficiency(%)
DC1X	2.5	DC3X	0.2
DC1X'	2.5	DC3X'	0.5
DC1Y	3.0	DC3Y	0.5
DC1Y'	3.0	DC3Y'	0.5
DC2X	1.0	DC4X	0.5
DC2X'	1.0	DC4X'	0.2
DC2Y	1.5	DC4Y	0.3
DC2Y'	1.5	DC4Y'	0.3

acceptance ratio, $A(K_L \to \pi^0 \nu\bar{\nu})/A(K_L \to e^+e^-\gamma)$ also increased. This is because the tracks from $K_L \to e^+e^-\gamma$ are more populated in the central region of the DC1, due to their higher momentum than that in $\pi^0 \to e^+e^-\gamma$. As a result of putting the intentional inefficiencies, the acceptance ratio changed by 1.89%. Hence, we determined the systematic uncertainty caused by the inefficiency in the tracking to be 1.89%.

8.3.2 Energy Measurement

The energy measurement of photons at the CsI calorimeter gave information to calculate kinematical variables such as an invariant mass etc.. In addition, the energy of charged particles measured by the calorimeter was used in the electron identification. Therefore, an energy dependence in the energy measurement with the calorimeter may cause a shift in the acceptance ratio.

We considered the following uncertainties which could change the acceptance ratio.

1. The overall energy scale.
2. The overall energy resolution.
3. The energy scale in the crystals around the beam holes, suffering from beam halo radiation damage.
4. The energy resolution in the crystals around the beam holes, suffering from beam halo radiation damage.

In order to estimate the size of uncertainty caused by the above sources, we put the artificial shift or smearing of energy in the analysis algorithm. In this way, it did not introduce a statistical uncertainty coming from the use of different set of MC sample. The modifications and the resulting changes in the acceptance ratio are listed in Table 8.3. The magnitude of intentional shift or

Table 8.3: Summary of systematic studies on the energy measurement.

What is changed	How much	Acceptance ratio	Variation
Cluster Energy Peak Shift	0.7%	0.18765	+0.800%
Cluster Energy Smearing	0.3%	0.18621	+0.0269%
Inner crystal Energy Peak Shift	1.0%	0.18614	−0.0107%
Inner crystal Energy Smearing	0.9%	0.18612	−0.0215%

smearing were determined from data by investigating the E/p distribution obtained run-by-run. Approximately, the maximum variation found in the data was used for the artificial tweaking.

By adding each error in quadratic, a total uncertainty due to the energy measurement in the acceptance ratio was determined to be 0.801%.

8.3.3 Momentum Measurement

A momentum dependence of the momentum measurement may cause a shift in the acceptance ratio because the momenta of charged particles were used to reconstruct kinematics and for the particle identification. The uncertainty in the acceptance ratio affected by the momentum measurement was evaluated by artificially tweaking the momentum scale, and the momentum resolution.

To determine the size of the artificial tweaking, we turned our attention to the invariant mass of $K_L \to \pi^+\pi^-$ events as well as the discrepancy of 0.2% in $m_{ee\gamma}$ distribution of $K_L \to e^+e^-\gamma$ as seen in Figure 6.17. The invariant mass of $K_L \to \pi^+\pi^-$ was reconstructed only from the spectrometer, and thus the disagreement between data and MC on the mass distribution was one of the measures for the magnitude of systematic contribution. Fitting with Gaussian around the peak, the data gave a mass of 497.59 MeV/c^2 with a width of 2.635 MeV/c^2, and thus a resolution of 0.530%. The mass peak in MC events was 497.64 MeV/c^2 with a width of 2.383 MeV/c^2(0.479% in resolution). Based on these numbers and the discrepancy of 0.2% in $K_L \to e^+e^-\gamma$ mass peak, the analysis algorithm was modified to embed the artificial tweaking for MC events. The magnitudes of the tweaking and its result are listed in Table 8.4. The quadratic sum was 0.0722%.

Table 8.4: Summary of systematic studies on the momentum measurement.

What is changed	How much	Acceptance ratio	Variation
Peak position	0.30%	0.18607	−0.0483%
Width	0.53%	0.18626	+0.0537%

8.3.4 Particle Identification by the TRD

The efficiency of TRD cut was evaluated from $K_L \to e^+e^-\gamma$ events in real data, assuming that the efficiency was independent of the electron momenta. Therefore, a momentum dependence of the efficiency for electrons in the TRD cut may lead to a shift in the acceptance ratio.

Using cleanly reconstructed $K_L \to e^+e^-\gamma$ events, i.e. the normalization sample without photon veto and charged veto cuts, we investigated the efficiency of our cut on the Pion Confidence Level(PCL). Table 8.5 lists the efficiency for an electron in the $K_L \to e^+e^-\gamma$ as a function of the track momentum. The efficiency was independent of the momentum for electrons with a momentum above 5 GeV/c within the statistical error; however, the efficiency for the electron with

Table 8.5: The efficiency of the cut on the TRD for single track in $K_L \to e^+e^-\gamma$ data sample. The PCL(Section 5.4.2) was required to be less than 0.01. The error is from statistics.

Momentum(P)	Efficiency(%)
$P < 5$	89.7 ± 1.6
$5 < P < 10$	94.4 ± 0.89
$10 < P < 15$	95.6 ± 0.98
$15 < P < 20$	95.5 ± 1.1
$20 < P < 25$	96.5 ± 1.4
$25 < P < 30$	96.1 ± 1.7
$30 < P < 35$	95.9 ± 2.0
all range	95.0 ± 0.43

a momentum less than 5 GeV/c was 3 σ apart from the average of 95.0%. Therefore, the shift of -5.3% was taken into account in the change of the acceptance ratio as shown below.

According to MC, the fraction of electrons with a momentum less than 5 GeV/c is 16.3% for $K_L \to \pi^0\nu\bar{\nu}$. It implies that the efficiency for single track in $K_L \to \pi^0\nu\bar{\nu}$ decreases from 95.0% to 94.1%. Accounting for two electrons are involved in the final states, the signal efficiency may be reduced from 90.3% to 88.6% for $K_L \to \pi^0\nu\bar{\nu}$. On the other hand, since the efficiency of 90.3% was estimated from real $K_L \to e^+e^-\gamma$ events, the efficiency for $K_L \to e^+e^-\gamma$ was still valid. Therefore, a possibility of the efficiency change from 90.3% to 88.6% was regarded as an error on the acceptance ratio. It was 1.88%.

8.3.5 E_{tot} Threshold

There was a possibility in the E_{tot} simulation to distort the acceptance ratio of $K_L \to \pi^0\nu\bar{\nu}$ and $K_L \to e^+e^-\gamma$, because of a difference in the momentum spectra. For the accepted events in the MC, $K_L \to \pi^0\nu\bar{\nu}$ has an average of 38 GeV in the total momentum, while $K_L \to e^+e^-\gamma$ has an average of 65 GeV. Therefore, an inconsistency in the E_{tot} simulation would give a major contribution to the error on the acceptance ratio[1].

To examine the E_{tot} simulation, we compared the measured number of K_L decays by applying a cut on a total energy measured by the calorimeter with different thresholds between 18 GeV to 26 GeV with an interval of 2 GeV. A change of the measured number would indicate a discrepancy in the E_{tot} threshold between data and MC. The resulting number of K_L decays was stable to within ± 0.06%, which was smaller than the statistical uncertainty of 0.792%. Therefore, we conclude that the contribution to systematic error from the E_{tot} system is negligible.

8.3.6 Dalitz Kinematics

Because of different shapes in Dalitz kinematical variables between $\pi^0 \to e^+e^-\gamma$ and $K_L \to e^+e^-\gamma$, a disagreement between data and MC in these variables would not be canceled out in acceptance ratio. We checked the consistency of the $\sum\cos\theta$ distribution between data and MC for $\pi^0 \to e^+e^-\gamma$ and $K_L \to e^+e^-\gamma$ decays by removing the Dalitz kinematics cuts.

Top of Figure 8.1 shows a superimposition of data and MC for the $\sum\cos\theta$ distribution in $\Lambda \to n\pi^0_D$. To enhance $\Lambda \to n\pi^0_D$ events, we selected events with π^0 mass($125 < m_{ee\gamma}$(MeV/c^2)

[1] Applying on offline threshold, with a few GeV higher than the E_{tot} threshold, on the total energy measured at the calorimeter could avoid the trigger bias. However, we did not do this so in order to maximize the signal acceptance because π^0 had a large acceptance in lower energy. For instance, we roughly lose 3% of signal with every 1 GeV increase of the threshold in total energy.

< 145) and p_t less than 100 MeV/c. The bottom is a ratio of the number of events in each bin between data and MC. The same distributions in $K_L \to e^+e^-\gamma$ events are shown in Figure 8.2.

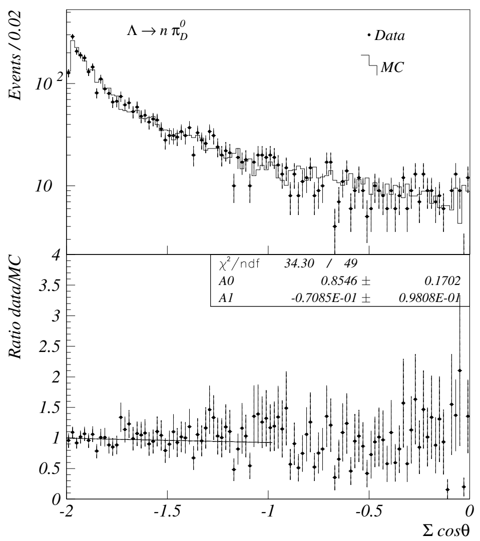

Figure 8.1: Top: The $\sum\cos\theta$ distribution in $\Lambda \to n\pi^0_D$. The Dalitz kinematics cuts are removed, and p_t is required to be less than 100 MeV/c. Dots represent data, and histogram is for MC. Bottom: The ratio of the number of events, data/MC.

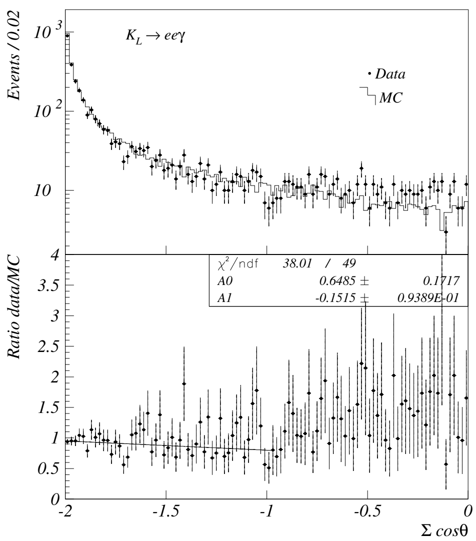

Figure 8.2: Top: The $\sum\cos\theta$ distribution in $K_L \to e^+e^-\gamma$. The Dalitz kinematics cuts are removed. Dots represent data, and histogram is for MC. Bottom: The ratio of the number of events, data/MC.

There are slightly different distributions between $\pi^0 \to e^+e^-\gamma$ and $K_L \to e^+e^-\gamma$, but the agreements between data and MC are excellent in both cases. To check the ratio numerically, we fit the ratio by a linear function for the range with the $\sum\cos\theta < -1$, avoiding the K_{e3} contribution. The slopes obtained from the linear fit are consistent with zero within an error of 1.6 σ. Hence, we neglect an error caused by different distributions in Dalitz kinematics between $\pi^0 \to e^+e^-\gamma$ and $K_L \to e^+e^-\gamma$.

8.3.7 Form Factor

The form factors are parametrized as

$$f(x) = \frac{1}{1-0.418x} + \frac{C\alpha^*}{1-0.311x} \times (\frac{4}{3} - \frac{1}{1-0.418x} - \frac{1}{9(1-0.405x)} - \frac{2}{9(1-0.238x)}),$$

with $C = 2.5$ for $K_L \to e^+e^-\gamma$ [88] where we assume α^* to be -0.28[2] [88, 89], and

$$f(x) = 1 + ax$$

with $a = 0.032$ for $\pi^0 \to e^+e^-\gamma$ [13] respectively. Figure 8.3 shows the Kroll-Wada spectrum with and without the form factor correction for $K_L \to e^+e^-\gamma$(a), and $\pi^0 \to e^+e^-\gamma$(b). Since virtual photon prefers to have smaller mass and the m_{ee} can be considered as the virtual photon mass, the distribution is enhanced in low mass region.

[2]The same parameter has been measured in also $K_L \to \mu^+\mu^-\gamma$[90]; however, the result does not agree with that of $K_L \to e^+e^-\gamma$.

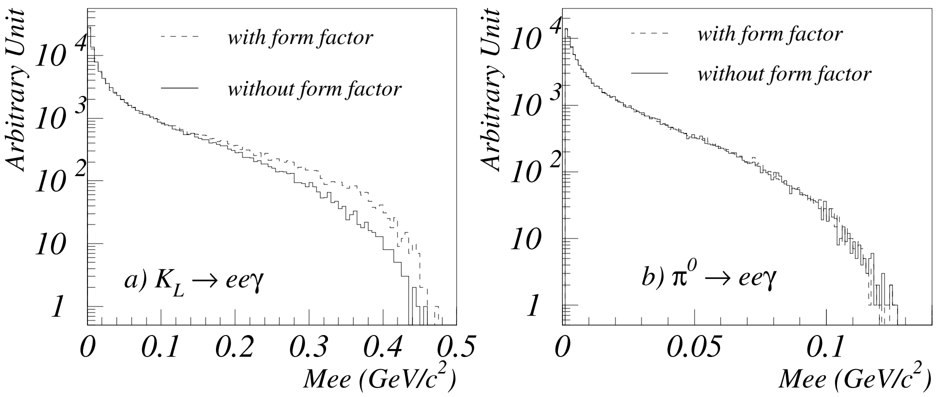

Figure 8.3: M_{ee} spectrum in $K_L \to e^+e^-\gamma$(a) and in $\pi^0 \to e^+e^-\gamma$(b) with form factor correction(dashed line) and without the correction(solid line). Since the M_{ee} can be considered as mass squared of virtual photon, it has a peak at zero and is enhanced in low mass region.

As discussed in Section 4.1.2, we used a constant form factor of unity in both π^0 and K_L Dalitz decay generations in the MC. We checked the acceptance shift due to the form factor using MC samples generated with the non-constant form factor.

As expected from Figure 8.3, a form factor in $\pi^0 \to e^+e^-\gamma$ did not affect the acceptance of $K_L \to \pi^0\nu\bar{\nu}$. The change in the acceptance from $0.1517 \pm 0.0011\%$ to $0.1520 \pm 0.0011\%$ is statistically negligible. Although we can see, in $K_L \to e^+e^-\gamma$, a small effect from a form factor in high $m_{e^+e^-}$ region in Figure 8.3, the change in the acceptance of $K_L \to e^+e^-\gamma$ was also within the statistical uncertainty. The original acceptance of $0.8151 \pm 0.0026\%$ changed to $0.8189 \pm 0.0026\%$ with the form factor.

Therefore, we conclude that the change in the acceptance ratio due to a form factor in $\pi^0 \to e^+e^-\gamma$ and $K_L \to e^+e^-\gamma$ is negligible.

8.4 Summary

Table 8.6 summarized the systematic uncertainty on the SES. The final uncertainty, which was obtained by summing each error quadratically, was dominated by an error on a branching ratio of $K_L \to e^+e^-\gamma$ and $\pi^0 \to e^+e^-\gamma$. The other contributions arose from a difference in momentum between K_L and π^0. The total error is 0.792% from the statistics of $K_L \to e^+e^-\gamma$ data sample, and 6.78% from the systematic uncertainty.

Table 8.6: Summary of the systematic error on the SES. We refer to the error coming from the statistics of $K_L \to e^+e^-\gamma$ events as "statistical error", and the remaining errors as "systematic error".

Source of Error	Size(%)
Statistical error	0.792
$Br(K_L \to e^+e^-\gamma)$	5.5
$Br(\pi^0 \to e^+e^-\gamma)$	2.7
MC statistics	0.805
DC inefficiency	1.89
Energy measurement	0.801
Momentum measurement	0.072
TRD efficiency	1.88
Total of systematic error	6.78

Chapter 9

Result and Discussion

This chapter describes the result on the $K_L \to \pi^0\nu\bar{\nu}$ search and discusses the implications of the new result.

So far, all the cuts have been applied for the masked data, the remaining background level has been estimated, and the systematic uncertainty on the search for $K_L \to \pi^0\nu\bar{\nu}$ decay has been evaluated. In Section 9.1, we finally open the signal box.

Since we collected a large number of normalization events, and calculated the detector acceptances for signal and normalization modes, we can now extract the single event sensitivity(SES) on this search based on the relation expressed in Equation 2.3. Thus, if there are signal events, we can calculate a branching ratio of $K_L \to \pi^0\nu\bar{\nu}$. In any case, we present the final result in Section 9.2.

Based on the new result, we first consider the physics implications in Section 9.3. We then discuss the new result from an experimental point of view in Section 9.4.

9.1 Inside the Signal Box

We carried out a careful background study, and estimated the remaining background level to be $0.12^{+0.051}_{-0.038}$ events. A statistically significant excess over the 0.12 events indicates a discovery of $K_L \to \pi^0\nu\bar{\nu}$ decay, and thus a direct CP violation within the Standard Model or new physics beyond the Standard Model.

Let us here discuss the "significant" excess. Because the contributions from $\Lambda \to n\pi^0_D$, $K_L \to \pi^0\pi^0_D$, and $K_L \to \pi^+\pi^-\pi^0_D$ were not involved in the total background level, the discussion consists of two parts: significant excess over the total expectation of 0.12 events; upper limits for those three background sources.

First, based on the expectation of 0.12 background events, we calculated the Poisson probabilities to observe n_{BG} background events as listed in Table 9.1. The criterion of "significance" involves human bias. Here, we assume 99.97% to be significant, which is 3.7 sigma effect in Gaussian distribution. This corresponds to observe 3.0 events.

Second, we calculated 99.97% confidence upper limits on the number of background events for $\Lambda \to n\pi^0_D$, $K_L \to \pi^0\pi^0_D$, and $K_L \to \pi^+\pi^-\pi^0_D$. They were 0.324, 0.081, and 0.081 events, respectively. The sum of the three limits was 0.486. Adding the 0.486 to the 3.0 events which comes from the total background level, we set an upper limit on the background level to be 3.5 events with a confidence level higher than 99.97%. Therefore, observing four events would be a significant excess in our assumption.

Finally, we opened the signal box as shown in Figure 9.1. It shows a scatter plot of p_t and $m_{ee\gamma}$

Table 9.1: Poisson probabilities to observe n_{BG} background events while 0.12 background events are expected.

n_{BG}	Poisson Probability
0	0.8869205
1	0.1064304
2	0.0063858
3	0.0002554
4	0.0000077
5	0.0000002

in data after applying all the cuts except those of p_t and $m_{ee\gamma}$. The signal box is also drawn in the figure. No events were observed in the signal region[1]. As a reference, the same distribution

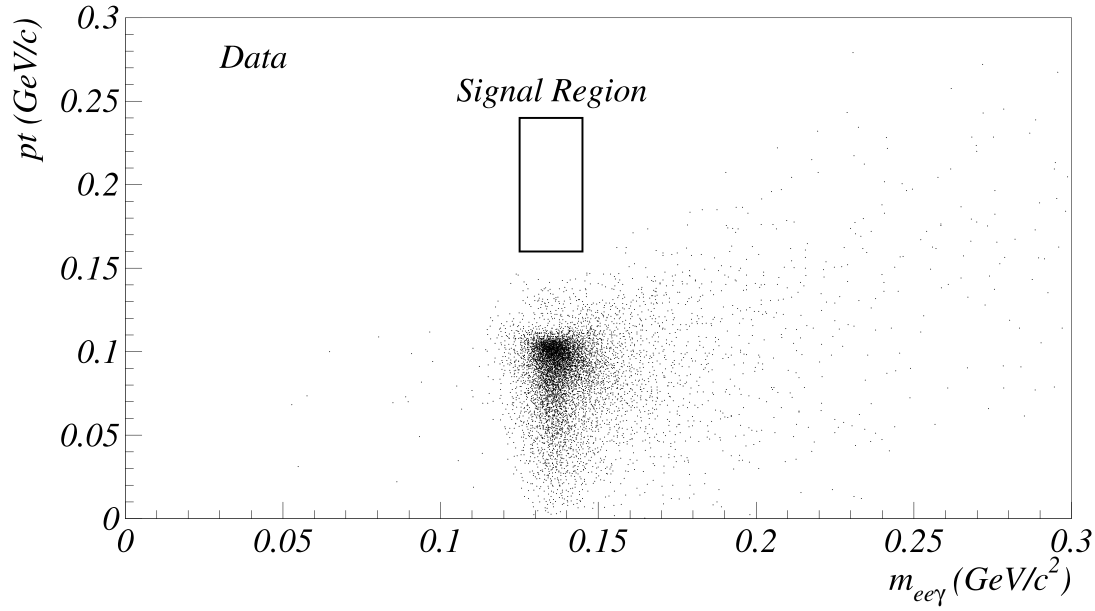

Figure 9.1: The final p_t versus $m_{ee\gamma}$ distribution in data with all the cuts. The defined signal window is indicated by a box.

in MC backgrounds is shown in Figure 9.2. These two distributions are visually identical, which implies the validity of our understanding of the background. More discussion on the background study using events in the signal region with relaxed cuts is covered in Appendix D.

[1] If we had observed "significant" number of events in the signal region, in order to claim them to be signals or to find a new source of backgrounds, we would need more background studies. If we had observed non-significant number of events in the signal region, again we would need more background studies to identify the source of backgrounds. In any case, it would take a year, five years... to publish a thesis.

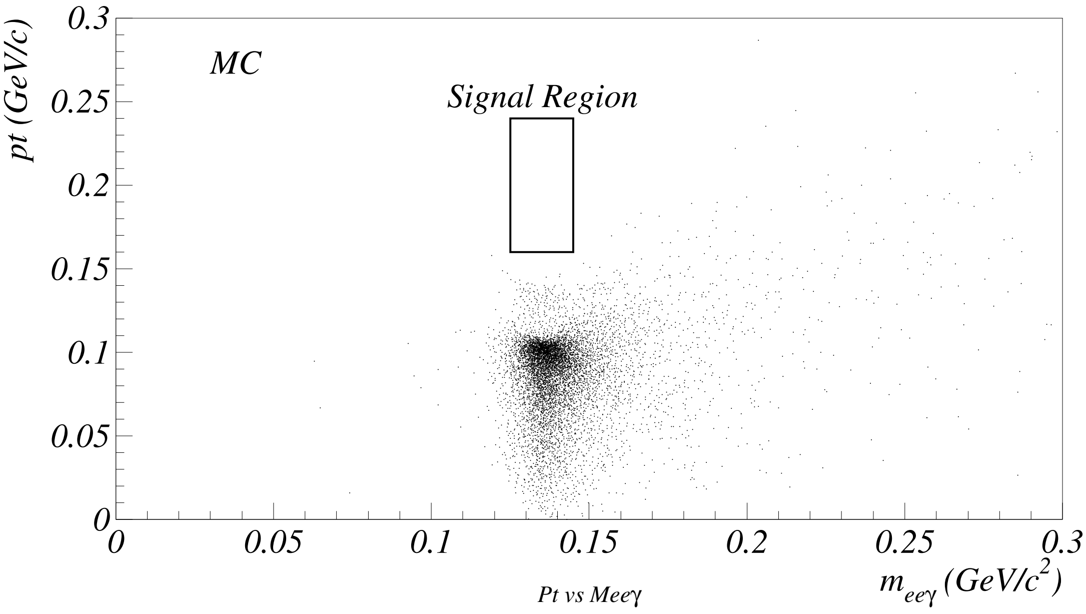

Figure 9.2: The p_t versus $m_{ee\gamma}$ in MC after all the requirements.

9.2 Result

We observed 15,951 $K_L \rightarrow e^+e^-\gamma$ events. Based on the calculations described in Chapter 6, the acceptance ratio of $K_L \rightarrow \pi^0\nu\bar{\nu}$ to $K_L \rightarrow e^+e^-\gamma$ was computed to be 0.186. Using a world average of $Br(K_L \rightarrow e^+e^-\gamma)$ and $Br(\pi^0 \rightarrow e^+e^-\gamma)$, we determined the single event sensitivity(see Equation 2.3) on this search to be

$$\begin{aligned} SES &= \frac{1}{A(K_L \rightarrow \pi^0\nu\bar{\nu})} \times \frac{A(K_L \rightarrow e^+e^-\gamma)}{N(K_L \rightarrow e^+e^-\gamma)} \times \frac{Br(K_L \rightarrow e^+e^-\gamma)}{Br(\pi^0 \rightarrow e^+e^-\gamma)} \\ &= [2.56 \pm 0.02(\boldsymbol{stat.}) \pm 0.17(\boldsymbol{sys.})] \times 10^{-7} \ . \end{aligned}$$

Since no events consistent with signal were observed with 0.12 expected background events, an upper limit of the branching ratio was set to be

$$Br(K_L \rightarrow \pi^0\nu\bar{\nu}) < 5.88 \times 10^{-7},$$

at the 90% confidence level(C.L.). This result represents an improvement of a factor of 98 over the current limit by the PDG [13], and a factor of 3 over the recent preliminary[2] limit reported by the KTeV collaboration(see Section 9.4.2) [105].

As discussed in Section 9.1, we had needed 4 signal events to claim a discovery of $K_L \rightarrow \pi^0\nu\bar{\nu}$ decays, based on the assumption that 99.97% was significance. In this case, $Br(K_L \rightarrow \pi^0\nu\bar{\nu})$ would be $2.56 \times 10^{-7} \times 4 = 1.0 \times 10^{-6}$. This is considered as a sensitivity to "discover" $K_L \rightarrow \pi^0\nu\bar{\nu}$ decays in our experiment, taking into account the size of the background level which is assumed to be correct.

[2]The result was submitted to Physical Review Letters, and it is under the judge right now when the author is writing this part.

9.3 Discussion on Physics

In this section, we discuss the new result by comparing it with the theoretical predictions described in Chapter 1.

The Standard Model

No $K_L \to \pi^0 \nu\bar{\nu}$ events were observed. Taking into account the Standard Model expectation, non-observation of $K_L \to \pi^0 \nu\bar{\nu}$ at the sensitivity of $O(10^{-7})$ is consistent with the Standard Model. If we take the Standard Model prediction seriously, searches with at least 4 orders of magnitude better sensitivity than this search will be required to observe $K_L \to \pi^0 \nu\bar{\nu}$ decays.

Let us now translate the new result to a constraint on η. Using Equation 1.55 with the most recent values of A, λ and top quark mass used in reference [31], our 90% C.L. result, $Br(K_L \to \pi^0 \nu\bar{\nu}) < 5.9 \times 10^{-7}$, indicates that η is less than 52. If we translate the error of 6.8% on the SES to the error for a limit on η, because the branching ratio of $K_L \to \pi^0 \nu\bar{\nu}$ is linear to η^2, the error of the limit on η is regarded as 3.4% by ignoring the uncertainties in A, λ and top quark mass[3]. This shows the potential in a measurement of $Br(K_L \to \pi^0 \nu\bar{\nu})$ to offer a clean determination of η. Although it is very loose, we also emphasize that our limit is a direct constraint on η, unlike the other indirect restrictions. Since our new upper limit on η is far away from the most probable value, 0.33 [34], a discovery of $K_L \to \pi^0 \nu\bar{\nu}$ signal at a sensitivity of $O(10^{-7})$ would strongly suggest a new effect outside the framework based on the CKM matrix. Our limit on $K_L \to \pi^0 \nu\bar{\nu}$ is consistent with the other constraints on the CKM parameters.

The Superweak Model

Because no evidence for a direct CP violation was found, the Superweak Model cannot be ruled out. However, it does not mean the confirmation of the Superweak Model, either. It is difficult to positively identify the Superweak Model because there is no direct effect, either in K decays or in B decays. Therefore, the Superweak Model could survive until it would be ruled out by a discovery of the direct CP violation, or could be indirectly confirmed by an absence of the direct CP violating effect in the region predicted by the Standard Model. This implies that searches for $K_L \to \pi^0 \nu\bar{\nu}$ with a sensitivity of the Standard Model prediction or better could still be a better way to discriminate between the two models.

Lepton Flavor Violation

As discussed in Section 1.3.2, if lepton flavor is violated, a larger branching ratio of $K_L \to \pi^0 \nu\bar{\nu}$ than that of the Standard Model is predicted through the dominant CP conserving contributions. Since we did not find any evidence of the larger decay rate than the Standard Model prediction, our result is consistent with the lepton flavor conservation.

General Discussion

There is a theoretical upper limit of $Br(K_L \to \pi^0 \nu\bar{\nu})$ to be less than 1.1×10^{-8} as mentioned in Section 1.3.2. An observation of $K_L \to \pi^0 \nu\bar{\nu}$ with the SES of 2.6×10^{-7} would be a strong evidence of really new physics. Unfortunately, our new upper limit is consistent with their theoretical prediction, and would not frighten the theorists.

[3] Such assumption will be valid in the future because these uncertainties(currently 36% in total) will likely be further reduced, in contrast to the remaining theoretical uncertainties in the other measurements, like $B_d^0 - \bar{B}_d^0$ mixing.

Since their estimation uses the isospin symmetry relation, $A(K_L \to \pi^0\nu\bar{\nu})/A(K^+ \to \pi^+\nu\bar{\nu}) = 1/\sqrt{2}$, with an isospin breaking factor of 0.954 [44], the consistency of our result with their expectation indicates the validity of theoretical treatment of isospin relation between the two decay modes, which is often used in the numerical prediction for $Br(K_L \to \pi^0\nu\bar{\nu})$. Therefore, the current numerical prediction in $Br(K_L \to \pi^0\nu\bar{\nu})$ can be considered as reliable, with only uncertainty in the CKM parameters.

The other possibility to confirm the direct CP violation is a precise measurement of ϵ'/ϵ as described in Section 1.1.2. Non-zero value of the ϵ' would be an evidence of direct CP violation, however, cancellation between two penguin diagrams(one with γ or Z, and the other with a gluon) reduces the size of ϵ'. Recent theoretical calculations, including large uncertainty arising from charm mass and from QCD, prefer a small value of a few times 10^{-4} or even a negative value. If the ϵ' could not be found to be non-zero, to reduce the experimental error by another order of magnitude will be required, which is very challenging. In such a case, a search for $K_L \to \pi^0\nu\bar{\nu}$ would provide another opportunity to discover direct CP violation in the context of the Standard Model.

9.4 Discussion from Experimental Point of View

This section discusses the new result from experimental point of view.

We compare two experimental approaches for identifying π^0's, Dalitz mode and two photon mode, based on the new result. It begins with a summary of the search described in this thesis, which is covered in the first subsection. In the next subsection, we briefly describe a special run for a $K_L \to \pi^0\nu\bar{\nu}$ search with $\pi^0 \to \gamma\gamma$ mode. Section 9.4.3 describes the pros and cons in each technique, and compare the two approaches. In Section 9.4.4, a prospect for $K_L \to \pi^0\nu\bar{\nu}$ searches in the future deduced from the discussion is presented. In our event selection, we optimized the criteria by using a technique called Blind Analysis. We mention about it at the last subsection.

9.4.1 A Search with $\pi^0 \to e^+e^-\gamma$

In this experiment, the biggest contribution in the backgrounds came from beam interactions in the vacuum window(Table 7.2). The Ξ decays and $K_L \to \pi^0\pi^0\pi^0_D$ also had a contribution of the same order of magnitude. Nobody considered such backgrounds as beam interactions with the vacuum window or Ξ decays in the Dalitz method before the experiment. We found another interesting background, $\Xi \to \Lambda\pi^0_D$, where Λ does not decay in the vacuum volume and hits the photon veto counter(BA) located downstream of the beam holes of the CsI calorimeter. This situation is similar to $\Lambda \to n\pi^0_D$, but this decay has a much higher limit on p_t, 135 MeV/c. In order to suppress these backgrounds, our selection criteria had to be tight, and thus, the signal acceptance was three times lower than the proposed acceptance [109]. In the future experiments, one should be aware of these backgrounds.

Next, let us estimate improvements one could attain in the current KTeV apparatus. Here, we assume that all the background sources have been covered in this thesis. For the two major background sources, beam interactions and Ξ decays, we expect to achieve one order of magnitude better suppression by imposing tighter z and p_t cuts with a cost of 26% signal loss in total, as explained in Appendix E. Assuming the same selection criteria except for the z and p_t cuts, all the other backgrounds we considered in Chapter 7 will increase in linear to the number of K_L decays. With 10 times more K_L decays, the expected number of background events would be $\sim$0.5 in total with a SES of 3×10^{-8}. Therefore, we will be able to lower the limit by one order of magnitude with π^0 Dalitz mode if the current apparatus would be used without any modifications.

How many days then do we need to accumulate ten times more statistics? Since 46 days of data taking with a proton intensity of 5×10^{12} per spill and with a 100% live accelerator performance corresponds to our collected statistics, it will take at least 460 days to reach one order better sensitivity. Assuming 50% live time in the accelerator realistically, it would take 2.5 years to accumulate the statistics for the sensitivity of $\sim 3 \times 10^{-8}$.

9.4.2 A Search with $\pi^0 \to \gamma\gamma$

Using the technique described in Section 2.1.2, a one day special run dedicated for $K_L \to \pi^0\nu\bar{\nu}$ search with two photon mode was carried out. This run concentrated the data acquisition on $K_L \to \pi^0\nu\bar{\nu}$ trigger with different beam parameters from nominal run described in Chapter 3. To achieve a better p_t resolution, we used only one K_L beam with a reduced beam size of 0.065 μstr(compared to 0.25 μstr for nominal run), because lack of vertex information required to assume the π^0 decay point to be at the center of the beam to calculate p_t. In order to achieve more hermetic photon veto coverage, an additional photon veto counter was installed at z = 122.2 m. It was located inside the vacuum tank as a wall with 9.0 cm $\times$ 9.0 cm beam holes[4]. Lowering thresholds in the photon veto detectors with lower accidental activities from the small beam helps to reduce backgrounds with extra photons, such as $K_L \to \pi^0\pi^0\pi^0$, $K_L \to \pi^0\pi^0$, Ξ decays, etc.. In order to reduce accidental activities, the proton intensity incident on the target was reduced to 3.5×10^{12}. In order to get a larger K_L/neutron ratio, an extra absorbers were installed.

The result just came out in reference [105]. No signal was observed and an upper limit was given as

$$Br(K_L \to \pi^0\nu\bar{\nu}) < 1.6 \times 10^{-6} ,$$

at the 90% confidence level. This result was limited by the existence of background, which is attributed to beam neutron interactions in the vacuum window. A contribution from the other sources is also expected to be much larger than that in the Dalitz mode. At the single event sensitivity of 4.0×10^{-7}, 3.7 background events are expected, and one event was observed.

9.4.3 Comparison of the Experimental Methods by Utilizing KTeV Detector

Before starting a comparison between the two experimental techniques, there is one thing to note. The detector performance in the two photon mode was optimized for the $K_L \to \pi^0\nu\bar{\nu}$ search at the run with low intensity beam(3.5×10^{12} protons per spill) and with the extra absorber, resulting in 0.3 MHz K_L and 0.7 MHz neutron flux at BA. On the other hand, the data in the Dalitz mode was collected at higher intensity(4 or 5×10^{12} protons per spill) beam without such extra absorbers, resulting in 12 MHz K_L and 44 MHz neutron flux at BA. The resulting difference can be seen in photon veto detectors, for example. Figure 9.3 shows BA1 energy distribution due to accidental activities in the search with $\pi^0 \to e^+e^-\gamma$ mode and $\pi^0 \to \gamma\gamma$ mode. Because of the lower average energy deposited in BA in the two photon mode, the applied threshold in the two photon mode was much lower than that in the Dalitz mode. If we applied the same set of thresholds as the two photon mode, we would have lost more than 96%(more than 90% come from BA) of signal in the search with Dalitz mode.

Now let us start the comparison of the two techniques with a description of pros and cons in each technique. In the following comparisons, we assume the current KTeV apparatus without any modifications. More discussion for the future experiments will be summarized in the next subsection.

[4] The geometrical configuration along z was the same as RC.

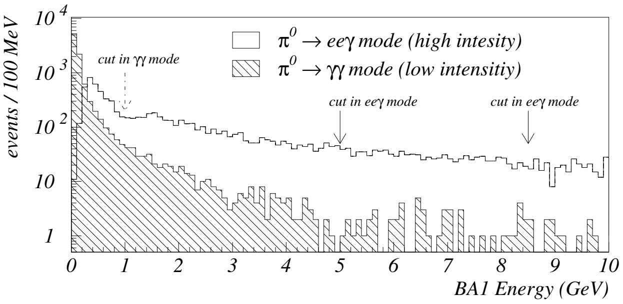

Figure 9.3: BA1 energy distribution in Accidental trigger. Open histogram represents the Dalitz mode: we typically had 5×10^6 K_L decays per spill, and shaded one for the two photon mode: typically 1×10^5 K_L decays per spill. Solid arrows show the cuts in π^0 Dalitz mode(the cuts were separately applied on the vertex side and the other side). Dashed arrow shows the cuts in π^0 two photon mode.

There is a statistical advantage in the two photon mode compared to the Dalitz mode, due to 80 times larger branching fraction of π^0. Also the signal acceptance is one order of magnitude larger than that in the Dalitz mode because the narrow opening angle of e^+e^- in the Dalitz decay makes the track finding and vertex finding inefficient.

On the other hand, the Dalitz mode has an advantage in the background suppression. While 3.7 background events are expected in the two photon mode with a SES of 4.04×10^{-7}, only 0.07 background events are expected in the Dalitz mode at the same sensitivity. This difference of a factor of 50 in the background level comes from the extra constraint of vertex information, which enabled us to reconstruct $m_{ee\gamma}$ for a positive identification of π^0. In contrast, in the two photon mode, vetoing extra photons or neutrons was the only tool to suppress backgrounds, and we could not positively select the π^0 decays. Let us discuss a beam neutron background, for instance, which is the most serious background in both modes. In the two photon mode, the remaining event came from a production of multiple π^0's, mainly two π^0's, in which two photons missed both the calorimeter and the photon veto counters, and a wrong pairing of two photons was used to calculate the z position(Figure 9.4). Due to this mis-pairing, both the z and p_t were incorrectly measured. The characteristic of this event is similar to $K_L \to \pi^0\pi^0$, but the yield is expected to be one order of magnitude larger than $K_L \to \pi^0\pi^0$. In the Dalitz mode on the other hand, a wrong selection of a photon was strongly suppressed because the vertex position was determined from charged tracks, and it gives us a capability to identify a π^0 by the invariant mass(Figure 9.4). Therefore, the remaining events mostly had a right combination of $e^+e^-\gamma$, which could be removed by the requirement on the z position. Taking into account the much higher thresholds on the photon veto detectors and drift chamber hits in the Dalitz mode[5], the net benefit from vertex information is much larger than the factor of 50.

In summary, the statistical advantage in the two photon mode is completely canceled out by a background rejection power of the Dalitz mode. Without any changes in the apparatus, there is still a small room to achieve better sensitivity in the Dalitz mode by tightening the selection criteria. On the other hand, the result from the two photon mode was already limited by the backgrounds coming from beam interactions with the detector materials. In addition, the search with $\pi^0 \to \gamma\gamma$ method needs a special run condition which cannot be shared with other physics trigger. Therefore, the Dalitz mode is a better method to search for $K_L \to \pi^0\nu\bar{\nu}$ under the constraint that we use the

[5]For instance, the tighter cuts on the photon veto counters in the two photon mode is expected to give at least one order of magnitude better suppression for backgrounds coming from $K_L \to \pi^0\pi^0\pi^0_D$ in the Dalitz method.

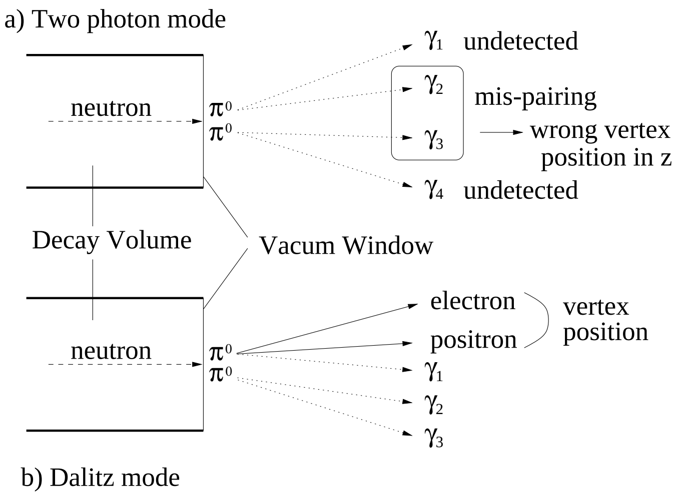

Figure 9.4: Schematic picture of the multi π^0's production due to beam interactions at the vacuum window. (a):Mis-pairing of photons(γ_2 and γ_3) caused a wrong measurement of vertex position in z in the two photon mode. (b):The vertex position was determined from e^+e^-, and the wrong coupling of photon(γ_2 or γ_3) to e^+e^- was suppressed by the $m_{ee\gamma}$ requirement.

current KTeV apparatus.

9.4.4 Future Experiments

The comparison described so far in this section concentrated on the use of the current KTeV configuration. Now we briefly consider future experiments without such a constraint.

First, let us estimate the statistics needed for the accuracy, which was discussed in Section 1.3.1, in the determination of CKM parameters. If we consider only statistical uncertainty, an observation of 25 events can determine η with an accuracy of 10%. Therefore, the single event sensitivity of at least 1.2×10^{-12} is required to be comparable with the strategy in B factories.

In order to reach above sensitivity, we need at least five orders of magnitude better sensitivity. Based on the discussion in Section 9.4.1, even with 30 times more K_L decays per unit time, which is proposed in a future experiment [106], it would take $O(10^3)$ years for the Dalitz method to reach the level. On the other hand, the search with $\pi^0 \to \gamma\gamma$ could allow us to reach the level in roughly 1 year of running with the use of such higher flux beam. These are the reasons why future experiments [106, 107, 108] propose to use the two photon mode.

However, it also implies the necessity of at least six orders of improvement in background suppression in the two photon mode. The ideas to achieve such a huge suppression are: veto events involving extra particles, such as $K_L \to \pi^0\pi^0$, with much higher efficiency, which obviously requires more efficient and completely hermetic photon veto system; reduce detector materials between the decay region and the calorimeter, which directly relates to the background level caused by beam interactions. For such purpose, the calorimeter(at least the active area) should be installed in the vacuum region or placed right downstream of a vacuum window.

A construction of new photon veto counters located downstream of the calorimeter's beam holes, is another critical issue. The BA, which was the photon veto counter located downstream of the beam holes in our experiment, suffered from a large number of accidental activities from beam neutrons and non-decayed K_L's in the Dalitz mode. If one will achieve single event sensitivity of

1×10^{-12} in a year, 10^6 K_L decays per second will be needed assuming an acceptance of 3%. Using the same beam parameters as our experiment, 50 MHz K_L and 125 MHz neutron flux at the photon veto counter will be expected(In reality, a future experiment at Fermilab will expect a neutron flux of 200 MHz or 500 MHz). In the environment of two or three orders of magnitude higher neutron flux than that in the two photon mode, the same thresholds as used in the two photon mode will be required(Section 9.4.3). Therefore, it will be crucial to build a hadronic transparent photon veto counters with keeping a high detection efficiency for photons.

We summarize the experimental status on searches for a $K_L \to \pi^0\nu\bar{\nu}$ decay. Figure 9.5 shows the experimental upper limit on $Br(K_L \to \pi^0\nu\bar{\nu})$ in two published results [64, 65], one preliminary result [105], and our new result, as a function of date. Also shown is the Standard Model prediction. It took 6 years to gain 3 orders of magnitude in single event sensitivity. To simply extrapolate

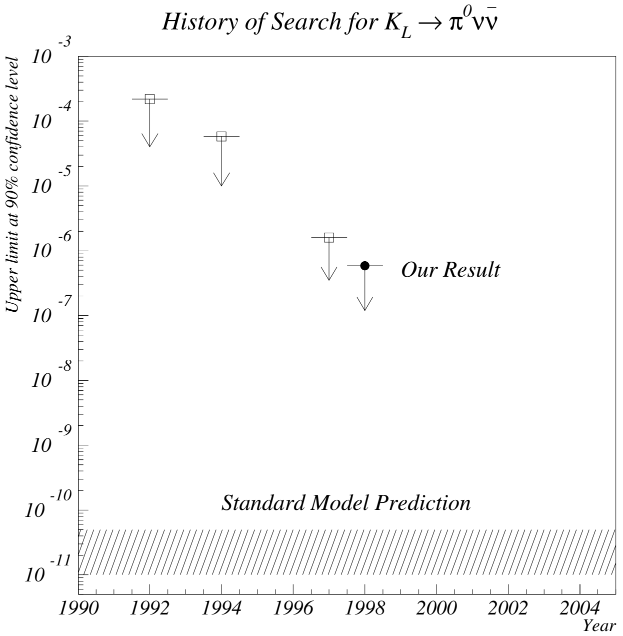

Figure 9.5: History of $K_L \to \pi^0\nu\bar{\nu}$ search. Open squares show previous limits, and a black circle shows our new limit. The hatched region is current theoretical prediction from the Standard Model.

the slope obtained from the four experiments, the sensitivity might reach the Standard Model prediction in 8 years. Or recent particular interests and efforts for future experiments to search for $K_L \to \pi^0\nu\bar{\nu}$ could make the slope steeper. The other scenario is a discovery of $K_L \to \pi^0\nu\bar{\nu}$ before reaching the Standard Model prediction, which is the most interesting scenario.

9.4.5 Blind Analysis

A bias from theoretical prediction could conceal a discovery of new phenomena coming from really new physics. Avoiding such a bias is also important when the sensitivity is close to the theoretical prediction, and one has to judge whether the remaining event is signal or background. In order to avoid such a dangerous bias, the selection cuts were determined by background studies using MC and by evaluating only the side band region in data. To be exact, we made a data sample, which did not contain any events in the signal window on p_t vs $m_{ee\gamma}$ plane, for the optimization of selection criteria. The recent discovery of one $K^+ \rightarrow \pi^+ \nu\bar{\nu}$ event reported by BNL 787 collaboration was made by using such a technique called Blind Analysis.

Table 9.2 shows results of recent experiments which looked for rare decays in neutral kaon system. There are three groups which gave the current upper limits on the list by the PDG. It seems that each experimental group has different policy to determine the selection criteria.

Table 9.2: The observed events and expected background level in recent experiments on rare kaon decay search, in which they did not find a signal and set upper limits. The results from three experimental group, A, B and C, are listed. Different line from same group represents different decay mode or updated one.

Experiment	Observed events	Expected Backgrounds
A mode1	0	2.1
A mode2	0	negligible
A mode3(result1)	0	1.0
A mode3(result2)	1	3.7
Total in A	1	6.8
B mode4	0	< 0.15
B mode5	0	not estimated
Total in B	0	< 0.15
C mode6	7	6.7
C mode7	3	2.2
Total in C	10	8.9

Group B required criteria tight enough to suppress the background, and the result seems to be statistically limited, whereas the criteria in group C are too loose, or their result might be limited by backgrounds. Interesting results can be seen in group A. It is difficult to judge whether the result is statistical or background limited, and is not clear how the criteria were chosen. Each measurement looks statistically consistent, but by combining the four results, the probability of observing < 1 events while expecting 6.8 events is only 0.8%. Due to the fewer observed events than the expected numbers, they could have set upper limits closer to their single event sensitivities.

If there were no human biases, optimization of selection criteria after looking at data in signal region would not have any problems. However, it seems difficult to remove any bias, and to decide a fair selection strategy. Once we look at data in a signal window, removing such bias must be more difficult. It could be especially true when the discovery could upset a common sense in the world, like Copernicus. Therefore, the Blind Analysis is one of the best methods to optimize the selection criteria in rare decay searches.

Chapter 10

Conclusion

We searched for a rare decay, $K_L \to \pi^0 \nu \bar{\nu}$, with a Single Event Sensitivity of 2.6×10^{-7}. No signal evens were observed. An upper limit on the branching ratio was set to be

$$Br(K_L \to \pi^0 \nu \bar{\nu}) < 5.9 \times 10^{-7} ,$$

at the 90% confidence level. This represents an improvement of a factor of 98 over the current limit listed by the PDG, and a factor of 3 over the recent preliminary result.

We understood both the sources and levels of background in our sensitivity. Although we did not observe $K_L \to \pi^0 \nu \bar{\nu}$ events in this experiment, we believe that the understanding of backgrounds and the idea born in this analysis will help future searches for $K_L \to \pi^0 \nu \bar{\nu}$. Those experiments would reach the sensitivity of the Standard Model prediction or could discover new physics beyond the Standard Model.

In conclusion, this experiment did not find any evidence of direct CP violation. The result of the upper limit on branching ratio is consistent with the Standard Model prediction. At the same time, we still cannot rule out the Superweak Model. Taking into account the Standard Model expectation, our result indicates that phenomena arising from beyond the Standard Model was not observed.

Appendix A

$K_L \to \pi^0 e^+ e^-$ decay

In this appendix, we discuss contributions to a CP violating decay $K_L \to \pi^0 e^+ e^-$ with the framework of the Standard Model.

Given that K_L is a superposition of the K_1 and K_2, there are three contributions to $K_L \to \pi^0 e^+ e^-$ decays as shown in Figure 1.6. The process (a) in Figure 1.6 is a CP conserving contribution. The CP odd K_2 decays into CP odd final state via $\pi^0\gamma^*\gamma^*$ intermediate state. Recent experimental results [110, 111] on $\gamma\gamma$ mass spectrum prefer chiral perturbation theory instead of Vector Meson Dominance(VMD) model [27]. In the chiral perturbation theory, the CP conserving contribution to a branching ratio of $K_L \to \pi^0 e^+ e^-$ is expected to be less than 10^{-12}.

The process (b) in Figure 1.6 is an indirect CP violating contribution. The decay $K_1 \to \pi^0\gamma^*$ is a CP allowed decay and its rate can be estimated by measuring the rate of $K^+ \to \pi^+ e^+ e^-$. Based on the measurement [112] of

$$Br(K^+ \to \pi^+ e^+ e^-) = (2.99 \pm 0.22) \times 10^{-7}, \tag{A.1}$$

the upper limit on the indirect contribution is estimated [28, 29] as;

$$Br(K_L \to \pi^0 e^+ e^-)_{indirect} < (1.27 \sim 1.6) \times 10^{-12}. \tag{A.2}$$

If we could measure the branching ratio $Br(K_S \to \pi^0 e^+ e^-)$, the indirect CP violating contribution of $K_L \to \pi^0 e^+ e^-$ is estimated through the relation,

$$Br(K_L \to \pi^0 e^+ e^-)_{indirect} = |\epsilon|^2 \frac{\tau_{K_L}}{\tau_{K_S}} Br(K_S \to \pi^0 e^+ e^-)\,, \tag{A.3}$$

because $K_S \to \pi^0 e^+ e^-$ is dominated by the same process of $K_1 \to \pi^0\gamma^*$. The experimental limit is [113]

$$Br(K_S \to \pi^0 e^+ e^-) < 4.5 \times 10^{-5}, \tag{A.4}$$

which can be interpreted that K_L branching ratio due to the indirect contribution is less than 1.3×10^{-7}. In order to reduce the theoretical ambiguity, it is necessary to measure the branching ratio of $K_S \to \pi^0 e^+ e^-$.

The process (c) in Figure 1.6 is a direct CP violating contribution. The expected rate from this contribution is [28]

$$Br(K_L \to \pi^0 e^+ e^-) = 0.32 \times 10^{-10}\eta^2 A^4 I(m_t)\,, \tag{A.5}$$

where

$$I(m_t) \simeq 0.73(\frac{m_t^2}{m_W^2})^{1.18}. \tag{A.6}$$

Numerically, theories predict the level at around $10^{-11} - 10^{-12}$ [29, 30] although there is a small disagreement between those theories.

The current experimental limit on $K_L \to \pi^0 e^+ e^-$ is obtained by E799-I at Fermilab [114, 115] as

$$Br(K_L \to \pi^0 e^+ e^-) < 4.3 \times 10^{-9}\,, \tag{A.7}$$

at the 90% confidence level, and there is no evidence of direct CP violation yet.

Appendix B

Calibration of Photon Veto Detectors

This appendix describes the calibration of photon veto detectors which had an important role to suppress backgrounds in the $K_L \to \pi^0 \nu \bar{\nu}$ search. The calibration was carried out in two stages. First path was to calibrate the gain of each channel using the response for a Minimum Ionizing Particle(MIP). The Muon Runs gave the opportunity to collect such responses for RC, SA/CIA and BA. For CA, we used charged pions in K_{e3} events to look at the response for a MIP. Once we understood the gain of every channel in all the detectors, the next step was to relate the output signal from the detector with the energy of photon hitting the photon veto counters. The following covers the two procedures in the calibration.

B.1 Cross Calibration between Modules

A MIP allows us to examine the response of each counter due to its constant deposited energy. In the Muon Runs, we calibrated the gain of photon veto detectors except for CA. The first step was to select events in which a muon hit a specific counter. In the event selection, we required a coincidence of hits in the two nearest neighboring counters. In case of channel 10 of RC9(RC6), for instance, a coincidence of hits in channel 10 of RC8(RC7) and RC10(RC8) was required. In order to ensure the muon hit in the center of the module, the adjacent modules in both sides were also required not to have any activities. This event selection yielded a nice MIP peak as shown in Figure B.1 The distribution represents only for one channel in RC9 in unit of ADC counts after pedestal subtraction.

The next step was an extraction of the peak position in each ADC distribution. Fitting the distribution with a skewed Gaussian function expressed as

$$f(x) = P1 \times exp[-\frac{1}{2} \times (\frac{x - P2}{P3 + P4(x - P2)})^2] \,, \tag{B.1}$$

we determined the peak position to be P2, and width to be P3. Repeating the same procedure for a total of 356 channels in photon veto detectors, we quantified the response for a MIP. Since some of the photon veto detectors were used as a part of online triggering, the gain was adjusted to within $\pm 10\%$ in each counter by trimming the high voltage supplied to PMTs.

For only CA, charged pions in K_{e3}'s in nominal runs were used to calibrate the gain because the Muon Runs did not supply enough statistics for CA due to its small size. The K_{e3} events were selected by the following criteria:

- Existence of two charged tracks.

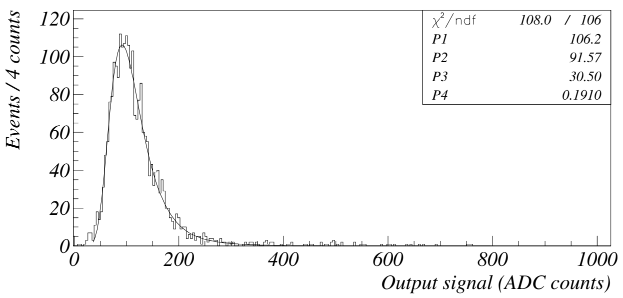

Figure B.1: The output signal from one channel in RC for muon in unit of ADC counts. The distribution is fitted with skewed Gaussian function defined in the text.

- One of the tracks must point to CA, more than 5 mm away from the edge.
- The two tracks must match to the cluster positions.
- Reconstructed vertex position in z was $95 < z(\mathrm{m}) < 158$.
- Vertex χ^2 was less than 5.
- The charged particle not pointing to the CA had an E/p of $0.9 < E/p < 1.1$.

With these event selections, the response for pions were collected, and the gain was evaluated by again fitting the output signal with the skewed Gaussian function. The on-spill pedestal was subtracted for CA calibration because its gain was small enough to be affected by the difference between on-spill and off-spill pedestals[1].

The typical ADC counts for a MIP were 80 for RC's, 200 for SA's/CIA, and 5 for CA and BA(0.25 pC/count). With respect to the gains, a long term stability was studied for RCs and SAs by using the result of MIP calibration. Through the entire runs($\sim$ 1 year[2]), the biggest variation in gain was found in RC6 to be $\pm 15.7\%$ on average for all the modules in RC6. The other RCs typically had a $\pm 10\%$ of the shift. The gain shift in SA's/CIA was within $\pm 4\%$ on average of each counter.

B.2 Energy Scale for Photons

The next step in the photon veto counters calibration was to find a relation between the output signal from each counter and the energy of photon hitting to the counter. Since the gain of each channel was calibrated now, the relation between the output and photon energy can be expressed by one conversion factor in each counter because the conversion factor was determined uniquely by the configuration of the counter and independent of the gain.

To relate the incident photon energy to the deposited energy, we looked at the response for the photons decayed from π^0 in $K_L \to \pi^+\pi^-\pi^0$ events, in which one photon was missing and π^+, π^- and another photon were detected by the calorimeter. Assuming the parent particle to be K_L, the energy and position of missing photon can be extracted by requiring the sum of p_t in the final state particles to be zero. In this calculation, one obtains two possible solutions. To solve the ambiguity, we also required the invariant mass reconstructed from the observed and missing photon to be

[1] BA also used on-spill pedestal in the gain calibration with the same reason.

[2] This studies were performed including E832 experiment which used the photon veto counters in common.

consistent with π^0 mass. The general discussion about the kinematics for missing particles can be found in reference [69].

The event selection to collect such $K_L \to \pi^+\pi^-\pi^0$ events can be summarized as:

- Two opposite charged tracks were found.
- No activities in the muon counters.
- To reject $K_{\mu 3}$'s, momenta of both tracks were required to be greater than 8 GeV/c, because the range of steel associated with muon counters was about 7 GeV/c.
- The number of clusters was required to be three, in which the two of them matched to the position pointed by charged tracks, and the rest did not match.
- To reject K_{e3}'s, E/p was required to be less than 0.8 for both charged tracks.
- Vertex was found in the range $128 < z(\mathrm{m}) < 155$.
- The vertex position projected from the target to the front face of the calorimeter must be inside of 13 cm $\times$ 13 cm squares centered at the beam holes.
- To reject $K_L \to \pi^+\pi^-$ events, an invariant mass reconstructed from the two charged particles by assuming them to be pions, $m_{\pi\pi}$, must be less than 400 MeV/c^2.
- To reject $K_L \to \pi^+\pi^-\gamma$, an invariant mass reconstructed from the three observed particles by assuming the two charged particles to be pions was required to be less than 480 MeV/c^2.
- The invariant mass reconstructed from an observed and a missing photon was required to be greater than 125 MeV/c^2 and less than 145 MeV/c^2.
- The missing photon must point to any of the photon veto counters.
- No activities in photon veto counters, except for the counter which was expected to have the hit of missing photon, was ensured by applying thresholds. The thresholds were 100 MeV for RCs and SAs/CIA, 1 GeV for CA, and 4 GeV for BA1.

For the events passing the above requirements, the energy deposited in the module, which was expected to have a hit of the missing photon, was related with the predicted photon energy as shown in Figure B.2. It shows the correlation between the deposited energy in terms of number of MIPs and the expected energy of photon in RC10, where the deposited energy is defined as the sum of energy in the pointed module and its adjacent modules. The slope in this correlation can be considered as a conversion factor which we want to extract. In fact, we fit the deposited energy distribution, in 100 MeV bin in the expected energy starting from 150 MeV, with the skewed Gaussian form shown in Equation B.1 to find the peak in each range. Fitting the peak values in each energy bin with a straight line as a function of incident photon energy, the relation between the output signal from the counters and the photon energy was established. The slope obtained in the linear fit was the conversion factor. The result was summarized in Table B.1.

The resolution defined as the P3, in the skewed Gaussian fit, divided by photon energy, σ/E_γ was also measured in the calibration of the energy scale. Since the reconstruction of missing photon also had uncertainties in both energy and position, the subtraction of the resolution in expected energy was necessary to measure the intrinsic resolution of photon veto detectors. The intrinsic resolution in each energy range was determined to be

$$\frac{\sigma_{intrinsic}}{E_\gamma} = \sqrt{(\frac{\sigma_{raw}}{E_\gamma})^2 - (\frac{\sigma_{reconst}}{E_\gamma})^2} \ ,$$

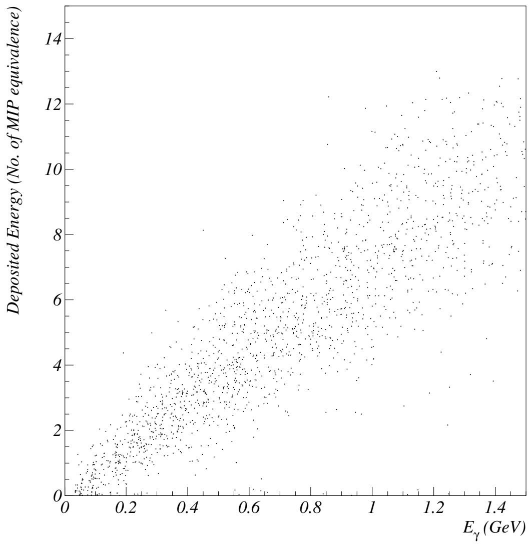

Figure B.2: Correlation between the deposited energy and expected energy of photon incident in RC10.

Table B.1: Energy conversion factor from a MIP to photon energy in the photon veto counters, and their intrinsic resolution.

Detector Element	Photon energy equivalent to a MIP	Resolution= σ/E_γ
RC	133 MeV	$7\%/\sqrt{E/(\mathrm{GeV/c})} + 19\%$
SA/CIA	195 MeV	$10\%/\sqrt{E/(\mathrm{GeV/c})} + 1\%$
CA	260 MeV	25%
BA	99 MeV	15%

where the $\sigma_{reconst}/E_\gamma$ denotes the energy resolution in reconstruction procedure, and was determined by MC studies in which we can know the true energy of the missing photon. Assuming the resolution had an energy dependence with a form of

$$\sigma/E_\gamma = \frac{A1}{\sqrt{E_\gamma}} + A0 \ ,$$

we determined the coefficients by a fit as shown in Table B.1. It is interesting to compare the energy resolution for photons and muons. Based on the results listed in Table B.1, the resolution for 133 MeV(195 MeV) photon, which should have the same energy deposited with a MIP, is expected to be 38%(24%) for RC(SA)'s, while the resolution for a MIP was measured to be 35%(30%) in RC(SA)s. This agreement implies both of energy scale and resolution were well calibrated.

Appendix C

Number of Hyperon Decays

The number of Λ and Ξ decays were directly related to the size of backgrounds from $\Lambda \to n\pi^0_D$ and other Cascade decays. This appendix outlines the estimation of the number of decayed $\Lambda's$ and $\Xi's$.

C.1 Number of Λ Decays

The principle to measure the number of decayed $\Lambda's$ was the same as used in K_L. We used $\Lambda \to p\pi^-$ events as a substitute of $K_L \to e^+e^-\gamma$.

The event selection of $\Lambda \to p\pi^-$ was summarized as below:

- There was at least one hit in trigger hodoscope.
- Two tracks with opposite charge were found.
- Decay vertex was found. In the vertex finding, we required that at least one cluster matched to the position pointed by a charged particle because most of protons went into the beam holes due to their high momenta.
- A charged pion was identified by the requirement of E/p to be less than 0.9. The other charge particle was considered as a proton.
- A proton was required to go through the beam hole.
- The same requirements as in $K_L \to \pi^0\nu\bar{\nu}$ or $K_L \to e^+e^-\gamma$ with respect to vertex quality(Section 5.3) were imposed.
- Vertex position in z was $95 < z(\mathrm{m}) < 158$.
- Proton momentum must be 3 times larger than that of pion's.
- Proton momentum must be larger than 100 GeV.
- Sum of ${p_t}^2$ was required to be less than 0.001 $(\mathrm{GeV/c})^2$.
- An invariant mass reconstructed from proton and π^-, $m_{p\pi^-}$, was required to be $1.106 < m_{p\pi^-}(\mathrm{GeV/c^2}) < 1.126$.

With the above event selection, we collected 680 $\Lambda \rightarrow p\pi^-$ events for a small data sample(the number of K_L decays was 5×10^9) with a L1 prescale factor of 20,000. The detector acceptance for the $\Lambda \rightarrow p\pi^-$ was calculated to be 21.1% from MC. Using the PDG value of $Br(\Lambda \rightarrow p\pi^-)$, 63.9%, the number of decayed $\Lambda's$ was measured to be 1.0×10^8. This implies that the ratio in the number of decays between K_L's and $\Lambda's$ was 50:1.

Based on this ratio, a total number of Λ decays was estimated to be $2.15 \times 10^{11} \times 0.02 = 4.3 \times 10^9$.

C.2 Number of Ξ Decays

The number of Cascade decays was estimated by normalizing the area of p_t distribution in MC with that in data shown in Figure 7.6. The normalization was performed in the range $130 < p_t(\mathrm{GeV/c}) < 150$. As a result, the Cascade flux was estimated to be 1.6×10^8.

Appendix D

More Background Studies

This appendix describes more background studies. The first section discusses the consistency between the background level in data and our expectation for events in the final signal region. The next section describes uncertainties on the background level estimation.

D.1 Consistency of the Number of Events in the Signal Region

Since we opened the signal box in Chapter 9, more background studies using data in the signal region can be carried out.

In order to reconfirm our understanding of the shape of each background, and the rejection factor of the cuts, and thus the expected background level, we compared the number of events in the signal region between data and our expectation by relaxing some cuts. Table D.1 lists the number of remaining events in the final signal region with the loose selection criteria. The

Table D.1: Comparisons of the number of events in the final signal region between data and our estimation, with relaxed cuts. For the photon veto cuts, the requirements on RCs, SAs and CA were removed, and a cut with a threshold of 8.5 GeV on BA1 was only applied without a distinction of the vertex position in x. With respect to the charged veto, all the requirements were removed. For the vertex quality, the cuts on vertex χ^2, σ_z, and offmag χ^2 were not applied. The requirement for the vertex position in z was relaxed to be $110 < z(\mathrm{m}) < 158$.

Relaxed Cut(s)	MC	Beam neutron interactions	Total expected	Data
Photon Vetos	1.5	1.5	3.0	5
Charged Veto	0.25	1.0	1.3	3
Vertex Quality	1.8	0.5	2.3	2
Z position	0.043	0.5	0.54	0
Z & Vertex Quality	2.3	13	15	14

numbers in the table implies that the expectation is consistent with the actual number in data within statistical error. The agreement is still excellent[1], even with the relaxed requirements with

[1] The systematic uncertainty on the background estimation will be discussed in Section D.2, however, it would

respect to both z and vertex quality, which increased the expected background level by a factor of 134.

D.2 Uncertainty on Background Estimation

The estimated background level was a product of three components: the number of decayed parent particles, branching ratio, and acceptance. This section outlines the contributions from each component to the uncertainty in the background level estimation.

D.2.1 The Number of Decayed Parent Particle

The numbers of decayed K_L's, $\Lambda's$, and $\Xi's$ are directly related to the background level.

Since the number of K_L decays was measured by normalizing $K_L \to e^+e^-\gamma$ yields, the acceptance ratio between $K_L \to e^+e^-\gamma$ and each background source is relevant to the estimation of the background level for backgrounds associated with K_L decays, which is discussed in Section D.2.3. Hence, here we only consider the statistics of the collected $K_L \to e^+e^-\gamma$ events and uncertainty on $Br(K_L \to e^+e^-\gamma)$ as sources introducing an error on the number of K_L decays. As described in Section 8.2, the MC statistics led to an error of 0.318%, and the number of observed $K_L \to e^+e^-\gamma$ led to an uncertainty of 0.792%. The quadratic sum of the two sources came to be 0.85%.

As mentioned in Appendix C.1, the number of decayed $\Lambda's$ was calculated based on $\Lambda \to p\pi^-$ events. The uncertainty in this measurement was estimated by comparing the number of events, between data and MC, in specific kinematical region where $\Lambda \to n\pi^0_D$ was expected to dominate. The event sample was the same as used in the evaluation of BA's detection efficiency for hadron(see "Hadron Detection by BA" in Section 6.2.3). The MC expected 102,489 events in the region, while real data contained 120,451 events. We regarded the disagreement of 15% as a systematic error on the number of Λ decays, neglecting the contamination of other backgrounds(the contamination was predicted to be $\sim 0.5\%$ based on MC studies).

Since we extracted the number of decayed $\Xi's$ by normalizing the area of the small peak at around 135 MeV/c in p_t distribution(Figure 7.6) after all the cuts, as mentioned in Appendix C.2, the source of error in this evaluation was a statistics of the events(the contamination of other background contributions can be negligible according to MC studies). The number of events to be used to the normalization was 59, and thus it contained an error of 13% statistically. Therefore, we conclude the error on the number of Ξ decays to be 13%.

D.2.2 Branching Ratio

As well as $\pi^0 \to e^+e^-\gamma$ or $K_L \to e^+e^-\gamma$, the Particle Data Group's branching ratios were used to estimate the background level. Table D.2 lists the uncertainties in the branching ratios for every background source. In the case that a background source is a product of multiple decays, the uncertainties were added in quadrature.

D.2.3 Acceptance Calculation

The errors in acceptance calculation were dominated by MC statistics for some modes, which is discussed at first. The next major contributions arose from uncertainties on the efficiency for the electron identification, photon vetos, and p_t cut in $\Xi \to \Lambda(\to p\pi^-)\pi^0_D$ and $\Xi \to \Lambda(\to n\pi^0)\pi^0_D$. Because of the large errors from these sources, most of other systematic contributions caused by a discrepancy between data and MC in kinematical variables, such as $m_{ee\gamma}$, had negligible effects.

be negligible compared to the statistical error.

Table D.2: The contribution of branching ratio uncertainties to the background level estimation.

Background	Uncertainty on Branching Ratio(%)
$K_L \to \pi^0\pi^0\pi^0_D$	3.2
$K_L \to \pi^+\pi^-\pi^0_D$	3.6
$K_L \to \pi^0\pi^0_D$	3.3
K_{e3}	0.7
$\Lambda \to n\pi^0_D$	3.2
$\Xi \to \Lambda(\to p\pi^-)\pi^0_D$	3.0
$\Xi \to \Lambda(\to n\pi^0)\pi^0_D$	3.2
$\Xi \to \Lambda(\to n\pi^0_D)\pi^0$	3.2

The size of background associated with beam interactions was evaluated by using real(masked) data. The size of uncertainty on the background level estimation in the beam interactions is covered at last.

MC Statistics

We calculated the acceptance for each background by generating 8×10^{-3} to 30 times larger MC sample than real data(we refer to the number of generated events equal to a product of the measured number of parent particle's decay and a branching ratio as the same size as data). In order to enhance MC events, we used two tricks described below.

First, we evaluated the efficiency of some cuts, using enhanced MC sample by relaxing the uncorrelated cuts[2]. The significant gain in statistics(a factor of $\sim 20,000$) could be attained in K_{e3}'s, but it was only about a factor of 10 for the other modes. The relaxed cuts are summarized in D.3 for each background source.

Second, the efficiencies of p_t cut on $\Xi \to \Lambda(\to p\pi^-)\pi^0_D$ and $\Xi \to \Lambda(\to n\pi^0)\pi^0_D$ were obtained by the fit of p_t shape, not by statistics.

Because of the limited CPU time[3], these two techniques were crucial to estimate each background level to the order of 0.01 events. Table D.3 summarizes the statistical uncertainties on the MC event samples. As shown in the table, the background estimation in $K_L \to \pi^0\pi^0\pi^0_D$, $K_L \to \pi^+\pi^-\pi^0_D$, K_{e3}'s, and $\Xi \to \Lambda(\to n\pi^0_D)\pi^0$ had significant contributions from the MC statistics.

Particle Identification

The charged pion rejection efficiencies in E/p cut, shower shape χ^2 and TRD were evaluated from real $K_L \to \pi^+\pi^-\pi^0$ events as mentioned in Section 5.4. Because the contamination of other events in the $K_L \to \pi^+\pi^-\pi^0$ sample was negligible, we considered only the statistical error as a source of uncertainties on the π/e separation factor.

With respect to the E/p cut, 1,126 charged particles in a total of 25,786(12,893 events in total) tracks passed the E/p requirement, and thus we estimated the fraction of pions passing the

[2] Between the two selection criteria (a) and (b), if the efficiencies of those cuts satisfy;

$$\epsilon_a \times \epsilon_b = \epsilon_{ab} \ ,$$

within $\pm 25\%$ plus a statistical error of 1σ, we considered the two cuts as uncorrelated.

[3] It would take two years in CPU time to generate K_{e3} MC sample with the same statistics of real data by a use of 10 CPUs of 440 MHz alpha chip. To evaluate the magnitude of the background with the order of 0.01 event, we need 200 years!!

Table D.3: Statistical contributions in MC sample with respect to the background level estimation. (*): The efficiencies of p_t cut were estimated from the shape, not by a statistics. The second column lists the relaxed cuts to enhance MC events. PV denotes photon veto cuts, CHV for charged veto cuts, EPH for the cut on photon energy, VQ for cuts on vertex qualities, Z for the cut on vertex position, MPT for the cuts on $m_{ee\gamma}$ and p_t, PID for the particle identification, and DAL for the Dalitz kinematics cut. Also shown is the size of MC sample generated for each background source.

Background	Stat. Error in MC(%)	Uncorrelated cuts	MC size ($\times$ data)
$K_L \to \pi^0\pi^0\pi^0_D$	100	PV&CHV&EPH&VQ	12
$K_L \to \pi^+\pi^-\pi^0_D$	100	PV&CHV&EPH&{(VQ&Z) or MPT}	4
$K_L \to \pi^0\pi^0_D$	-	PV&CHV&EPH&VQ	30
K_{e3}	90	(PID&DAL), (PID&MPT)	8×10^{-3}
$\Lambda \to n\pi^0_D$	-	-	27
$\Xi \to \Lambda(\to p\pi^-)\pi^0_D$	1.2*	-	24
$\Xi \to \Lambda(\to n\pi^0)\pi^0_D$	2.3*	-	24
$\Xi \to \Lambda(\to n\pi^0_D)\pi^0$	100	PV&CHV&EPH&(VQ&Z)	24

requirement to be $0.4367 \pm 0.01298\%$. It contained a 3.0% of relative uncertainty. With the same manner as the E/p, the efficiency in shower shape χ^2 cut and TRD were expected to have a relative uncertainty of 2.5% and 1.7%, respectively. Summing the three errors in quadrature, the total error in particle identifications in K_{e3} was determined to be 4.3%. In a case of $K_L \to \pi^+\pi^-\pi^0_D$, the error of 4.3% comes to be 8.6% because of there were two charged tracks.

Photon Veto Rejection Factor

The photon veto counters' detection efficiency directly contributed to the background level in modes which had an extra π^0 and thus a photon. The systematic contribution was studied by artificially shifting the threshold in all photon veto counters, in which the size of artificial shift was determined from the gain variation within one period of the calibration. The results of a 10% shift in the threshold are summarized in Table D.4. As shown in the table, the change in BA's

Table D.4: The variation in efficiency of photon veto cuts for backgrounds, when the threshold was artificially shifted by 10% in the photon veto counter.

Background	Shift in efficiency(%)			
	RC 10% shift	SA/CIA 10% shift	BA 10% shift	All 10% shift
$K_L \to \pi^0\pi^0\pi^0_D$	2.8	1.8	6.0	9.6
$K_L \to \pi^0\pi^0_D$	3.8	1.4	8.5	12
$\Xi \to \Lambda(\to n\pi^0)\pi^0_D$	2.1	1.4	3.4	4.9
$\Xi \to \Lambda(\to n\pi^0_D)\pi^0$	4.9	3.9	13	15

threshold largely affected the rejection factor simply because of its high geometrical acceptance. Finally, the variations of 9.6%, 12%, 4.9% and 15% were regarded as the systematic errors on the photon veto's rejection factor for the four modes in the Table D.4, respectively.

Rejection Factor in p_t Cut

By fitting the p_t shape to estimate the efficiency of the p_t cut for $\Xi \to \Lambda\pi^0_D$ events, we attained a statistical gain of a factor of 5[4]. This gain in statistics cost another systematic contribution.

Fitting the range, $0.135 < p_t(GeV/c) < 0.150$, we modeled the high p_t tail in $\Xi \to \Lambda\pi^0_D$ events as

$$f(p_t) = exp[-318.4 \times p_t/(\mathrm{GeV/c}) + 48.41]\,, \tag{D.1}$$

with a χ^2 of 8.488 for 16 degrees of freedom. Integrating this form from 160 MeV/c to 240 MeV/c, we estimated the efficiency of the p_t cut. The slope term is relevant in this fit, because the constant term corresponds to the normalization factor. Therefore, we considered the shift in the integrated area of the signal region due to the variation in slope as the error in the p_t efficiency. In Equation D.1, the slope had an error of ± 14.81. Using the slope of -318.4 ± 14.81 and normalizing the area of $0.135 < p_t(GeV/c) < 0.150$, we obtained two functions as

$$f(p_t) = exp[-303.6 \times p_t/(\mathrm{GeV/c}) + 46.44]\,,$$

and

$$f(p_t) = exp[-333.2 \times p_t/(\mathrm{GeV/c}) + 50.38]\,.$$

Integrating the above two function between 160 MeV/c and 240 MeV/c in p_t, the deviation from the original area was +56.0% and −35.9%, respectively. We conclude that +56.0% and −35.9% are the error in the efficiency estimation in the p_t cut for $\Xi \to \Lambda\pi^0_D$.

Beam Interaction Background

Since the two fits(for p_t and z distributions) were used to predict the background level from beam interactions at the vacuum window, the error arising from the two fits were added in quadrature. Each error was estimated by exactly the same procedure as used in the estimation of p_t cut for $\Xi \to \Lambda\pi^0_D$. As a result, the integral of z distribution contained an error of +13.8% and −11.0%. That in p_t integral was +16.3% and −14.8%. The quadratic sum of the two errors came to be +21.4% and −18.4%. From the size of relative error, the expected number can be written as $0.042^{+0.009}_{-0.008}$ events.

By estimating the background level from beam interactions with a different method, we considered the error on our background estimation. To investigate the contamination of non-exponential shape in z(see Figure 6.9), we looked into the side band of $m_{ee\gamma}$ distribution for high p_t events as shown in Figure D.1, which is $m_{ee\gamma}$ of events with p_t greater than 240 MeV/c and z greater than 150 m after all the other cuts. The peak at π^0 mass represents the correct reconstruction of $\pi^0 \to e^+e^-\gamma$ whose π^0 was produced by a beam interaction at the vacuum window. They corresponded to the peak at $z = 159$ m and should have a steep fall off in z. On the other hand, there is another component in high mass area with a contamination of $\Lambda \to n\pi^0_D$ events. The side band events may result from a wrong selection of a photon or an electron due to a production of multi particles in beam interactions. The contribution to π^0 mass region from the wrong combinatorial events was estimated to be 2.2 events by fitting the events in $175 < m_{ee\gamma}(\mathrm{MeV/c^2}) < 250$ with an exponential shape. The χ^2 of the fit was 15.4 for 25 degrees of freedom. As a cross check, we also fit the shape with a linear function. Based on the linear fit, the contamination was estimated to be negligible. Finally, we regarded the wrong combinatorial contamination to the signal region as 2.2 events by using the maximum number.

[4] If the gain was much large, say factor of 100, we could not estimate the rejection power by the fit because there is a possibility to emerge non-exponential tail in p_t, which is caused by photon conversions at the DC2, and can be seen in $\Lambda \to n\pi^0_D$ (Appendix E). The Ξ flux was 30 times smaller than that of $\Lambda's$, we evaluated the p_t rejection efficiency by the fit.

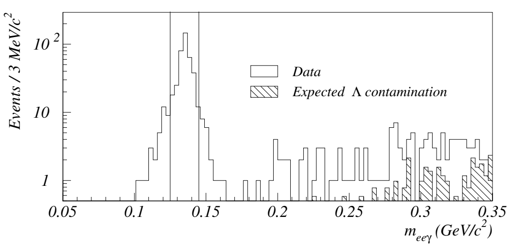

Figure D.1: The $m_{ee\gamma}$ distribution of event with $z > 150$ m and $p_t > 240$ MeV/c after applying all requirements. Open histogram shows the data, and the hatched histogram represents the expected contamination from $\Lambda \to n\pi^0_D$.

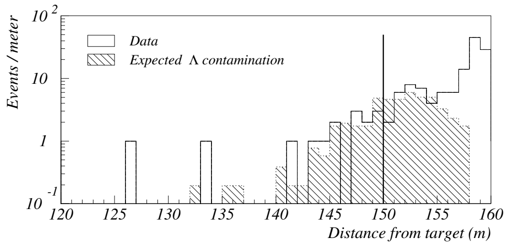

Figure D.2: The z distribution of events with $0.17 < m_{ee\gamma}(\mathrm{GeV/c^2}) < 0.35$ and $p_t > 240$ MeV/c after applying all requirements. Open histogram shows the data, and the hatched histogram represents the expected contamination from $\Lambda \to n\pi^0_D$.

Next, the z distribution of the wrong combinatorial events with $m_{ee\gamma}$ greater than 170 MeV/c^2 and less than 250 MeV/c^2 was investigated as shown in Figure D.2. The expected $\Lambda \to n\pi^0_D$ contamination was determined from MC studies. The data in $140 < z(\mathrm{m}) < 155$ is in good agreement with expected level of $\Lambda \to n\pi^0_D$. The data contains 17 events in the z less than 150 m, while the 19 events are expected to come from $\Lambda \to n\pi^0_D$. However, there were two events in the z less than 135 m although the probability to observe a $\Lambda \to n\pi^0_D$ event in the z range was 0.3%. So we assumed the two events as the ones originated from beam interactions. On the other hand, by subtracting the $\Lambda \to n\pi^0_D$ contribution, 84 events from beam interactions were expected at z greater than 150 m.

Assuming the z distribution is independent of the $m_{ee\gamma}$, $2.2 \times (2.0/84) \times 0.501(p_t\,\mathrm{shape}) = 0.026$ wrong combinatorial events in beam interactions could contaminate in the final signal region, although there was not such a tail in the z distribution shown in Figure 7.2. Therefore, we put the 0.026 events into a systematic error, and thus the final expected number of background events due to beam interactions comes to be $0.042^{+0.035}_{-0.008}$.

D.2.4 Summary

Based on the discussion in Section D.2, we finalized the error in background level for each source as shown in Table D.5. By adding each error in quadrature, the expected background level in total was determined to be $0.12^{+0.051}_{-0.038}$ events.

Table D.5: The magnitude of errors in background level estimation.

Decay mode	Expected number
$K_L \to \pi^0\pi^0\pi^0_D$	0.03 ± 0.030
$K_L \to \pi^0\pi^0_D$	< 0.01
$K_L \to \pi^+\pi^-\pi^0_D$	< 0.01
$K_L \to \pi e\nu + \gamma$	0.02 ± 0.018
$\Lambda \to n\pi^0_D$	< 0.04
$\Xi \to \Lambda(\to p\pi^-)\pi^0_D$	$0.01^{+0.006}_{-0.004}$
$\Xi \to \Lambda(\to n\pi^0)\pi^0_D$	$0.01^{+0.006}_{-0.004}$
$\Xi \to \Lambda(\to n\pi^0_D)\pi^0$	0.01 ± 0.010
$n + X \to \pi^0 X'$	$0.04^{+0.035}_{-0.008}$
Total	$0.12^{+0.051}_{-0.038}$

Appendix E

Further Background Suppression

In Section 9.4.1, we mentioned the background level at the sensitivity with one order of magnitude better than our result. We here discuss the further suppression for major backgrounds in a $K_L \to \pi^0 \nu\bar{\nu}$ search with π^0 Dalitz decay by tightening the selection criteria.

For backgrounds coming from beam interactions in the vacuum window, tighter z requirement could reduce its magnitude, assuming non-exponential shape would not emerge even in the sensitivity with one order of magnitude better than ours. For instance, the requirement, $z < 146$ m, will give 16 times more suppression with a 14% signal loss. This shows an excellent advantage in the Dalitz mode, in contrast to the two photon mode which suffers from this background.

In order to reduce background from $\Xi \to \Lambda\pi^0_D$, we can tighten the p_t requirement. Since the tail of p_t at high end is falling down exponentially as shown in Figure 6.15, raising the lower bound of p_t from 160 MeV to 170 MeV will suppress the Cascade backgrounds by a factor of 20 with a cost of 14% signal loss.

The only effective way to further suppress backgrounds from $K_L \to \pi^0\pi^0\pi^0_D$ is to have a more powerful photon veto system. This is because the events passing our cuts on kinematics chose a wrong photon to reconstruct $m_{ee\gamma}$ and thus distributed uniformly in p_t and $m_{ee\gamma}$ plane[1]. Since the geometrical acceptance of BA is quite higher than the other photon veto detectors, tightening a cut on BA gives the best rejection. An additional BA cut, BA1 energy to be less than 2 GeV, is expected to reduce $K_L \to \pi^0\pi^0\pi^0_D$ by a factor of 2.3 whereas it costs a signal loss of 37% over the current level. Therefore, given a 10 times more K_L decays with a 2 GeV threshold for BA, the SES would be improved by a factor of 6 with $0.13(=0.03 \times 10/2.3)$ expected $K_L \to \pi^0\pi^0\pi^0_D$ background events. To suppress the $K_L \to \pi^0\pi^0\pi^0_D$ in much better sensitivity, say $O(10^{-9})$, an improvement in photon veto detectors will be necessary.

Since the background level from K_{e3}'s is expected to be 0.2 events with 10 times better sensitivity, it would not be crucial in a search with a sensitivity of order 10^{-8}. Besides, we can obtain an additional rejection factor of $\sim$2 from tighter E/p cut with a percent level signal loss, factor of $\sim$3 from tighter requirement on TRD with a cost of 20% signal loss. However, it seems difficult to suppress K_{e3}'s to the same level with our search at a sensitivity better than two orders of magnitude without any improvements in detector technology.

The background level from $\Lambda \to n\pi^0_D$ was estimated to be < 0.04 events in our sensitivity. For a search with better sensitivity, photon conversions at the DC2 in $\Lambda \to n\pi^0_D$ events will be severe backgrounds, because e^+e^- would be created sometimes with very asymmetric energy and the lower energy particle would be swept out by the momentum kick at the analyzing magnet. The remaining particle could be identified as a photon with an incorrect kinematics due to a lack of track

[1] Even in case of wrong selection of photon, p_t tends to be lower than 200 MeV as can be seen in Figure 6.1. It is limited by other π^0's energy. Therefore, we can reduce $K_L \to \pi^0\pi^0\pi^0_D$ by requiring p_t to be less than $\sim$200 MeV, but it is not realistic because of huge signal loss.

in upstream segment and thus it can not be regarded as a physical track. When the conversion will occur more upstream, it would be recognized as three track event and can be removed. Also, the conversion at more downstream will not bring such a problem because the energy and flight direction of the e^+e^- is almost the same with the original photon due to its extremely narrow opening angle between electron and positron, and kinematically identical with the original photon. The background caused by such a photon conversion at the DC2 does not have a exponential tail in high p_t region. Our estimation is limited by statistics to study the contamination due to such backgrounds to the signal region. Therefore, what we can now predict about this background is that it must be less than 0.4 events in 10 times better sensitivity. More studies for this background are crucial in further searches with Dalitz mode.

Bibliography

[1] W. Pauli, *Niels Bohr and the Development of Physics.* Pergamon Press, Elmsford, N.Y., 1955.

[2] J. Schwinger, *Phys. Rev.* **91,** 713(1953).

[3] T.D. Lee and C.N. Yang, *Phys. Rev.* **104,** 254(1956).

[4] C.S. Wu *et al.,* Phys. Rev. **105,** 1413(1957).

[5] T.D. Lee, R. Oehme, and C.N. Yang, *Phys. Rev.* **106,** 340(1957).

[6] J.H. Christenson, J.W. Cronin, V.L. Fitch, and R. Turlay, *Phys. Rev. Lett.* **13,** 138(1964).

[7] M. Gell-Mann and A. Pais, *Phys. Rev.* **97,** 1387(1955).

[8] T.D. Lee, R. Oehme, and C.N. Yang, *Phys. Rev.* **106** 340(1957).

[9] T.T. Wu and C.N. Yang, *Phys. Rev. Lett.* **13** 380(1964).

[10] R.G. Sachs, *Ann. Rev.* **22** 239(1963).

[11] R.G. Sachs, *The Physics of Time Reversal,* The University of Chicago Press, Chicago, 1987.

[12] C.O. Dib and B. Guberina, *Phys. Lett.* **4B255,** 113(1991).

[13] Particle Data Group, *Phys. Rev.* **D54,** 1(1996).

[14] T.R. Wu and C.N. Yang *Phys. Rev. Lett.* **13,** 380(1964).

[15] O.E. Overseth. *Phys. Lett.* **B111,** 286(1982).

[16] L.Bergstřom, E. Massó, and P. Singer, *Phys. Lett.* **B131,** 229(1983).

[17] L.K. Gibbons et al., *Phys. Rev. Lett.* **70,** 1203(1993).

[18] G.D. Barr et al., *Phys. Lett.* **B317,** 233(1993).

[19] B. Winstein and L. Wolfenstein, Rev. Mod. Phys. **65,** 1113(1993).

[20] M. Kobayashi and Maskawa T., *Prog. Theory. Phys.* **49,** 652(1973).

[21] N. Cabibbo, *Phys. Rev. Lett.* **10,** 531(1963).

[22] L. Maiani, in *Proceedings of the International Symposium on Lepton and Photon Interacton at High Energeies,* DESY, Hamburg, edited by F. Gutbrod (DESY, Hamburg), p.867.

[23] L. Wolfenstein, *Phys. Rev. Lett.* **51,** 1945(1983).

[24] O. W. Greenberg, *Phys. Rev.* **D42,** 1841(1985).

[25] C. Jarlskog, *Phys. Rev. Lett.* **55,** 1039(1985).

[26] D. D. Wu, *Phys. Rev.* **D33,** 860(1986).

[27] L. M. Sehgal, *Phys. Rev.* **D38,** 808(1988).

[28] L. Littenberg and G. Valencia, *Ann. Rev. Nucl. Part. Sci.* **43,** 729(1993).

[29] A.J. Buras, M.E. Launtenbacher, M. Misiak, and M. Munz. *Nucl. Phys.* **B423,** 349(1994).

[30] J. F. Donoghue, B. R. Holstein, and G. Valencia, *Phys. Rev.* **D35,** 2769(1987).
C. O. Dib, I. Dunietz, and F. J. Gilman, *Phys. Rev.* **D39,** 2639(1989).
P. Heiliger and L. M. Sehgal, *Phys. Rev.* **D47,** 4920(1993).
G. Ecker, A. Pich, and E. de Rafael, *Nucl. Phys.* **B291,** 692(1987).
G. Ecker, A. Pich, and E. de Rafael, *Phys. Lett.* **B183,** 363(1987).

[31] P. Paganini, F. Parodi, P. Roudeau, and A. Stocchi. hep-ph/9711261(1997).

[32] S. Stone. *B Decays,* 2nd edition, World Scientific, Singapore (1994).

[33] A.J. Buras, hep-ph/9711217.

[34] P. Paganini, F. Parodi, P. Roudeau, and A. Stocchi. hep-ph/980229(1998).

[35] L.S. Littenberg, *Phys. Rev.* **D39,** 3322(1989).

[36] G. Buchalla and G. Isidori. hep-ph/9806501(1998).

[37] J.L. Ritchie and S.G. Wojcicki, *Rev. Mod. Phys.* **65,** 1149(1993).

[38] H.S. Hagelin and L.S. Littenberg, MIU-THP-89/039(1989).

[39] D. Rein and L.M. Sehgal, *Phys. Rev.* **D39,** 3325(1989).

[40] G. Buchalla and A.J. Buras, *Nucl. Phys.* **B398,** 285(1993).

[41] G. Buchalla and A.J. Buras, *Nucl. Phys.* **B400,** 225(1993).

[42] C.O. Dib, I. Dunietz and F.J. Gilman, *Mod, Phys. Lett.* **A6,** 3573(1991).

[43] A.J. Buras, *Phys. Lett.* **B333,** 476(1994).

[44] W.J. Marciano and Z. Parsa, *Phys. Rev.* **D53,** R1(1996).

[45] G. Buchalla and A.J. Buras, *Phys. Rev.* **D54,** 6782(1996).

[46] H. Leutwyler and M. Roos. *Z. Phys.* **C25,** 91(1984).

[47] S. Adler et al., *Phys. Rev. Lett.* **79,** 2204(1997).

[48] L. Wolfenstein, *Phys. Rev. Lett.* **13** 562(1964).

[49] J. Liu and L. Wolfenstein, *Phys. Lett.* **B197,** 536(1987).

[50] J.M. Gérard and T. Nakada, *Phys. Lett.* **B261,** 474(1991).

[51] B. Winstein, *Phys. Rev. Lett.* **68** 1271(1992).

[52] C.E. Carlson, G.D. Dorata, and M. Sher, hep-ph/9606269(1996).

[53] G. Bélanger, C.Q. Geng, and P. Turcotte, *Phys. Rev.* **D46,** 2950(1992).

[54] G.C. Branco. *Phys. Rev.* **D22,** 2901(1980).

[55] J. Liu and L. Wolfenstein. *Nucl. Phys.* **B289,** 1(1987).

[56] S. Weinberg. *Phys. Rev. Lett.* **37,** 657(1976).

[57] T. Hattori, T. Hasuike, and S. Wakaizumi, hep-ph/9804412(1998).

[58] Y. Grossman and Y. Nir, SLAC-PUB-7380, hep-ph/9701313(1997).

[59] Y. Grossman, SLAC-PUB-7443, hep-ph/9704208(1997).

[60] S. Adler et al., *Phys. Revv. Lett.* **76,** 1421(1996).

[61] S. Adler et al., *Phys. Revv. Lett.* **79,** 2204(1997).

[62] J.W. Cronin et al., *Phys. Rev. Lett.* **18,** 25(1967).

[63] P.C. Wheeler, PhD thesis, Princeton University, 1968.

[64] G.E. Graham et al., *Phys. Lett.* **B295,** 169(1992).

[65] M. Weaver et al., *Phys. Rev. Lett.* **72,** 3758(1994).

[66] K. Arisaka et al., KTeV Design Report, FN-580(1992).

[67] T. Nakaya, PhD thesis, Osaka University, 1995.

[68] F. Leber, et al., *Phys. Lett.* **B369,** 69(1996).

[69] L.K. Gibbons, PhD thesis, University of Chicago, August 1993.

[70] X. Artru, G.B. Yohl, and G. Monessier, *Phys. Rev.* **D12,** 1289(1975).

[71] M.C. Ter-Milikaelian, High Energy Electromagnetic Processes in Condensed Media (Wiley-Interscience, NY 1972).

[72] A. Roodman, *Conference Record of ICHEP 96,* July 1996.

[73] M. Asner et al., *Nucl. Inst. and Meth.* **A291,** 577(1990).

[74] M.J. Haney et al., *Conference Record of the 1992 Nuclear Science Symposium,* 338(October 1992).

[75] C. Bown, E. Cheu, J. Dusatko, H. Sanders, and M. Zeleznik, *Nucl. Inst. and Meth.* **A369,** 248(1996).

[76] P. Mikelsons, *KTeV Internal Memo* **0347,** November 1995.

[77] R. Kessler, *KTeV Internal Memo* **0361,** January 1996.

[78] V. O'Dell and T. Yamanaka, *KTeV Internal Memo* **0184,** June 1994.

[79] T. Nakaya et al., *Proceedings of CHEP 95,* September 1995.

[80] R. Brun et al., *CERN DD 78-2, "Simulation program for particle physics experiments, GEANT: user guide and reference manual",* 1978.

[81] Application Software Group Computing and Networks division CERN, CERN Program Libraray Long Writeup W5013, 1993.

[82] A.J. Malensek, Preprint FN-341, Fermi National Accelerator Laboratory, October 1981.

[83] L.G. Pondrom, *Physics Report* **122,** XX(1985).

[84] Skubic et al., *Phys. Rev.* **D18,** 1355(1978).

[85] N.G. Deshpande and G. Eilam, *Phys. Rev. Lett.* **53,** 2289(1984).

[86] Particle Data Group, *Phys. Rev. Lett.* **B111,** 73(1982).

[87] N.M. Kroll and W. Wada, *Phys. Rev.* **98,** 1355(1955).

[88] K.E. Ohl et al., *Phys. Rev. Lett.* **65,** 1407(1990).

[89] G. D. Barr et al., *Phys. Lett.* **B240,** 283(1990).

[90] M.B. Spencer et al., *Phys. Rev. Lett.* **74,** 3323(1995).

[91] M.V. Chizhov. CERN Preprint hep-ph/9511287(1995).

[92] G. Donaldson et al., *Phys. Rev.* **D9,** 2960(1974).

[93] H.A. Bethe, *Phys. Rev.* **89,** 1256(1953).

[94] W.T. Scott, *Rev. Mod. Phys.* **35,** 231(1963).

[95] J.W. Motz, H. Olsen, and H.W. Koch, *Mod. Phys.* **36,** 881(1964).

[96] R. Ford and W. Nelson, Technical Report UC-32, SLAC, June 1978.

[97] W.R. Nelson, H. Hirayama, and W.O. Rogers, The egs4 code system, Preprint SLAC Report-265, Stanford Linear Accelerator Center, 1985.

[98] A.F. Bielajew, Preprint PIRS-0287(1991).

[99] R. Talman, *Nucl. Inst. and Meth.* **159,** 189(1979).

[100] H. Maccabee and D. Papworth, *Phys. Lett.* **A30,** 241(1969).

[101] R.A. Briere. PhD thesis, University of Chicago, June 1995.

[102] H. Cramér, *Mathematical Methods of Statistics,* Princeton University Press, New Jersey (1958).

[103] R.A. Fisher, *Statistical Methods for Research Workers,* 8th edition, Edinburgh and London (1941).

[104] E.D. Zimmerman. *KTeV Internal Memo* **0493,** January 1998.

[105] T. Nakaya, Flavor Changing Neutral Current Conference, Santa Monica, CA (1997). KTeV Collaboration. hep-ex/9806007(1998).

[106] E. Cheu et al., Fermilab EOI, "An Expression of Interest to Detect and Measure the Direct CP Violating Decay $K_L \rightarrow \pi^0\nu\bar{\nu}$ and Other Rare Decays at Fermilab Using the Main Injector", hep-ex/9709026(1997).

[107] I-H. Chiang et al., BNL Proposal P926, "Measurement of $K_L \rightarrow \pi^0\nu\bar{\nu}$", September 1996.

[108] T. Inagaki et al., KEK Proposal, "Measurement of the $K_L \rightarrow \pi^0\nu\bar{\nu}$ decay", June 1996.

[109] M. Weaver et al., PhD thesis, University of California, Los Angeles, January 1995.

[110] V. Papadimitriou et al., *Phys. Rev.* **D44,** R573(1991).

[111] G. D. Barr et al., *Phys. Lett.* **B284,** 440(1992).

[112] C. Alliegro et al, *Phys. Rev. Lett.* **68,** 278(1992).

[113] L. K. Gibbons et al., *Phys. Rev. Lett.* **61,** 2661(1988).

[114] D. A. Harris et al., *Phys. Rev. Lett.* **71,** 3918(1993).

[115] D. A. Harris, PhD thesis, University of Chicago, April 1994.